DISS. ETH NO. 22189

Smart soft materials for microrobotics

A thesis submitted to attain the degree of

DOCTOR OF SCIENCE of ETH ZÜRICH

(Dr. sc. ETH ZÜRICH)

presented by

Stefano Fusco

MSc., Politecnico di Milano

Born on December, 3rd, 1983

Citizen of Italy

accepted on the recommendation of

Prof. Dr. Bradley J. Nelson, examiner

Prof. Dr. Kostas Kostarelos, co-examiner

Dr. Salvador Pané Vidal, co-examiner

2014

Table of Contents

Acknowledgements	viii
Abstract	xii
Sommario	xvi
CHAPTER 1	
Introduction	1
1.1 Thesis motivation and background	2
1.2 Aims of the thesis	4
1.3 Dissertation outline	5
1.4 References	7
CHAPTER 2	
Soft microrobots: the impact of materials on the new generation of biomedical intelligent microdevices	9
2.1 Introduction	10
2.2 Soft polymeric materials in MEMS and biomedical robotics	12
2.3 Smart hydrogels in MEMS	16
2.3.1 Hydrogel based smart surfaces	18
2.3.2 Self folding devices	22
2.4. Soft microrobots: state of the art	25
2.5 Summary and perspective	31

2.6 References 32

CHAPTER 3

Chitosan electrodeposition for microrobotic drug delivery 41

3.1 Chapter overview 42

3.2 Electrodeposition of chitosan from aqueous solutions 44

3.3 State of the art in electrodeposition of chitosan 48

3.4 Motivation: a smart microrobot for drug delivery in the eye 53

3.5 Materials and methods 56

3.5.1 Preparation of the solutions and the substrates 56

3.5.2 Electrodeposition of chitosan and post deposition treatments 57

3.5.3 Electrodeposition on microrobotic platforms 58

3.5.4 Characterization of the chitosan growth 58

3.5.5 Cryo-SEM imaging 59

3.5.6 Chemical characterization 59

3.5.7 Drug delivery experiments 60

3.6 Results 61

3.6.1 Analysis of growth and control of the thickness 61

3.6.2 Post-deposition treatments 63

3.6.3 Drug loading and release experiments 70

3.6.4 Electrodeposition on microcapsules 80

3.7 Discussion 82

3.8 Conclusions and outlook 90

3.9 Bibliography 93

CHAPTER 4

An integrated microrobotic platform for on-demand, targeted therapeutic interventions 97

4.1 Chapter overview 98

4.2. Self-folding: from nature to biomedical applications 100

4.2.1 Self-folding in nature: a peculiar case of self-assembly 100

4.2.2 Self-folding in micro fabrication of biomedical devices 102

4.2.3 Self-folding hydrogel films: state of the art 105

4.3 Motivation: a soft, smart microrobotic platform for cell and drug delivery 110

4.4 Materials and Methods 114

4.4.1 Materials 114

4.4.2 Graphene oxide synthesis and characterization 114

4.4.3 Hydrogel bilayer fabrication 115

4.4.4 Cryo-SEM imaging 117

4.4.5 Swelling studies 118

4.4.6 NIR light actuation of the hydrogel nanocomposite 119

4.4.7 Fabrication of magnetic microbeads 119

4.4.8 Cytotoxicity tests 121

4.4.9 Bead loading, magnetic manipulation and actuation 122

4.5 Results 123

4.5.1 GO hydrogel nanocomposites: fabrication and characterization 123

4.5.2 Beads fabrication 128

4.5.3 Backside photolithographic fabrication of hydrogel bilayers 130

4.5.4 Cytotoxicity tests on the hydrogel bilayers and on alginate beads 131

4.5.5 Characterization of the bilayers and preparation of the microrobots 135

4.5.6 Manipulation and actuation 136

4.6 Discussion 139

4.7 Conclusion and Outlook 146

4.8 Bibliography 148

CHAPTER 5

Towards the modeling of hydrogel bilayer actuation 153

5.1 Chapter overview 154

5.2. Synthesis and characterization of acrylic hydrogel structures 157

5.2.1 Synthesis and physical structure 157

5.2.2 Equilibrium swelling theory 160

5.2.3 Rubber elasticity 161

5.2.4 Swelling kinetics of hydrogel networks 163

5.2.5 Characterization methods of hydrogel properties 168

5.3 Modelling the bending of a hydrogel bilayer 172

5.3.1 The Timoshenko beam theory and other analytical models 172

5.3.2 FEM based models of bilayers 177

5.4 Motivation: predicting the actuation of a hydrogel bilayer 179

5.5 Materials and methods 182

5.5.1 Materials 182

5.5.2 Hydrogel fabrication 182

5.5.3 Chemical analysis 183

5.5.4 Swelling experiments 184

5.5.5 Rheological measurements 185

5.5.6 Tensile tests 185

5.5.7 In situ imaging of the bending of rectangular bilayers 187

5.5.8 FEM simulation 188

5.6 Results 190

5.6.1 FTIR analysis 190

5.6.2 Swelling kinetics 191

5.6.3 Diffusion coefficients and swelling related parameters 194

5.6.4 Temperature dependence of the swelling ratio. Influence of synthesis parameters 198

5.6.5 Interpenetration: analysis of the equilibrium swelling ratio 200

5.6.6 Rheological studies 202

5.6.7 Tensile tests 205

5.6.8 Visual analysis of bilayers 209

5.6.9 Analysis of curvature based on Timoshenko model 213

5.6.10 FEM model 215

5.7 Discussion 218

5.8 Conclusions and Outlook 226

5.9 Bibliography 228

CHAPTER 6

Morphing microrobots for medical applications: the influence of shape in drug delivery and locomotion 233

6.1 Chapter overview 234

6.2. The role of shape in the microscale 237

6.3 Motivation: the influence of shape in drug delivery and locomotion 240

6.4. Materials and methods 242

6.4.1 Materials 242

6.4.2 Hydrogels fabrication 242

6.4.3 Characterization of the magnetic nanoparticles 244

6.4.4 Characterization of the hydrogel magnetic nanocomposites 244

6.4.5 Drug delivery experiments 245

6.4.6 Manipulation of the magnetic hydrogel bilayers 246

6.4.7 Simulations of the behavior of the microstructures 246

6.5. Results 249

6.5.1 Characterization of the self-folding microtubes 249

6.5.2 Drug delivery experiments 256

6.5.3 Magnetic composites actuation and manipulation 259

6.5.4 FEM based analysis of drug release from differently shaped tubular structures 259

6.5.5 FEM based analysis of drag forces acting on microrobots in a water flow 261
6.6 Discussion 263

6.7 Conclusions and Outlook 270

6.8 Bibliography 272

CHAPTER 7 277

7.1 Conclusions 278

7.2 Bibliography 285

APPENDIX I 289

APPENDIX II 293

Publications 295

Acknowledgements

The truth is, if I had to mention something about all the people that passed by, smiled, talked, worked or just thought about helping to arrive to this point, I would probably fill the entire pages of this dissertation and more. 4 years and some months have led me to the conclusion that nothing can be done alone. So I am happy to share this with all the people that contributed to this PhD work.

I want to start with my colleagues. Thanks to the entire IRIS group, I always found myself pretty comfortable in the office, at every day and every night hour. Thanks to Sandro, Hsi Wen, Simone, Juho, Berna, André, Naveen, Ayoung, Janis, Olgac, Roel (Rüül), and to the people that left before i finished, Kathrin, Simon, BK, Kartik, Kaiyu, Didi, Christos and Li. Special mention to whoever happened to share the office with me; from Arif to Dimitris, to today's squad: Taylor, George, Franzi, Bumbum, and Famin. I had lot of fun and random noise with you guys.

Only one criticism to all of us: guys, we should run more.

Thanks to Brigitte and Kerstin. They make life easier, which is a very good thing. And they smile and laugh, which is extremely important.

Special thanks to the students I had the pleasure to supervise or "be supervised ". From Valia, to Matthias, André, Rocco, Nathanel, Sascha, and Moritz, they always listened to me, also when I would not have listened to me myself. And they worked! Same for the collaborators I had, from Damiano, to Tessa, to Gautam, to Arabella, to Christian; it was very instructive, productive and mostly funny to work with all of you. Thanks to

Peter, from the other side of the world, for the fast and careful proofreading of my thesis.

My biggest gratitude goes to two researchers who guided me through these years. Salvador, your help has been incalculable in some hard situations. I will be happy to see you becoming a professor some of these days. Same for you, Selman, I sincerely think you are doing a great job, and you will be successful in it.

Thanks to Prof. Bradley Nelson. I truly appreciated all our discussions, the criticisms and the immense support to my work. If I wanted to be a professor, I would have a good example to follow. I still do not understand why you hired me, but eventually you were right.

Thanks to Prof. Kostas Kostarelos, who decided to co-supervise my thesis, even without having met me before. I hope this work is worth it.

There's a ton of people I knew during these years, and most of them have really pushed me forward, and constitute the nicest memories of these years. Thanks to the Trombino FC, the most unsuccessful and convulsionary football team that could be established. I am proud to lose every time with you guys. And thanks to the people of Tuesday Football, together we did something that should be banned from every football field of the world.

Thanks to the Muddy Roots, the best band that could have ever played in the dirtiest bars of Zurich. Beppe, Fiore, Antonio, Chris and then Paola, Taylor, Martin, it was a pleasure to make noise with you.

Thanks to the All President's women, a nice group of random dudes and girls.

Thanks to the Wednesday Potato's lunch guys, Stefano, Carlo, and Valerio

and the runners Megan, Maxi, Stefano and Johannes. We did approximately 100 km together around Europe. And approximately 15 cheeseburgers per half marathon.

Thanks to my Friends in Italy, Paolo, Marcello, and Daniele. And then again Claudia, Elisa, Matteo, Ross, and the doctors Mara and Paolo. Despite the mountains and the seas in the middle, I somehow have the feeling that we are not too far away and that we walk together. Nobody knows where.

Thanks to Samuele Tosatti, and to that lady that interviewed me at Roche in 2009. They were both sure I would have gained a lot from this experience. Somehow I trusted them.

My life in Zurich started seven years ago, in the house of Chiara (ciao Chiara!), and then moved to a smelly kitchen in the Vinzenz Studentenhaus. Then it moved to a nice house in Oerlikonerstrasse, with a fireplace and a big terrace. Then finally it settled down in a 3 rooms apartment in Hönggerstrasse, with a jukebox on the corner of the living room. The people I lived with are somehow my Zurich family and I am happy to pay them back (if possible) for all the good times that we shared together.

Simone and Guido, you are wonderful companions, flatmates, football TV watchers, dinner partners, and beer drinkers. I am looking forward to sharing much more with you and your families in the future.

Spampi and Lucy, you are extraordinary people, and I am grateful to you for the great relaxing atmosphere in Oerlikonerstrasse, during the most challenging times of this experience. And also when Pina cut down my tomato plant: that was traumatic.

Sghi, I did not live with you but somehow I cannot put you in any other box. I slept in the same bed with you a lot of times though. So I guess it counts. Thanks for having shown me that you can be a good researcher and a perfect fool at the same time.

Beppe (and Clara) and Fiore, thanks for having insulted me for the last five years. It was a karmic moment, and I know it is our way to show that we love each other.

Grazie alla mia famiglia, quella vera. Grazie a papà, mamma, Nico (& Stefano) e Maria Chiara. Per la maggior parte di questa avventura nessuno di noi sapeva veramente che cosa stessi facendo. Ma voi sapevate che stavo facendo la cosa giusta. Grazie per esserci sempre; ah, ora piu o meno so che cosa ho fatto, magari poi ve lo spiego.

Last, but not least, thank you to my sweet Franziska. You have been there for most of this thesis, and if I did a dedication, I would dedicate this work to you. I love the way you shape my life.

Abstract

Microrobots have increasingly been associated with life science applications in the last twenty years. It is the current belief that micro and nanometer sized mobile agents will soon be able to accomplish many therapeutic tasks in the body in a minimally invasive and targeted way. The current goal of many research groups is to provide the tools and the methods for their fabrication, navigation, control, and interaction with the human body. The field has currently taken advantage of well-established MEMS (microelectromechanical systems) technologies to fabricate devices that are "small enough" for the purpose, while their intelligence, locomotion and actuation abilities rely on complex externally automated platforms. The state of the art is currently based on wireless magnetic manipulation, while tracking methods range from computer vision to magnetic detection, ultrasound, and thermal imaging.

The aim of this doctoral work is to show the possibility to achieve "on board" additional features, targeted toward biomedical applications, by including soft smart hydrogels during the fabrication process. These polymeric networks resemble biological tissues in their chemical and physical properties and are often used for biomedical applications, thanks to their intrinsic biocompatibility. Moreover they are able to respond to external stimuli, such as a change of pH, temperature, or concentration gradients. Hydrogels are particularly attractive because their properties and actuation can be tailored, with regard to their application, biological environment, or kind of stimuli required.

In the first part of this thesis, soft hydrogel-based microrobots and micro- and nanofabrication methods for shaping polymer and soft-materials for robotics applications are briefly reviewed. These examples can be linked with the more general trend in robotics to exploit soft polymeric materials for the design of biomimetic robots, with enhanced properties compared to the traditional stiff machines.

Following this introduction, four chapters describe the experimental work that constitutes the core of this dissertation. Considering the current majority of microrobotic prototypes, the first goal was to develop a strategy for soft smart hydrogel coatings on hard complex substrates and overcome the typical problems of delamination or poor actuation of the polymeric parts. This was achieved by electrodeposition of chitosan, a pH responsive biopolymer, which forms stable highly swelling hydrogels at basic conditions. Chitosan can be cathodically electrodeposited on conductive substrates with different shapes and architectures due to the induced electrolysis of water. The formation of hydrogen at the cathode (substrate) leads to an increase of pH, which, in turn, causes the immobilization of responsive chitosan films. This method was used to manufacture smart drug delivery platforms for targeted therapies in the posterior segment of the eye. The films provided a sustained drug release by diffusion at physiological pH. Slight acidic conditions (similar to the ones found in tumors or inflamed tissues) caused solubilization of chitosan and significant acceleration of drug release. The described method can be adapted for different available biopolymers (such as alginate, or hyaluronic acid) and implemented for the fabrication of multifunctional smart films on microdevices capable of responding to changes in the environmental conditions.

The second experimental work combines a self-folding, near infrared light (NIR) sensitive bilayer, magnetic alginate beads, and a 3D electromagnetic manipulation system in a targeted, on-demand drug and cell delivery platform. This approach enables the fabrication of smart fully hydrogel-based microrobots whose behavior can be remotely and reversibly controlled and modified.

Self-folding assembly provided the flexible strategy to create 3D structures of different shapes and sizes through photolithography. The intrinsic thermal responsive properties of N-isopropylacrylamide (NIPAAM) were exploited and modified with acrylamide (AAM) and graphene oxide (GO) to create a highly-swelling, light-sensitive film with a phase transition around 40°C. The layer was combined with a stiffer poly(ethyleneglycol) diacrylate (PEGDA) film to reach a full-closed folded conformation upon swelling. Magnetic alginate beads were encapsulated in the bilayer and used for magnetic actuation and as cell scaffolds. Characterization of the material properties, actuation, and manipulation in water environments are described and show the potential of this prototype for *in vivo* applications in body fluids. The self-folding bilayer was further characterized in an attempt to provide a modelling tool based on the swelling and mechanical properties of the layers. Results suggest that it is not possible to predict the final curvature with the traditional analytical model of the Timoshenko equation of bending bilayers. Moreover, this fabrication method and the bilayer configuration introduce deviations from the behaviors of the single layers. These problems need to be taken into account to approach the final curvature by means of finite element method (FEM) based simulations.

Finally, the consequences of changes in shape in swimming biomedical hydrogel-based microrobots are analyzed in terms of locomotion and

actuation. Tubular shaped bilayers, which unfold forming open squares, were made of nanocomposites responsive to NIR light or magnetic fields. The first ones were used to study the drug delivery performance as a function of their unfolded/folded states. The behavior of magnetic-responsive hydrogels was investigated in a fluid environment and the drag forces simulated in the different conditions and orientations to the flow. These studies illustrate again the importance of responsive hydrogel materials in microrobotics and constitute a step forward to fully autonomous medical microdevices.

Sommario

Negli ultimi vent'anni, la microrobotica è stata sempre più frequentemente associata al campo delle scienze mediche e biomediche. E' infatti convinzione comune che agenti mobili di dimensione micro e nanoscopica possano essere presto in grado di compiere interventi mirati all'interno del corpo umano in maniera da ridurre al minimo l'invasività delle operazioni. L'obiettivo comune di molti gruppi di ricerca impegnati nel campo è di creare gli strumenti e i metodi per la fabbricazione, il controllo e l'azionamento di questi microdispositivi all'interno del corpo umano. Al momento, l'industria dei MEMS (microelectromechanical systems) costituisce la base tecnologica per la produzione di dispositivi che siano " piccoli abbastanza" per lo scopo finale, mentre l'intelligenza, la capacità di locomozione e attivazione dei microrobot si basano su attrezzature esterne per il controllo magnetico, e su mezzi di localizzazione che spaziano dal rilevamento ottico, a quello magnetico a quello termico o a base di ultrasuoni.

Lo scopo di questa tesi di dottorato è dimostrare la possibilità di raggiungere gradi di funzionalità aggiuntive, finalizzati a trattamenti biomedici, attraverso l'introduzione di idrogeli intelligenti durante il processo di fabbricazione dei microrobot. Gli idrogeli sono delle strutture tridimensionali polimeriche che assomigliano ai tessuti biologici in termini di proprietà fisiche e chimiche, e per questo e la loro naturale biocompatibilità, sono spesso usati in applicazioni biomediche. In aggiunta, alcuni specifici materiali sono in grado di rispondere a stimoli esterni, come un cambio di pH, di temperatura o del livello di concentrazione di un soluto, modificando il loro grado di interazione con l'acqua. Per finire, risultano particolarmente attraenti per la loro flessibilità, ossia per la possibilità di modificare le loro

proprietà, in base all'applicazione finale, al contesto e al tipo di stimolo necessario.

Una prima parte della tesi propone una descrizione dei pochi esempi di microrobot fabbricati con materiali idrogelici, descrivendoli come facenti parte di una generale tendenza del campo della robotica e dei microsistemi di adottare materiali soffici e polimerici. Questo cambiamento è legato principalmente ad un approccio sempre più biomimetico, e alla necessità di creare strutture che possano interagire in maniera sicura con esseri viventi, fino al livello cellulare.

Il lavoro sperimentale è descritto nei quattro capitoli centrali della tesi. Considerando la natura della maggior parte dei prototipi microrobotici, un primo obiettivo sperimentale era stabilire un metodo per la creazione di rivestimenti funzionali a base di idrogeli su dispositivi e substrati metallici, e superare i tipici problemi di delaminazione e limitata attuazione propri di questi materiali. L'obiettivo è stato raggiunto tramite un processo di deposizione elettroforetica di chitosano, un polimero biologico sensibile a cambiamenti di pH, in grado di formare degli idrogeli in condizioni basiche. Il processo di elettrolisi dell'acqua in soluzioni di chitosano fornisce la possibilità di creare gradienti di pH su superfici conduttive di diverse forme e natura, ed è stato utilizzato per immobilizzare, in maniera controllata, film sensibili al pH, per il rilascio controllato di farmaci nel segmento posteriore dell'occhio. Si è dimostrato che i film di chitosano producessero un rilascio sostenuto e prolungato in condizioni fisiologiche, e un rilascio aumentato, accompagnato dalla dissoluzione delle matrici, in condizioni lievemente acide, come quelle che si possono trovare in prossimità di tumori o zone infiammate. Il metodo descritto può essere adattato a diversi altri polimeri biologici (come l'alginato o l'acido ialuronico) e usato per la fabbricazione

di parti intelligenti su microdispositivi, che sappiano rispondere a dei cambiamenti di condizioni al contorno.

Un approccio alternativo al problema si basa sulla fabbricazione di microrobot interamente composti da materiali soffici, il cui comportamento può essere modificato e controllato in maniera remota da un utente esterno. Il secondo lavoro sperimentale presentato in questa tesi unisce la fabbricazione di un doppio strato idrogelico autopieghevole e sensibile ai raggi infrarossi, con delle microparticelle magnetiche ricoperte di alginato e un sistema di manipolazione magnetica in tre dimensioni, a creare una piattaforma robotica per il rilascio controllato e specifico di cellule e farmaci. La tecnica degli origami polimerici è stata qui impiegata per la creazione di strutture tridimensionali di varie forme e dimensioni tramite fotolitografia. Le proprietà intrinseche dell'isopropilacrilamide, un polimero sensibile a cambi di temperature, sono state modificate tramite tecniche di copolimerizzazione con acrilamide e inclusione di ossido di grafite, per creare un materiale sensibile ai raggi infrarossi, ad alto rigonfiamento e con una temperatura di transizione intorno ai 40°C. Film di questo nanocomposito sono stati integrati con uno strato piu rigido di polietilenglicol diacrilato a formare strutture in grado di ripiegarsi completamente su se stesse tramite interazione con l'acqua. Microparticelle magnetiche ricoperte di alginato sono state utilizzate e inglobate in questi dispositivi per il duplice scopo di fornire un supporto per il trasporto e rilascio di cellule e un substrato magnetico per il controllo remoto. Il progetto è descritto nelle varie fasi di caratterizzazione dei materiali, delle strutture finali, in termine di controllo della posizione, dell'attivazione remota in acqua, per presentare al lettore tutte le potenzialità della piattaforma per applicazioni nel corpo umano.

La struttura a doppio strato idrogelico è ulteriormente analizzata con lo scopo di fornire dati e un metodo per la modellizzazione della forma finale, a partire dalle caratteristiche meccaniche e di rigonfiamento dei materiali utilizzati. I risultati proposti mostrano come non sia possibile predire la forma finale delle strutture attraverso il tradizionale modello analitico di Timoshenko. Inoltre il metodo di fabbricazione e la stessa struttura a doppio strato introducono delle deviazioni dal comportamento dei singoli strati idrogelici, che devono essere tenute in considerazione per lo sviluppo di un modello meccanico agli elementi finiti.

Infine sono analizzate le conseguenze relative a un cambio di forma in una microstruttura a scopo biomedico, come quelle possibili nei dispositivi descritti, con particolare attenzione relativa alla locomozione e allo scopo finale. Per questo motivo strutture cilindriche, in grado di mutarsi e assumere la forma di un foglio aperto, sono state fabbricate in maniera simile a quanto descritto precedentemente con dei nanocompositi sensibili ai raggi infrarossi o a campi magnetici. I primi sono stati studiati come piattaforme per il rilascio controllato di farmaci e la capacità di questi dispositivi analizzata nelle varie configurazioni (cilindro o film quadrato). L'attivazione e locomozione dei secondi sono state simulate tramite modelli agli elementi finiti con lo scopo di verificare la variazione delle forze di attrito e la facilità di movimento nei vari orientamenti spaziali.

Questi ultimi esempi dimostrano la possibilità di causare comportamenti intelligenti o autonomi in microrobot, attraverso il solo utilizzo di materiali sensibili o in grado di cambiare forma e dimensione.

CHAPTER 1

The Nautilus was piercing the water with its sharp spur, after having accomplished nearly ten thousand leagues in three months and a half, a distance greater than the great circle of the earth. Where were we going now, and what was reserved for the future?

Jules Verne

Introduction

1.1 Thesis motivation and background

There is perhaps not a better image of microrobotics than the one offered by the popular science fiction movie “Fantastic Voyage”. The movie, produced in 1966, was an adaptation of a short story co-written by the French writer Jerome Bixby and the German Otto Klement in an attempt to modernize the ideas of “Voyages extraordinaires” by Jules Verne [1]. In the movie, a miniaturized submarine and the on-board team are injected into the body of the scientist Jan Benes, with the difficult mission to remove a blood clot from his brain and allow him to recover from his coma.

The image of a miniaturized mobile vehicle with some kind of on-board intelligence capable of travelling inside the human body would remain for many years in the popular culture as an example of something at the borders of science-fiction. This was the opinion of the great Isaac Asimov when he was asked to write the novel from the script. As reported in his autobiography “In Joy Still Felt” [2], the American author “turned down the proposal out of hand” claiming the impossibility of miniaturization of matter and protesting against the lack of scientific accuracy and biological investigation.

Eventually, Asimov, who was associate professor at Boston University School of Medicine at that time, wrote another novel, combining his knowledge in biochemistry and human body with the catchy plot, to present a more “scientific” version of the story.

Of course, the miniaturization of humans is still impossible for human science and knowledge, however microrobots are currently a reality thanks to impressive advances in the field of microelectromechanical systems (MEMS) in the last 30 years.

Microrobots are defined as miniaturized robotic systems that are able to operate at small scales, for example by handling and transporting micrometer-sized objects, or by providing mobile sensing capabilities in a small volume. Their applications include industrial processes, and targeted medical treatments. This rather weak definition is based on scaling down the common concept of a robot, a reprogrammable multifunctional working machine [3], to the size of few micrometers up to a few millimeters. As with robots, the design and fabrication of microrobots classically involves a variety of disciplines, from mechanics, to physics, to computer science, to electronics.

Again in accordance with progress in robotics, microrobots are increasingly being designed with biomimetic shapes and functions [4], and more recently address biological and medical applications, in order to define a new level of interaction with humans. This shift of interest has brought researchers to explore the field of materials science and chemistry to find ways to imitate various biological entities or mechanisms. The inclusion of new materials has defined new ways to solve the challenges of the field of microrobotics: how to embed intelligence in such a tiny volume, how to achieve motion, how to accomplish a task.

From this perspective, smart hydrogels, polymeric networks capable of changing their physical and chemical state in response to an environmental change (pH, temperature, ionic strength, and electromagnetic fields) constitute a powerful class of materials with enclosed mechanisms of sensing and actuation [5]. Moreover, these polymers are biocompatible and, hence, are widely investigated for biomedical and biotechnological applications. For these reasons, hydrogels are especially attractive materials for medical microrobotics [6]. However, there are some issues related to the integration of soft hydrogels into microrobotic platforms which have strongly limited

their use. For example, problems arise in the fabrication of hybrid soft-hard devices, where hydrogels attached to substrates often delaminate or limit their actuation range. Also, it is difficult to achieve high forces or to realize complex 3D conformations that are desirable for manipulation tasks.

A successful implementation of these materials in microrobotic agents requires advanced knowledge in the physical chemistry of polymer networks and the development of robust micro fabrication methodologies to miniaturize them.

1.2 Aims of the thesis

Medical microrobots have been traditionally conceived of as microagents able to swim or be steered in body fluids, and specifically designed for medical targeted therapies, such as drug or cell delivery, small surgeries or collection of biological data. Their fabrication has mostly involved hard materials and techniques mostly employed in MEMS production.

The goal of this doctoral work was to develop robust methods to incorporate stable and functional smart hydrogels on microrobotic platforms. Two approaches are presented aimed at fabricating hard-soft hybrid or fully soft microdevices.

The first approach is based on the evidence that the majority of microrobotic platforms are made of hard bodies fabricated with traditional MEMS technologies. For this reason, a method to immobilize stable, millimeter-sized responsive hydrogel films on hard metallic substrates is proposed and developed. The second strategy investigates the potential of

full hydrogel self-folding bilayers in creating smart soft actuators with a 3D shape. These devices have been demonstrated to be capable of embedding and releasing drugs and/or micro objects by an on-demand mechanism.

A second goal of this study is to investigate the numerous advantages of the use of highly responsive smart hydrogels in microrobots. Apart from the intrinsic properties of biocompatibility, sensing, and actuation, these materials provide a chemical level of intelligence for microdevices. Moreover their use implies the possibility of achieving autonomous or semi-autonomous behavior. Autonomy, in a broad definition, calls for embedded sources of intelligence that define a sort of behavior for motion, sensing, or actuation tasks.

1.3 Dissertation outline

This thesis is structured in seven chapters, briefly described below.

Chapter 1 defines the general aim and organization of the thesis.

Chapter 2 is a review covering the current paradigm shift from hard to soft materials in robotics, MEMS and microrobotics. The review also provides the state of the art for hydrogel-based microrobots.

Chapter 3 proposes electrodeposition of pH responsive chitosan hydrogel as a smart, flexible method for the integration of soft responsive coatings on hard microrobots [1]. The work is part of a more general study about minimally invasive therapies in the eye. It includes the characterization of electrodeposited chitosan in terms of the morphology and the response of the

material to changes in pH. A strategy to modify the drug release kinetics of the films is also presented.

Chapter 4 describes the design and fabrication of near-infrared light (NIR) responsive hydrogel-based microrobots based on the mechanism of self-folding bilayers [2]. The microdevices are fabricated by means of a photolithographic process, which successfully coupled a layer of N-isopropylacrylamide (NIPAAM)-based graphene oxide nanocomposite with a stiffer poly (ethylene glycol) diacrylate (PEGDA) film. The internal stress between the two layers ensures a 3D closed conformation which is used to protect and carry magnetic cell laden alginate microbeads. These devices can be opened by short exposure to a NIR light source. The platforms are used as actuators for drug and cell delivery.

In **Chapter 5** the design of the self-folding hydrogel microrobots and a detailed characterization of their mechanical, swelling and folding properties are presented. Timoshenko's theory of bimetal thermostats [3] is used as an analytical model in an attempt to predict the bending effect. As an alternative, a finite element method based simulation is proposed to support the results of the characterization of the bilayer.

Chapter 6 deals with the effects on locomotion and drug delivery of medical tubular microrobots due to changes in their shape. Experiments and finite element-based simulations of drag forces and drug release of closed cylinders or rectangular plates suggest the possibility of changing the behavior of microrobots by means of shape changing effects and the inclusion of smart polymers.

Chapter 7 synthesizes the major findings of the presented research.

1.4 References

[1] J. Verne, Voyages Extraoirdinaires, Pierre-Jules Hetzel, **1863**.

[2] I. Asimov, *In Joy still felt*, Doubleday, **1980**.

[3] B. Siciliano, O. Khatib, Springer Handbook of Robotics, **2008**.

[4] C. Chang, *Behav Brain Sci* **2001**, 24, 1054.

[5] N. A. Peppas, J. Z. Hilt, A. Khademhosseini, R. Langer, *Adv Mater* **2006**, 18, 1345.

[6] B. J. Nelson, I. K. Kaliakatsos, J. J. Abbott, *Annu Rev Biomed Eng* **2010**, 12, 55.

[7] S. Fusco, G. Chatzipirpiridis, K. M. Sivaraman, O. Ergeneman, B. J. Nelson, S. Pane, *Adv Healthc Mater* **2013**, 2, 1037.

[8] S. Fusco, M. S. Sakar, S. Kennedy, C. Peters, R. Bottani, F. Starsich, A. Q. Mao, G. A. Sotiriou, S. Pané, S. E. Pratsinis, D. Mooney, B. J. Nelson, *Adv Mater* **2014**,26(6), 952.

[9] S. Timoshenko, *J Opt Soc Am Rev Sci* **1925**, 11, 233.

CHAPTER 2

Then you better start swimmin'

Or you'll sink like a stone

For the times they are a-changin'

The Times they are a changing'- Bob Dylan (1964)

Soft microrobots: the impact of materials on the new generation of biomedical intelligent microdevices

2.1 Introduction

Medicine and the medical industry are currently benefiting from the development of microsystem technology (MST) over the last twenty years. The integration of sensors, actuators and microelectronics into medical devices and other related products simplifies many medical procedures, and, at the same time, significantly reduces risks and side-effects for patients. Clear examples of this progress are devices for home healthcare monitoring, such as sensors or drug release platforms, clinical data collector systems, or motion sensors for surgical tools and prosthesis positioning [1]. According to recent market research, microelectromechanical sytems (MEMS) in medical applications will grow from 1.8 billion USD in 2012, at an annual rate of 20% over the next five years [2]. The implementation of automated control systems with smart sensors and actuators will enable the development of minimally invasive robotic medical treatments such as localized surgery [3], implanting and positioning controllable structures [4] (sensors, stents, occluders, and electrodes), or providing targeted drug or cell delivery [5]. Ideally these would affect delicate and hard to access areas of the body, such as the eye, the brain, the central nervous system, the vascular network, and the inner organs.

Microrobots, untethered mobile active microdevices, have the potential to perform tasks that are beyond human skills, or that require extreme precision and accuracy. The idea of using microrobots for minimally invasive therapies is not new and has been formulated almost sixty years ago [6] by Richard Feynman, who envisioned the possibility “to swallow the surgeons to “look around” in the body”. However, practical examples targeting medical applications were only proposed in the last fifteen years. Advances in physics,

micro- and nanosystem technologies, computer science for vision and control led to the production of several biomedical microrobotic devices such as micro cameras for wireless endoscopy [7], biologically inspired magnetic devices that could be steered, and tracked in complex 3D environments [8], wireless oxygen sensors for eye diagnosis of hypoxia [9], drug delivery carriers [10], and bacteria driven platforms [11]. Most of these efforts used hard bodies, made predominantly of metals or alloys. Their manipulation was achieved wirelessly by means of external magnetic fields created by electromagnet coils [12, 13] or by permanent magnets [14]. Most efforts were dedicated to manipulation and control, leaving the development of the appropriate materials as a side aspect. However, materials can enhance the properties of the microrobot and facilitate some tasks, such as sensing a change of temperature, or maneuvering a micro entity.

The recent growing interest in soft robotics and biomimetics [15] is leading to a new development in the field by boosting the integration of soft responsive polymers in microrobotic platforms. In this chapter, we first introduce the advantages in the use of soft materials in biomedical robotics and MEMS technology. This motivates a paradigm shift in microrobot fabrication and inspires future applications in the micro scale.

The second part concentrates on smart hydrogels. These are responsive polymeric networks that are widely used in biological and biomedical applications. Their intrinsic properties of sensing and actuation, together with their synthesis flexibility, make them attractive candidates to be integrated in microrobotic platforms.

The third section summarizes recent research on soft hydrogel-based microrobotics, mainly focusing on the challenges that have been addressed and overcome due to the use of these materials.

The last part presents an outlook of the opportunities and challenges for the development of intelligent soft micromachines for medical applications.

2.2 Soft polymeric materials in MEMS and biomedical robotics

MEMS have been developed extensively in the last forty years and successively integrated into commercial products, with the final aim to miniaturize complex devices and limit their cost of production. Sensors, actuators, power producing devices, chemical reactors and biomedical devices have been produced thanks to a variety of materials and methods, extensively summarized in previous reviews [16]. The MEMS field evolved from the semiconductor industry, and the two are still strongly connected. Indeed, most of the materials used in cleanrooms and related facilities are mainly silicon, silicon dioxide and metals. Aside from that, diamond and ceramics have been proposed for applications where hardness and resistance are crucial [17]. To date, only a few polymers can be classified as "standard materials" in MEMS. As described by Liu et al. [18] these materials, such as SU-8, PDMS or other elastomers, exhibit properties that are not present in standard silicon, including higher strains, lower costs of production, unlimited size, a huge range of treatments to tailor their properties, or a higher chemical and biological compatibility. Despite challenges in the fabrication processes, these materials are now extensively used, especially for the

production of lab-on-a chip devices in applications with living organisms [19, 20]. At the same time, the use of soft matter in MEMS parts and devices has resulted in a young branch of robotics, soft robotics, which attempts to more closely mimic the locomotion and actuation mechanisms of living entities.

Biological systems are mainly made of soft, elastic and flexible materials that allow continuous morphing, or adaptation to different needs or environmental conditions. Soft robotics directs its efforts at substituting partially or entirely rigid joints, sensors, and actuators of traditional automated systems with soft and highly deformable components in order to achieve a bio-inspired behavior [21,22]. This change implies a significant challenge for the robotic community, as it needs to include aspects of material science, shape design and biology that were previously not considered [23]. Some of these concepts have been well introduced by Ilievski et al. [24] in their paper "Soft-Robotics for Chemists", which stressed the contribution of developing new materials, techniques and fabrication processes in the field. This work describes a new kind of actuators called PneuNets, which were made of an embedded, inflatable pneumatic network of elastomeric channels capable of bending and achieve complex motions. The materials selection together with the orientation design of the channels determined the response of the device and the grasping ability of produced grippers (figure 2.1a). Other materials were also incorporated in these devices in order to achieve a programmed directional bending. In this case, a relatively hard layer of PDMS together with softer, inflatable Ecoflex active layers were integrated. Additionally the authors investigated several engineered surface textures to improve the device performance in the manipulation of fragile objects.

Soft robots often make use of pneumatic systems. These systems have a distributed actuation along the structure, thus making the modeling of their

mobility not possible by means of traditional kinematic schemes. Moreover, due to their material composition limited forces and stiffness are achievable, subsequently limiting their areas of application. Nevertheless, these complications are balanced by the possibility of defining interactions with the environment that are otherwise not feasible. A rigid robot arm, for example, would need a specialized effector to grasp an object, with no options for adaptation. Soft grippers, similar to the one mentioned before [25], or the electrically driven pre-stretched devices described by Kofod et al. [26], can use a whole arm system, and reconfigure their shape depending on the object.

The complex and adaptive behavior of soft materials has also been exploited to build robots that can move in a biomimetic way. This is the case of worm-like and caterpillar-like robots, extensively reviewed by Kim et al. [27], (figure 2.1b). These devices have alternatively been produced with pneumatic actuators [28] or a combination of a soft body with actuators made of shape memory alloys [29, 30] to drive the reversible bending and to achieve planar motion or rolling capabilities. An untethered version of the same principle was developed by Saga et al. [31] by using a magnetic fluid distributed in segments of a rubber cell body, and actuated by an external permanent magnet.

Similarly, a variety of octopus inspired robots have been developed, using compartmentalized actuation. The PneuNets system was recently adapted to the shape of a tetrapod [32]. Pressure distributed in a sequential way and controlled by an external user allowed the fabricated robots to execute different motions and accomplish tasks that could be impossible for a “hard” robot. Thanks to the use of light materials, the tetrapods were able to pass over or underneath an obstacle (figure 2.1c).

Alternatively, shape memory alloys (SMA) actuators have been used to elongate or increase the stiffness of soft muscle fibers distributed longitudinally and transversally in a biomimetic robot arm [33]. The antagonistic behavior and control of the actuators produced complex motion and locomotion [34].

Finally, muscular cells, interfaced with a soft deformable platform have been used to achieve free swimming by imposing electric field stimulation (figure 2.1d) [35]. This hybridization of synthetic and natural components, although being inefficient for long-term applications and still not biocompatible, translates the concept of tissue engineering to a wider field of applications.

These soft materials are now being largely employed in MEMS, as the evolution of electronic circuits [36], solar cells [37], and batteries [38] has recently demonstrated [39]. However, there is still room for improvement and integration of other materials for robotic applications. One possible direction, currently poorly exploited, is the integration of smart responsive hydrogels in robotic platforms. These polymers have the ability to incorporate autonomous mechanisms of response that can be used for sensing and actuating procedures without the need of an external user and in an untethered way. However, applications in the large scale are hindered by the slow diffusion process that drive their actuation and by their weak mechanical properties. More adaptability and higher potential can be found in the microscale, where diffusion paths are limited, and time of response can be reduced to seconds.

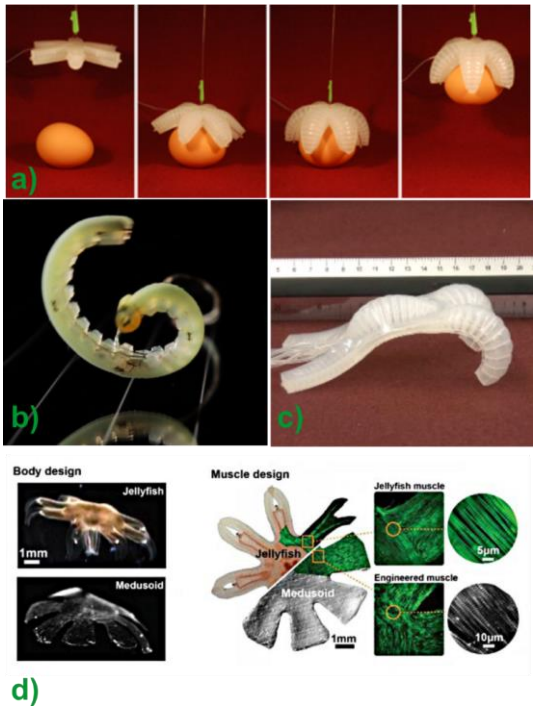

Figure 2.1. *a) PneuNets grippers acting on a boiled egg [24]. b) GoQbot, a caterpillar inspired rolling robot. The total size of the SMA actuated device is approximately 10 cm. [29]. c) Pneumatic tetrapod can crawl and undulate to navigate around an obstacle [32]. d) Design and architecture of the medusoid built by seeding rat myocardiac cells on a PDMS layer [35].*

2.3 Smart hydrogels in MEMS

Hydrogels are three-dimensional (3D) polymer networks that are crosslinked to form highly deformable matrices. Their hydrophilicity allows

them to retain significant amounts of water (or similar liquids) inside their structure and modify their physical and chemical behavior accordingly. Gels have been formed from either natural or synthetic materials, using a large variety of methods, including change in the environmental conditions (pH, temperature, and ionic interactions), photo or thermal induced radical polymerization, enzymatic crosslinking, and have mainly been used for biological and biomedical applications [40]. Their relevance and appeal resides in the intrinsic properties of biocompatibility, high elasticity, and deformability, together with the possibility of finely tuning their different physical, chemical and mechanical parameters during the synthesis process. Several papers review the variety of hydrogels that have been produced and investigated and their main characteristics [41, 42]. Here, we briefly focus on a class of polymeric networks, which are classified as "smart" because they can reversibly change their physical-chemical status upon the application of an external stimulus. This class of materials includes synthetic and natural polymers that react to changes of pH, temperature, or ionic strength, thus resembling, on a wider scale, the behavior of shape memory alloys [43]. Additionally, they include hydrophilic matrices, which have been made responsive to stimuli such as light or magnetic fields by incorporating nanostructures such as magnetic nanoparticles [44], carbon nanotubes [45] or graphene foils [46]. They also include materials that have been tailored to recognize particular molecules and change conformation, for example by imprinting techniques [47] [48]. Finally there is a group of smart hydrogels whose degradation is controlled depending on environmental conditions [49].

Incorporation of smart hydrogels into MEMS is a relatively recent idea that has attracted great interest in the field of biosciences and has pushed researchers to create or adapt previous fabrication techniques to the

characteristics of these materials [50]. The resulting area of research has been included into the broad discipline of BioMEMS [19, 51, 52], or has recently found an alternative name in Microchemomechanical systems [53]. This last term well represents the idea of a shift from electrical actuation, the most extensive mechanism used in MEMS, to a chemical trigger of a mechanical motion.

It is not the scope of this review to cover the full range of applications of smart hydrogel-based MEMS [20, 52], which include drug delivery devices [54], sensors [55], tissue engineering platforms [42, 56], microfluidic systems [57], and small actuators [58]. We rather concentrate the attention on two techniques that could be beneficial for the integration of smart hydrogels in microrobotic platforms, smart surfaces and self-folding bilayers.

2.3.1 Hydrogel based smart surfaces

Hydrogels suffer from poor adaptability to various techniques of microfabrication (for example etching or bonding) that limit their integration into existing hard microsystems. Moreover, they easily delaminate from surfaces due to their poor adhesion in the swollen state.

This problem can be addressed with functional binding coatings such as like acrylate-terminate silanes [59] [60], or surface-initiated polymerization techniques such as reversible addition−fragmentation chain-transfer (RAFT) [61] or photografting [62]. All these techniques have been shown to be successful and reliable, however, a significant loss of material performance, due to the physical constraints, was observed, when compared to free swelling hydrogels [63]. Smart surfaces formed by the attachment of acrylic gels on substrates have been used to regulate fluid flow in microfluidic

channels [64], or incorporated in sensing platforms [65]. Another smart application is the use of thermoresponsive scaffolds to control the adhesion of cells, proteins or analytes.

Poly-isopropyl acrylamide (PNIPAAM) is well known for its ability to switch from a hydrophilic to a hydrophobic state above a certain transition temperature (lower critical solution temperature, or LCST) [66]. This reversible change of configuration and water content has been found to deeply influence the adhesion of cells, which appear anchored to the substrates above LCST, and spontaneously detach when the polymer swells without damaging the tight intercellular junctions (figure 2.2a). Yamada et al. were the first to speculate about the feasibility of creating cell sheets using this approach and in this way substitute the traditional harsh methods for cell harvesting [67]. Such a concept was then developed by Okano and coworkers, which produced thin (30 nm) layers of PNIPAAM hydrogels and successfully demonstrated the concept on blood platelets [68]. The cell sheet harvesting strategy spread in the last 15 years to produce a variety of tissues [69] including corneal epithelial cells [70], cardiomyocites [71] and keratinocytes. Additional work was done to achieve 3D structures and combine different tissues on the same platforms [72], to template cell adhesion with proteins [73], or to integrate this mechanism in remotely actuated devices (for example by light activation) [74].

A completely different approach to create smart polymer coatings on hard surfaces relies on the ability of some natural polymers to respond to changes of pH with a sol-gel transition. The electrophoretic mobility of these macromolecules and the possibility to create pH gradients on electrodes by electrolysis of water constitute the driving factors for the electrodeposition of

hydrogel layers. This technique provides a temporally and spatially controlled method for the functionalization of microdevices.

Chitosan has been the most extensively investigated polymer in the area due to its pH sensitivity, high biocompatibility, low costs, and facile chemical and physical modification [75]. Many chitosan properties, including the possibility of being electrodeposited [76], stem from the presence of a primary amine group in each polymer unit. At low pH the amines are protonated while an increase over their pK_a value (~ 6.5) produces a loss of charges and solubility. Moreover, chitosan units possess accessible functional groups for crosslinking or functionalization [77].

Electrodeposition was used to immobilize chitosan and protein on substrates for enzymatic recognition (figure 2.2b) [78]. For example, Shi et al. reported a two-step approach for the electrochemical activation of protein assembly [79], involving the cathodic deposition of the polymer and the subsequent activation of aldehyde binding groups by anodic oxidation. Fluorescent labeling was used to show the successful immobilization of proteins on electrodes. Alternatively, simple co-electrodeposition, exploiting the electrophoretic mobility of proteins, was successful for creating chitosan-hemoglobin films [80].

Electrodeposition has also been used to create composite films and incorporate functional nanoparticles on surfaces. This is the case of carbon nanotubes [81], gold nanoparticles [82], and hydroxyapatite [83]. Few reviews [84] have covered the different options offered by electrodeposited chitosan, such as the functionalization of microfluidics components [85] or the assembly of lab-on-a-chip devices [86]. In parallel, other polymers have also been electrodeposited to fabricate multifunctional biological assemblies

on surfaces [87]. Alginate films were created by anodic protonation [88] or by crosslinking through the formation of calcium ions and used for controllable cell assembly [89]. Hyaluronic acid was electrodeposited together with hydroxyapatite to create scaffolds for cell growth [90]. Gelatin has been immobilized with chitosan by oxidation through tyrosinase molecules [91]. All these examples reveal the ability of electrodeposition to create stable and thick functional hydrogel layers, with no limitation given by the size and the shape of the substrate. This technique is particularly attractive for the microfabrication of complex microrobotic systems.

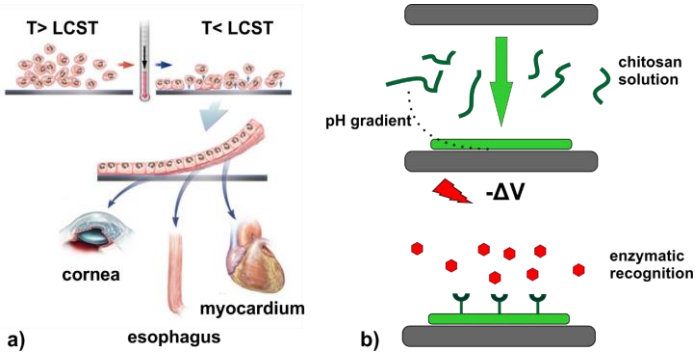

Figure 2.2. *a) Cell sheet engineering through immobilization of thermosensitive hydrogel layers on surfaces, and remote control of their temperature. The method has been tested in vitro for different tissues (readapted from Richard Koepsel Website drawings, www.ptei.org). b) Mechanism of electrodeposition of chitosan, for the immobilization of hydrogel films, and protein assembly.*

2.3.2 Self folding devices

Self-folding is the result of the stress caused by material heterogeneities or by the application of an inhomogeneous field on a responsive homogeneous material. Both techniques have been explored [92] to create smart polymeric devices, mainly for medical applications, however, the photolithographic fabrication of bilayers with an active responsive part has been the most popular method so far. He et al. [93] have been the first to fabricate a drug delivery platform incorporating a pH-sensitive hydrogel which could curl inside the intestine, and adhere to the walls of the organ for a confined prolonged release [94]. Leong et al. successfully created a microgripper for *in vivo* biopsy, and addressed the problem of limited strength of hydrogel materials by coupling polymeric responsive hinges with a structural metal film (figure 2.3a) [95, 96]. These microgrippers could close by means of enzymatic degradation of gelatin or carboxymethylcellullose and be steered to a specific position by means of magnetic fields. Zakharchenko et al. reported the fabrication of a thermosensitive all-polymeric platform, which could be magnetically manipulated, while at the same time exhibited continuous degradation [97]. Rolled tubes of PNIPAAM magnetic nanocomposites, or polycaprolactone (PCL) have been produced by photolithography combined with spin coating and used for the manipulation of microbeads or for the encapsulation of cells. A similar strategy was taken by Pedron et al. [98] and Shim et al. [99], who produced star-shaped structures (figure 2.3b) by means of a simple two-step photolithographic method. Soft microorigami [100] have been produced from a large variety of responsive materials and can fold to form several 3D shapes such as tubes [101] or helices (figure 3c) [102].

Self-folding films, like the previously reviewed smart surfaces, could also be used for the fabrication of soft microrobots and intelligent platforms that are able to perform specific goals in a controllable and programmable way [103]. These systems can exploit the sensing and actuation abilities of smart hydrogels as end effectors for manipulation and interaction tasks, while providing mobility and control by means of wireless drive units. Alternatively, they could use the sensitivity of hydrogels to an environment to achieve a desired behavior or locomotion.

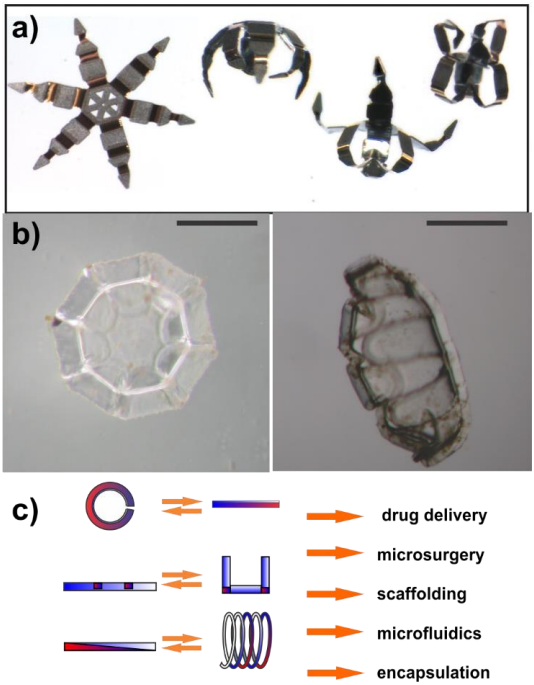

***Figure 2.3**. a) Enzyme responsive grippers, made of magnetic metallic materials and polymeric hinges [95].b) Star and Venus flytrap shaped hydrogel bilayers. Scale bars are 200 µm. c) Different designs of hydrogel bilayers are possible depending on the geometry of the structure. Applications are from drug delivery, to encapsulation of cells and bead, to microsurgery.*

2.4. Soft microrobots: state of the art

Despite the vast literature in material science and the clear advantages demonstrated in MEMS applications, hydrogels have been rarely employed for microrobotic platforms. The reason for this lack of attention can be attributed to the relatively infancy of the field, and presumably to the background and expertise of the micro-roboticists. As already mentioned, most of the work done till now has focused on manipulation and control challenges and in the use of traditional MEMS materials for the fabrication of sensors and actuators [104]. The shift of interests towards biological and medical applications has contributed to a more multidisciplinary development of the research area also involving soft-materials scientists, chemists and biologists.

The first demonstration of the use of hydrogels for medical microrobots was reported by Osada et al. [105], who showed the possibility of creating net motion on a hydrogel strip surrounded by a surfactant solution.

An electric field was used to drive the direction of association between the surfactant and the stretched hydrogel causing controlled shrinking and bending. Net motion was achieved by reversibly exploiting this mechanism and by using mechanical hooks in order to avoid back-sliding. This work was taken as a reference by other research groups. Kim et al. [106] designed a clamp to be used in the gastrointestinal tract using thermosensitive PNIPAAM hydrogels. By changing the state of a millimeter-sized structure from hydrophilic to hydrophobic, the friction between the hydrogel and the walls of a pig intestine could be increased. Net motion could be imparted to an endoscopic capsule made of soft and hard parts by spatially controlling

this transition with electro-heaters wrapped around the polymeric structure. Their local activation allowed a controlled break of symmetry within the capsule and the environment, which subsequently triggered the movement. This mechanism was further characterized and explained by Yeghiazarian et al [107]. In their review "Teaching hydrogels how to move like an earthworm" [108], they described the concept of anisotropic activation of gel transition and emphasized its great potential for the fabrication of cargo systems (figure 2.4a). Wireless motion and actuation was also suggested by means of controlled light adsorption, magnetic fields, and thermal gradients. The use of these external stimuli constitutes an advantage for hydrogel-based microrobots when compared to the ones based on electroactive polymers or shape memory alloys, since they can be controlled in an untethered fashion [109].

Net motion of hydrogel microstructures could also be achieved by exploiting reversible bending of moisture sensitive hydrogel bilayers (figure 4b) [110]. Ma et al. proposed a series of composite hydrogels by coupling a layer of polyacrylic acid/poly (allylamine hydrochloride) (PAA/PAH) and a UV curable non responsive ester. A change in humidity caused the first layer to expand and the entire structure to curl. Unidirectional walking was shown on two-legged devices moving on a ratchet substrate.

Alternatively, self-oscillating hydrogel systems based on the Belousov-Zhabotinsky reaction [111] of metal-ion oxidation and the consequent change in hydrated volume were also investigated. The resulting structures resembled ameboids in their shape and oscillatory movement.

The most impressive results in this category are the Aquabots developed by Kwon et al [112]. A microfluidic-based method for UV polymerization

was used to design and fabricate millimeter-sized full hydrogel structures resembling living organisms (octopus, sperm and miriapods). The technique produced different microrobots out of a variety of smart hydrogels. Electroactuated Aquabots were shown to swim or walk by alternation of an asymmetric (in duration and amplitude) electric impulse, which caused a bending response in the "legs" of the devices (figure 2.4c). A glucose-sensing moving octopus was fabricated by combining electroactive "legs" with a head containing glucose oxidase and horseradish peroxidase. In the presence of glucose, a chain reaction would activate a fluorescent signal. This mechanism could be slightly modified to add an induced drug delivery option. Magnetically movable Aquabots were also fabricated out of hydrogel-nickel nanoparticles and combined with a pH responsive mechanism to control the drag of the device on demand. Finally thermoresponsive "arms" of NIPAAM hydrogels were implemented for the capture and the release of targets.

This last example introduces the second field of applications for smart responsive hydrogels in microrobotics. Manipulation of micrometer sized objects, such as cells or beads, in complex environments is related to a series of requirements. The handling should be "soft" and not harmful for the targets. It should be carried out preferentially with a wireless method of actuation in a relatively quick way and with the possibility of parallel interventions. Micrometer sized hydrogels intrinsically satisfy most of these needs facilitating the entire design of manipulation platforms.

The concept is well illustrated in the work of Hu et al. [113]. A manipulation system based on laser-induced and controllable cavitation bubbles were applied on structured poly(ethyleneglycol) diacrylate (PEGDA) hydrogels for the direct contact and manipulation of single yeast cells. Despite not being intrinsically responsive, the proposed hydrogels disks

could steer and move on a planar substrate due to the bubbles generated by the α-Si layer of the substrate and entrapped on their bottom [114]. The temperature gradient generated at the bubble surface helped to lift the structures and move them. The soft material acted as a buffer between the cells and the bubbles reducing shear stresses and invasiveness of the system. The researchers demonstrated parallel control and wireless actuation of multiple hydrogel microrobots while performing different microassembly tasks (figure 2.4d).

A third advantage of hydrogel-based microrobots was recently pointed out by Palagi et al. [115]. By analyzing the problem of gravity compensation of magnetic microrobots in case of gradient propulsion, the researchers compared standard metal-based spherical microstructures with alginate hydrogel-based magnetic beads of similar volume. Despite the inferior magnetic properties of the latter, quasi-buoyant hydrogel structures of sizes larger than a few tens of microns would require lower gradients with respect to their counterparts when moving at relatively low speeds. This is mainly due to the almost negligible need for gravity compensation and to the decrease in the drag force effects when increasing the size of the microrobots.

Considering all the properties of smart hydrogels and the beneficial effects of their use, it would be natural to suppose a large range of hydrogel based microrobotic platforms for biomedical applications. Up to 2011, only one work has successfully demonstrated the advantages of smart responsive hydrogels in minimally invasive therapies. Tabatabaei et al. [116] explored the potential of millimeter sized PNIPAAM magnetic nanocomposites spheres for *in vivo* drug delivery applications. Magnetic steering and tracking was proposed by gradient propulsion and imaging inside an MRI scanner previously developed for *in vivo* applications [12]. Phase transition and

subsequent shrinking of the microrobot and release of water was achieved by applied an AC magnetic field of 4 kA/m at 160 kHz. The work concludes with the challenges related to the safety and efficacy of such treatments and sets some important limitations related to *in vivo* applications. Nevertheless, this work contributes to defining a new microrobotics approach which focuses not only on control, manipulation and locomotion, but also on the integration of different areas of research, including material science, computer vision and medicine.

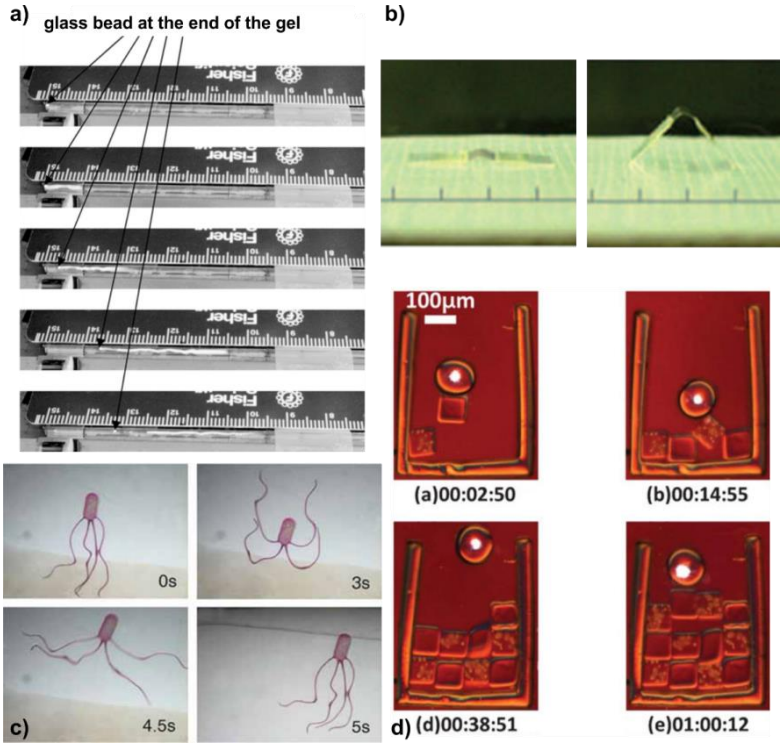

Figure 2.4*. A few examples of hydrogel based microrobots. a) earthworm-like movement and cargo transport of a gel beads by phase transition of NIPAAM hydrogel rods [108]. b) Locomotion of a walking device constituted of a humidity sensitive hydrogel bilayer. The device is 2 mm long [110]. c) Example of octopus like Aquabot, fabricated with electroactive hydrogels. The entire structure is 4-5 mm long [112]. d) PEGDA laser responsive structure used for the assembly of cell-laden microgels.[113].*

2.5 Summary and perspective

Robotics is a multidisciplinary field involving researchers with different backgrounds, including mechanics, computer science, biotechnology, chemistry and material sciences. The integration of soft materials has not only been seen as a step towards a more biomimetic approach, but has also brought additional advantages derived from the intrinsic properties of the polymers used.

The same trend has been observed in the microscale, where MEMS fabrication increasingly involves the use of "intelligent" polymers, or the development of methods to fabricate soft devices for biological and biomedical applications.

Microrobotics, a branch of robotics that is strongly focused on minimally invasive biomedical applications, can take advantage of this paradigm shift by including the "appropriate" materials for different tasks. Smart responsive hydrogels constitute a vast, flexible set of resources, ready to be implemented. The ability to wirelessly respond to an external impulse, their biocompatibility, the favorable scaling effects of diffusion law, the established fabrication routes, and their light density and softness, are all qualities difficult to combine in other classes of materials. These qualities are all beneficial for the development of medical microrobots.

2.6 References

[1] M. O. Schurr, S. Schostek, C. N. Ho, F. Rieber, A. Menciassi, *Minim Invasiv Ther* **2007**, 16, 76.

[2] Bhansali, S. V., A., *Mems for biomedical applications*. Elsevier Science and Technology: **2012**; p 512..

[3] J. Hunter, Sackier JM, *Minimally invasive surgery*, New York **1993**.

[4] F. Li, M. Chen, Z. K. Qiu, J. Lu, W. H. Wu, *Ann Thorac Surg* **2008**, 85, 1067; W. N. Taylor, I. T. McDougall, *J Urology* **2002**, 168, 2020; C. Bach, M. N. Kabir, A. Goyal, R. Malliwal, S. Kachrilas, M. E. El Howairis, J. Masood, N. Buchholz, I. Junaid, *J Endourol* **2013**, 27, 1543; A. Wang, S. Banerjee, B. A. Barth, Y. M. Bhat, S. Chauhan, K. T. Gottlieb, V. Konda, J. T. Maple, F. Murad, P. R. Pfau, D. K. Pleskow, U. D. Siddiqui, J. L. Tokar, S. A. Rodriguez, A. T. Comm, *Gastrointest Endosc* **2013**, 78, 805.

[5] W. C. Broaddus, G. T. Gillies, J. Kucharczyk, Neuroimag Clin N Am 2001, 11, 727; H. D. Toeg, A. Ahmadi, T. G. Mesana, M. Ruel, E. J. Suuronen, *Can J Cardiol* **2010**, 26, 47d.

[6] R. P. Feynman, *Microelectromechanical Systems, Journal of* **1992**, 1, 60.

[7] A. Menciassi, M. Quirini, P. Dario, *Minim Invasiv Ther* **2007**, 16, 91; G. Iddan, G. Meron, A. Glukhovsky, P. Swain, *Nature* **2000**, 405, 417.

[8] L. Zhang, J. J. Abbott, L. Dong, B. E. Kratochvil, D. Bell, B. J. Nelson, *Appl Phys Lett* **2009**, 94, 064107; K. E. Peyer, L. Zhang, B. J. Nelson, *Nanoscale* **2013,** 5, 1259.

[9] O. Ergeneman, G. Chatzipirpiridis, J. Pokki, M. Marin-Suarez, G. A. Sotiriou, S. Medina-Rodriguez, J. F. F. Sanchez, A. Fernandez-Gutierrez, S. Pane, B. J. Nelson, *Ieee T Bio-Med Eng* **2012**, 59, 3104.

[10] K. M. Sivaraman, K. Bayrakceken, O. Ergeneman, S. Pane, T. Luhmann, H. Hall, B. J. Nelson, *Ieee Eng Med Bio* **2010,** 4359; S. Fusco, G. Chatzipirpiridis, K. M. Sivaraman, O. Ergeneman, B. J. Nelson, S. Pané, *Adv Healthc Mater* **2013**, 2, 1037.

[11] S. Martel, C. C. Tremblay, S. Ngakeng, G. Langlois, *Appl Phys Lett* **2006**, 89; S. J. Park, S. H. Park, S. Cho, D. M. Kim, Y. Lee, S. Y. Ko, Y. Hong, H. E. Choy, J. J. Min, J. O. Park, S. Park, *Sci Rep-Uk* **2013**, 3.

[12] S. Martel, O. Felfoul, J. B. Mathieu, A. Chanu, S. Tamaz, M. Mohammadi, M. Mankiewicz, N. Tabatabaei, *Int J Robot Res* **2009**, 28, 1169.

[13] M. P. Kummer, J. J. Abbott, B. E. Kratochvil, R. Borer, A. Sengul, B. J. Nelson, *Ieee T Robot* **2010**, 26, 1006.

[14] A. J. Petruska, J. J. Abbott, *Ieee T Magn* **2013**, 49, 811.

[15] D. Trivedi, C. D. Rahn, W. M. Kier, I. D. Walker, *Appl Bionics Biomech* **2008**, 5, 99.

[16] S. M. Spearing, Acta Mater 2000, 48, 179; J. W. Judy, *Smart Mater Struct* **2001**, 10, 1115.

[17] M. Pavlin, D. Belavic, F. Novak, *Sensors-Basel* 2012, 12, 320; O. Auciello, J. Birrell, J. A. Carlisle, J. E. Gerbi, X. C. Xiao, B. Peng, H. D. Espinosa, *J Phys-Condens Mat* **2004**, 16, R539.

[18] C. Liu, *Adv Mater* **2007**, 19, 3783.

[19] R. Bashir, *Adv Drug Deliver Rev* **2004**, 56, 1565; B. Ziaie, A. Baldi, M. Lei, Y. D. Gu, R. A. Siegel, *Adv Drug Deliver Rev* **2004**, 56, 145.

[20] A. C. R. Grayson, R. S. Shawgo, A. M. Johnson, N. T. Flynn, Y. W. Li, M. J. Cima, R. *Langer, P Ieee* **2004**, 92, 6.

[21] D. Trivedi, C. D. Rahn, K. W. M., W. I. D., *Applied Bionics and Biomechanics* **2008**, 5, 99.

[22] B. Bhushan, *Philos T R Soc A* **2009**, 367, 1445.

[23] R. Pfeifer, F. Iida, J. Bongard, *Artif Life* **2005**, 11, 99.

[24] F. Ilievski, A. D. Mazzeo, R. E. Shepherd, X. Chen, G. M. Whitesides, *Angew Chem Int Edit* **2011**, 50, 1890.

[25] R. V. Martinez, J. L. Branch, C. R. Fish, L. H. Jin, R. F. Shepherd, R. M. D. Nunes, Z. G. Suo, G. M. Whitesides, *Adv Mater* **2013**, 25, 205.

[26] G. Kofod, M. Paajanen, S. Bauer, *Appl Phys a-Mater* **2006**, 85, 141.

[27] S. Kim, C. Laschi, B. Trimmer, *Trends Biotechnol* **2013**, 31, 23.

[28] E. V. Mangan, D. A. Kingsley, R. D. Quinn, H. J. Chiel, **2002** *Ieee International Conference on Robotics and Automation, Vols I-Iv, Proceedings* **2002**, 347.

[29] H. T. Lin, G. G. Leisk, B. Trimmer, *Bioinspir Biomim* **2011**, 6.

[30] S. Seok, C. D. Onal, K. J. Cho, R. J. Wood, D. Rus, S. Kim, *Ieee-Asme T Mech* **2013**, 18, 1485; A. Menciassi, S. Gorini, G. Pemorio, P. Dario, 2004 *Ieee International Conference on Robotics and Automation, Vols 1- 5, Proceedings* **2004**, 3282.

[31] N. Saga, T. Nakamura, J Appl Phys **2002**, 91, 7003; N. Saga, T. Nakamura, *Smart Materials & Structures* **2004**, 13, 566.

[32] R. F. Shepherd, F. Ilievski, W. Choi, S. A. Morin, A. A. Stokes, A. D. Mazzeo, X. Chen, M. Wang, G. M. Whitesides, *P Natl Acad Sci USA* **2011**, 108, 20400.

[33] C. Laschi, B. Mazzolai, V. Mattoli, M. Cianchetti, P. Dario, *Experimental Robotics* **2009**, 54, 25; C. Laschi, M. Cianchetti, B. Mazzolai, L. Margheri, M. Follador, P. Dario, *Adv Robotics* **2012**, 26, 709.

[34] M. Calisti, M. Giorelli, G. Levy, B. Mazzolai, B. Hochner, C. Laschi, P. Dario, *Bioinspir Biomim* **2011**, 6.

[35] J. C. Nawroth, H. Lee, A. W. Feinberg, C. M. Ripplinger, M. L. McCain, A. Grosberg, J. O. Dabiri, K. K. Parker, *Nat Biotechnol* **2012**, 30, 792.

[36] G. A. Salvatore, N. Munzenrieder, T. Kinkeldei, L. Petti, C. Zysset, I. Strebel, L. Buthe, G. Troster, *Nat Commun* **2014**, 5, 2982; J. A. Rogers, Y. G. Huang, *P Natl Acad Sci USA* **2009**, 106, 10875.

[37] Z. Yu, X. Niu, Z. Liu, Q. Pei, *Adv Mater* **2011**, 23, 3989.

[38] G. Kettlgruber, M. Kaltenbrunner, C. M. Siket, R. Moser, I. M. Graz, R. Schwodiauer, S. Bauer, *J Mater Chem A* **2013**, 1, 5505; C. Yan, P. S. Lee, *Small* **2014**, n/a.

[39] S. Bauer, S. Bauer-Gogonea, I. Graz, M. Kaltenbrunner, C. Keplinger, R. Schwodiauer, *Adv Mater* **2014**, 26, 149.

[40] N. A. Peppas, J. Z. Hilt, A. Khademhosseini, R. Langer, *Adv Mater* **2006**, 18, 1345.

[41] N. A. Peppas, P. Bures, W. Leobandung, H. Ichikawa, *Eur J Pharm Biopharm* **2000**, 50, 27; N. Annabi, A. Tamayol, J. A. Uquillas, M. Akbari, L. E. Bertassoni, C. Cha, G. Camci-Unal, M. R. Dokmeci, N. A. Peppas, A. Khademhosseini, *Adv Mater* **2014**, 26, 85; B. V. Slaughter, S. S. Khurshid, O. Z. Fisher, A. Khademhosseini, N. A. Peppas, *Adv Mater* **2009**, 21, 3307.

[42] A. C. Jen, M. C. Wake, A. G. Mikos, *Biotechnol Bioeng* **1996**, 50, 357.

[43] J. F. Mano, Adv Eng Mater 2008, 10, 515; S. Chaterji, I. K. Kwon, K. Park, *Prog Polym Sci* **2007**, 32, 1083.

[44] D. Das, T. Kar, P. K. Das, Soft Matter 2012, 8, 2348; N. S. Satarkar, J. Z. Hilt, *Acta Biomater* **2008**, 4, 11; K. Haraguchi, *Curr Opin Solid St M* **2007**, 11, 47.

[45] X. Zhang, C. L. Pint, M. H. Lee, B. E. Schubert, A. Jamshidi, K. Takei, H. Ko, A. Gillies, R. Bardhan, J. J. Urban, M. Wu, R. Fearing, A. Javey, *Nano Lett* **2011**, 11, 3239.

[46] A. Sahu, W. I. Choi, G. Tae, Chem Commun **2012**, 48, 5820; C. H. Zhu, Y. Lu, J. Peng, J. F. Chen, S. H. Yu, *Adv Funct Mater* **2012**, 22, 4017.

[47] M. E. Byrne, K. Park, N. A. Peppas, *Adv Drug Deliver Rev* **2002**, 54, 149.

[48] N. M. Bergmann, N. A. Peppas, *Ind Eng Chem Res* **2008**, 47, 9099.

[49] P. D. Thornton, R. J. Mart, R. V. Ulijn, *Adv Mater* **2007**, 19, 1252.

[50] G. M. Whitesides, *Abstr Pap Am Chem S* **1996**, 212, 31.

[51] R. Bashir, *Abstr Pap Am Chem S* **2003**, 225, U989; B. Ziaie, R. A. Siegel, *Proceedings of the 26th Annual International Conference of the Ieee Engineering in Medicine and Biology Society*, Vols 1-7 **2004**, 26, 2670.

[52] M. A. C. Stuart, W. T. S. Huck, J. Genzer, M. Muller, C. Ober, M. Stamm, G. B. Sukhorukov, I. Szleifer, V. V. Tsukruk, M. Urban, F. Winnik, S. Zauscher, I. Luzinov, S. Minko, *Nat Mater* **2010**, 9, 101.

[53] J. S. Randhawa, K. E. Laflin, N. Seelam, D. H. Gracias, *Adv Funct Mater* **2011**, 21, 2395.

[54] T. Traitel, R. Goldbart, J. Kost, *J Biomat Sci-Polym E* **2008**, 19, 755; R. S. Shawgo, A. C. R. Grayson, Y. W. Li, M. J. Cima, *Curr Opin Solid St M* **2002**, 6, 329.

[55] J. Z. Hilt, A. K. Gupta, R. Bashir, N. A. Peppas, *Biomed Microdevices* **2003**, 5, 177; A. Richter, A. Bund, M. Keller, K. F. Arndt, *Sensor Actuat B-Chem* **2004**, 99, 579.

[56] H. Geckil, F. Xu, X. H. Zhang, S. Moon, U. Demirci, *Nanomedicine-Uk* **2010**, 5, 469.

[57] D. J. Beebe, J. S. Moore, J. M. Bauer, Q. Yu, R. H. Liu, C. Devadoss, B. H. Jo, *Nature* **2000**, 404, 588.

[58] H. van der Linden, S. Herber, W. Olthuis, P. Bergveld, Sensor Mater **2002**, 14, 129; W. R. K. Illeperuma, J. Y. Sun, Z. G. Suo, J. J. Vlassak, *Soft Matter* **2013**, 9, 8504; Y. Zhang, S. Kato, T. Anazawa, *Smart Mater Struct* **2007**, 16, 2175.

[59] M. E. Harmon, D. Kuckling, C. Frank, *Abstr Pap Am Chem S* **2003**, 225, U709; A. Revzin, R. J. Russell, V. K. Yadavalli, W. G. Koh, C. Deister, D. D. Hile, M. B. Mellott, M. V. Pishko, *Langmuir* **2001**, 17, 5440; M. J. Lesho, N. F. Sheppard, *Sensor Actuat B-Chem* **1996**, 37, 61.

[60] M. Guvendiren, J. A. Burdick, S. Yang, *Soft Matter* **2010**, 6, 2044.

[61] F. Audouin, A. Heise, Eur Polym J 2013, 49, 1073; H. M. Ma, R. H. Davis, C. N. Bowman, *Macromolecules* **2000**, 33, 331.

[62] Z. Gao, D. B. Henthorn, C. S. Kim, *Journal of Micromechanics and Microengineering* **2008**, 18; L. Liang, X. D. Feng, L. Peurrung, V. Viswanathan, *J Membrane Sci* **1999**, 162, 235.

[63] M. E. Harmon, T. A. M. Jakob, W. Knoll, C. W. Frank, *Macromolecules* **2002**, 35, 5999.

[64] M. E. Harmon, M. Tang, C. W. Frank, *Polymer* **2003**, 44, 4547.

[65] I. Tokarev, I. Tokareva, V. Gopishetty, E. Katz, S. Minko, *Adv Mater* **2010**, 22, 1412.

[66] H. G. Schild, *Prog Polym Sci* **1992**, 17, 163.

[67] N. Yamada, T. Okano, H. Sakai, F. Karikusa, Y. Sawasaki, Y. Sakurai, *Makromol Chem-Rapid* **1990**, 11, 571; G. Rollason, J. E. Davies, M. V. Sefton, *Biomaterials* **1993**, 14, 153.

[68] K. Uchida, K. Sakai, E. Ito, O. H. Kwon, A. Kikuchi, M. Yamato, T. Okano, *Biomaterials* **2000**, 21, 923.

[69] M. E. Nash, D. Healy, W. M. Carroll, C. Elvira, Y. A. Rochev, *J Mater Chem* **2012**, 22, 19376.

[70] M. Nitschke, S. Gramm, T. Gotze, M. Valtink, J. Drichel, B. Voit, K. Engelmann, C. Werner, *J Biomed Mater Res A* **2007**, 80A, 1003.

[71] T. Shimizu, M. Yamato, Y. Isoi, A. Kikuchi, T. Okano, *Tissue Engineering for Therapeutic Use 6* **2002**, 1243, 57.

[72] K. Ohashi, T. Yokoyama, M. Yamato, H. Kuge, H. Kanehiro, M. Tsutsumi, T. Amanuma, H. Iwata, J. Yang, T. Okano, Y. Nakajima, *Nat Med* **2007**, 13, 880.

[73] T. Sumide, K. Nishida, M. Yamato, T. Ide, Y. Hayashida, K. Watanabe, J. Yang, C. Kohno, A. Kikuchi, N. Maeda, H. Watanabe, T. Okano, Y. Tano, *Faseb J* **2006**, 20, 392.

[74] J. Edahiro, K. Sumaru, Y. Tada, K. Ohi, T. Takagi, M. Kameda, T. Shinbo, T. Kanamori, Y. Yoshimi, *Biomacromolecules* **2005**, 6, 970.

[75] S. T. Koev, P. H. Dykstra, X. Luo, G. W. Rubloff, W. E. Bentley, G. F. Payne, R. Ghodssi, *Lab Chip* **2010**, 10, 3026.

[76] Y. Cheng, X. L. Luo, J. Betz, S. Buckhout-White, O. Bekdash, G. F. Payne, W. E. Bentley, G. W. Rubloff, *Soft Matter* **2010**, 6, 3177; L. Q. Wu, A. P. Gadre, H. M. Yi, M. J. Kastantin, G. W. Rubloff, W. E. Bentley, G. F. Payne, R. Ghodssi, *Langmuir* **2002**, 18, 8620.

[77] J. Berger, M. Reist, J. M. Mayer, O. Felt, N. A. Peppas, R. Gurny, *Eur J Pharm Biopharm* **2004**, 57, 19.

[78] T. H. Chen, D. A. Small, L. Q. Wu, G. W. Rubloff, R. Ghodssi, R. Vazquez-Duhalt, W. E. Bentley, G. F. Payne, *Langmuir* **2003**, 19, 9382; B. Y. Wu, S. H. Hou, M. Yu, X. Qin, S. Li, Q. Chen, *Mat Sci Eng C-Bio S* **2009**, 29, 346.

[79] X. W. Shi, X. H. Yang, K. J. Gaskell, Y. Liu, E. Kobatake, W. E. Bentley, G. F. Payne, *Adv Mater* **2009**, 21, 984.

[80] Y. Li, X. Pang, R. F. Epand, I. Zhitomirsky, Mater Lett **2011**, 65, 1463; A. L. Sun, G. R. Chen, Q. H. Zhu, *Advanced Composite Materials, Pts 1-3* **2012**, 482-484, 164.

[81] Q. M. Zhou, Q. J. Xie, Y. C. Fu, Z. H. Su, X. Jia, S. Z. Yao, *J Phys Chem B* **2007**, 111, 11276.

[82] X. L. Luo, J. J. Xu, Y. Du, H. Y. Chen, *Anal Biochem* **2004**, 334, 284.

[83] J. Redepenning, G. Venkataraman, J. Chen, N. Stafford, *J Biomed Mater Res A* **2003**, 66A, 411.

[84] Y. Liu, X. W. Shi, E. Kim, L. M. Robinson, C. K. Nye, R. Ghodssi, G. W. Rubloff, W. E. Bentley, G. F. Payne, *Carbohyd Polym* **2011**, 84, 704; Y. Cheng, X. L. Luo, G. F. Payne, G. W. Rubloff, *J Mater Chem* **2012**, 22, 7659.

[85] J. J. Park, X. L. Luo, H. M. Yi, T. M. Valentine, G. F. Payne, W. E. Bentley, R. Ghodssi, G. W. Rubloff, *Lab Chip* **2006**, 6, 1315.

[86] C. H. Kuo, W. H. Huang, C. K. Lee, Y. C. Liu, C. M. J. Chang, H. H. Yang, C. J. Shieh, *Int J Electrochem Sc* **2013**, 8, 9242; L. Caseli, D. S. dos Santos, M. Foschini, D. Goncalves, O. N. Oliveira, *Mat Sci Eng C-Bio S* **2007**, 27, 1108.

[87] G. F. Payne, E. Kim, Y. Cheng, H. C. Wu, R. Ghodssi, G. W. Rubloff, S. R. Raghavan, J. N. Culver, W. E. Bentley, *Soft Matter* **2013**, 9, 6019.

[88] M. Cheong, I. Zhitomirsky, *Colloid Surface A* **2008**, 328, 73.

[89] Y. Cheng, C. Y. Tsao, H. C. Wu, X. L. Luo, J. L. Terrell, J. Betz, G. F. Payne, W. E. Bentley, G. W. Rubloff, *Adv Funct Mater* **2012**, 22, 519.

[90] F. Sun, I. Zhitomirsky, *Surface Engineering* **2009**, 25, 621.

[91] T. H. Chen, H. D. Embree, L. Q. Wu, G. F. Payne, *Biopolymers* **2002**, 64, 292.

[92] L. Ionov, *Adv Funct Mater* **2013**, 23, 4555

[93] H. He, X. Cao, L. J. Lee, *Journal of Controlled Release* **2004**, 95, 391.

[94] H. Y. He, J. J. Guan, J. L. Lee, *J Control Release* **2006**, 110, 339.

[95] T. G. Leong, C. L. Randall, B. R. Benson, N. Bassik, G. M. Stern, D. H. Gracias, *P Natl Acad Sci USA* **2009**, 106, 703.

[96] N. Bassik, A. Brafman, A. M. Zarafshar, M. Jamal, D. Luvsanjav, F. M. Selaru, D. H. Gracias, *J Am Chem Soc* **2010**, 132, 16314.

[97] S. Zakharchenko, N. Puretskiy, G. Stoychev, M. Stamm, L. Ionov, *Soft Matter* **2010**, 6, 2633; S. Zakharchenko, E. Sperling, L. Ionov, *Biomacromolecules* **2011**, 12, 2211.

[98] S. Pedron, S. van Lierop, P. Horstman, R. Penterman, D. J. Broer, E. Peeters, *Adv Funct Mater* **2011**, 21, 1624.

[99] T. S. Shim, S. H. Kim, C. J. Heo, H. C. Jeon, S. M. Yang, *Angew Chem Int Edit* **2012**, 51, 1420.

[100] L. Ionov, *Soft Matter* **2011**, 7, 6786.

[101] V. Luchnikov, L. Ionov, M. Stamm, *Macromol Rapid Comm* **2011**, 32, 1943; M. Jamal, A. M. Zarafshar, D. H. Gracias, *Nat Commun* **2011**, 2.

[102] M. Jamal, S. S. Kadam, R. Xiao, F. Jivan, T. M. Onn, R. Fernandes, T. D. Nguyen, D. H. Gracias, *Adv Healthc Mater* **2013**, 2, 1142; H. Therien-Aubin, Z. L. Wu, Z. H. Nie, E. Kumacheva, *J Am Chem Soc* **2013**, 135, 4834.

[103] S. Fatikow, U. Rembold, *Mycrosystem Technology and Microrobotics*, Karlsruhe **1997**.

[104] A. Kortschack, S. Fatikow, *Smart Structures, Devices, and Systems* 2002, 4935, 1; R. Bogue, *Ind Robot* **2010**, 37, 341.

[105] Y. Osada, H. Okuzaki, H. Hori, *Nature* **1992**, 355, 242.

[106] J. Kim, S. Kim, Y. Jeong, S. Park, H. C. Kim, K. Chun, B. Kim, 2005 *27th Annual International Conference of the IEEE Engineering in Medicine and Biology Society*, Vols 1-7 **2005**, 4046.

[107] L. Yeghiazarian, S. Mahajan, C. Montemagno, C. Cohen, U. Wiesner, *Adv Mater* **2005**, 17, 1869.

[108] L. Yeghiazarian, H. Arora, V. Nistor, C. Montemagno, U. Wiesner, *Soft Matter* **2007**, 3, 939.

[109] L. W. Shi, S. X. Guo, M. X. Li, S. L. Mao, N. Xiao, B. F. Gao, Z. B. Song, K. Asaka, *Sensors* 2012, 12, 16732; A. P. Gerratt, S. Bergbreiter, *Smart Materials and Structures* **2013**, 22.

[110] Y. Ma, Y. Zhang, B. Wu, W. Sun, Z. Li, J. Sun, *Angewandte Chemie International Edition* **2011**, 50, 6254.

[111] M. Piovanelli, T. Fujie, B. Mazzolai, L. Beccai, 2012 *4th Ieee Ras & Embs International Conference on Biomedical Robotics and Biomechatronics (Biorob)* **2012**, 612.

[112] G. H. Kwon, J. Y. Park, J. Y. Kim, M. L. Frisk, D. J. Beebe, S.-H. Lee, *Small* **2008**, 4, 2148.

[113] W. Q. Hu, K. S. Ishii, Q. H. Fan, A. T. Ohta, *Lab Chip* **2012**, 12, 3821.

[114] W. Q. Hu, K. S. Ishii, A. T. Ohta, *Appl Phys Lett* **2011**, 99.

[115] S. Palagi, B. Mazzolai, C. Innocenti, C. Sangregorio, L. Beccai, *Appl Phys Lett* **2013**, 102, 124102.

[116] S. N. Tabatabaei, J. Lapointe, S. Martel, *Adv Robotics* **2011**, 25, 1049.

CHAPTER 3

Sugarman

You're the answer

That makes my questions disappear…

Sugar Man-Rodriguez (1977)

Chitosan electrodeposition for microrobotic drug delivery

Work partially published in:

Advanced Healthcare Materials (2013) 7: 1037-1044

S.Fusco, G. Chatzipirpiridis, K.Sivaraman, O.Ergeneman, B.J. Nelson, S. Pané

3.1 Chapter overview

This chapter describes a scalable method to incorporate smart hydrogel components onto magnetic microrobotic platforms by means of controlled electrodeposition of chitosan. The microrobots are intended to deliver drugs specifically into the eye with an embedded sensitivity to the environmental conditions.

As a necessary background for the understanding of the contribution of this work, the state of the art in the field of electrodeposition of chitosan is briefly reported at the beginning of the chapter.

Following that, a short report of medical issues related to the treatment of posterior eye diseases is presented, together with the strategies that are currently used. The advantages of a microrobotic approach to the problem are briefly reported, and the ideal requirements of a medical microrobot are analysed. Chitosan electrodeposition is proposed as one possible solution for the incorporation of a smart hydrogel on microrobots. The polymer is used as a smart matrix to release brilliant green (BG), a small model drug, in an environmentally controlled way.

Results include a study of the electrodeposition performance in terms of growth, quality of the layers, and electrochemical parameters. A chemical and physical characterization of the deposited material is performed by FTIR, Cryo-SEM, and optical imaging. Three possible treatments to modify the characteristics of the matrices, neutralization, ionic crosslinking in an acid solution, and ionic crosslinking in a basic solution, are proposed and analyzed. A detailed overview of the drug delivery abilities of the different platforms in simulated physiological and pathological (acid pH) conditions is presented

to demonstrate the “intelligence” of the system. A final prototype is also presented before outlining the contribution of the work to the area of microrobotics and materials science and possible future directions.

3.2 Electrodeposition of chitosan from aqueous solutions

Electrodeposition (ED) is a vastly used and relatively inexpensive processing technique that exploits the electrophoresis mechanism for the movement and the deposition of charged particles on complex substrates. ED is usually carried out in a two electrode cell (three in case of a reference electrode), as shown in figure 3.1, where an electric source supplies current and create a potential difference across the system. Deposition of films has been explained with different theories. Hamaker and Verwey [1] proposed a sort of sedimentation process where the pressure created by the accumulating particles on the electrode overcomes the repulsive forces and results in a deposit. Grillon [2] proposed charge neutralization and, therefore, a change of solubility of particles in contact to the electrode to explain the deposition of monolayers. Another plausible mechanism proposed by Sarkar et al. [3] involves thinning of the electrical double layer of the particles to explain the predominance of attractive interactions on the electrode. Additional theories, especially applied to biomolecules, include the formation of a pH gradient by oxidation of water, which drives a sol-gel transition. Most probably a combination of all these theories helps to understand the physics occurring at the electrodes. From a practical point of view, electrodeposition provides coatings or free-standing structures with different properties depending on the process parameters such as time, electric field, and chemical and physical conditions of the electrolytic solution.

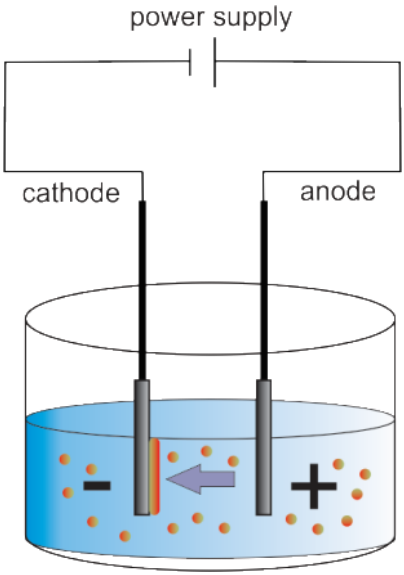

Figure 3.1. *Electrophoretic deposition cell showing the deposition of positively charged particles onto the cathode due to the potential imposed between the two electrodes.*

In the last twenty years ED was employed for the development of a variety of advanced biomaterials, including ceramic coatings [4], composites, porous materials [5] and polymers [6]; the advantage of this technique is that it produces uniform deposits with high microstructural homogeneity, and with very simple and non-toxic procedures. Moreover, additional advantages are related to the possibility of simultaneously manipulating biological entities and produce biofilms [7]. Almost ten years ago a class of pH responsive biopolymers was found to form stable films due to the application of an electric potential between surfaces. Among these, the amino polysaccharide chitosan was the first material to be electrodeposited by cathodic

neutralization mechanisms [8], followed by anodic deposition of the acidic polysaccharide alginic acid [9] and hyaluronic acid [10].

Chitosan is one of the most promising and the most studied of these molecules due to its unique combination of properties. It is a polysaccharide derived from naturally occurring chitin, one of the most recurring biopolymers on earth after cellulose. Chitin can be found as a supporting material of crustaceans, insects, fungal cell walls, nematodes eggs, and gut linings (see figure 3.2). It consists of long chains of N-acetylglucosamine or glucosamine, and it can be converted into chitosan with thermochemical treatments by alkaline deacetylation in NaOH [11] or biologically through a fermentation process [12]. Considering its sources, chitosan is abundant and biocompatible. Moreover, it is biodegradable and metabolized by certain human enzymes [13]. It is bioadhesive [14], and it also acts as a penetration enhancer by opening tight epithelial junctions [15].

Most chitosan properties are derived from the presence of the primary amine groups on its repeating units. At low pH the amines are protonated allowing chitosan to be soluble in aqueous acid solutions. When the pH exceeds the value of pK_a ~6.5, the amines become increasingly deprotonated resulting in a loss of solubility and the formation of stable pH responsive chitosan films. The amine groups also play a key role in tailoring the properties of chitosan as they can be bonded to other chemical entities by means of covalent attachment or physical interaction [16-18].

Chitosan films can be produced from acidic solutions by different methods, most of which are compatible with the presence of biological entities, including casting or printing and self-assembly [19]. However, only electrodeposition provides spatial and temporal control and more fabrication

flexibility, because it enables chitosan to grow on 3D geometries or patterns and complex shapes. The process can be performed in a simple and reversible way for a variety of final applications.

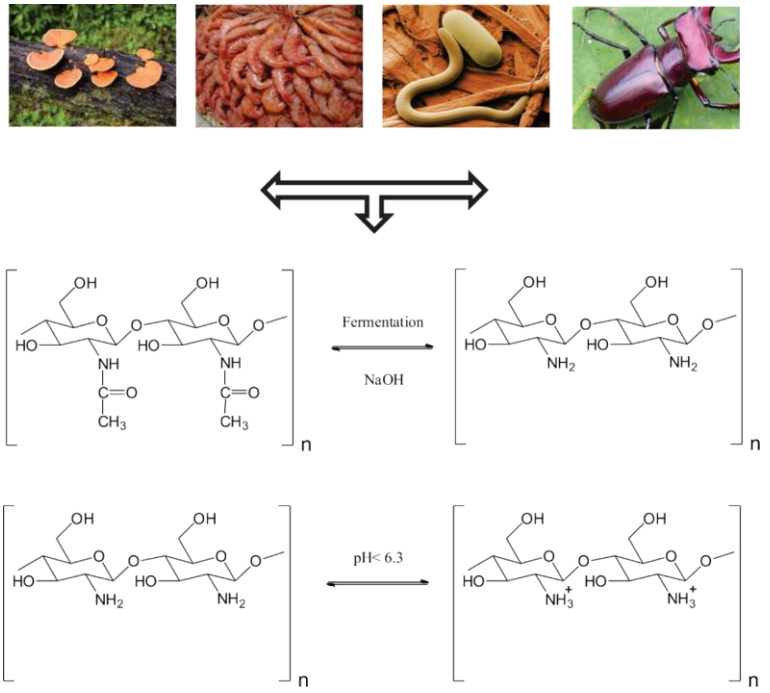

Figure 3.2. *Chitin (upper left) and chitosan (upper right) are found in fungal cell walls, crustacean shells, nematodes eggs, and insect exoskeletons. The deacetylation process involves the loss of the acetyl group by fermentation or basic treatment and the conversion from chitin to the pH responsive chitosan.*

3.3 State of the art in electrodeposition of chitosan

The first work in the area of electrodeposition of chitosan was performed at the beginning of 2001 by Redepenning et al. [8] in order to render electrodeposited hydroxyapatite coatings more "like living bone, a material that could be viewed as a complex composite with mechanical properties very different from crystalline hydroxyapatite". The results of the composite deposition of brushite and chitosan were characterized primarily by SEM observation, X-ray powder diffraction and thermogravimetric analysis. However, the first study considering the conditions for deposition was proposed by Wu et al. as part of the Maryland Biochip Collaborative Group [20]. The researchers showed that by applying a negative voltage in a slightly acidic chitosan aqueous solution (pH 5, 1 w/v %), it was possible to prepare micron-sized layers of insoluble polymer on gold electrodes. The rate of deposition was monitored by profilometry for different conditions of solution concentrations, time and applied voltage. Additionally, the effect of NaOH neutralization after electrodeposition was investigated visually, and a sort of smoothing effect was observed when compared to as-prepared samples. The interest of the group focused later on the functionalization of miniaturized systems for sensing applications, as can be seen in the works of Fernandes et al [21], Park et al [22]. Yi et al [23], Lewandowski [24] Luo[25], Shi[26] and Buckhout-White et al[27].

Many of these efforts straightforwardly explain strategies for spatially-controlled assembly of biomolecules on electrodes and hard substrates using chitosan as scaffold. By taking advantage of the chemical reactivity of the amine groups of the polysaccharide and of the electrodeposition process, fluorescent markers like GFP protein, DNA strands and active enzymes were

immobilized with chitosan and deposited on substrates. The assembly methods involved:

- Co-deposition after blending of the biomolecule in the chitosan solution. This is also the case of other works by Zhitomirsky et al [28] with hemoglobin molecules, and of the literature related to glucose oxidase immobilization for sensor platforms [29].

- Covalent *ex situ* conjugation between the two molecules and subsequent co-electrodeposition of the pH responsive complex.

- Electrodeposition of chitosan and subsequent in situ activation and functionalization.

The same group investigated the mechanisms and the characteristics of the chitosan electrodeposition process. The hypothesis that the hydrogel deposition at the cathode surface resulted from a high localized pH was first proposed and tested by applying a low current density to a very acidic chitosan solution (pH = 2) in order to limit the pH gradient extending from the electrode [21]. Simchi et al. [30] studied the linear film growth as a function of pH and biopolymer concentration. A change of conformation of the chitosan chains from a semi-rigid rod to a bulky helical structure was hypothesized as a result of an increase of pH, thus explaining the decrease of solubility and the aggregation into stable films. Cheng et al. [31] developed a direct, non-destructive, *in situ* visualization method of the pH profile created during the electrodeposition of chitosan by using a universal pH indicator solution. They described the three reactions happening into the electrolytic cell as:

Anode: $2\ H_2O \rightarrow O_2 + 4H^+ + 4e^-$ (3.1)

Cathode: $2\ H_2O + 2e^- \rightarrow H_2 + 2\ OH^-$ (3.2)

Cathode: $\text{Chitosan-}NH_3^+ + OH^- \rightarrow \text{Chit-}NH_2 + H_2O$ (3.3)

Consequently, they linked the cathodic gelation to the number of OH^- anions created in reaction 3.2, and limited the influence of the electrophoretic migration of chitosan molecules to a contributing effect. This was explained by considering the much higher mobility of the hydroxyl ions as compared to that of the chitosan cations, and was visualized by means of fluorescently-tagged chitosan molecules. Physical crosslinking, responsible for the hydrogel formation, was facilitated by the partial change of conformation of the chitosan chains, and allowed gelation even without complete de-protonation of the amine groups. That is to say, electrodeposited chitosan gels are formed in an inhomogeneous way by entangling neutralized chitosan molecules to partially positively charged zones, which move toward the cathode thanks to the electric field and contribute to a pH dependent density distribution of the film.

Zangmeister et al. [32] identified the reactions involved in the electrodeposition of chitosan by cyclic voltammetry and matched the voltage of deposition with the reduction potential of water (-1.1 ± 0.1 V). Moreover, they confirmed the open and conductive structure of the deposited chitosan by checking the permeability of the film to charged redox species. Finally, Liu et al. [33] investigated the influence of the addition of NaCl in the electrolytic bath on the chitosan film formation. NaCl is known to screen electrostatic repulsions, thus altering chitosan solution properties and promote aggregation. Indeed, thicker, more compact and rougher films were

produced by electrodeposition, as seen by profilometry and AFM. QCM-D measurements were performed to evaluate the increase of the swelling ability of chitosan hydrogels as a function of the salt content increase in the bath, and the respective decrease of the layer stiffness, and again revealed the possibility to tailor the material during electrodeposition.

A wide area of applications of chitosan electrodeposition deals with the fabrication of composite materials. Matrices resembling natural bone [8] have been electrodeposited by introducing hydroxyapatite in chitosan solutions. The same materials together with silver ions were electrodeposited on various substrates to create an Ag^{+} long term releasing matrix with prolonged antibacterial properties [34]. In the same way, co-deposition or blending was performed to achieve matrices with chitosan and other polymers, such as alginate [35] or poly(vinyl)alcohol [36], for tissue engineering or drug delivery.

Chitosan and functionalized carbon nanotubes have been shown to interact covalently and co-electrodeposit on surfaces of stainless steel, thus increasing the Young's modulus and the fatigue properties of the substrate [37]. The same principle has been widely used for sensing applications [38] by exploiting the excellent electrical and electrochemical properties of the nanostructures.

Recently graphene oxide and reduced graphene oxide have been attached or immobilized into chitosan matrices to produce composites for sensing and drug delivery applications [39]. This again showed that the field of the electrodeposition of this biopolymer offers a huge variety of applications and combinations for the field of MEMS and micro devices (figure 3.3).

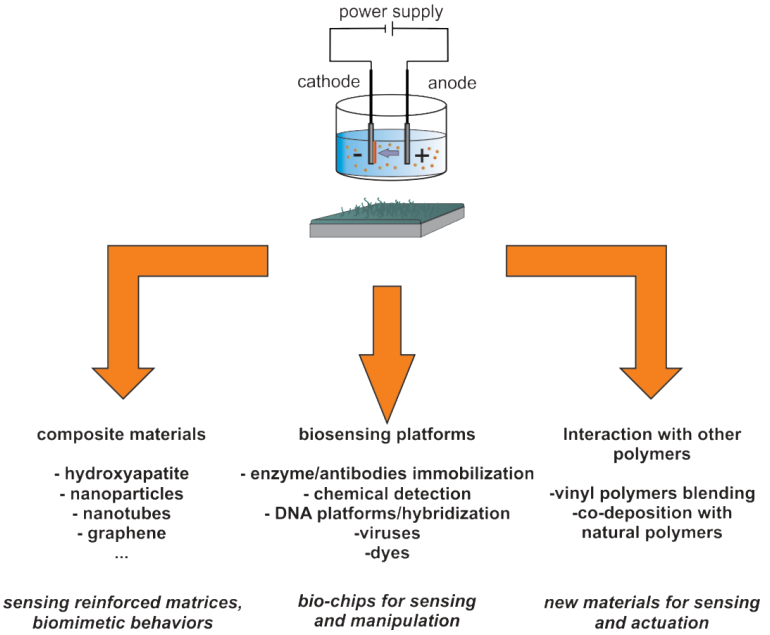

Figure 3.3. *Electrodeposition of chitosan has been used in different areas of research. The natural physical and chemical properties of the polymer make it attractive for interaction with a large variety of molecules and entities, including nanoparticles, enzymes, and other polymers.*

3.4 Motivation: a smart microrobot for drug delivery in the eye

The number of eye diseases affecting the posterior segment of the eye (vitreous, retina, choroid) such as age related macular degeneration (AMD), diabetic retinopathy, diabetic macular edema (DME), and retinal vein occlusion (RVO), is currently increasing with the aging world population. Although laser therapy or vitreoretinal surgery still constitutes the standard treatments, drug delivery has become progressively important and more frequently used. Nevertheless, due to the nature of the eye and its anatomical position and physiology, many challenges and complications must be overcome in the design of ophthalmic drug delivery systems.

Topically administered eye drops or systemic administration suffer from limited efficacy due to negligible intraocular penetration [40], rapid excretion through lachrymal fluids or blood flow [41], and indiscriminate distribution [42], which can lead to severe side effects. Intravitreal injections offer several advantages over conventional methods by increasing the drug level without causing systemic side effects. These injections are routinely applied in clinical settings, though repeated sessions are needed in order to compensate for the elimination of the drugs from the vitreous. This often causes often patient discomfort and, in some situations, leads to complications such as infections or irreversible damage [43].

Micro and nanofabrication technologies provide the possibility of designing small-scale carriers capable of delivering precise doses of drugs as near the target as possible. Ideally drug delivery systems should be sufficiently miniaturized to reach the disease site but with enough volume to

accommodate a relevant dose of drug (tens to hundreds of micrograms to be comparable with the current doses of potent systemic drugs [44]). In addition, they should satisfy biocompatibility and non-toxicity standards throughout their desired time of action. Finally, the device should be trackable and able to release drugs on demand based on external commands or local biochemical changes. For example, altered biological conditions are usually accompanied by local acidosis due to local accumulation of H^+ created by elevated glycolysis, which could be exploited as a triggering condition [45].

Magnetic microrobotic systems have the potential to provide continuously controllable sub-millimeter wireless platforms for targeted drug delivery. These devices usually consist of soft-magnetic cylindrical or elliptical bodies [46, 47] wirelessly moved by permanent magnets or, more efficiently, by electromagnetic systems [47, 48]. Their size can reach that of recently developed commercial drug delivery devices, like the Vitrasert [49] or the Medidur [50] (few millimeters in length) so that they can be inserted through a small incision in a minimally invasive way.

Their intelligence is mainly related to the externally controlled systems used for their manipulation. However, the use of a smart material able to respond to external stimuli can enhance the capabilities and the "intelligence" of these devices. Including smart hydrogels into the previously described microrobotic platforms constitutes an excellent and desired strategy for the design of a new generation of micro devices.

Some requirements and constraints must be specified at this point:

- The fabrication method for the incorporation of hydrogels onto magnetic microrobots needs to be compatible with the designed system and

previous fabrication steps. It must work on magnetic bodies with complex 3-dimensional shapes and geometries, and it should be applicable to a variety of substrates.

- Additional processes to integrate a smart hydrogel into the platform must be compatible with the incorporation of biological active components such as drugs or cells. This implies avoiding hard chemicals, reagents or extreme conditions.

- The chosen smart hydrogel should be able to incorporate a quantity of active agents comparable to the ones stored in the commercial drug delivery devices.

- The proposed material should release the stored drug in a smart way by responding to an external imposed stimuli related to the pathological condition. The release should be sustained and prolonged over days, if not weeks.

Considering these constraints, we identified the electrodeposition of chitosan as the optimal candidate for the desired applications.

3.5 Materials and methods

3.5.1 Preparation of the solutions and the substrates

Chitosan from crab shells (CS, 75-85% deacetylation), sodium tripolyphosphate (TPP, 85% assay), Brilliant Green (BG, dye content 90%) and PBS were used for electrodeposition and drug release. All chemicals were purchased from Sigma Aldrich and used without further purification. Gold-coated silicon chips were used as substrates to prepare chitosan-based films. The chips were obtained by evaporating a 150 nm gold layer (with a 50 nm titanium adhesion layer, and a 50 nm titanium protective layer) on a <100> silicon substrate diced into squares of 10 mm each side. Before electrodeposition the chips were cleaned by sequentially dipping them into 0.5 % HF (to remove the titanium protective layer), acetone, isopropanol and Millipore Milli-Q-Water. The chips were immersed in Piranha (H_2SO_4: H_2O_2 7:3) solution for 5 minutes and briefly rinsed with Millipore Milli-Q-Water to completely remove any organic contamination before use.

Chitosan solutions were prepared by adding chitosan flakes to 1% acetic acid solution and stirred until full dissolution. After mixing overnight, the solutions were filtered using a vacuum filter system to remove undissolved particles, stabilized at pH 5.0 with the addition of drops of 1 M NaOH, and brought to a final concentration of 0.5 w/v%. Electrodeposited chitosan-BG films were obtained from electrolytes containing additional 0.1 w/v% (2 mM) of BG. The pH of the chitosan solution was not influenced by this step.

3.5.2 Electrodeposition of chitosan and post deposition treatments

The electrodeposition of chitosan films was performed in a three-electrode single compartment cell using Ag/AgCl reference electrode and a platinized titanium mesh counter electrode. A Gamry Reference 3000 (Gamry Instruments, Usa) potentiostat/galvanostat controlled by a Gamry Framework software was used to control the deposition. Chitosan layers were grown galvanostatically for different times (2.5, 5 and 10 minutes) and different current density conditions (5, 10, 15, 20, 40 A/m^2) to study the dimensional control of the process. The area of deposition was set to 0.5 cm^2. After deposition, the chitosan coated electrodes were removed from the solution and rinsed with water to ensure removal of unbound material. Following that, different treatments were performed. Neutralization of the layers was induced by shortly dipping the samples into 1 M NaOH solution (1 minute) and subsequently rinsing with water. Crosslinked samples were deposited for 5 minutes, then neutralized (1 M NaOH for one minute), and subsequently immersed in aqueous solutions of 10 w/v% TPP for 30 minutes. As the pH of this solution influences the crosslinking reaction and efficiency, two solutions with different pH, 8.5 and 5, were used. The first value refers to the natural pH of a TPP water solution, the second was adjusted by adding drops of acetic acid into the first solution.

A similar process was used for the preparation of drug releasing hydrogels on gold chips. The deposition of the chitosan-loaded samples was carried out at -1.5 mA/cm^2 for 10 minutes. Cyclic voltammetry was used to monitor the consequent electrochemical processes occurring at the cathode between 0 V and -3 V (vs. Ag/AgCl). Rinsing and neutralization were performed as described above. Crosslinking was performed for 30 minutes at pH 8.5 or alternatively for 10 or 30 minutes at pH 5.

3.5.3 Electrodeposition on microrobotic platforms

Stainless steel micro-needles (UPC medical USA) served as three-dimensional substrates to build up a drug-delivery magnetic microrobotic prototype. An electrolyte containing cobalt and nickel salts and other additives was used to implement soft-magnetic coatings on the needles. Electrodeposition of chitosan-BG films was subsequently performed on the three-dimensional magnetic microdevices. Electrodeposition of chitosan films on the micro needles was performed at the same current density tested on the chips for 70 minutes in order to provide the same amount of charge with respect to previous experiments.

3.5.4 Characterization of the chitosan growth

The time dependent growth of the chitosan during electrodeposition was recorded using a USB digital microcamera (Dnt Gmbh, Germany) focused on the lateral profile of the growing hydrogel. The change in the intensity of the transmitted light due to sol-gel transition and the profile of the deposition was monitored. A quantitative and qualitative analysis of the process was performed using the commercial software DigimicroScale 2.0. The swelling characteristics of the different chitosan layers were also monitored in this way. The dried thickness of the deposited layers was measured by profilometry (Tencor model P10 Surface profiler, Tencor Instruments, USA) and averaged over at least 5 measurements on each of 5 samples. Profilometry measurements were also used to provide some insights on the resistance of the matrices to dissolution or reorganization. Samples treated in different ways after deposition were immersed in water for 1,2,3, and 6 days, and dried at every time interval. Their thickness changes were monitored and compared to the original sample.

3.5.5 Cryo-SEM imaging

The surface and interior morphology were characterized by Cryo-SEM. Sections of the electrodeposited layers were detached from the substrate using a disposable biopsy punch and saved in their natural swollen state using a high pressure freezing method (HPM010, BalTec/Leica, Vienna, Austria). A pressure of 2200 bar was rapidly applied prior to freezing with supercritical liquid nitrogen. Cryo-fracturing was performed in liquid nitrogen by scratching the surface of the samples before being transferred in a freeze etching device (BAF060, BalTec/Leica, Vienna, Austria) and precooled at -120°C under high vacuum. The hydrogels were then left at -100°C (ramp 90°C/hr) for 1 hour and subsequently brought back to -120°C (ramp 90°C/hr) to sublimate the water. Finally, the samples were shadowed (evaporation by electron beam) with tungsten within the BAF 060 from an elevation angle of 45° to an averaged layer thickness of 6 nm and then from a variable angle between 45° and 90° for an additional 3 nm layer. Frozen and coated samples were transferred under high vacuum (2.0x 10-7 mbar) at -120°C to a cryo-SEM (LEO, Gemini 1530, Carl Zeiss, Oberkochen, Germany). The images were taken at -120°C with an acceleration voltage of 2 kV.

3.5.6 Chemical characterization

Chemical analysis was performed on samples deposited for 20 minutes at -1.5 mA/cm^2. Non-crosslinked and crosslinked samples were scanned by FTIR (FTIR Spectrum 100, Perkin Elmer Waltham, MA, USA) over a wave number range of 4600 to 600 cm^{-1}. The results were analyzed using the commercial software Spectrum (Perkin Elmer, MA, USA).

3.5.7 Drug delivery experiments

A preliminary analysis of the quantity of BG loaded onto electrodeposited chitosan hydrogels was performed by completely dissolving the deposited layers in 2 ml of PBS adjusted to pH 6.0 at room temperature. The solvent was collected and measured by UV/VIS spectroscopy (Infinite M200 Pro, Tecan AG, Mannendorf, Switzerland) at 624 nm. A minimum of five samples was analyzed, and the influence of neutralization, ionic crosslinking and the pH of the treatment were investigated.

In vitro release of BG entrapped in the chitosan matrix during electrodeposition was performed for a minimum of five samples for each condition, in PBS medium at pH 7.4 and pH 6.0 in order to mimic different environmental conditions. Dried samples were placed in 2 ml of PBS buffer at 37°C and allowed to swell and release the dye. At defined times the solvent volumes were collected, measured by UV/VIS spectroscopy at 624 nm wavelength and replaced with fresh solution (in order to mimic a perfect sink condition). Release was monitored for three weeks, and the kinetics was evaluated by fitting the *in vitro* data to different empirical models using MATLAB (The Mathworks, Natick, MA, USA).

3.6 Results

3.6.1 Analysis of growth and control of the thickness

The electrochemical deposition of chitosan was analyzed to define the kinetics of growth at different experimental conditions. A roughly linear profile was observed at various applied current densities. The results are shown in Figure 3.4 where the central thickness of the layers is reported as a function of time for the first 300 seconds of deposition. An increase in the standard deviation of thickness at higher current densities and longer deposition times was observed, together with the formation of hydrogen bubbles entrapped in the layer.

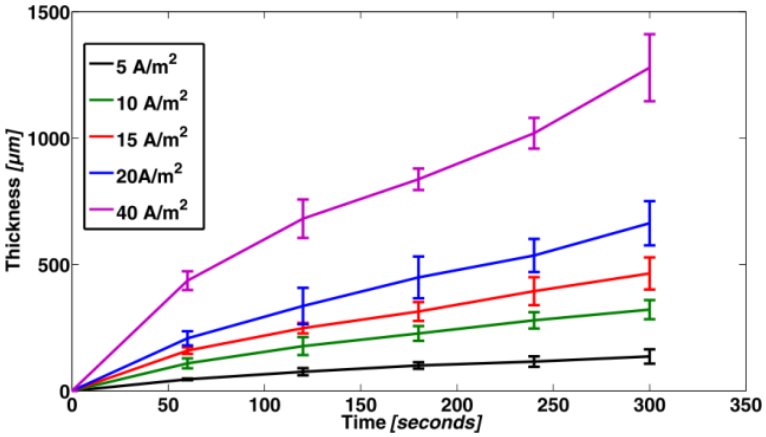

***Figure 3.4**. Thickness growth of the electrodeposited chitosan samples monitored by in situ direct visualization. An increase in the time or current density allows the formation of thick but less ordered layers.*

Profilometry analysis of the deposited material, after being dried in air, shows a rather non-linear behavior for most of the combinations of time and current densities. At relatively low current densities or too short deposition times, we observed a limitation in the thickness of the chitosan films. A high standard deviation in the results is clearly visible when the layers were grown at higher current densities or for relatively long times of deposition, thus rendering the process less controllable. A linear behavior with low standard deviations can be found for current densities lower than -15 A/m^2, even for 10 minutes of deposition (figure 3.5). The layers deposited in this way showed only little inhomogeneities related to the entrapment of hydrogen bubbles.

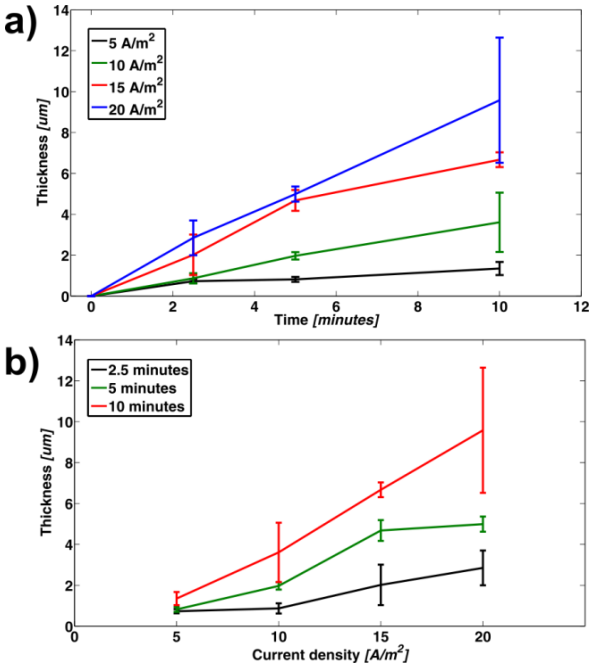

***Figure 3.5**. (a) Time dependency of the thickness of chitosan layers electrodeposited at different current densities. (b) The same results can be read as a function of current density to understand the effect of this parameter.*

3.6.2 Post-deposition treatments

Neutralization was performed right after rinsing by dipping the samples for one minute in a solution of 1 M NaOH. This process was also used to stabilize the layers before ionic crosslinking with TPP, in the way described above.

Samples immersed in 1 M NaOH showed an instantaneous change in color appearing whiter and more defined. No significant difference was observed in the wet layer thickness during the process. However, when immersed in

PBS after neutralization, the layers significantly swelled compared to the original thickness (see figure 3.6a and b). In the same way, their dried thickness, measured by profilometry increased when compared to their respective not neutralized layers. Moreover, higher internal inhomogeneities were found for every sample after this treatment (see figure 3.6c).

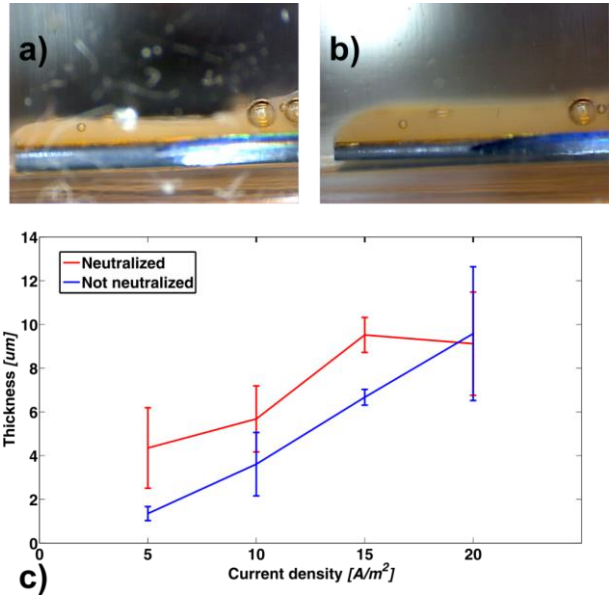

***Figure 3.6**. (a) and (b) show the effect of one minute neutralization in 1 M NaOH. The hydrogel layers get significantly and visibly expanded by the treatment. (c) Neutralization effect on samples deposited for 10 minutes. The process also modifies the dried thickness of the layers by increasing their average thickness and producing higher standard deviations, even at low current densities.*

Crosslinking with TPP performed at pH 5 led to a fast and significant shrinkage of the layers (by approximately a factor of four) followed by a

recovery of the original thickness when re-immersed in water. When measured by profilometry the deposited hydrogels were found to be comparable in size but smoother than the non-treated ones in their topography.

Crosslinking performed at pH 8.5 did not cause any visible change during treatment. However, the dried samples appeared generally much thicker than the non-treated ones with a less uniform surface profile.

The swelling ratio, defined as:

$$\text{Swelling ratio} = \frac{wet\ thickness\ (by\ in\ situ\ visualization)}{dried\ thickness\ (by\ profilometry)} \tag{3.4}$$

was also measured and found to be significantly affected by neutralization. Samples treated at pH 8.5 or pH 5 recovered a behavior similar to the original matrix after the neutralization step. All data relative to dried thickness and swelling ratio are reported in table 3.1.

Treatment	Dried thickness (5 mins deposition)	Swelling ratio (5 mins deposition)
As deposited chitosan	4.7±0.5	11.7 ±3.0
Neutralized chitosan (1 M NaOH, 1 minute)	5.8 ±1.9	20.1 ±5.5
Crosslinked pH 8.5 (30 minutes)	9.6 ±3,4	10.8 ±1.0
Crosslinked pH 5 (30 minutes)	5.1 ±1.5	7.8 ±1.2

Table 3.1. *Dried thickness, measured by profilometry and swelling ratio values for four analyzed conditions of chitosan membranes. Swelling ratio measurements based on a set of a minimum of three samples per condition obtained by comparative visual and profilometric analysis, while dried thickness is the results of a minimum of five samples for condition.*

FTIR analysis was performed to confirm the chemical changes following the different processes. Results are presented in figure 3.7.

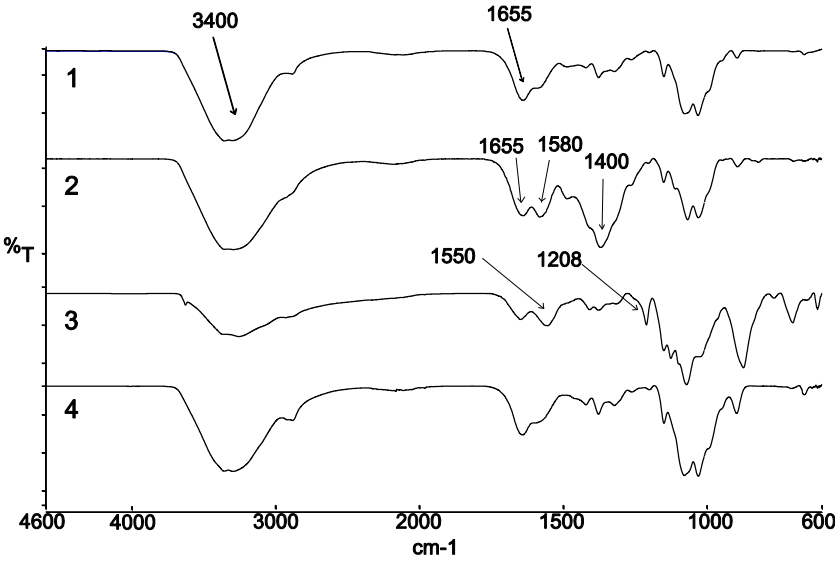

Figure 3.7*. FTIR spectra for the differently treated chitosan layers. From top to bottom, chitosan as electrodeposited (1), neutralized in NaOH (2), crosslinked at pH 5 for 30 minutes (3), crosslinked at pH 8.5 for 30 minutes (4).*

The typical bands of chitosan chains related to the stretching vibration of the amine and the hydroxyl groups are visible in all the curves at 3400 cm^{-1}, together with the ones related to the amide groups (1655 cm^{-1}). Neutralization induces the appearance of new peaks around 1580 cm^{-1} and 1400 cm^{-1}, which are attributed to the N-H stretching of the amine groups and the removal of acetate anions.

Crosslinking with TPP at pH 5 (curve 3 in the figure) generated new bands at 1550 cm^{-1} and at 1208 cm^{-1} related to the anti-symmetric deformation in NH_3^+ ions and the anti-symmetric stretching vibrations of PO_2^- groups. These peaks confirm the formation of ionic links between these groups. In contrast

to that, curve 4, related to the crosslinking performed at pH 8.5, shows only a very low signal for phosphorous groups at 1200 cm^{-1}, and a general profile resembling more the one of neutralized samples. This analysis seems to confirm the fact that the generated matrix had properties coming both from the interaction with phosphate groups and the concurrent presence of hydroxyl ions.

The microstructure of the as-deposited and modified hydrogel networks was investigated by Cryo-SEM, (figure 3.8). Images realized by the use of the in-lens detector (3.8A for the as deposited samples, 3.8B for the crosslinked at pH 5) revealed a gel pore size on the order of 500 nm for both cases. The fiber-like structure of the non-treated hydrogels or the neutralized layers appeared to be strengthened by the crosslinking process. Globular structures were observed growing on the fibers (3.8D in comparison to the control 3.8C, both obtained from a secondary lateral detector), with an increased effect with longer times of processing or when the ionic complexes were created at a lower pH.

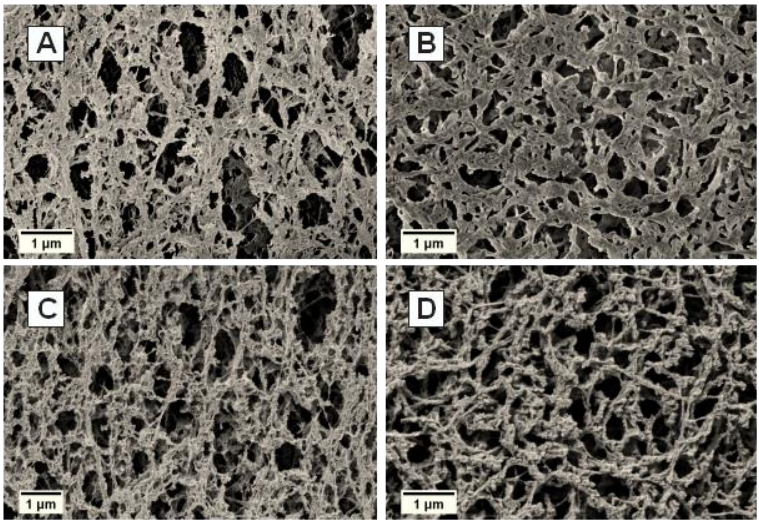

Figure 3.8*. Cryo-SEM micrographs of hydrogel matrices obtained from two different detectors. (A) and (B) show as deposited and crosslinked (pH 5) hydrogels, respectively obtained from an in lens detector. (C) and (D) represent the same areas taken from a secondary lateral detector which gives a better indication of topography. The material presents a uniform porous structure and filamentous fibers when not treated. Crosslinking with TPP thickens the structure and creates nodular structures that become more visible when the process is performed in an acidic environment.*

The different treatments influenced the stability of the layers after repetitive immersion into water. In general, measurements performed on samples deposited for 5 minutes at 1.5 A/m^2 showed that neutralization and crosslinking were causing a significant reduction of the thickness of the layers along the analyzed period of time. Untreated layers lost only 30% of their original thickness after one week (figure 3.9), while neutralized chitosan membranes decreased to more than half the original value. Crosslinking induced either large inhomogeneity among the various sections of the

different films (crosslinking at pH 5) or massive decrease of thickness (~70% of the initial value).

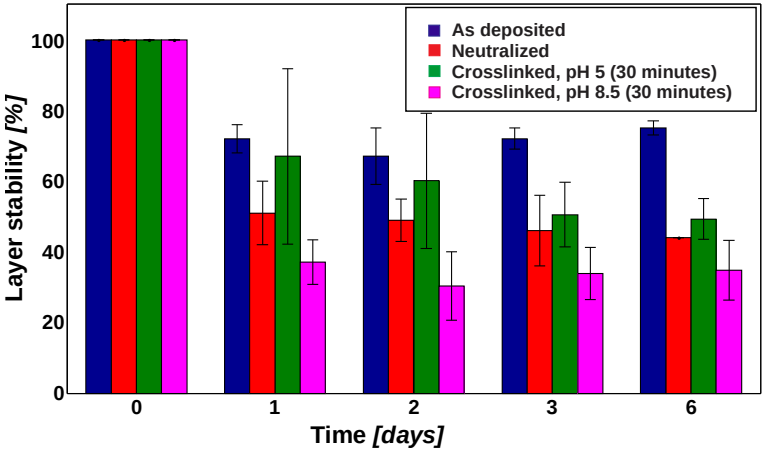

***Figure 3.9**. Layer stability of the differently treated chitosan films, as measured by comparing the thicknesses measured by profilometry after different intervals of time. Large variations were induced by crosslinking or alkaline treatments.*

3.6.3 Drug loading and release experiments

Drug release experiments were performed after including BG as a drug model in the electrolytic bath at a concentration of 2mM and co-electrodepositing it on the substrates. The deposition conditions were set at -15 A/m^2 for 10 minutes, following the results previously described. In this way films with a relatively high thickness and acceptable homogeneity could be deposited.

The influence of the addition of the positively charged small dye was investigated by cyclic voltammetry. Curve 1 in Figure 3.10 shows a

representative curve of a chitosan solution at pH 5. The onset of a large current density increase and hydrogen evolution was observed past -1.0 V and is attributed to the reduction of water (which occurs at potentials more negative than E=-1.04 V versus Ag/AgCl[32]). The curve then follows a linear trend at potential lower than -1.5 V. A similar pattern is recorded when BG is added to the bath (curve 2). However, at the current density used for our system (see dashed line), the drug loaded bath responds with a current 0.6 mA lower than the reference. This value and the shift of the curves reveal quantitatively and qualitatively the decrease of conductivity of the entire solution.

Records of the galvanostatic deposition of chitosan in the absence or in the presence of BG are presented in Figure 3.11. The addition of the drug modifies the initial deposition onset, probably because of the simultaneous adsorption of the drug on the electrode. However, after the first few seconds the two processes converge, eventually approaching a comparable potential response after the first minutes.

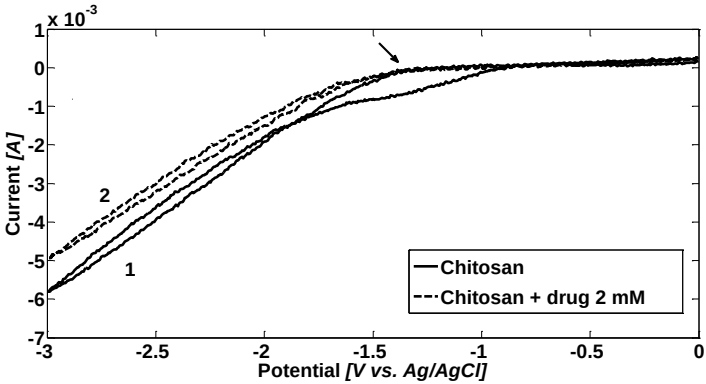

Figure 3.10. *Cyclic Voltammetry recorded for baths containing 0.5 w/v% chitosan (1) and chitosan with 2mM Brilliant Green (2). The arrow points to the average condition of deposition experienced*.

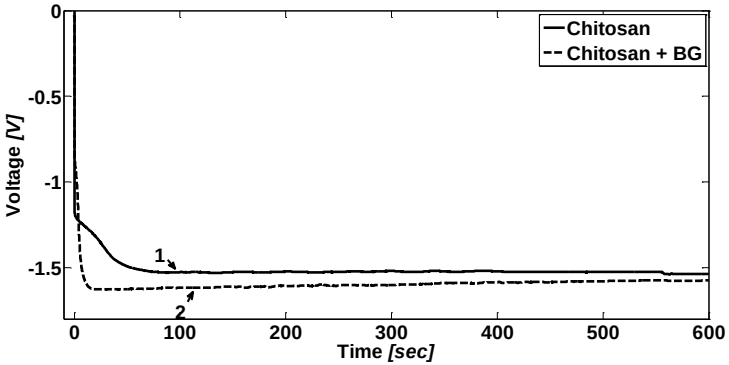

Figure 3.11. *Comparison of the evolution of the deposition of chitosan (1) and chitosan+drug (2) during 10 minutes. The two profiles, though differing at the beginning, tend towards the same stable condition.*

The amount of drug loaded during co-electrodeposition with chitosan was evaluated by immersing the matrices in an acidic environment with pH < pK_a of chitosan, thus promoting their fast dissolution. Table 3.2 reports the values detected when electrodeposition was performed from chitosan solutions containing an initial concentration of 2 mM BG. The values are normalized over the macroscopic area of the substrate (0.5 cm^2) in order to provide a scale suitable for the final application on a microrobotic platform. Taking the first condition as reference, only 30 minutes of crosslinking at pH 5 induced a significant loss of loaded material (final loading is ~46 % with respect to as-deposited samples). By reducing this treatment to 10 minutes, no significant change in the total loaded amount was recorded.

Condition	**Amount of drug loaded ($\mu g/cm^2$)**
As deposited	77.83 ± 10.21
Neutralized	72.72 ± 6.57
Crosslinked pH 5, 30 minutes	42.15 ± 9.4
Crosslinked pH 5, 10 minutes	73.33 ± 1.23
Crosslinked pH 8.5, 30 minutes	80.33 ± 6.32

Table 3.2*. Comparison between the amounts of BG loaded in the non-treated and treated electrodeposited chitosan hydrogels as measured after full release at pH 6 by spectrophotometry.*

The cumulative release profiles of the differently treated chitosan layers in physiological media at pH 7.4 are shown in Figure 3.12. As-deposited

chitosan hydrogel layers released ~ 60% of the loaded amount of drug in three weeks. This value was obtained by comparing the results presented in table 3.2 with the total amount of drug released in the investigated time. In order to confirm that the samples contained the same amount of loaded drug, the matrices used for the experiment were subsequently immersed in pH 6, and the remnant release was evaluated as a control. No discrepancy was observed. Films crosslinked at pH 8.5 or neutralized showed a significantly lower release with values respectively of 30 and 40% of the total loaded drug.

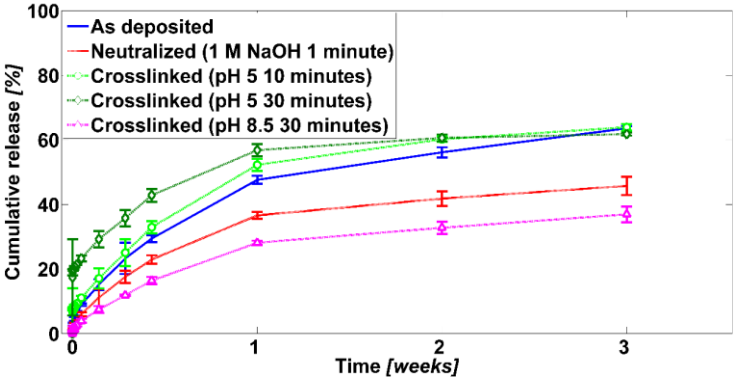

Figure 3.12*. Drug release profiles for samples immersed at pH 7.4. Curve 1 represents untreated samples. Curve 2 shows the effect of neutralization. The effect of ionic crosslinking at acidic pH is shown by curve 3 (10 minutes of treatment) and curve 4 (30 minutes of treatment). Crosslinking at basic pH (curve 5) provides the slowest release option.*

Hydrogel layers crosslinked at pH 5 for 30 minutes exhibited an initial burst release of 20% of the loaded drug occurred in the first 30 minutes followed by three days of essentially zero order release. Subsequently, a final plateau was reached corresponding to 60% of the total loaded BG. The initial

burst release amount could be controlled by changing the crosslinking time as it can be seen in figure 3.13.

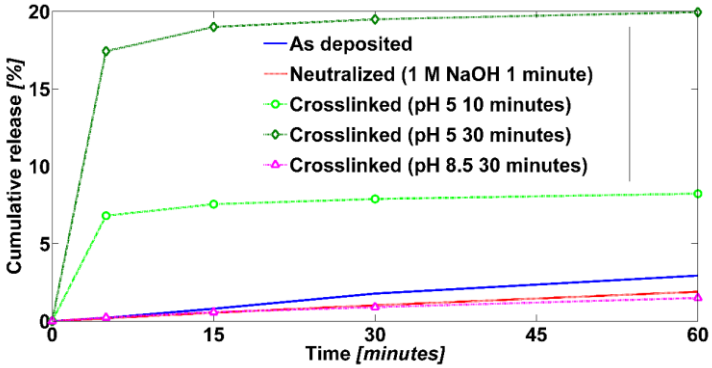

Figure 3.13. *First 60 minutes of release at pH 7.4 for untreated and treated samples. Neutralization linearizes the first release. The effect of crosslinking at acidic pH is clearly visible producing a burst release. The amount of drug released instantaneously is controllable by the time of treatment (10 minutes in light green or 30 minutes in dark green). Crosslinking at basic pH (pink) only slightly modifies the pattern of neutralized samples.*

The interpretation of the values obtained in the experiments was facilitated by fitting the data versus a series of empirical equations [51, 52] that represent the drug profiles as a function of time (Table 3.3 displays some models and a qualitative description of each one of them). These models, though not providing a complete parameterization of all the mechanisms involved in the release (including diffusion, erosion, and degradation of the film [53]), allowed us to classify the results and provide theoretical insights on the different processes.

Non-treated chitosan matrices and chitosan films treated in alkaline environment show a typical Fickian diffusion driven profile. First order kinetics, with different law constants, fits precisely the data coming from chitosan treated in acidic environments.

The same analysis can be performed for the samples releasing under different environmental conditions. As can be seen in figure 3.14, at pH 6.0, all the chitosan matrices release almost the entire loaded drugs in only 72 hours. This amount is in average five times higher than the release measured over the same period at pH 7.4. The Fickian diffusion release seen at pH 7.4 is replaced by a first order kinetics, common in this case for all the analyzed conditions, with different release parameters. Interestingly, samples treated at basic conditions exhibit a slightly higher kinetics constant than the controlas opposed to what was observed at pH 7.4. The fitting parameters and a classification of different cases for simulated physiological (pH 7.4) and pathological (pH 6.0) conditions can be found in tables 3.3 and 3.4, respectively.

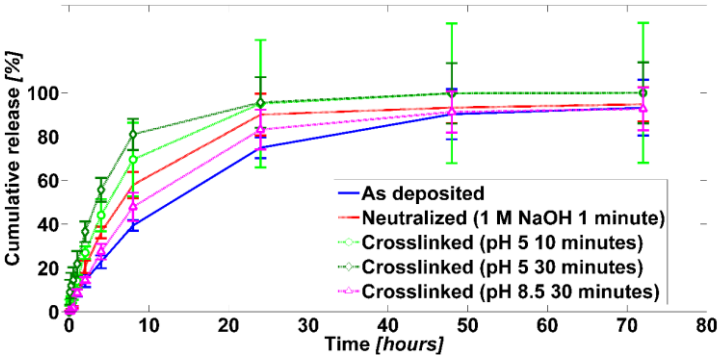

Figure 3.14. *Drug release profiles for samples immersed at pH 6 simulating a pathological environment. Release reaches the totality of the loaded drug in all cases. Electrodeposited chitosan without modifications (1) appears to be less sensitive than the neutralized (2) ones. Crosslinking at acid pH (curve 3 and 4) and at basic pH (curve 5) does not produce significant differences as at pH 7.4.*

Model	Expression	Application
Zero Order Kinetics	$\frac{Qt}{Q\infty} = Kt$	Drug dissolution is linearly dependent with time.
Higuchi Model	$\frac{Qt}{Q\infty} = Kt^{1/2}$	Diffusion process based on the Fick's law.
Korsmeyer-Peppas Model	$\frac{Qt}{Q\infty} = Kt^{n}$	Generalized expression of the above two models. Depending on the release exponent the process can be defined as diffusive or not. Only the portion of the release $\frac{Qt}{Q\infty}$ <0.6 should be used to determine the exponent.
First-Order Kinetics	$\frac{dC}{dt}$=-KC or $\text{LogC} = \text{LogCo} - \frac{Kt}{2.303}$	Typical formula for water soluble drugs in porous matrices. The rate of the release is proportional to the concentration of the drug in the matrix.

Table 3.3*.Empirical mathematical models for drug release kinetics as described in the literature [53].*

System	Kinetic constant k (h^{-n})	Mechanism	r
As deposited chitosan	0.052	Fickian diffusion, Higuchi Model	0.997
Neutralized chitosan	0.055	Fickian diffusion, Higuchi Model	0.988
Chitosan crosslinked pH 5 (10 minutes)	0.018	First Order kinetics	0.996
Chitosan crosslinked pH 5 (30 minutes)	0.025	First Order kinetics	0.992
Chitosan crosslinked pH 8.5 (30 minutes)	0.047	Fickian diffusion, Higuchi Model	0.988

Table 3.4*. Fitting of solute release data of chitosan electrodeposited matrices at pH 7.4.*

System	Kinetic constant k (h^{-n})	Mechanism	r
As deposited chitosan	0.16	First Order kinetics	0.999
Neutralized chitosan	0.20	First Order kinetics	0.981
Chitosan crosslinked pH 5 (10 minutes)	0.29	First Order kinetics	0.999
Chitosan crosslinked pH 5 (30 minutes)	0.28	First Order kinetics	0.994
Chitosan crosslinked pH 8.5 (30 minutes)	0.18	First Order kinetics	0.999

Table 3.5*. Fitting of solute release data of chitosan electrodeposited matrices at pH 6.0.*

3.6.4 Electrodeposition on microcapsules

As a proof of concept, microcapsules with dimensions similar to commercially available devices for drug delivery in eye [49] were produced

by electroforming and functionalized with electrodeposited chitosan (figure 3.15). The process, performed for approximately 70 minutes, followed the same pattern and showed the same characteristics recorded for flat gold chips. The additional challenge of a three-dimensional surface and deposition partially affected the final result and the possibility to create a loading matrix for drug delivery. Although feasible and controllable, the deposition revealed a visible higher level of inhomogeneity and voids created in the film.

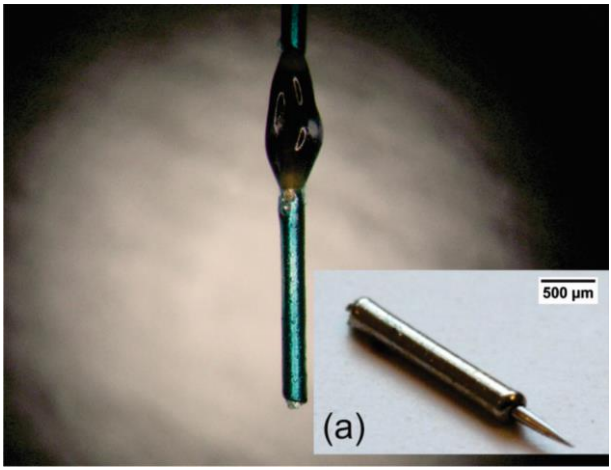

Figure 3.15. *Electroformed capsule functionalized with chitosan and BG drug. The deposition was performed selectively on the implants using the current density tested on gold chips. In the inset (a), a final implant with an additional needle*.

3.7 Discussion

The electrodeposition of chitosan represents an easy and flexible method to functionalize conductive surfaces and provide a responsive layer for smart sensing and drug delivery. Chitosan exhibits the inherent ability to change its solubility when passing through the pK_a (6.3) value of its amine groups. This allows the immobilization of films on substrates, due to the electro generation of hydroxide ions at the cathode of an electrochemical cell in aqueous chitosan solutions. At the same time it provides a pH responsive behavior in an important physiological pH range. It is well known that high proton concentrations are commonly found in inflamed tissues (down to pH 5.4) or around malignant tumors [54] due to the altered catabolism of glucose. Chitosan solubility increases dramatically when passing from a physiological environment to such pathological conditions, thus allowing a faster drug release close to a hypothetical target. Moreover, chitosan films can be easily chemically or physically modified with mild treatments, which appear to be mostly well-matched with biomedical applications [18].

Electrodeposition from chitosan acidic solutions occurs due to simultaneous formation of a locally high pH adjacent to the cathode, the neutralization of chitosan amines, and the change of conformation of the molecule in the new electrical state [30]. The process exploits the reduction of water, which happens at potentials more negative than E = – 1.0 V, and is accompanied by hydrogen evolution. Applied current density, duration of the process, and chitosan concentration are the main parameters to control for the deposition of films and the homogeneity of the layers. *In situ* visualization of the linear growth rate and profilometric analysis of the dried films helped define the optimal parameters for film thickness, homogeneity of the layer

and drug loading. Current densities higher than –15 A/m^2 (average voltage response -1.6V vs Ag/AgCl), or deposition times longer than 10 minutes, although allowing fast growth, were usually unable to create uniform layers, due to the massive inclusion of hydrogen bubbles in the films. Current densities lower than -10 A/m^2 (-1.2 V vs Ag/AgCl) and short deposition times provided relatively thin layers.

For this reason, -15 A/m^2 was defined as the reference for most of the characterization processes and 10 minutes of deposition was fixed for the experiments related to drug loading and release. Afterwards, the influence of different post deposition dip coating treatments on the electrodeposited films was characterized. Neutralization with NaOH and ionic crosslinking with TPP at pH 5 and pH 8.5 were performed and the results investigated in terms of microstructure, chemical composition, stability of the matrices, and swelling properties. Neutralization with NaOH has been often used to ensure complete conversion of the amine groups from a protonated to a deprotonated state [20]. However, multiple consequences could be observed in terms of chemical and physical behavior. Profilometric analysis and *in situ* visualization of the treated layers showed a significant increase of the dried thickness and the swelling capability (swelling almost double, when compared to as deposited layers), together with a reduction of homogeneity of the surface. The chitosan films appeared more hydrophilic, in accordance to previous reported studies [55, 56], probably due to the simultaneous appearance of alkoxide ions (from OH lateral groups reacting to form a salt) and the deacetylation process, which removed acetate ions and increased the presence of amide and amine groups.

Chemical imaging by FTIR was used to confirm our hypothesis. We observed the appearance of a strong signal at 1580-1590 cm^{-1} corresponding

to the stretching of amine groups, and another one around 1400 cm^{-1} which can be attributed to the deformation of CH_3, CH_2 groups, following the removal of neutralization of acetate ions. In this way we were able to enhance the affinity to water of the electrodeposited matrices, a property that appears to be useful for drug loading and delivery, actuation and even cell-hydrogel interactions [55].

The same tools were used to characterize the ionic crosslinking with TPP. This small molecule has been frequently used to produce polyelectrolyte complex beads in a mild and not-toxic way for drug delivery [57]. The process of crosslinking is time and pH dependent, since it involves the interaction by diffusion of counter ions, such as the phosphoric groups $P_3O_9^{3-}$ of TPP and chitosan NH_3^+. In our system, chitosan appeared as a partially neutralized matrix after electrodeposition with few cationic sites potentially still available. TPP aqueous solutions are a mixture of hydroxyl and phosphoric ions following dissociation of the molecule in water and have a pH of 8.5. In order to maximize the interaction between the mentioned ions, we adjusted the pH of TPP to 5 to eliminate the competing hydroxyl groups. The nature of crosslinking appeared strongly modified by this change.

A short neutralization process was performed for all the matrices, as it was seen to increase the effect of the crosslinking process and at the same time the adhesion of the layers to the substrates. Following that, crosslinking was performed for 30 minutes alternatively at pH 8.5 and pH 5.

Significant morphological and behavioral changes of the chitosan matrix could be introduced by the ionic crosslinking at pH 5. The layers appeared compact, with decreased swelling properties and a strongly reinforced matrix, resistant to complete dissolution in acidic environment. Cryo-SEM revealed

a thickening of the original fiber structure of the chitosan matrix with globular units appearing around the network. Matrices crosslinked at pH 8.5 appeared more similar to the neutralized matrices in the swelling, structure, and dimensional behavior, with only a higher standard deviation in the dried thickness measurements. We can assume that this general behavior is due to a less efficient crosslinking caused by the competition between OH^- groups and trypolyphosphate ions at pH 8.5, while the higher roughness of the surfaces is related to the formation of salt aggregates that affect the uniformity of the layers, as recently reported in similar systems [33]. FTIR strengthened our hypothesis by showing a strong signal of peak vibrations of phosphate groups (1200 cm^{-1}) only for samples crosslinked in acidic conditions. This enhanced mechanical strength together with the natural properties of chitosan could be useful for more complex microrobotic devices where chitosan would be functionalized with stable moieties for real time sensing or tracking [58].

The stability of chitosan film thickness in a water environment was significantly modified by the different treatments. Hydrogels immersed in basic solutions (neutralized or crosslinked) lost half (or even more) of their original thickness after the first 24 hours of experiment. More stability was recorded for samples treated at pH 5 (although high standard deviations need to be mentioned) or for untreated matrices. These data probably constitute a sum of all the effects mentioned above. Tthe low stability of the films subjected to neutralization or basic crosslink is related to the loss of salt aggregates, poorly attached chitosan molecules, a relatively higher loosening of the network. Samples crosslinked at pH 5 show a higher resistance, probably due to the more compact and reinforced matrix. However, the samples are presumably subjected to the same effect of loss of aggregates

which is responsible of the high standard deviation recorded during the measurements.

The characterization of the electrodeposited chitosan films was used to provide guidelines and details on the drug loading and release capabilities of these systems. BG was used as a model of an ionic drug due to its limited size and common use as antiseptic for eye treatments (figure 3.16) [59]. Co-electrodeposition with chitosan was found to be an efficient and non-toxic method for loading drugs.

No significant dimensional changes during deposition were observed when BG was added in the electrolyte during electrodeposition. Being a cationic molecule, its presence in the bath modifies the general characteristics of the process increasing the resistance of the solution. The difference was primarily found in the first part of the deposition process. The initial deposition onset was steeper than the one recorded for only chitosan deposition, probably due to an initial motion and deposition of the dye on the cathodic substrate, which would cause an increase in the resistance of the system. However, co-deposition asymptotically tended to the values of pure chitosan deposition.

The system was able to store 40-80 $\mu g/cm^2$ of drug depending on the applied series of treatments. This drug loading capacity could be further optimized by adjusting different variables related to the electrodeposition process. Longer process times introduce voids and imperfections and reduce the reproducibility of the process but have the potential to increase loading to hundreds of $\mu g/cm^2$. Other parameters such as the applied current density [60] and the concentration of the electrolytes in the bath considerably influence the film structure and composition.

Comparative studies of the drug loaded chitosan matrices showed the possibility of achieving different profiles and release kinetics by varying the post-treatment conditions. For all the cases, prolonged release was observed for approximately three weeks under physiological conditions involving a fraction up to ~ 60 % of the loaded drug. A typical diffusion-based process was recorded for the as-deposited samples, as well as for the samples crosslinked at pH 8.5 or those simply neutralized in NaOH. These two conditions showed a relatively more limited release (~ 40%) suggesting that a zero order profile could be achieved by tuning the time and the intensity of the treatment. Surprisingly, a burst release was attained with chitosan films crosslinked at pH 5 with an effect increasing with the time of the treatment. A plausible explanation could be found in the fabrication and processing used for the preparation of the samples. A dip coating process in acid solution, aside from providing optimal conditions for the ionic crosslinking, facilitates a partial dissolution of the chitosan film. In contrast, TPP solutions at pH 8.5, despite not being efficient for crosslinking, provide a further possibility to stabilize the film through neutralization. Moreover, while one can assume a uniform drug distribution in the deposited chitosan layers, a basic process may have redistributed the drug away from the polymer/solvent interface or induced its partial precipitation (as experimentally observed on a solution of only dye).

Dimensional factors and swelling properties also play an important role in the profile design [52, 61]. As shown before and briefly represented in figure 3.17, crosslinking at pH 5 produces a contraction of the matrix with a relative reduction of the distance that the solvent has to penetrate. Assuming no change in the layers porosity during crosslinking, this contraction has been shown to provide dramatic consequences on the fractional drug release [62].

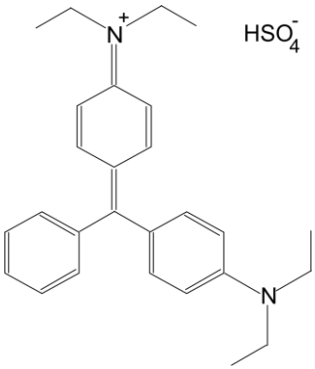

Figure 3.16. *Chemical structure of brilliant green, used as model for an ionic drug.*

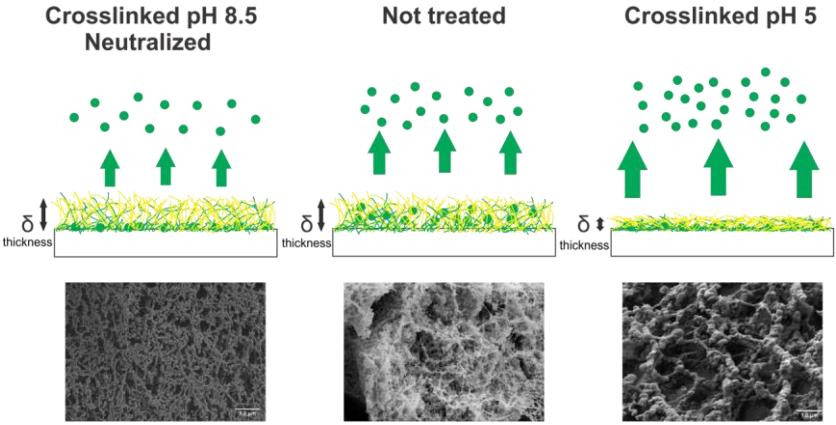

Figure 3.17*. Possible mechanisms of drug release from crosslinked and non crosslinked films. Dimensional modification that occurs during the process may induce the significant differences recorded during the experiments. Another possible reason could be the distribution of the drug inside the matrices with BG tending to accumulate at the bottom of chitosan films treated in alkaline solutions.*

All the layers exhibited strong pH responsive behavior when immersed at pH 6. This was manifested by the increased drug release (almost 100% of the loaded amount), reduced time of action, change of release kinetics and complete dissolution of the matrix after three days for almost all cases. Only TPP/chitosan films crosslinked at pH 5 retained their integrity, suggesting a greater number of stable links. However, their sensitivity to the change in the environmental conditions in terms of release could indicate an incomplete crosslinking process, which would otherwise hinder this behavior [63]. In all cases a strong swelling caused by electrostatic repulsion among the protonated amine groups of the polymer network are responsible for the increased diffusion and drug delivery [64]. Interestingly, in acid conditions, layers neutralized with NaOH or crosslinked in basic solutions showed faster release than the control suggesting a looser and weaker network.

In order to provide a proof for future work and investigations, tests of co-deposition of the studied matrices and BG dye were performed on self-made magnetic microneedles produced by electroforming. The parameters tested on flat gold chips appeared to provide a successful coating over the entire surface of the capsules. The relatively long time needed for the process, however, was found to be a potential source of inhomogeneity. As previously stated, hydrogen evolution effects become more evident with increasing deposition time. Further studies, focused in the incorporation of more relevant drugs, are still needed to define the full capabilities of the investigated system.

3.8 Conclusions and outlook

The study proposed here represents a first step for the creation of complex microdevices able to sense, act and react to complex environments such as the human body. These features can be implemented in magnetic microdevices by electrodeposition of a smart material in a controlled fashion. The microdevices consist of a magnetic cobalt-nickel cylinder which provides the locomotion, coated by a chitosan film, which is the pH-sensitive drug delivery component. Due to their intrinsic properties, these chitosan films exhibit a sustained release (approximately 1 month) in simulated physiological conditions and an accelerated kinetics when the pH approaches values similar to ones in inflamed tissues. Moreover, mild and non-toxic treatments allow physicochemical modification of the chitosan matrices that allow adjustments in the release profiles as a function of the targeted area and therapy.

The platform possesses the following qualities that are beneficial for a microrobotic platform for targeted drug delivery:

- it exploits a flexible and versatile fabrication technique for coatings of magnetic microdevices, such as electrodeposition.

- It contains a responsive polymer, chitosan, whose properties are naturally tuned for drug delivery in the human body.

- It takes advantage of a biocompatible and externally controllable method (the pH of the environment) for loading a drug, tuning the chemical properties of the films, and controlling the release kinetics.

Nevertheless, the path towards final commercial devices for targeted therapies requires additional steps.

Drug release studies on final devices, such as magnetic microrobots, must be carried out to understand the similarities and the differences to the model study. We demonstrated the feasibility of the technique by electrodepositing the drug loaded chitosan on electroformed Co-Ni cylinders. We noticed that the shape of the substrate influenced the deposit thickness and consistency. Additional studies should include an optimization of the electrode for electrodeposition on cylindrical microdevices and an in-depth analysis on the biocompatibility of the used materials and methods.

Chitosan hydrogels are widely recognized to be biocompatible and biodegradable in all its forms (nanoparticles, films, scaffolds) and in most combinations with other natural materials (collagen, alginate, silk) [13, 17, 65]. Moreover, depending on the hydrophilic properties of the layers, cells could be stimulated to attach or to detach from the matrices. CoNi substrates are currently being investigated and treated to maximize their biocompatibility. From this perspective, a gold coating covering the magnetic material could limit the problem and be beneficial for the goal.

An *in vivo* investigation of the potential of the platform, originally designed for the treatment of posterior eye diseases, would need to include a specific drug and not a model as BG. Additional studies on the compatibility of this drug with the method would need to be conducted. An ionic drug would most probably participate to the electrophoretic phenomena happening during electrodeposition, while a non-ionic molecule would need a certain interaction with the depositing chitosan films to be loaded into the device. *In vivo* studies would also give insight into the enzymatic degradation kinetics

of the different chitosan films, which would definitely influence the profile and duration of the drug release.

These challenges and future experiments show the complexity of the full problem and at the same time the potential of the presented work. Moreover, only a few of the many options for chemical and physical modification of chitosan films have been taken into consideration. For example, additional features would be possible if chitosan were able to crosslink to specific synthetic polymers, allowing their electrodeposition and the inclusion of their properties on microrobots made of hard materials.

3.9 Bibliography

[1] H. C. Hamaker, E. J. W. Verwey, *Transactions of the Faraday Society* **1940**, 35, 180.

[2] F. Grillon, D. Fayeulle, M. Jeandin, *J Mater Sci Lett* **1992**, 11, 272.

[3] P. Sarkar, P. S. Nicholson, *J Am Ceram Soc* **1996**, 79, 1987.

[4] O. Van der Biest, L. Vandeperre, S. Put, G. Anne, J. Vleugels, Layered, *Functional Gradient Ceramics, and Thermal Barrier Coatings: Design, Fabrication and Applications* **2007**, 333, 49.

[5] I. Corni, M. P. Ryan, A. R. Boccaccini, *J Eur Ceram Soc* **2008**, 28, 1353.

[6] M. P. M.Schlesinger, *Modern Electroplating*, Wiley, **2010.**

[7] S. Seuss, A. R. Boccaccini, *Biomacromolecules* **2013**, 14, 3355; A. T. Poortinga, R. Bos, H. J. Busscher, *Biotechnol Bioeng* **2000**, 67, 117.

[8] J. Redepenning, G. Venkataraman, J. Chen, N. Stafford, *J Biomed Mater Res A* **2003**, 66A, 411.

[9] M. Cheong, I. Zhitomirsky, *Colloid Surface A* **2008**, 328, 73.

[10] F. Sun, I. Zhitomirsky, *Surface Engineering* **2009**, 25, 621.

[11] M. N. V. Ravi Kumar, *Reactive and Functional Polymers* **2000**, 46, 1.

[12] D. Kafetzopoulos, A. Martinou, V. Bouriotis, *P Natl Acad Sci USA* **1993**, 90, 2564.

[13] R. A. A. Muzzarelli, *Cell Mol Life Sci* **1997**, 53, 131.

[14] A. A. Elzatahry, M. S. M. Eldin, E. A. Soliman, E. A. Hassan, *J Appl Polym Sci* **2009**, 111, 2452.

[15] M. Thanou, J. C. Verhoef, H. E. Junginger, *Adv Drug Deliver Rev* **2001**, 52, 117.

[16] J. Berger, M. Reist, J. M. Mayer, O. Felt, N. A. Peppas, R. Gurny, *Eur J Pharm Biopharm* **2004**, 57, 19.

[17] J. Berger, M. Reist, J. M. Mayer, O. Felt, R. Gurny, *Eur J Pharm Biopharm* **2004**, 57, 35.

[18] M. N. V. R. Kumar, R. A. A. Muzzarelli, C. Muzzarelli, H. Sashiwa, A. J. Domb, *Chem Rev* **2004**, 104, 6017.

[19] S. T. Koev, P. H. Dykstra, X. Luo, G. W. Rubloff, W. E. Bentley, G. F. Payne, R. Ghodssi, *Lab Chip* **2010**, 10, 3026.

[20] L. Q. Wu, A. P. Gadre, H. M. Yi, M. J. Kastantin, G. W. Rubloff, W. E. Bentley, G. F. Payne, R. Ghodssi, *Langmuir* **2002**, 18, 8620.

[21] R. Fernandes, L. Q. Wu, T. H. Chen, H. M. Yi, G. W. Rubloff, R. Ghodssi, W. E. Bentley, G. F. Payne, *Langmuir* **2003**, 19, 4058.

[22] J. J. Park, X. L. Luo, H. M. Yi, T. M. Valentine, G. F. Payne, W. E. Bentley, R. Ghodssi, G. W. Rubloff, *Lab Chip* **2006**, 6, 1315.

[23] H. M. Yi, L. Q. Wu, W. E. Bentley, R. Ghodssi, G. W. Rubloff, J. N. Culver, G. F. Payne, *Biomacromolecules* **2005**, 6, 2881; H. M. Yi, L. Q. Wu, R. Ghodssi, G. W. Rubloff, G. F. Payne, W. E. Bentley, *Langmuir* **2005**, 21, 2104.

[24] A. T. Lewandowski, H. M. Yi, X. L. Luo, G. F. Payne, R. Ghodssi, G. W. Rubloff, W. E. Bentley, *Biotechnol Bioeng* **200**8, 99, 499.

[25] X. L. Luo, A. T. Lewandowski, H. M. Yi, G. F. Payne, R. Ghodssi, W. E. Bentley, G. W. Rubloff, *Lab Chip* **2008**, 8, 420.

[26] X. W. Shi, Y. Liu, A. T. Lewandowski, L. Q. Wu, H. C. Wu, R. Ghodssi, G. W. Rubloff, W. E. Bentley, G. F. Payne, *Macromol Biosci* **2008**, 8, 451.

[27] S. L. Buckhout-White, G. W. Rubloff, *Soft Matter* **2009**, 5, 3677.

[28] Y. Li, X. Pang, R. F. Epand, I. Zhitomirsky, *Mater Lett* **2011**, 65, 1463.

[29] X. L. Luo, J. J. Xu, Y. Du, H. Y. Chen, *Anal Biochem* **2004**, 334, 284; M. H. Xue, Q. Xu, M. Zhou, J. J. Zhu, *Electrochem Commun* **2006**, 8, 1468; Q. L. Sheng, K. Luo, L. Li, J. B. Zheng, *Bioelectrochemistry* **2009**, 74, 246.

[30] A. Simchi, F. Pishbin, A. R. Boccaccini, *Mater Lett* **2009**, 63, 2253.

[31] Y. Cheng, X. L. Luo, J. Betz, S. Buckhout-White, O. Bekdash, G. F. Payne, W. E. Bentley, G. W. Rubloff, *Soft Matter* **2010**, 6, 3177.

[32] R. A. Zangmeister, J. J. Park, G. W. Rubloff, M. J. Tarlov, *Electrochim Acta* **2006**, 51, 5324.

[33] Y. Liu, B. Zhang, K. M. Gray, Y. Cheng, E. Kim, G. W. Rubloff, W. E. Bentley, Q. Wang, G. F. Payne, *Soft Matter* **2013**, 9, 2703.

[34] X. Pang, I. Zhitomirsky, *Surf Coat Tech* **2008**, 202, 3815.

[35] Z. Wang, X. Zhang, J. Gu, H. Yang, J. Nie, G. Ma, *Carbohyd Polym* **2014**, 103, 38.

[36] S. N. Alhosseini, F. Moztarzadeh, M. Mozafari, S. Asgari, M. Dodel, A. Samadikuchaksaraei, S. Kargozar, N. Jalali, *Int J Nanomed* **2012**, 7, 25.

[37] F. L. Jia, J. M. Gong, K. W. Wong, R. X. Du, *Nanotechnology* **2009**, 20.

[38] L. H. Lu, W. Chen, *Nanoscale* **2011**, 3, 2412.

[39] S. L. Yang, Z. Z. Lu, S. L. Luo, C. B. Liu, Y. H. Tang, *Microchim Acta* **2013**, 180, 127.

[40] K. Järvinen, T. Järvinen, A. Urtti, *Adv Drug Deliver Rev* **1995**, 16, 3.

[41] Y. Shirasaki, *J Pharm Sci-Us* **2008**, 97, 2462.

[42] P. M. Hughes, O. Olejnik, J.-E. Chang-Lin, C. G. Wilson, *Adv Drug Deliver Rev* **2005**, 57, 2010.

[43] A. K. Mitra, B. S. Anand, S. Duvvuri, in Ad*vances in Organ Biology*, Vol. Volume 10 (Ed: J. Fischbarg), Elsevier, **2005**, 307.

[44] D. A. LaVan, T. McGuire, R. Langer, *Nat Biotechnol* **2003**, 21, 1184.

[45] D. Zhu, X. Xu, Z. Zheng, Q. Gu, *Eye* **2009**, 23, 2105.

[46] O. Ergeneman, G. Chatzipirpiridis, J. Pokki, M. Marin-Suarez, G. A. Sotiriou, S. Medina-Rodriguez, J. F. F. Sanchez, A. Fernandez-Gutierrez, S. Pane, B. J. Nelson, Ieee *T Bio-Med Eng* **2012**, 59, 3104.

[47] F. Ullrich, C. Bergeles, J. Pokki, O. Ergeneman, S. Erni, G. Chatzipirpiridis, S. Pane, C. Framme, B. J. Nelson, *Invest Ophth Vis Sci* **2013**, 54, 2853.

[48] M. P. Kummer, J. J. Abbott, B. E. Kratochvil, R. Borer, A. Sengul, B. J. Nelson, *Ieee T Robot* **2010**, 26, 1006.

[49] D. C. Musch, D. F. Martin, J. F. Gordon, M. D. Davis, B. D. Kuppermann, *New Engl J Med* **1997**, 337, 83.

[50] B. D. Kuppermann, *Retina-J Ret Vit Dis* **2009**, 29, S24.

[51] P. L. Ritger, N. A. Peppas, *J Control Release* **1987**, 5, 23; R. W. Korsmeyer, R. Gurny, E. Doelker, P. Buri, N. A. Peppas, *Int J Pharm* **1983**, 15, 25; P. Costa, J. Manuel, S. Lobo, *Eur J Pharm Sci* **2001**, 13, 123.

[52] P. L. Ritger, N. A. Peppas, *J Control Release* **1987**, 5, 37.

[53] Y. Fu, W. J. Kao, *Expert Opin Drug Del* **2010**, 7, 429.

[54] K. H. Steen, A. E. Steen, P. W. Reeh, *J Neurosci* **1995**, 15, 3982; X. M. Zhang, Y. X. Lin, R. J. Gillies, *J Nucl Med* **2010**, 51, 1167.

[55] S. Noriega, *International Journal of Carbohydrate Chemistry* **2011**, 2011.

[56] G. R. Mahdavinia, M. J. Zohuriaan-Mehr, A. Pourjavadi, *Polym Advan Technol* **2004**, 15, 173.

[57] F. L. Mi, S. S. Shyu, C. Y. Kuan, S. T. Lee, K. T. Lu, S. F. Jang, *J Appl Polym Sci* **1999**, 74, 1868; F. L. Mi, S. S. Shyu, T. B. Wong, S. F. Jang, S. T. Lee, K. T. Lu, *J Appl Polym Sci* **1999**, 74, 1093; A. Hasanovic, M. Zehl, G. Reznicek, C. Valenta, *J Pharm Pharmacol* **2009**, 61, 1609; H. Jonassen, A. L. Kjoniksen, M. Hiorth, *Biomacromolecules* **2012**, 13, 3747.

[58] A. Kaushik, P. R. Solanki, A. A. Ansari, G. Sumana, S. Ahmad, B. D. Malhotra, Sensors and *Actuators B: Chemical* **2009**, 138, 572; M. Xie, H.-H. Liu, P. Chen, Z.-L. Zhang, X.-H. Wang, Z.-X. Xie, Y.-M. Du, B.-Q. Pan, D.-W. Pang, *Chem Commun* **2005**, 5518.

[59] J. K. Narat, *Ann Surg* **1931**, 94, 1007.

[60] A. Khangtragool, S. Ausayakhun, P. Leesawat, C. Laokul, R. Molloy, *J Appl Polym Sci* **2011**, 122, 3160.

[61] X. Huang, C. S. Brazel, *J Control Release* **2001**, 73, 121.

[62] C. S. Brazel, N. A. Peppas, *Eur J Pharm Biopharm* **2000**, 49, 47.

[63] X. Z. Shu, K. J. Zhu, *Int J Pharm* **2002**, 233, 217; X. Z. Shu, K. J. Zhu, *Eur J Pharm Biopharm* **2002**, 54, 235.

[64] X. Z. Shu, K. J. Zhu, *Int J Pharm* **2002**, 233, 217; H. Zhang, S. Mardyani, W. C. W. Chan, E. Kumacheva, *Biomacromolecules* **2006**, 7, 1568.

[65] A. K. Azab, V. Doviner, B. Orkin, J. Kleinstem, M. Srebnik, A. Nissan, A. Rubinstein, J *Biomed Mater Res A* **200**7, 83A, 414; J. D. Chen, K. H. Nan, S. H. Yin, Y. J. Wang, T. Wu, Q. Q. Zhang, *Colloid Surface B* **2010**, 81, 640.

CHAPTER 4

And if you feel that you can't go on. And your will's sinkin' low

Just believe and you can't go wrong.

In the light you will find the road. You will find the road

In the light-Led Zeppelin (1975)

An integrated microrobotic platform for on-demand, targeted therapeutic interventions

Work partially published in:

Advanced Materials (2014), 26: 952-957

S.Fusco, M.S.Sakar, S.Kennedy, C. Peters, R.Bottani, F.Starsich, A.Q.Mao, G.A. Sotiriou, S. Pané, S. Pratsinis, D.Mooney, B.J. Nelson.

4.1 Chapter overview

This work describes the design and development of a prototype of a soft, hydrogel-based microrobot, intended to move through the body lumina, carry cells or drugs, and deliver them by external actuation using near infrared light (NIR) in a targeted area. The prototype consists of two parts:

- a hydrogel bilayer film designed to carry drugs and create a protected internal environment.

- A series of magnetic alginate microbeads proposed as cell carriers and at the same time locomotion systems for untethered magnetic manipulation of the full platform.

Self-folding of bilayer films constitutes a flexible, scalable and highly reproducible strategy to fabricate hydrogel microcarriers with size and shape adapted to the final task. For this reason, it is here proposed and integrated into a microrobotic platform for automated manipulation and actuation. The chapter starts with the state of the art in the field of self-folding polymer bilayers. This is intended to give the reader information to understand the background and the relevance of the work presented here.

Following that, the main requirements that microrobots must fulfill to become vectors for minimally invasive therapies are identified. The use of soft, smart hydrogels assembled in self-folding configurations is therefore suggested to approach these challenges. The materials and methods section covers the photolithographic-based method used to fabricate differently shaped microdevices. The hydrogel synthesis process is briefly reported together with the synthesis of graphene oxide, the nano-material used to

produce near infrared light nanocomposites. Alginate magnetic microbeads are then proposed as material for the dual task of untethered magnetic manipulation of the full platform and cell transport.

Characterization of the hydrogel nanocomposites is realized in terms of morphology (Cryo-SEM), swelling properties, cell interaction, and near-infrared light actuation. Manipulation of the single alginate beads and of the full platform provides the final proof-of-concept for the work.

A conclusion paragraph reports the observed challenges and the possible additional features that could be implemented in the same platform.

4.2. Self-folding: from nature to biomedical applications

4.2.1 Self-folding in nature: a peculiar case of self-assembly

Self-assembly is the autonomous organization of small components into patterns or larger structures without the use of any external intervention. The concept is visible in nature at all scales, from the molecular nanocrystals or DNA ribbons to the cosmic dimensions of planet systems [1]. It is mainly driven by complex interactions between different forces, which are difficult to control at the micro- and mesoscale [2]. Because of this, self-assembly has rarely been used for the production of micro devices or microstructures [3] despite being ideal for microfabrication (there is no need for long experimental steps and the smart exploitation of natural forces can achieve 3D shapes from 2D patterns). Similarly present in nature, self-folding refers to the reorganization and re-orientation of different connected planar units in three-dimensional structures upon change of physical conditions. The concept is highly exploited in plants, to achieve active motion upon inhomogeneous changes in hydration states.

An example is the appearance of wrinkles on fruits left drying (figure 4.1a). Leaves, in the same way, start to curl up before falling from trees. The pine cones of the Aizoaceae use anisotropic contraction, related to a change of humidity, to protect their seeds or release them when the right environmental conditions are reached (figure 4.1b) [4]. Even more interesting examples are related to rapid and reversible movements of some plant systems. The leaf folding of mimosa pudica (figure 4.1c) is an adaptive movement in response to mechanical disturbances (such as contact), which occurs in just a few

seconds. The phenomenon involves the appearance of quick electric signals and the change of turgor pressure through different vacuolar systems, which causes an inhomogeneous bending of the natural "joints". A few minutes later the leaves reopen [5].

The same mechanism, a fast change of turgor pressure in some parts of the plant, is responsible for the rapid closure of the Venus flytrap leaf, which happens in approximately 100 ms (figure 4.1d). The trap consists of different leaves, each one divided into two parts. The upper leaf has sensitive trigger hairs positioned together with a pigment that attracts insects. The lower leaf has a typical leaf-like structure. The closing process essentially involves a change of the leaf's curvature driven by an elastic energy release. The closure is initiated by the mechanical stimulation of trigger hairs by insects attracted by the pigment of the plant. The trigger opens water pores connecting the upper and the lower layer of each leaf and fluid travels from one to the other layer. This causes a fast relative volume change between the two hydraulic layers and the closure to an energetically relaxed state of the plant. This state is maintained for 5-7 days, allowing for complete digestion of the entrapped prey to occur [6]. This rapid exchange in the amount of water in connected plant tissues can result in various shape changes. Apart from the already mentioned wrinkling and folding, twisting and bending are also observed due to programmed orientation of the fibers of the plants.

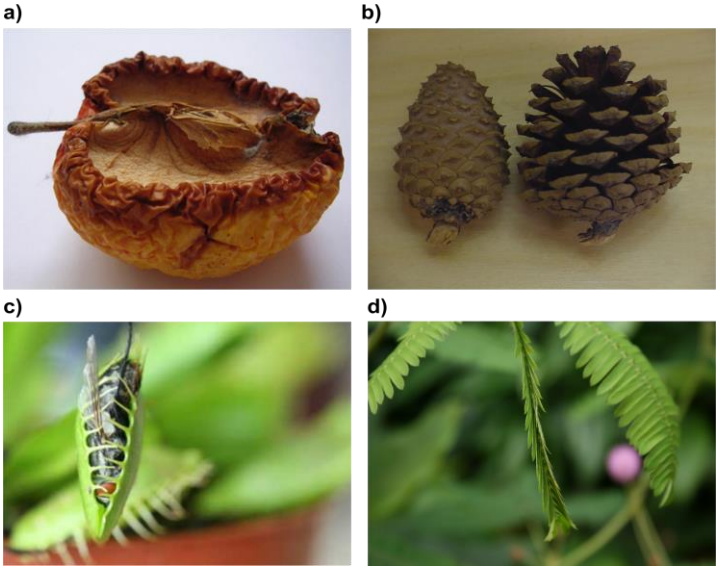

Figure 4.1. *Different examples of self-folding mechanisms in nature. a) Wrinkles are a common phenomenon involving the loss of liquids from fruits. b) The pine cone releases its seeds by changing the state of hydration of the scales, normally after the dry season, c) The Venus flytrap uses its active snapping mechanism of the leaves to capture its preys. The speed of the closure is in the order of 100 ms. d) The mimosa pudica uses a change in the turgor state of its two layers to close the leaves in a protected conformation.*

4.2.2 Self-folding in micro fabrication of biomedical devices

One of the challenges in manufacturing miniaturized biomedical devices is to achieve a predefined 3D shape without complicated fabrication paths. Self-folding represents an appealing strategy for fabrication at the small scale. It allows the use of conventional microfabrication methods, such as photolithography, molding, inkjet printing and electrodeposition, which are

inherently 2D, to define templates that would spontaneously convert into 3D structures, thus simplifying the task and reducing the complexity of the process.

As previously mentioned, self-folding is the result of material heterogeneities that are either stimulated (in nature) or can be engineered by fabrication to appear at defined situations. Alternatively it can appear in the presence of a heterogeneous field (such as a temperature gradient) that is applied to homogeneous materials.

A number of different mechanisms can be used to force self-folding effects, including pneumatic forces, surface forces, gradients of stress upon inhomogeneous thin films, thermal or shape memory alloy actuation, muscular actuation, and swelling [7].

Whitesides et al. developed a new class of robots by soft lithography, called Pneunets, based on PDMS and Ecoflex, a soft elastomeric material, which can be inflated causing curling of the final structures. The robots can be actuated in different directions and different final shapes due to the inclusion of fibers in programmed locations [8]. However, as one can imagine, these devices must be tethered to allow air to actuate them.

Surface forces actuated systems are based on the minimization of interfacial free energy between a material and a liquid drop by minimization of the surface area. The concept has been demonstrated by Py et al. [9] on small PDMS sheets in contact with water and expanded by Gracias et al., to produce metal or polymeric based polyhedral structures, ranging from millimeters to hundreds of nanometers, used as carriers or sensors [10]. However, a relatively high temperature is required during fabrication, thus

limiting the use in a biological environment. Moreover, the folding is not reversible.

The same group also proposed a series of containers formed by differentially stressed bilayers, which fold automatically upon release from a substrate. The inclusion of magnetic materials and thermally responsive polymeric parts allowed magnetically driven transport to a desired location, loading of cells, and removal of material [11-14]. Again, irreversible folding constitutes the main limitation of the systems.

A new idea of self-folding that can overcome this problem is based on the inclusion of muscle cells into artificial devices. The cells, grown on metallic or polymer thin films, induce bending upon contraction triggered by electrochemical signals. The technique, although providing repeatability and reversibility, is still not robust enough, and encounters problems of biocompatibility for theoretical *in vivo* applications [15].

The swelling of polymers has been used to produce hybrid soft-hard structures, which could fold upon change of hydration. Smela et al. [16] used electrochemically sensitive polypyrrole to drive the folding of gold based devices. The exchange of ions caused by the application of a potential changed the state of oxidation of the layer and created the strain responsible for the folding. The process was miniaturized and operated in dry environments [17].

Considering all the requirements needed for applications in biological environments, swelling of hydrogel-based films appears to be an even more attractive strategy due to a series of important features:

- There is a variety of hydrogels that are sensitive to different stimuli, such as pH or temperature, and can be tuned to provide a remotely actuated mechanism [18] [19].
- Hydrogels are typically biocompatible and can be made to be biodegradable [20], thus avoiding complications for *in vivo* applications.
- Reversible swelling is a common feature, which allows the theoretically infinite re-use of the fabricated devices.
- Hydrogels are widely used and studied for areas of applications that are appealing for medical microrobotics (drug delivery, scaffolding, etc…).

4.2.3 Self-folding hydrogel films: state of the art

Self-folding hydrogel-based films were first proposed in 1992 by Osada and coworkers [21] as a biomimetic system converting chemical energy to mechanical motion. The "muscle" was based on a millimetric strip of a gel, which underwent reversible shrinking and swelling in an electric field due to complexation with surfactant molecules, which were added in the experimental setup. Three years later Hu et al. [22] proposed the concept of exploiting differential swelling of a hydrogel double strip to achieve the same bending effect. This work proposed the use of environmentally sensitive hydrogels, such as polyacrylamide (PAAM) or N-isopropylacrylamide (NIPAAM) to externally modulate the effect, thus opening a new path to the use of hydrogels for complex active systems.

The idea was soon used for drug delivery systems. He et al. studied the influence of pH sensitive bilayer strips on release kinetics of small drugs,

either by using them as an external barrier enclosing a drug reservoir [23], or by exploiting their bending to provide enhanced mucoadhesion and minimizing the leakage of drug in porcine intestines [24]. Both efforts employed soft lithography techniques to produce micro- and millimeter-sized objects in PDMS molds.

The same fabrication technique based on microtransfer molding was used with chitosan/poly (ethyleneglycol) diacrylate bilayers with the first one being a passive non-swelling layer. Guan et al. [25] demonstrated a control on the folding degree based on the modulation of the swelling properties of the two layers and good agreement between the experimental curvature and an analytical model of bending of elastic bilayers.

Luchnikov et al. [26] were the first to explore the self-folding technique for the fabrication of microtubes. Microcontact printing was used to obtain complex inner geometries, such as helices, or lamellae.

Standard photolithography was employed to produce pH-responsive valves similar to the biological ones that can be found in veins [27]. Beebe and coworkers studied the regulation of flows in a microfluidic system, theorizing their use in more complicated chemical sensors.

Based on these preliminary studies, experimental work on hydrogel bilayers followed different directions (figure 4.2). The main contributions in the field are currently based on the work of Ionov and coworkers [28, 29]. The Leibniz group exploited the use of the temperature-responsive hydrogel NIPAAM to achieve control on the folding/unfolding of differently shaped structures. Photolithographic methods applied on different 2D shapes have provided examples of microdevices for the controlled encapsulation and

release of cells, drugs and microbeads. Additionally, biodegradable moieties or magnetic nanocomposites have been introduced to address the challenges of *in vivo* use [30, 31]. The same group also proposed empirical laws connecting the initial 2D shape to the final folded structure. For instance, Stoychev et al. reported different scenarios for the final rolling of rectangular bilayers. Following similar theories on inorganic systems [32], they experimentally showed that diffusion-driven detachment of films from a substrate could lead to the following:

- Long side rolling if the length of the rectangles is considerably larger than the width and the deformed circumference, with these two comparable between them.
- Diagonal rolling if the length and the width are comparable and the deformed circumference comparable to the size of the bilayer.
- All side rolling when the width and the length are comparable and much bigger than the deformed circumference.

Energetic considerations were taken into account in a finite element method based (FEM) model, where the slow lateral diffusion and the adhesion forces to the substrate were used as driving force and constraints for the deformation.

Later, the same group of researchers showed that isotropic polymer bilayers could achieve more sophisticated 3D shapes by exploiting the effect of the swelling path and the use of shapes with convex or concave angles. Four empirical rules were defined by the experimental results involving the direction of swelling (from the periphery to the inner part of the geometries) and the effect of the hindrance of already folded parts on neighboring features.

The final fabricated features were similar to the ones that could be obtained by having patterned hinges on homogeneous metal films [11, 12].

Final shapes resembling spheres or tubes have also been proposed with materials that were responsive to pH [33]. A series of efforts have exploited similar mechanisms of folding for anisotropically patterned films to obtain complex shapes like cubes [34], saddles [35] or helices [36].

However, only a few examples have addressed the challenges involved in a final biomedical application. Pedron et al. proposed thermoresponsive tubes [37] that could act as protected scaffold for cardiomyocites *in vitro* culture. The tubes were intended to be delivered to a targeted area and later degrade and unfold upon thermal or biological stimulation. The work considered the biological implications related to shape and the choice of materials, focusing on cell culture and growth, but did not cover any aspects about the delivery of the device at the final target.

Co-workers from the group of Gracias used polymer bio-origami as scaffolds for long-term cell culture, theoretically simplifying the passage from in vitro culture to the formation of final tissues [38]. Achieving 3D configuration for cell cultures is challenging, and the procedure could help both *in vivo* work (for instance the mimicry of vascular tissues) and research to understand cell behavior in complex environments.

Finally, Baek et al. [39] provided a simple example to demonstrate that self-folded tubes would be able to prolong the time of delivery of drugs, due to the limited diffusion. This work envisions an additional property of hydrogel bilayers for biomedical applications, which is the possibility to have shape-related behaviors and to control them.

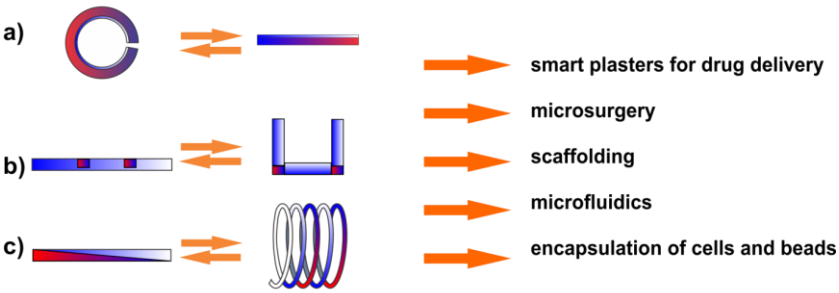

Figure 4.2 *Different shapes of self-folding are producing by organizing the bilayers in geometrically different ways. a) Homogeneous layers produce symmetric structures, while hinges(b) allow the formation of sharp edges. c) Helices can be formed by triangular layers. Different applications have been investigated in the past in the field of biomedical engineering. However, no multifunctional design has been presented till now.*

4.3 Motivation: a soft, smart microrobotic platform for cell and drug delivery

One of the core problems in the development of mobile untethered microrobots for medical applications is the integration of mechanisms for actuation and propulsion. Currently, the most popular approaches for propulsion of microdevices rely on their wireless manipulation by magnetic fields [40, 41]. The main reason for this is related to the relative "biocompatibility" of magnetic fields, even at relatively high strengths [42], and to the fact that they do not require any special environmental properties such as conductivity and transparency. This approach allows for the precise manipulation of magnetic objects toward specific locations in a 3D environment by means of different setups. These setups include moving permanent magnets [43], Helmholtz or Maxwell coils [44], and more sophisticated systems [45, 46] including real-time tracking and automated navigation. Many magnetically actuated microrobots have been recently developed including helical swimmers [47], microgrippers [11, 48, 49], magnetotactic bacteria based platforms [50], and soft microparticles [51]. Some of these microdevices have already been tested for *in vivo* or *ex vivo* applications, showing the advantages of their use in remote and delicate areas of the body, such as the eye, the large vessels in the circulatory systems, the ventricles of the central nervous system, and the urinary track.

Among the many features of interest for intelligent micro robotic agents, the ability to interact with the environment represents a desirable quality. A possible way to approach the challenge is to include materials and methods that naturally provide this ability in the fabrication process.

A simple method to fabricate smart microrobots for biomedical applications relies on the use of smart hydrogels [52] self-organized in three-dimensional structures by self-folding [14, 16, 29]. Folding appears when two coupled layers swell or contract differently in response to a specific chemical or physical change, or to remote actuation. Conventional 2D photolithography, compatible with a large variety of hydrogel monomers and with the inclusion of biological entities, has been used in this field to create different structures ranging from simple tubes to more complicated star-like or sphere-like capsules.

We investigated the possibility to integrate near infrared (NIR) light responsive hydrogel bilayers into a magnetic platform to demonstrate wirelessly controllable micro agents for cell and drug delivery. The microrobot exploits the concept of compartmentalization [53] and consists of a group of magnetic alginate microbeads encapsulated by a hydrogel bilayer structure (figure 4.3). The smart microstructures, resembling the shape of biological entities such as jellyfishes or the Venus flytrap, were fabricated by conventional 2D photolithography. A two-step process was used to couple a graphene oxide (GO) composite of a highly swelling thermoresponsive hydrogel layer made of NIPAAM with a layer of poly(ethyleneglycol) diacrylate (PEGDA). The first layer was specifically designed to collapse at temperatures higher than 40°C or by short exposure to a NIR laser source. This source of actuation was chosen as a controllable trigger mechanism, because it can penetrate body tissues without causing damage even at repeated doses [54]. NIR light-sensitive materials were recently presented in the form of gold or graphene nanocomposites for selective cell detection and destruction [55] [56] and drug delivery [57]. The second and passive layer

was designed to achieve complete folding of the final structures upon immersion into water.

The fabricated bilayers were used for two purposes: the first was to embed in their networks a model drug for targeted delivery, and the second was encapsulation of cell laden magnetic alginate microbeads. In this way, the microbeads were protected by external foreign body reactions (for example, by immune systems cells), and at the same time concentrated to provide higher magnetization to the device and enough signal for tracking. These complex structures could to be steered in 3D by means of a 5 degrees of freedom (DOF) electromagnetic manipulation system and actuated on demand. NIR remote control allowed the release of the material enclosed in the internal compartment and the modification of the diffusion driven drug release process (see chapter 6).

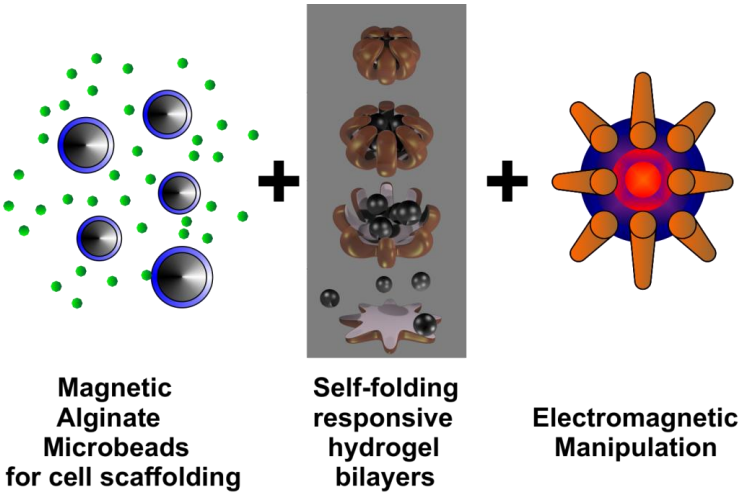

Figure 4.3. *The microrobotic platform is the result of a combination of three parts; magnetic alginate microbeads are used for cell scaffolding and magnetic manipulation. Self-folding hydrogel bilayers are used for NIR actuation and load protection. Electromagnetic manipulation systems are used for untethered steering in 3D.*

4.4 Materials and Methods

4.4.1 Materials

N-Isopropylacrylamide monomer (NIPAAM), Acrylamide (AAM), Poly(ethyleneglycol) diacrylate (average MW 575, PEGDA), 2,2-dimethoxy-2 phenylacetophenone (99%, DMPA), Ethyl Lactate (98%, EL), anhydrous hexane (95%) brilliant green dye, sodium nitrate ($NaNO_3$), potassium permanganate ($KMnO_4$), calcium chloride (CaCl), iron oxide powder, were purchased from Sigma Aldrich (USA). 1H, 1H, 2H, 2H-Perfluorodecyltrichlorosilane (PFDTCS) and graphite powder were purchased from ABCR (Germany). 1H,1H,2H,2H-perfluorooctanol was purchased from Alfa Aesar (USA). The fluorinated oil HFE-7500 was purchased from 3M™ Novec™ Engineering Fluid. The main NIPAAM monomer was recrystallized after double treatment in n-hexane solution, while all other chemicals were used as received. SU-8 photoresist and developer and Lift-Off Resist (LOR), used as a sacrificial layer, were purchased from Microchem (USA), while AZ 4562 photoresist and AZ 826 developer were purchased from Clariant (Germany). Protoanal LF20/40 high molecular weight (~250 kDa) and LF10/60 low molecular weight (~120 kDa) alginates were purchased from FMC BioPolymer (Philadelphia, PA, USA).

4.4.2 Graphene oxide synthesis and characterization

GO sheets were synthesized from natural graphite powder, by a modified Hummers method [58]. Three grams of graphite (0.25 moles) and 3.6 grams of $NaNO_3$ (~0.05 moles) were mixed in concentrated H_2SO_4 (~150 ml), and the mixture was cooled at 4°C by immersion in a water/ice bath. After 30 minutes, 18 grams of $KMnO_4$ (~0.10 moles) were slowly added under

rigorous stirring, producing a slight exothermic reaction, until 35-40°C. This temperature was maintained and the reaction of oxidation maintained under stirring for 7 hours, in which an increase in viscosity of a brown grey solution was observed. Following that, water (150 ml) was slowly added producing a large exotherm to 95°C. The dilute suspension, brown in color, was stirred for 30 minutes and then further diluted with 200 ml of water and 6 ml of H_2O_2 (30 %), to reduce and solubilize the residual permanganate. Upon this treatment the solution turned into a light yellow color. The diluted suspension was stirred for additional 16 hours, after which it was filtered and the solid product washed repetitively with diluted HCl and water until the pH reached neutral values. The product was then dried in vacuum and exfoliated in nanosheets by ultrasonication to produce a highly stable water dispersible powder. Chemical analysis was performed on a sample of the reagent and the final product to confirm the oxidation process. FTIR (FTIR Spectrum 100, Perkin Elmer Waltham, MA, USA) was performed over a wave number range of 4600 to 600 cm^{-1}. The results were analyzed using the commercial software Spectrum (Perkin Elmer,MA, USA).

4.4.3 Hydrogel bilayer fabrication[1]

The microstructures were the result of a two-step, backside exposure, photolithographic process (figure 4.4) [59], where two different layers were subsequently created, without employing any alignment, on a glass photo mask. Thickness of the layers was controlled by using SU-8 spacers previously fabricated on the bottom silicon substrate. The masks were designed on plastic foil (Selba S.A., Switzerland) and reproduced on glass wafers by photolithography using the positive photoresist AZ4562. A 100 nm chromium layer was evaporated on the substrates and removed from the features areas by rinsing the photoresist from below with acetone and

isopropanol. The final masks were then coated with an LOR sacrificial adhesive layer to provide a uniform adhesion of the hydrogel layers. SU-8 spacers of different thickness (from 1.5 to 40 µm measured by surface profilometry) were prepared by photolithography on SiO_2 substrates. A non-adhesive layer based on PFDTCS was added by vapor silanization overnight and activated at 90°C to prevent adhesion of hydrogels.

After placing the mask on the spacer substrate, a hydrogel solution composed of PEGDA with 3 wt% DMPA photo initiator and 50 wt% ethyl lactate was infiltrated by capillarity into the photopolymerization cell and polymerized at 365 nm for two minutes (Karl Süss Microtec, 300 W mercury lamp, 4 mJ/cm^2, Germany). After separating the two substrates the 10 µm (nominal thickness of the SU-8 spacers) thick hydrogels remained attached to the mask side ensuring the possibility for a second polymerization step. A NIPAAM-AAM-PEGDA (molar ratio 85/15/0.5) solution, with 3 wt% DMPA photoinitiator and 70 wt% ethyl lactate was used for the responsive layer production. 3 wt% GO was added and dispersed into the solution by ultrasonication (4000 J, by means of a probe sonicator, SONICS, USA). The solution was introduced into the space between the photomask and another substrate after removing the previously polymerized solution. Thicker spacers were used in this case (40 µm), and polymerization was carried out for additional three minutes. After UV curing the cell was opened and the bilayers, attached to the mask, were released through immersion in water.

1. *The process was developed in collaboration with Christian Peters, Micro and Nanosystems. ETH Zurich.*

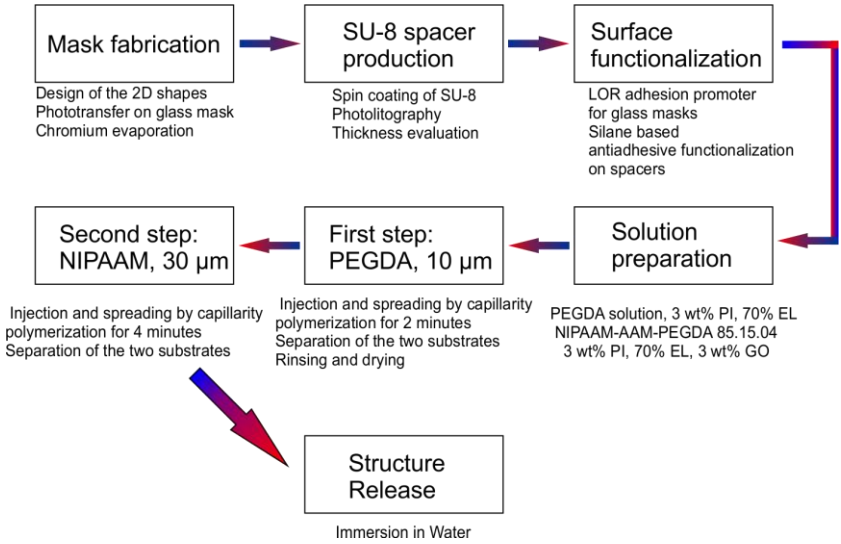

Figure 4.4. *Flowchart of the two step process to fabricate hydrogel bilayers.*

4.4.4 Cryo-SEM imaging

Sections of the gels were taken in their natural swollen state using a high pressure freezing method (HPM100, BalTec/Leica, Wien, Austria). A pressure of 2200 bar was rapidly applied prior to freezing with supercritical liquid nitrogen. Cryo-fracturing was performed in liquid nitrogen by scratching the surface of the samples before transfer to a freeze etching device (BAF060, BalTec/Leica, Wien, Austria) and precooled at -120°C under high vacuum. The hydrogels were then left at -100°C (ramp 90°C/hr) for 1 hour and subsequently brought back to -120°C (ramp 90°C/hr) to sublimate the water. Finally, the samples were shadowed (evaporation by electron beam) with tungsten within the BAF 060 from an elevation angle of 45° to an averaged layer thickness of 6 nm and then from a variable angle between 45°

and 90° for an additional 3 nm layer. Frozen and coated samples were transferred under high vacuum (2.0 x 10^{-7} mbar) at -120°C to a cryo-SEM (LEO, Gemini 1530, Carl Zeiss, Oberkochen, Germany). The images were taken at -120°C with an acceleration voltage of 2 kV.

4.4.5 Swelling studies

The swelling ratio and transition temperature of the hydrogels were determined gravimetrically using gel discs (diameter 4.5 mm, thickness 2 mm) produced by UV polymerization (2 minutes at 365 nm). The gels (a minimum of three per type) were produced and incubated in a water bath (Julabo, Germany) at temperatures ranging from 25 to 55°C. At predefined time intervals (minimum eight hours to ensure swelling equilibrium), the samples were removed from water, carefully wiped, and their weight was recorded. The Equilibrium Swelling Ratio *(ESR)* at each temperature was defined as:

$$ESR=\frac{M_s}{M_d} \tag{4.1}$$

where M_s and M_d are the mass of the swollen hydrogel and the dried mass, respectively.

Volume swelling ratio *(VSR)* was defined in a similar way as:

$$VSR= \frac{V_s}{V_d} \tag{4.2}$$

with V_s and V_d being the volume of the swollen and the dried samples, respectively. These were measured by monitoring the change of the major dimensions of the gel discs with a digital camera (DNT, DigiMicroscale 2.0,

Germany). The same tool was used to perform a temperature dependence analysis of the folding-unfolding of some representative samples of the final structures. Images were taken at different temperature set in a water bath until complete opening of the bilayers.

4.4.6 NIR light actuation of the hydrogel nanocomposite

The photo-thermal phase transitions of the nanocomposite layer and of the final double layers were investigated by irradiation in water by using a focused NIR laser (wavelength 785 nm, 1.5 W power, laser spot 5 mm, SLOC lasers, China). Heating of the samples related to time of irradiation was monitored by means of a thermal camera (Flir, USA) until a reference temperature of 60°C was reached. Different cycles of excitation and recovery as well as different power levels were recorded to analyze the feasibility of the method.

As a complement to these studies, a statistical investigation on the repeatability of the actuation of the GO nanocomposite was performed. Three different samples were exposed to two subsequent cycles of actuation/rest (power set to 1.5 W, 7.8 W/cm^2). As a control, we exposed similar disks of pure NIPAAM-AAM-PEGDA hydrogels (without GO) to the same cycles.

4.4.7 Fabrication of magnetic microbeads[2]

Magnetic microbeads were formed by nebulizing a mixture of LF10/60 (low molecular weight) alginate, LF20/40 (high molecular weight) alginate, iron oxide and phosphate buffered saline (PBS) in a bath of calcium chloride. High and low molecular weight alginates were first dissolved in deionized water and dialyzed with a molecular weight cutoff of 3500 Da for one week

in decreasing concentrations of NaCl in deionized water. After dialysis alginates were mixed with activated charcoal for 1 hour and filtered (0.22-µm filter) to remove charcoal and then sterilized, frozen, and lyophilized for 2 weeks. Lyophilized alginate was dissolved in PBS at 2.5% wt. using a ratio of 4:1, LF10/60:LF20/40 alginate, and mixed with 100 mg/ml of iron (II, III) oxide powder (< 5 µm diameter). This alginate/iron-oxide mixture was then nebulized over a 100 mM calcium chloride bath. The alginate mixture was forced through the nebulizer at 3.13 ml/min as nitrogen gas was used to aspirate the alginate mixture at a volumetric flow rate of 30 standard cubic feet per minute. Nebulized alginate/iron-oxide droplets crosslinked as spheres in the calcium chloride bath (see Figure 1d) and formed magnetic microbeads. Microbeads were rinsed three times in deionized water and stored in deionized water until use.

Smaller, micron-scale magnetic beads were produced from similar materials. Briefly, LF 10/60 alginate precursor (Pronovo) was mixed with iron oxide particles (Fe_3O_4, 5 µm) to a final concentration of 1% alginate in deionized water and 2% ferrous oxide particles to form the aqueous phase. The continuous phase was prepared from the fluorinated oil HFE-7500 with 1% biocompatible surfactant. The continuous and aqueous phases were flowed into a polydimethylsiloxane (PDMS)-glass microfluidic device with a flow ratio of continuous to aqueous phases of 8:1 using a syringe pump (Harvard Apparatus). The resultant emulsion was incubated with 1.4 M CaCl with gentle agitation for 30 minutes and subsequently broken using 20% 1H,1H,2H,2H-perfluorooctanol in HFE-7500.

2. The fabrication of magnetic alginate beads was carried out by Dr. Stephen Kennedy, and Angelo Mao, Wyss Institute for Biologically Inspired Engineering,

School of Engineering and Applied Science, Harvard University, Cambridge, MA, USA.

4.4.8 Cytotoxicity tests

3T3 fibroblasts (ATCC, Manassas, Virginia, USA) were cultured in Dulbecco's minimal essential medium (DMEM) with 10% fetal bovine serum (FBS) and 1% penicillin/streptomycin at 10% CO_2 at 37°C. The hydrogels were firstly washed intensively by multiple immersions in DI water, until no signal of unreacted materials was detected by UV-VIS spectrophotometry. They were subsequently sterilized with UV light and submerged in culture medium in a 6-well plate. After 24 hours of incubation, the gel-conditioned medium was transferred to the cultured cells. Cells seeded in fresh media were used as a control. After incubation for 48 h, WST-1 reagent (Roche, Switzerland) was added to each well according to the manufacturer's instructions. Three hours later 50 μL of the solution was transferred into a 96-well plate, and the absorbance was measured at 435 nm to calculate the relative intensity of the absorbance. Ten parallel experiments were done for every sample. The materials were also tested by direct contact with cells for 48 hours.

To test the viability of cells inside the alginate beads, D1 mouse mesenchymal stem cells (mMSCs) (ATCC, Manassas, Virginia, USA) were cultured in Dulbecco's minimal essential medium (DMEM) with 10% fetal bovine serum (FBS) and 1% penicillin/streptomycin at 10% CO_2 at 37°C. Prior to micro bead encapsulation, D1s were rinsed three times in PBS through centrifugal washing. D1s were pelleted and the culture medium was replaced with a 2.5% wt 4:1 LF10/60:LF20/40 alginate, 100 mg/ml iron (II,III) oxide solution in PBS (without Ca^{2+} and Mg^{2+}), again through

centrifugal washing. The D1, alginate, iron oxide and PBS mixture was nebulized over a calcium chloride bath as described in the magnetic microbead fabrication subsection. After encapsulation, D1-containing microbeads were rinsed three times in PBS (w/ Ca^{2+} and Mg^{2+}) and cultured in 6-well plates in culture medium as described above. At one, three, and seven days, LIVE/DEAD Cell Viability Assays (Invitrogen, Carlsbad, California, USA) were performed to assess the results of and number of D1s encapsulated per microbead.

4.4.9 Bead loading, magnetic manipulation and actuation

The magnetic alginate microparticles were loaded inside the sealed compartments of the folded bilayers by mixing the two components in water at temperature higher than 40°C. The subsequent cooling allowed the hydrogel bilayers to close and to trap the beads inside.

Magnetic manipulation of the final platform was achieved by means of a 5 DOF electromagnetic system, which consists of eight stationary electromagnets with soft-magnetic cores capable of producing magnetic fields and gradients up to 50 mT and 0.5 T/m at frequencies up to 100 Hz. Visual tracking was assured by a Leica M80 microscope (Germany) at 6.0 X magnification, placed above the workspace. The NIR laser used for actuation was included in the setup, mounted at an angle of approximately 60°C, at a distance of 30 cm from the workspace. More details about the setup can be found in the publication by Kummer et al. [45].

4.5 Results

4.5.1 GO hydrogel nanocomposites: fabrication and characterization

GO sheets were synthesized by means of a controlled oxidation of graphite with $KMnO_4$ and $NaNO_3$ in concentrated H_2SO_4. It should be noted that the reaction involves the generation of toxic and explosive gases (NO_2, N_2O_4, ClO_2). The reaction process could be in this sense optimized by introducing H_3PO_4 as reported by Marcano et al [60], or substituting $NaNO_3$, as described by Chen et al. [61].

The produced black powder was filtered and allowed to dry, and then analyzed by FTIR to confirm the oxidation state (figure 4.5a). Compared to the blank spectrum of graphite powder, the GO was characterized by the following features: O-H stretching vibrations at 3400 cm^{-1}, stretching vibrations from C=O at 1720cm^{-1}, skeletal oxidation from unoxidized graphitic domains around 1600 cm^{-1}, bending vibration from C-H groups at 1400 cm^{-1}, and C-OH stretching vibrations at 1220 cm^{-1} [62,63] [62, 63]. The analysis confirmed the presence of a small percentage of unconverted material. However, a separation between the oxidized and the non-oxidized powder was automatically performed when the graphitic material was dissolved into water-like solvents and sonicated. GO was able to form stable solutions in water, or ethyl lactate (the solvent used for the fabrication) for hours, thanks to the presence of oxidized groups.

The dispersion of GO in solutions of NIPAAM-AAM-PEGDA hydrogels by ultra-sonication and the consequent polymerization (4 mins) produced hydrogel-based nanocomposites with a slight brown color. The internal structure analyzed by Cryo-SEM revealed a pore size in the order of 100 nm

and a uniform distribution of nanometer-sized graphene sheets (visible in figure 4.5b, as white dots).

Swelling properties of the two layers involved in the fabrication of self-folding devices, PEGDA and NIPAAM-AAM-PEGDA, were analyzed gravimetrically. Results (figure 4.5c) show that PEGDA hydrogels are able to double their weight by absorption of water, without significant changes in the range of temperature between 25 and 55°C. NIPAAM-AAM-PEGDA hydrogels are, instead, strongly thermoresponsive, passing from an equilibrium swelling ratio of ca. 16 to a full collapse (ESR ~ 2, comparable to the PEGDA layer) at around 43°C. The same experiment, performed on GO nanocomposites revealed a significant influence on the swelling ability of the hydrogels, with an ESR ~ 10 (around 3 times the original volume) found at room temperature. No difference was reported in the temperature of transition of the gel.

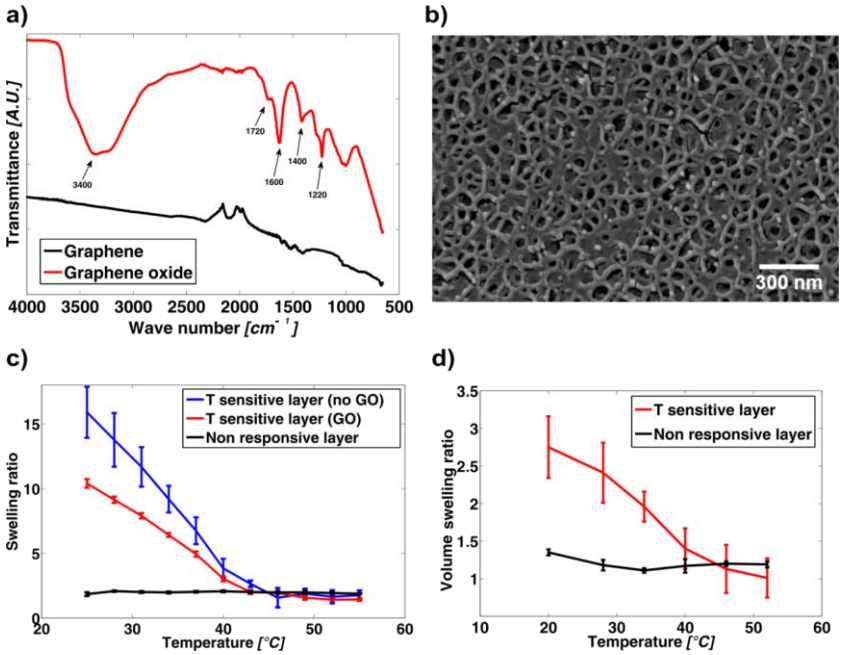

Figure 4.5. *a) FTIR analysis of the oxidation process of graphene. B) Cryo-SEM imaging of the polymer network of the nanocomposites. The white dots are the graphene sheets dispersed around the matrix. c) Weight swelling ratio of the two polymer layers (red and black) used in the microstructures. The graphene oxide nanocomposite has a significant decrease of swelling ratio when compared to the hydrogel (blue).d) Volume swelling ratio of the two layers.*

The inclusion of the nanometer-sized GO sheets allowed the fast and reproducible photothermal actuation of the matrix, by means of a 785 nm NIR laser. Different power levels of the laser sources were tested in order to fully characterize the feasibility of the actuation process by NIR. In general it was always possible, even at low power levels to reach a feasible temperature for

actuation (T > 40°C) (figure 4.6a). However, a full control over the induced temperature could be reached only in a certain power range (1-1.7 W, 5-8 W/cm^2). Insufficient power levels could not provide enough energy to raise the temperature over 40 °C, while excessive power levels would produce temperatures higher than 80 °C almost immediately. By setting the power to 1.5 W, we achieved an almost linear temperature raise (figure 4.6b), with an average layer response time in the order of seconds. The actuation was fully repeatable upon several cycles of exposure (figure 4.6c), without any detectable change in the material. Complementary to the representative curves, three different samples were exposed to two subsequent cycles of actuation/rest (power set to 1.5 W, 7.8 W/cm^2). The kinetics (figure 4.6c) of the process was found similar for both the phases of the experiment in all three samples. As a control, we exposed similar disks of pure NIPAAM-AAM-PEGDA hydrogels (without GO) to the same cycles. Results show that it was not possible to induce any increase of temperature, even after continuous exposure for more than 40 seconds (figure 4.6d).

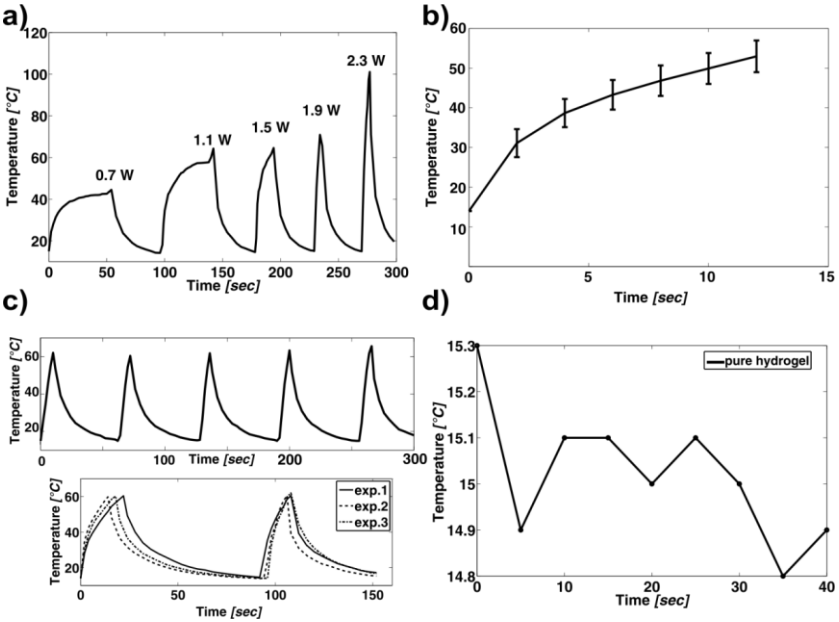

Figure 4.6. *a) Temperature response of a GO hydrogel nanocomposite to different levels of power of the laser source. B) Laser sensitivity to IR laser exposure at a power of 1.5 W. The almost linear kinetics was perfectly controllable at this energy lever.c) Representative curves of the temperature change of the double layer as a function of NIR exposure-rest cycles. The process appears repeatable in terms of time and for different samples. d) Control sample (without GO) exposed to laser source showed no change in temperature, even when exposed for almost a minute.*

4.5.2 Beads fabrication

Magnetic alginate beads were produced by adding dropwise the solution of dissolved alginate and Fe_3O_4 over a calcium chloride bath. The size of the drop was limited by nebulization, thus giving particles in the order of 30-100 μm (see figure4.7a). Additionally, a microfluidic device was used to mix the alginate-iron oxide mixture together with fluorinated oil; the emulsion was prepared to reduce and stabilize the size of the drops, according to recent works [64]. After that, the micro-droplets were crosslinked using calcium chloride and removed from oil by means of perfluorooctanol. This allowed reducing the size of the beads down to 10 μm (see figure 4.7b).

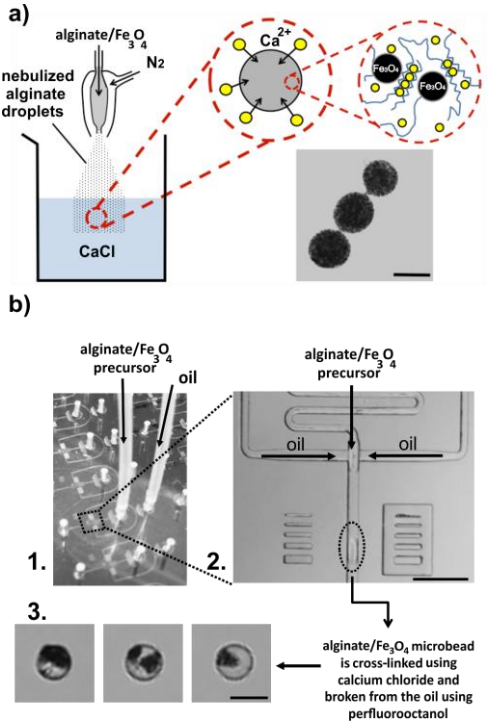

Figure 4.7. *a) Standard process of bead fabrication. The nebulization of a solution of alginate and iron oxide into a calcium chloride bath allows the formation of microbeads. Scale bar is 100 µm. b) Microfluidic driven process for the formation of micron sized magnetic alginate beads. (1) A microbead precursor aqueous solution containing iron oxide and oil are injected into a microfluidics device to generate magnetic microbeads. (2) Within the device, oil is used to pinch off micro-droplets of alginate/Fe_3O_4. The scale bar is 200 µm. After being processed in the microfluidics device, micro-droplets are crosslinked using calcium chloride and removed from oil using 20% perfluorooctanol. (3) The resulting product are iron-oxide-containing alginate microbeads. The scale bar is 10 µm.*

4.5.3 Backside photolithographic fabrication of hydrogel bilayers

Hydrogel bilayers with different shapes (from simple tubes to cross-shaped, jellyfish-like, and Venus flytrap-like structures) were produced following a two-step photolithographic procedure, reported elsewhere [59]. Hydrogel layers were patterned in an assembled chamber composed of a glass photomask and a silicon wafer with thin SU-8 spacers. The SU-8 spacers were used to fix the thickness of the layers. Additionally, the hydrogel layers were forced to adhere to the glass mask using a highly hydrophobic silane functionalization of the silicon substrates and a polymeric lift-off layer on the mask side. In this way, no alignment was needed between the two steps of the fabrication process. The closed conformation of the photolithographic chamber allowed limiting the scavenging effect of oxygen during UV-photopolymerization.

The process was able to produce layers thicker than 10 µm. Fabrication of thinner layers suffered from a mismatch between the set thickness and the obtained one, possibly due to the viscosity of the used solutions, which tended to expand the space between the substrate and the mask. Layers thicker than 40-50 µm were found to be inhomogeneous on a 4-inch wafer.

A 10-µm thick spacer was used for the PEGDA layer, followed by a 40-µm thick second substrate. These values were found experimentally to be enough to ensure the complete closure of the platforms. The opposite order was found to produce misalignment, due to swelling of NIPAAM features in their own solution. Despite not being optimized, the fabrication process allowed an efficient and repeatable production of completely self-folded features.

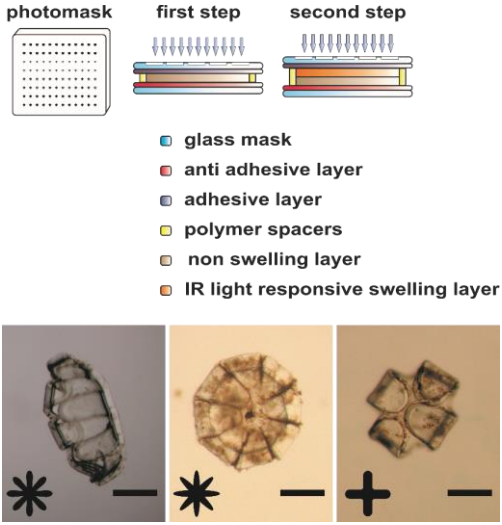

Figure 4.8. *Schematic representation of the photolithographic chamber. The 2D shapes drawn on the photomask (upper left) fold into 3D microstructures, shown in the optical images after release. Scale bar is 200 µm. The process exploits backside exposure and the use of anti-adhesive coating to avoid misalignment between the first and the second step.*

4.5.4 Cytotoxicity tests on the hydrogel bilayers and on alginate beads

The hydrogel bilayers revealed a high presence of monomers and unreacted materials concentration after fabrication. Therefore, the samples were repetitively rinsed with distilled water until the signal of their solution, recorded by UV-VIS spectroscopy, showed no contamination (figure 4.9a). Additionally, they were sterilized by UV light before any cell toxicity test. Ten parallel experiments of WST assays were done to evaluate the toxicity of gel-conditioned cell medium towards fibroblasts in comparison to control (fresh medium) cell cultures. Results, in figure 4.9b, show that the cell culture

was able to resist and proliferate, without being influenced by the bilayers. Direct contact for 48 hours showed similar results, confirming the absence of cytotoxicity of the used polymers.

LIVE/DEAD assays were performed with mesenchymal stem cells, cultured and encapsulated in the alginate microbeads during the fabrication process. For this reason, the cell culture medium was substituted by a mixture of alginate, iron oxide solution and PBS. The mixture contained roughly 10^6 cells/ml. The fabrication process showed a limited influence on the viability of the cell. However, the encapsulation provided the right conditions for the proliferation of the culture; as it can be seen in figure 4.10, the viability increased after 7 days, to a value significantly higher than the initial one.

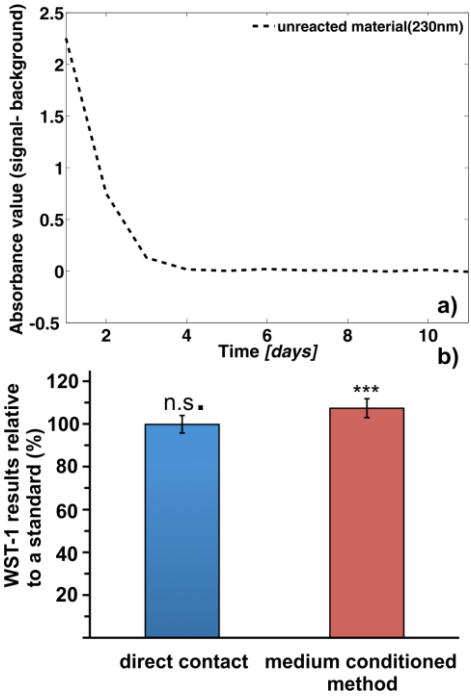

Figure 4.9. *a) UV-VIS spectrophotometry measurements were performed after every wash of the sample in DI water and the spectrum was recorded and compared to a pure DI water background. The difference between the two signals was mainly found around the wavelength of 230 nm. This wavelength was considered and checked until no difference between the signal and the background was recorded. b). The WST-1 assay was conducted to measure the cytotoxicity of the hydrogel bilayers. We monitored the viability of fibroblasts after incubation directly with bilayers (direct contact) or hydrogel-conditioned medium (medium-conditioned method) for 2 days. No statistically significant decrease in the proliferation was observed compared to the control in both cases. However, when the media was conditioned with our hydrogels, surprisingly, proliferation was actually enhanced (***, $p < 0.001$ when compared to controls). Error bars represent the standard deviation.*

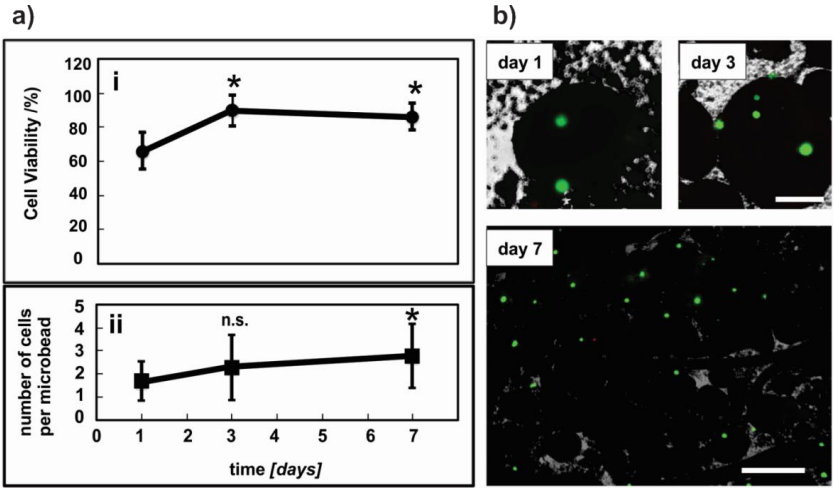

Figure 4.10. *LIVE/DEAD Assays were used to assess the viability and proliferation of D1s mesenchymal stem cells encapsulated inside magnetic alginate microbeads. (a) The viability is statistically lower on day 1 because some cells did not survive the rough microbead fabrication process (i). However, D1s proliferate very rapidly, so by day 3, the cells that did survive split leading to a statistically greater number of viable cells (ii). (b) Fluorescence micrographs of live (green) versus dead (orange-red) encapsulated cells on days one, three and seven. The scale bars are 200 μm and 500 μm. In part (a), values are represented as means with standard deviation. * indicates statistical significance ($p < 0.05$) compared to day 1 values.*

4.5.5 Characterization of the bilayers and preparation of the microrobots

To confirm the material choice and formulation, the bilayers were characterized in terms of shape change dependence on the external temperature. The opening of the structures was found to be completed at around 38 °C, a temperature slightly below the one observed for the full collapse of the thermoresponsive layer (figure 4.11). Their transition was completed in the order of tens of seconds due to their limited size, which facilitated the process of water diffusion. The temperature-dependent unfolding of the bilayers was used to load magnetic alginate microbeads into their internal compartment. The procedure was performed by simply mixing the two parts together on a hot bath followed by the cooling and the folding of the hydrogel films. Depending on the shape of the bilayers, different configurations and organization of the beads could be found. Long Venus flytrap-like structures were able to create a sort of ordered distribution of the beads along the main axis, thus having a more defined magnetic axis. Jellyfish-like structures encapsulated the beads with no preferential order into their spheroidal shape. In both cases, the microbeads remained confined inside after complete cooling and throughout the magnetic manipulation experiments.

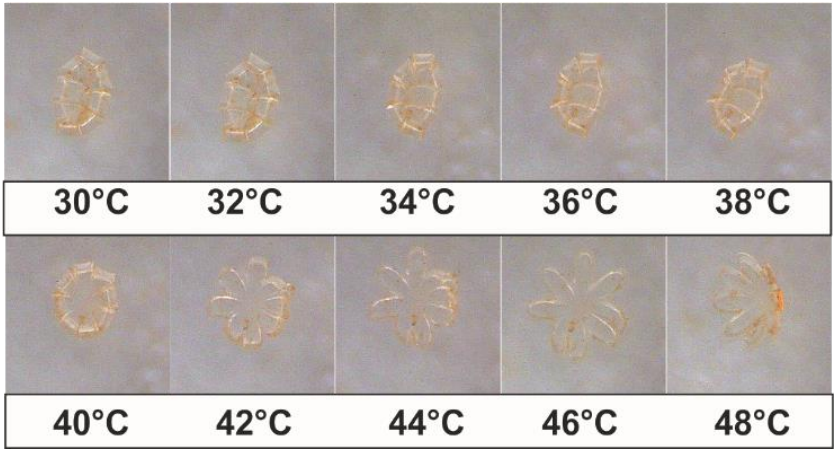

Figure 4.11. *Optical microscope images of temperature dependent unfolding of long venus flytrap-like hydrogel bilayers. The closed configuration at body temperature allows remote actuation in a physiological environment.*

4.5.6 Manipulation and actuation

Magnetic manipulation of the final platform on the surface of water was achieved using a 5-DOF electromagnetic manipulation system, previously designed for *in vivo* applications in the eye. Real time, closed-loop servoing of individual alginate beads was first performed by implementing a proportional controller. Once a bead was selected, the visual tracker was able to recognize it (blue frame in figure 4.12). The system then calculated and applied the required magnetic gradients to move the beads along pre-planned trajectories (the gray circles in the figure). Next we demonstrated automated maneuvering of hydrogel bilayers carrying magnetic microbeads using real-time optical tracking (figure 4.12d). An eight-figure trajectory was used as a target, and the robots were able to move along the path several times.

Rotational frequencies (f > 4 Hz) could be used to decouple the motion of the microbeads from the surrounding structure. This movement was possible even after more than seven days, thus revealing limited interaction between the internal surface of the bilayers and the cell-loaded alginate beads.

Exposure to laser irradiation allowed fast unfolding of the structures and sudden release of the particles stored in their internal compartment (figure 4.12e). More specifically, most of the microbeads were released by the rapid conformal changes of microstructures during unfolding. The release was completed by subsequent external magnetic field stimulation. Although the process was demonstrated to be repeatable and stable, problems were created by the attenuation of the NIR light source and thermal effects in water.

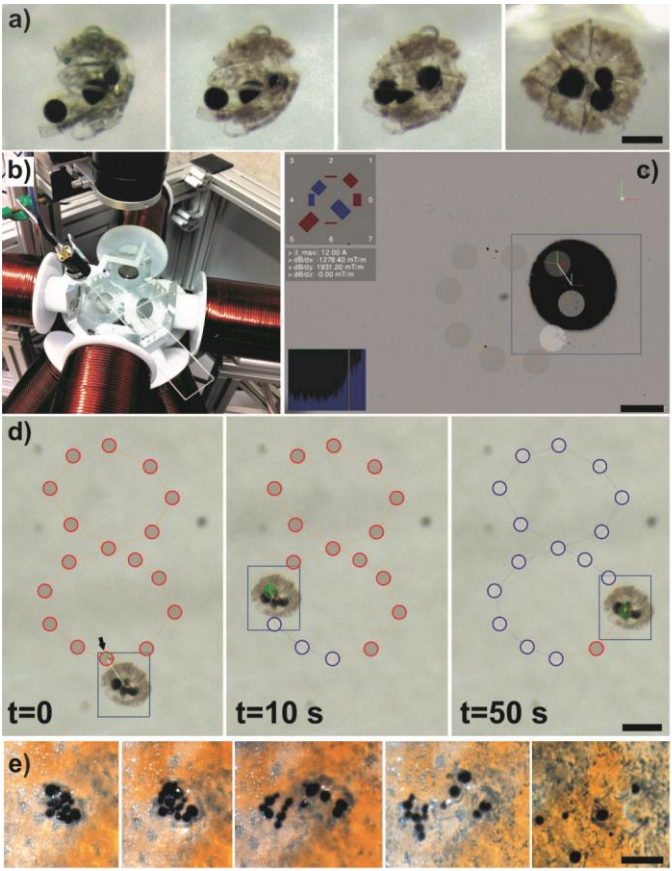

Figure 4.12. *a) Magnetic manipulation of platforms and NIR activated release of microparticles. a) Encapsulation of magnetic particles inside folding microstructures b) Octomag electromagnetic manipulation system integrated with NIR laser. c) Manipulation of single alginate beads. d) Microrobot manipulation over a selected pattern. The robot follows the preplanned trajectory. Red circles denote target destinations and the circles turn into blue as the robot passes over them. e) NIR activated release of microparticles. The scale bars are 200 μm, 50 μm and 500 μm.*

4.6 Discussion

This work combines the design and fabrication of a NIR light responsive hydrogel bilayer, the fabrication and use of magnetic cell-laden alginate microbeads, and a magnetic manipulation platform to provide a multifunctional, controllable micro agent for drug and cell delivery. The device is envisioned to be injected near the area of intervention, steered in the body fluids by magnetic field gradients to the target and then actuated by NIR light stimulation. After the task is completed, they could navigate to a reachable area of the body and removed by a second injection.

A simple and efficient two-step photolithographic process [59] was adapted and optimized from previous work [33, 37] to fabricate full polymeric structures. These structures ensure a closed and protected compartment in their relaxed swollen state, and can reversibly unfold to release their encapsulated material. The fabrication method has the advantages of being compatible with a large variety of photopolymerizable materials allowing further combinations and solutions for the platform. For example, biodegradable materials have been used recently in hydrogel bilayers [30], thus allowing fewer problems in terms of post-intervention removal. The shape of the devices was defined by the initial 2D design on the photo mask. The spheroid was created from a symmetrical 8-arm star, and the Venus flytrap from an elongated version of the previous design. Stars or tubes were also produced, although not presented here in the final form.

The size of the final structures was maintained on the order of 1 mm or below using inexpensive materials such as foil masks and microfabricated polymer spacers. Although *in vivo* steering of magnetic devices with a

comparable or larger size was recently demonstrated [41, 48] for different areas of intervention, the proposed method is completely compatible with the fabrication of smaller devices using high-resolution chromium masks and metal spacers. These smaller agents could be easily navigated inside the main arteries as demonstrated with microparticles by Pouponneau et al [65].

Complete closure of the hydrogel bilayers was assured by tuning the material properties and the thickness of the two defined layers. PEGDA was chosen as an internal inactive layer due to its properties of cell compatibility (as recently proposed also by Jamal et al. [66]). Its thickness was fixed experimentally to the nominal value of 10 μm, the minimum thickness achievable with the current fabrication setup.

The NIR responsive layer was formed by synthesizing and dispersing GO (3 wt% of the monomer weight) into a NIPAAM-AAM-PEGDA hydrogel solution in ethyl lactate. The hydrogel solution was designed and synthesized to achieve different tasks, namely:

- A thermoresponsive behavior ensured by the intrinsic properties of NIPAAM (which has a lower critical solution temperature, LCST, of ~ 30°C).
- A thermo induced collapse of the hydrogel at around 40°C. The shift of LCST to the desired temperature was achieved by increasing the quantity of hydrophilic groups into the hydrogel formulation due to a 15 mol% quantity of AAM [67]. The molar ratio between NIPAAM and AAM was experimentally found, by analyzing different combinations and characterizing the temperature dependent swelling behavior of the resulting polymers.

- A high swelling ratio, which was achieved by minimizing the quantity of PEGDA crosslinker to a value of 0.5 mol%.
- A low viscosity and complete compatibility with the fabrication setup. This was possible by adding a 70 wt% quantity of ethyl lactate. This solvent did not influence the functionalization of the spacers and the mask used in the photolithographic chamber, and at the same time increased the fluidity of the solution, filling the chamber by capillary forces.

A short UV exposure (2 minutes) allowed the formation of highly flexible hydrogels. GO, which has been recently proposed as a low cost material for NIR composites [68, 69], was produced and dispersed by ultrasonication into the ethyl lactate based solution. No significant difference was found in the polymerization time, although GO is known to have absorbance at 365 nm [70].

The nanocomposite was characterized in terms of morphology (Cryo-SEM revealed a network pore size in the order of 100 nm and a homogeneous distribution of the graphene sheets on the matrix) and swelling properties. As reported in the results, the inclusion of GO sheets into the nanocomposite significantly changed the swelling properties of the layer when compared to the pure hydrogel, while not affecting the LCST value. This result differs from that previously found in similar systems, where GO increased the swelling ratio and lowered the phase transition of NIPAAM polymers due to the hydrophilicity of the nanomaterial [68]. We believe that the difference is related to the limited interaction of GO with the hydrogel (there is no functionalization that chemically links the GO sheets with the polymer network) and the presence of agglomeration and impurities. Optimization of

the synthesis of GO and the dispersion method could affect this result and the swelling properties.

As reported previously, the photo excitation of GO with an NIR laser leads to the generation of excitons which emit heat warming the surrounding matter [71]. The mechanism of heat transfer was used to cause rapid photo thermal actuation of the hydrogel networks. The collapse of the nanocomposite was achieved upon irradiation by a 785 nm laser at different power levels, from 0.7 W to 2.3 W, with different kinetics. A reference of 1.5 W (20 W/cm^2) was chosen for most of the experiments due to the control and reproducibility of the procedure and the results. This value is reported to be in the range of physiological photothermal interaction between the tissue and the source of heat [72]. Additional efficiency and improvement in the heat transfer could be achieved by a straightforward tuned reduction process on GO [73], or by covalently crosslinking the sheets to the hydrogel matrix [68].

The hydrogel nanocomposite was polymerized on the top of the PEGDA layer, due to a short UV exposure (3 minutes) through the glass mask. A nominal thickness of 30-µm was found to be enough to ensure complete closure of the folding structures upon swelling in water. The formed bilayers, constituting the outer compartment of the microrobot, were found to change their shape from a closed to a completely open configuration around 38°C, a temperature slightly below the one observed for the full collapse of the thermoresponsive layer. A slight increase in the quantity of AAM (5 mol %) in the initial solution was sufficient to shift this value to 40°C. The transition could complete in a few seconds, and a similar timescale was found for the NIR light actuation of the microstructures, once the laser was focused on them.

We also tested the cytotoxicity of the bilayers, and no significant decrease in metabolic activity of fibroblasts was found. Fibroblasts were kept for 48 hours in contact with gel conditioned medium. These studies constitute only the first experiments needed to assure no harm in *in vivo* applications. Additionally, one could exploit the intrinsic properties of NIPAAM to modulate the adhesion of cells and proteins, which constitute the first step toward a foreign body reaction. For example, NIPAAM surfaces have been used as coatings to achieve anti-fouling or cell-releasing effects due to the high hydrophilicity at T < LCST [74].

To complete the microrobotic platform, magnetic alginate microparticles were fabricated and loaded inside the sealed compartment of the folded bilayers. Alginate, a natural biodegradable polysaccharide, is often chosen as a gelable polymer for long-term and sustained delivery of both drugs and cells [75]. Alginate gels can be formed in relatively mild pH and temperature conditions using divalent cations as crosslinkers and can be made in a sterile process, which is useful for cell encapsulation [76]. Here, iron (II, III) oxide particles (10 wt% Fe_3O_4, < 5 μm diameters) were encapsulated in alginate matrices resulting in soft magnetic ferrogel microparticles. The procedure, involving nebulization of alginate and iron oxide suspensions in a calcium chloride bath was also found to be compatible with the encapsulation and growth of mesenchymal stem cells, as was shown by the LIVE/DEAD assays performed for one week after fabrication. Cell viability was higher than 80% after seven days of incubation. It is likely that cell viability and proliferative capacity can be greatly improved by modifying alginate with RGD adhesion ligands, and by optimizing the cell density at which cells are seeded in the beads. Additionally, because iron oxide limits our ability to visualize cells

located more deeply in the interior of individual beads, cell densities/numbers are likely higher than indicated in figure 4.11.

Procedures to scale down alginate beads ranging from 50-100 µm, to 10-µm were also tested, using a microfluidic injection based on fluorinated oil. This, together with the previously mentioned works about nanometer size bilayers, allows us to think that the full system can be easily scaled down from this prototypical size.

The microparticles were loaded inside the photoresponsive bilayers in a hot bath by simple mixing the two components. The number and the orientation of beads trapped inside the bilayers varied depending on the shape of the folding films and the size of the microbeads. This self-assembly technique was not fully investigated, but it was empirically found to influence the magnetic properties of the final platform [77], in some cases facilitating the magnetic manipulation (such as for Venus flytrap-like structures).

Automated and complex 3D locomotion of the microrobots by means of a 5-DOF electromagnetic manipulation system was tested and shown to be effective in water environments, when the structure could be suspended on the surface of the experimental area or was free to swim in water. The robots were found to stick easily to the bottom or the borders of the swimming chambers, significantly affecting their swimming abilities. However, these experimental problems could be readily solved by functionalization of the fluidic chamber or by use of larger setups. Tracking was achieved by visual detection of the alginate beads. *In vivo* applications could exploit the IR signal of the GO [63] or magnetic tracking of the beads [65] (the detection could be facilitated by self-assembly of the beads inside the bilayers). Photothermal actuation was found to promote the release of the alginate beads, due to the

rapid conformal changes of the bilayers upon exposure and to magnetic field stimulation.

To conclude, we demonstrated the feasibility of the microrobotic platform as a potential and “intelligent” carrier for cell loaded alginate beads. Additionally, studies were performed on the capability of the hydrogel bilayer to load and release drugs by diffusion or by external actuation. These studies are presented in chapter 6.

4.7 Conclusion and Outlook

The proposed microrobotic platform possesses most of the required features that we envision for biomedical applications including 3D magnetic steering, the ability of carrying drugs and cells, and spatiotemporally controlled delivery. Compared to similar work found in the literature [37, 39, 48], this study presents for the first time a full approach to the problem by developing the "appropriate" materials and integrating them into an automated system.

The fabrication methods used for the design of the microrobot have been proposed and described to demonstrate the simplicity of the solution. However, they were not optimized for large scale production, and interesting potential for future work in this direction exists.

The definition of the thickness of the layers could be improved by ensuring complete adhesion of the two opposite substrates (the glass and the spacer), and by using better techniques of spacer production. SU-8 spacers were often found to be affected by poor homogeneity when the thickness was set to values higher than 28 μm due to imperfection in the spin coating process or extreme viscosity of the used solutions.

High-precision glass masks are needed for the down scaling of the process in order to achieve nanometer sized layers and to reduce the total dimension of the device to a few microns.

GO synthesis can also be optimized to increase the state of oxidation and, therefore, the efficiency of the photothermal actuation. In this way, less material would be needed with less influence on the swelling properties of

the hydrogel, or with the advantage of decreasing the required power for actuation.

Aside from optimization of the processes, challenges related to real *in vivo* applications also exist. With an approximately 10-fold shrinkage in the total dimension, the devices will become small enough to access remote places of the body such as the hepatic arteries, the hollow areas of the subarachnoid space, the gastrointestinal tract and other large cavities filled with fluids. The released magnetic beads could be navigated to even smaller conduits in the body, allowing a modular approach to the problem of cell and drug delivery.

This strategy would require investigation of the penetration of the electromagnetic fields and of the efficiency of the manipulation/actuation process in a biological environment, as well as additional biocompatibility tests. Nevertheless, the platform, based on smart and biocompatible materials, can provide a solid basis for future therapeutic targeted interventions.

The following chapters are intended to more deeply explore the potential of this solution, and to give a better understanding of the phenomena behind the self-folding of hydrogel bilayers.

4.8 Bibliography

[1] G. M. Whitesides, B. Grzybowski, *Science* **2002**, 295, 2418.

[2] K. J. M. Bishop, C. E. Wilmer, S. Soh, B. A. Grzybowski, *Small* **2009**, 5, 1600.

[3] T. L. Breen, J. Tien, S. R. J. Oliver, T. Hadzic, G. M. Whitesides, *Science* **1999**, 284, 948.

[4] J. W. C. Dunlop, R. Weinkamer, P. Fratzl, *Mater Today* **2011**, 14, 70.

[5] A. G. Volkov, J. C. Foster, T. A. Ashby, R. K. Walker, J. A. Johnson, V. S. Markin, *Plant Cell Environ* **2010**, 33, 163.

[6] Y. Forterre, J. M. Skotheim, J. Dumais, L. Mahadevan, Nature 2005, 433, 421; A. G. Volkov, T. Adesina, M. I. Volkova-Gugeshashvili, J. Williams, E. Jovanov, *Biophys J* **2007**, 111a.

[7] T. G. Leong, A. M. Zarafshar, D. H. Gracias, *Small* **2010**, 6, 792.

[8] R. F. Shepherd, F. Ilievski, W. Choi, S. A. Morin, A. A. Stokes, A. D. Mazzeo, X. Chen, M. Wang, G. M. Whitesides, *P Natl Acad Sci USA* **2011**, 108, 20400; R. V. Martinez, C. R. Fish, X. Chen, G. M. Whitesides, *Adv Funct Mater* **2012**, 22, 1376.

[9] C. Py, P. Reverdy, L. Doppler, J. Bico, B. Roman, C. N. Baroud, *Phys Rev Lett* **2007**, 98.

[10] J. H. Cho, A. Azam, D. H. Gracias, *Langmuir* **2010**, 26, 16534; T. G. Leong, P. A. Lester, T. L. Koh, E. K. Call, D. H. Gracias, *Langmuir* **2007**, 23, 8747; B. Gimi, D. Artemov, T. Leong, D. H. Gracias, Z. M. Bhujwalla, *Magn Reson Med* **2007**, 58, 1283; A. Azam, K. E. Laflin, M. Jamal, R. Fernandes, D. H. Gracias, *Biomed Microdevices* **2011**, 13, 51.

[11] T. G. Leong, C. L. Randall, B. R. Benson, N. Bassik, G. M. Stern, D. H. Gracias, *P Natl Acad Sci USA* **2009**, 106, 703.

[12] C. L. Randall, T. G. Leong, N. Bassik, D. H. Gracias, *Adv Drug Deliver Rev* **2007**, 59, 1547.

[13] T. G. Leong, B. R. Benson, E. K. Call, D. H. Gracias, *Small* **2008**, 4, 1605.

[14] C. L. Randall, E. Gultepe, D. H. Gracias, *Trends Biotechnol* **2012**, 30, 138.

[15] A. W. Feinberg, A. Feigel, S. S. Shevkoplyas, S. Sheehy, G. M. Whitesides, K. K. Parker, *Science* **2007**, 317, 1366.

[16] E. W. H. Jager, E. Smela, O. Inganas, *Science* **2000**, 290, 1540.

[17] M. Shahinpoor, Y. Bar-Cohen, J. O. Simpson, J. Smith, *Smart Materials & Structures* **1998**, *7, R15*.

[18] N. A. Peppas, W. Leobandung, *J Biomat Sci-Polym E* **2004**, 15, 125.

[19] J. Kopecek, J. Y. Yang, Polym Int 2007, 56, 1078; M. Zrinyi, *Colloid Polym Sci* **2000**, 278, 98.

[20] K. H. Bae, L.-S. Wang, M. Kurisawa, *J Mater Chem B* **2013**, 1, 5371.

[21] Y. Osada, H. Okuzaki, H. Hori, *Nature* **1992**, 355, 242.

[22] Z. Hu, X. Zhang, Y. Li, *Science* **1995**, 269, 525.

[23] H. He, X. Cao, L. J. Lee, *Journal of Controlled Release* **2004**, 95, 391.

[24] H. Y. He, J. J. Guan, J. L. Lee, *J Control Release* **2006**, 110, 339.

[25] J. J. Guan, H. Y. He, D. J. Hansford, L. J. Lee, *J Phys Chem B* **2005**, 109, 23134.

[26] V. Luchnikov, O. Sydorenko, M. Stamm, *Adv Mater* **2005**, 17, 1177.

[27] Q. Yu, J. M. Bauer, J. S. Moore, D. J. Beebe, *Appl Phys Lett* **2001**, 78, 2589.

[28] L. Ionov, Macromol Chem Phys **2013**, 214, 1178; L. Ionov, *Soft Matter* **2011**, 7, 6786; L. Ionov, S. Zakharchenko, G. Stoychev, E. Sperling, *Multifunctional Polymer-Based Materials* **2012**, 1403, 99.

[29] L. Ionov, *Adv Funct Mater* **2013**, 23, 4555.

[30] S. Zakharchenko, N. Puretskiy, G. Stoychev, M. Stamm, L. Ionov, *Soft Matter* **2010**, 6, 2633.

[31] G. Stoychev, N. Puretskiy, L. Ionov, *Soft Matter* **2011**, 7, 3277.

[32] S. Alben, B. Balakrisnan, E. Smela, *Nano Lett* **2011**, 11, 2280.

[33] T. S. Shim, S. H. Kim, C. J. Heo, H. C. Jeon, S. M. Yang, *Angew Chem Int Edit* **2012**, 51, 1420.

[34] X. B. Zhang, C. L. Pint, M. H. Lee, B. E. Schubert, A. Jamshidi, K. Takei, H. Ko, A. Gillies, R. Bardhan, J. J. Urban, M. Wu, R. Fearing, A. Javey, *Nano Lett* **2011**, 11, 3239.

[35] H. Therien-Aubin, Z. L. Wu, Z. H. Nie, E. Kumacheva, *J Am Chem Soc* **2013**, 135, 4834.

[36] K. U. Jeong, J. H. Jang, D. Y. Kim, C. Nah, J. H. Lee, M. H. Lee, H. J. Sun, C. L. Wang, S. Z. D. Cheng, E. L. Thomas, *J Mater Chem* **2011**, 21, 6824.

[37] S. Pedron, S. van Lierop, P. Horstman, R. Penterman, D. J. Broer, E. Peeters, *Adv Funct Mater* **2011**, 21, 1624.

[38] M. Jamal, S. S. Kadam, R. Xiao, F. Jivan, T.-M. Onn, R. Fernandes, T. D. Nguyen, D. H. Gracias, *Adv Healthc Mater* **2013**, 2,1142

[39] K. Baek, J. H. Jeong, A. Shkumatov, R. Bashir, H. Kong, *Adv Mater* **2013**, 25, 5568.

[40] S. Martel, O. Felfoul, J. B. Mathieu, A. Chanu, S. Tamaz, M. Mohammadi, M. Mankiewicz, N. Tabatabaei, *Int J Robot Res* **2009**, 28, 1169.

[41] F. Ullrich, C. Bergeles, J. Pokki, O. Ergeneman, S. Erni, G. Chatzipirpiridis, S. Pane, C. Framme, B. J. Nelson, *Invest Ophth Vis Sci* **2013**, 54, 2853.

[42] A. Nacev, A. Komaee, A. Sarwar, R. Probst, S. H. Kim, M. Emmert-Buck, B. Shapiro, *Ieee Contr Syst Mag* **2012**, 32, 32.

[43] A. W. Mahoney, J. J. Abbott, *Appl Phys Lett* **2011**, 99.

[44] D. R. Frutiger, K. Vollmers, B. E. Kratochvil, B. J. Nelson, *Int J Robot Res* **2010**, 29, 613.

[45] M. P. Kummer, J. J. Abbott, B. E. Kratochvil, R. Borer, A. Sengul, B. J. Nelson, *Ieee T Robot* **2010**, 26, 1006.

[46] S. Schuerle, S. Erni, M. Flink, B. E. Kratochvil, B. J. Nelson, *Ieee T Magn* **2013**, 49, 321.

[47] L. Zhang, J. J. Abbott, L. Dong, B. E. Kratochvil, D. Bell, B. J. Nelson, *Appl Phys Lett* **2009**, 94, 064107.

[48] E. Gultepe, J. S. Randhawa, S. Kadam, S. Yamanaka, F. M. Selaru, E. J. Shin, A. N. Kalloo, D. H. Gracias, *Adv Mater* **2013**, 25, 514.

[49] C. Elbuken, M. B. Khamesee, M. Yavuz, *Ieee-Asme T Mech* **2009**, 14, 434.

[50] S. Martel, 2006 28th *Annual International Conference of the IEEE Engineering in Medicine and Biology Society*, Vols 1-15 **2006**, 5727.

[51] S. N. Tabatabaei, J. Lapointe, S. Martel, *Adv Robotics* **2011**, 25, 1049.

[52] S. Chaterji, I. K. Kwon, K. Park, *Prog Polym Sci* **2007**, 32, 1083.

[53] S. Mitragotri, J. Lahann, *Nat Mater* **2009**, 8, 15.

[54] G. Reich, *Adv Drug Deliver Rev* **2005**, 57, 1109.

[55] J. H. Park, G. von Maltzahn, L. L. Ong, A. Centrone, T. A. Hatton, E. Ruoslahti, S. N. Bhatia, M. J. Sailor, *Adv Mater* **2010**, 22, 880.

[56] T. R. Kuo, V. A. Hovhannisyan, Y. C. Chao, S. L. Chao, S. J. Chiang, S. J. Lin, C. Y. Dong, C. C. Chen, *J Am Chem Soc* **2010**, 132, 14163; W. S. Kuo, C. N. Chang, Y. T. Chang, M. H. Yang, Y. H. Chien, S. J. Chen, C. S. Yeh, *Angew Chem Int Ed Engl* **2010**, 49, 2711.

[57] N. W. Kam, M. O'Connell, J. A. Wisdom, H. Dai, *Proc Natl Acad Sci U S A* **2005**, 102, 11600.

[58] N. I. Kovtyukhova, P. J. Ollivier, B. R. Martin, T. E. Mallouk, S. A. Chizhik, E. V. Buzaneva, A. D. Gorchinskiy, *Chem Mater* **1999**, 11, 771.

[59] C. Peters, S. Fusco, Y. Li, S. Kuhne, B. J. Nelson, C. Hierold, *26th European Conference on Solid-State Transducers, Eurosensor 2012* **2012**, 47, 1219.

[60] D. C. Marcano, D. V. Kosynkin, J. M. Berlin, A. Sinitskii, Z. Z. Sun, A. Slesarev, L. B. Alemany, W. Lu, J. M. Tour, *Acs Nano* **2010**, 4, 4806.

[61] J. Chen, B. Yao, C. Li, G. Shi, *Carbon* **2013**, 64, 225.

[62] E. Y. Choi, T. H. Han, J. H. Hong, J. E. Kim, S. H. Lee, H. W. Kim, S. O. Kim, *J Mater Chem* **2010**, 20, 1907.

[63] X. M. Sun, Z. Liu, K. Welsher, J. T. Robinson, A. Goodwin, S. Zaric, H. J. Dai, *Nano Res* **2008**, 1, 203.

[64] C. Holtze, A. C. Rowat, J. J. Agresti, J. B. Hutchison, F. E. Angile, C. H. J. Schmitz, S. Koster, H. Duan, K. J. Humphry, R. A. Scanga, J. S. Johnson, D. Pisignano, D. A. Weitz, *Lab Chip* **2008**, 8, 1632; S. Koster, F. E. Angile, H. Duan, J. J. Agresti, A. Wintner, C. Schmitz, A. C. Rowat, C. A. Merten, D. Pisignano, A. D. Griffiths, D. A. Weitz, *Lab Chip* **2008**, 8, 1110.

[65] P. Pouponneau, J. C. Leroux, G. Soulez, L. Gaboury, S. Martel, *Biomaterials* **2011**, 32, 3481.

[66] M. Jamal, *Adv Healthc Mater* **2013**, 2, 1066.

[67] H. Feil, Y. H. Bae, J. Feijen, S. W. Kim, *Macromolecules* 1993, 26, 2496.

[68] C. W. Lo, D. F. Zhu, H. R. Jiang, *Soft Matter* **2011**, 7, 5604.

[69] C. H. Zhu, Y. Lu, J. Peng, J. F. Chen, S. H. Yu, *Adv Funct Mater* **2012**, 22, 4017; H. Bai, C. Li, X. L. Wang, G. Q. Shi, *Chem Commun* **2010**, 46, 2376; C.-H. Zhu, Y. Lu, J. Peng, J.-F. Chen, S.-H. Yu, *Adv Funct Mater* **2012**, 22, 4016.

[70] J. Z. Shang, L. Ma, J. W. Li, W. Ai, T. Yu, G. G. Gurzadyan, *Sci Rep-Uk* **2012**, 2.

[71] D. Lee, J. Seo, X. Zhu, J. Lee, H. J. Shin, J. M. Cole, T. H. Shin, J. Lee, H. Lee, H. B. Su, *Sci Rep-Uk* **2013**, 3.

[72] A. Santamato, V. Solfrizzi, F. Panza, *Phys Ther* **2009**, 89, 999.

[73] J. T. Robinson, S. M. Tabakman, Y. Liang, H. Wang, H. S. Casalongue, D. Vinh, H. Dai, *J Am Chem Soc* **2011**, 133, 6825.

[74] M. Ebara, J. M. Hoffman, P. S. Stayton, A. S. Hoffman, *Radiat Phys Chem* 2007, 76, 1409; M. E. Nash, D. Healy, W. M. Carroll, C. Elvira, Y. A. Rochev, *J Mater Chem* **2012**, 22, 19376.

[75] J. F. Betz, Y. Cheng, C. Y. Tsao, A. Zargar, H. C. Wu, X. L. Luo, G. F. Payne, W. E. Bentleyad, G. W. Rubloff, *Lab Chip* **2013**, 13, 1854; L. Wang, J. Shansky, C. Borselli, D. Mooney, H. Vandenburgh, *Tissue Eng Pt A* **2012**, 18, 2000; X. H. Zhao, J. Kim, C. A. Cezar, N. Huebsch, K. Lee, K. Bouhadir, D. J. Mooney, *P Natl Acad Sci USA* **2011**, 108, 67.

[76] G. G. d'Ayala, M. Malinconico, P. Laurienzo, *Molecules* **2008**, 13, 2069.

[77] J. B. Mathieu, S. Martel, *J Appl Phys* **2009**, 106; S. H. Kim, J. Y. Sim, J. M. Lim, S. M. Yang, *Angew Chem Int Edit* **2010**, 49, 3786.

CHAPTER 5

And all this science, I don't understand

It's just my job five days a week

A rocket man, a rocket man

Rocket Man-Elton John (1972)

Towards the modeling of hydrogel bilayer actuation

5.1 Chapter overview

Hydrogel bilayer actuation is often based on the application of a homogeneous stimulus (swelling, temperature or NIR light, for example) to an inhomogeneous material. Researchers have been able to achieve different 3D shapes by conjugating two hydrogel layers with different volumetric change, and diversifying their mutual orientation [1, 2].

The system offers two levels of control of the desired final configuration:

- The first level is the tuning of the properties of the two materials. An advantage of acrylic hydrogel systems, such as the ones presented here, is the possibility to easily set their physicochemical properties during the synthesis process in order to achieve the desired values of stiffness, swelling, and interaction with the environment (degradation, or diffusion of substances).

- The second level is the geometrical combination of the two layers. The thickness, the mutual orientation, the presence of hinges, and the initial 2D shape are all contributing factors, as can be seen in the works of Stoychev et al. [3, 4] or Jamal et al. [5].

Evaluating and understanding the influence of each material or geometrical parameter is, therefore, a crucial first step in designing and modelling the behavior of these actuation systems.

Here, we propose the results of the characterization studies performed on hydrogels used to build the bilayer systems seen in chapter 4 for drug and cell delivery. The chapter starts with a brief overview on the synthesis and

structure of acrylic hydrogels with a special attention on the main theories used to describe their network and properties. A review about the common methods to characterize hydrogel swelling and mechanical properties is then presented.

The state of the art on the modelling of bilayers is also part of this chapter. The analytical model of thermal bending of bilayers originally developed by Timoshenko [6] is analyzed together with a series of numerical approaches.

Following that, the chemical, swelling, and mechanical properties of NIPAAM-AAM-PEGDA 85.15.03 (the three numbers define the molar ratio between the monomer and the crosslinker quantity in percentage), and PEGDA are experimentally defined. FTIR was used to chemically characterize the two hydrogels. Gravimetric and optical measurements were performed to study the kinetics of swelling, the influence of the different chemical components on this parameter, and the influence of nanoparticles and interpenetration processes. The data obtained were also used to define those values that, according to theory, fully represent a polymer gel: the polymer volume fraction in the swollen state, the molecular weight of the polymer chains between two crosslinks, and the mesh size. Mechanical characterization of the materials was performed by rheological measurements, to quantitate the inherent elastic behavior of the materials. Uniaxial tensile tests were also performed.

We completed the experimental analysis with a visual quantitative study on different rectangular bilayers produced by photolithography. The features were produced with different initial thicknesses of the two layers, and their geometry and radius of curvatures were measured at room temperature and at 43°C.

The obtained data were introduced in the Timoshenko formula for bending of bilayer thermostats. The deviation between the theory and the experimental results were analyzed, considering the original assumptions and evaluating possible sources of errors.

Alternatively, the data were used to support an FEM based model that could better approximate the final configuration. This part of the work will help future analysis on bilayers and provide material for the improvement of the full experimental setup.

5.2. Synthesis and characterization of acrylic hydrogel structures

5.2.1 Synthesis and physical structure

Hydrogels are hydrophilic polymer networks, which are mainly characterized by their ability to absorb an amount of water thousands of times more than their dry weight. This is primarily due to the presence of hydrophilic functional groups attached to a polymer backbone, while the resistance to dissolution is ensured by the presence of cross-links between network chains [7]. A large range of polymer compositions has been used to fabricate hydrogels, including natural materials, synthetic ones, and combinations thereof [8]. Synthetic acrylic hydrogels are the most commonly utilized, due to the relative ease of controlling and tuning their properties.

A common synthetic route is based on a free-radical cross-linking polymerization, which implies the formation of radical molecules, their attachment to a monomer and the propagation of the phenomena until spontaneous termination [9] (figure 5.1a). Among the different ways to start the reaction (thermal decomposition, redox reactions, plasma, sonication, electrochemical electrolysis), photo polymerization offers spatial and temporal control, fast curing rates, minimal heat production[10], and the possibility of performing *in situ* polymerization. This is highly desirable for different biomedical applications or molding processes. UV photopolymerization generally uses a photoinitiator that has high absorption at a specific wavelength of light to produce radical initiating species. In the case of acrylic hydrogels the photoinitiator is dissolved in the hydrogel precursor solution together with the chosen monomers, a solvent, and a

crosslinker. Upon exposure to light, a bulk polymerization process allows the formation of chains by propagation of the radical among the molecules containing an accessible carbon-carbon double bond [11].

The resulting hydrogels exhibit properties defined by the materials involved in the polymerization process and by their relative concentrations. Materials include the monomers, the crosslinker, the photoinitiator, and the solvent (figure 5.1b and 5.1c). The quantity of photoinitiator, for example, defines the number of radicals that are formed upon exposure, and therefore the number of chains that are contemporarily growing. By increasing this parameter, smaller chains form and entangle, thus creating a brittle macrostructure. The solvent used to dissolve the solid monomers and photoinitiator dilutes and increases the physical distance between the different molecules into the precursor solution, thus decreasing the rigidity of the network. The monomers and their functional groups define the affinity to water and other substances and the response of the full matrix to different stimuli such as pH or temperature. Finally, the degree of crosslinking determines the connections between the different chains and therefore the rigidity of the networks and mainly the mechanical properties. These properties are strictly interdependent. For example, a hydrogel that possesses a high degree of swelling will certainly have poor mechanical properties, due to the massive water content. Conversely, a very stiff material will not be able to store a lot of liquids inside its polymer networks.

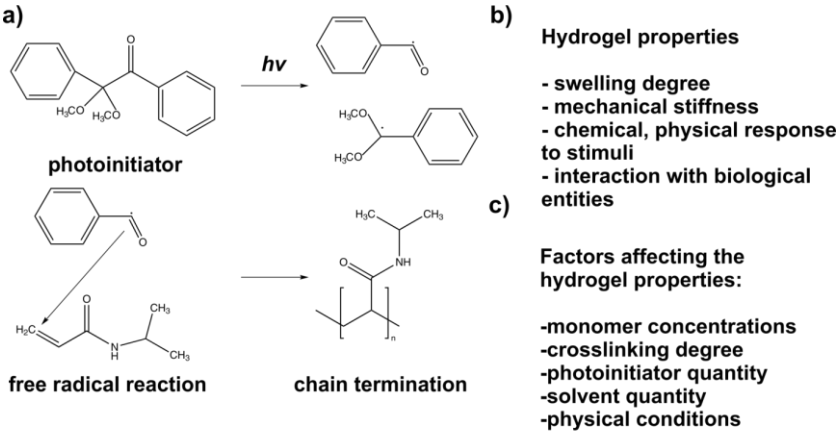

Figure 5.1. *a) Free radical polymerization mechanism. Starting from the bond cleavage of photoinitiator, free radicals keep forming and propagating, eventually leading to a chain. b) and c) The synthesis process defines the main properties of the hydrogel.*

Three important parameters have been identified as essential to define the structure of polymer networks:

- the polymer volume fraction in the swollen state ($V_{2,s}$), which is a measurement of the fluid retained by the hydrogel. It is defined by the ratio between the volume of the polymer V_p and the volume of the swollen gel V_{gel}, or as the reciprocal of the volume swelling ratio *VSR*:

$$V_{2,s} = \frac{V_p}{V_{gel}} = VSR^{-1} \tag{5.1}$$

- The number average molecular weight between cross-links, M_c, which can be related theoretically to the degree of crosslinking, *X*:

$$M_c = \frac{M_o}{2X} \quad (5.2)$$

where M_o is the molecular weight of the repeating unit of the polymer. Swelling experiments can be again used to define this parameter.

- The network mesh size, ξ, which is indicative of the distance between consecutive junctions, cross-links or tie points.

These parameters are determined based on two prominent theoretical treatments, equilibrium swelling theory and rubber elasticity theory [12].

5.2.2 Equilibrium swelling theory

In a crosslinked polymer material, the solvent absorption leads to the expansion of the network. This swelling is possible due to the elastic stretching of the polymer chain fragments (strands) between the crosslinking points. The stretching of the chain fragments increases their elastic retroactive force, which counteracts the network's expansion. The balance of these two opposing contributions governs the equilibrium volume of the polymer network. This is analytically described by Flory Rehner theory [13] and Gibbs free energy equilibrium:

$$\Delta G_{total} = \Delta G_{elastic} + \Delta G_{mixing} + \Delta G_{ionic} \quad (5.3)$$

Here, ΔG_{mixing} is related to the compatibility between the polymer and the solvent and is often expressed as the polymer-solvent interaction parameter, χ_1. Differentiation of equation 5.3, with respect to the number of solvent molecules results in an expression in terms of chemical potentials. At equilibrium zero net chemical potential is observed and this equates the elastic and mixing potentials. An expression can then be derived for the

determination of the molecular weight between two adjacent crosslinks, prepared in the presence of a solvent [14].

$$\frac{1}{M_c} = \frac{2}{M_n} - \frac{\left(\frac{v}{V_1}\right)[\ln(1-v_{2,s})+v_{2,s}+\chi_1(v_{2,s})^2]}{v_{2,r}[\left(\frac{v_{2,s}}{v_{2,r}}\right)^{\frac{1}{3}}-\frac{v_{2,s}}{2v_{2,r}}]} \quad (5.4)$$

Here, M_n is the average molecular weight of the polymer chains prepared in the absence of crosslinks, v is the specific volume of the polymer, V_1 is the molar volume of water, $V_{2,r}$ is the polymer volume fraction in the relaxed state, which is defined as the state of the polymer after polymerization and before swelling. Adaptations of this formula can also be found for ionic hydrogels where ionic strength is taken into account [15].

5.2.3 Rubber elasticity

The parameters related to the elastic potential and the mixing potential can be determined from the rubber elasticity theory [16]. This theory, originally developed for vulcanized rubber, was adapted to hydrogels, due to the similarity of the response of the two systems to applied stress. Again, this can be correlated to the molecular weight between crosslinks by the following equation:

$$\tau = \frac{\rho RT}{M_c}\left(1-\frac{2M_c}{M_n}\right)\left(\alpha-\frac{1}{a^2}\right)\left(\frac{v_{2,s}}{v_{2,r}}\right)^{\frac{1}{3}} \quad (5.5)$$

where τ is the stress applied to the polymer sample, ρ the density of the polymer, R the universal gas constant, T is the absolute temperature, M_c the desired molecular weight between crosslinks.

M_c can be strictly correlated to the mesh size of a hydrogel. This parameter defines the space between macromolecular chains or alternatively the pores of the network. The definition of the mesh size passes through the correlation length ξ, which is the linear distance between two adjacent crosslinks:

$$\xi = \alpha (r^2)^{\frac{1}{2}} \tag{5.6}$$

Here α is the elongation ratio of the polymer chains in every direction, and $(r2)^{1/2}$ is the root mean square of the end-to-end distance of the polymer chains between two neighboring crosslinks. The elongation ratio is related to the swelling through the polymer volume fraction $v_{2,s}$:

$$\alpha = v_{2,s}^{-\frac{1}{3}} \tag{5.7}$$

The second term in equation 5.6 can be calculated using the Flory characteristic ratio, C_n, the length of polymer backbone bonds (for vinyl polymer is 1.54 Å) and N, the number of links per chain that can be calculated as:

$$(r^2)^{\frac{1}{2}} = l(C_n N)^{\frac{1}{2}} \tag{5.8}$$

$$N = \frac{2\,M_c}{M_r} \tag{5.9}$$

M_r is the molecular weight of the repeating units of which the polymer chain is composed.

Mechanical tests and swelling measurements allow the calculation of the parameters defining the molecular structure of a hydrogel. This is strongly

related to the crosslinking degree of the polymer network, which can be due to a number of factors, such as covalent bonding, entanglements, hydrogel bonding, ionic bonding, etc. Similarly, the quantity of crosslinks influences the swelling and deswelling kinetics of polymer networks.

5.2.4 Swelling kinetics of hydrogel networks

Swelling is the dynamic process of transition from a glassy or partially rubbery state to a relaxed rubbery condition. Except for hydrogels with very large pores, where convection could play a role, this process is mainly driven by diffusion. Computational analysis utilizes Fick's law to quantify the concentration dependent movement of solvent into the gel:

$$\frac{dC_i}{dt} = \nabla(D(C_i)\nabla C_i \tag{5.10}$$

where D is the concentration-dependent diffusion coefficient of the species i in the gel. When an initial glassy hydrophilic polymer is placed in water, the molecules of the solvent begin to diffuse into the glassy region with a defined front, which moves inward at a velocity u. The molecules cause stress to the glassy system and an increase of the radius of gyration of the polymer molecules, which is macroscopically seen as swelling. Depending on the characteristic of the polymer, two main categories can arise [17]:

- Fickian, or case I transport, which appears when the glass transition temperature (T_g) of the polymer is well below the medium temperature. In this case, the polymer chains have high mobility, and the water penetrates easily in the rubber network. In slab samples, case I diffusion is accompanied by a linear increase of the

polymer weight gain (mass uptake) as a function of square root of sorption time.

- Non-Fickian diffusion process, which appears when the T_g is well above the experimental temperature. In this situation, the chain relaxation influences the diffusion. Case II transport is characterized by a rate of mass uptake that is directly proportional to time. Anomalous transport is observed when diffusion and relaxation rates are comparable.

A mathematical law can be used to describe all these behaviors, as proposed by Korsmeyer et al [18]:

$$\frac{M_t}{M_\infty} = kt^n \tag{5.11}$$

The constant *k* and *n* are characteristics of the solvent-polymer systems. The diffusion exponent is related to the transport mechanism (table 5.1), and assume slight different values depending on the geometries [19, 20]. The same authors specified that this law is able to model a maximum of 60% of the entire phenomena. Better models were then developed to cover all the kinetics (Berens-Hopfenberg model [21]) and to differentiate the relaxation from diffusion (Peppas model [22]).

Release exponent (n)	Solute transport mechanism	Rate as a function of time
0.5	Fickian diffusion, Case I	$t^{-0.5}$
0.5<n<1.0	Anomalous transport	t^{n-1}
1	Case II transport	t
n>1	Super case II transport	t^{n-1}

Table 5.1. *Interpretation of swelling mechanisms in polymeric films based on the model of Korsmeyer and Peppas.*

The short time approximation of these models can be used to define the diffusion coefficient of water (or any other solvent) into the polymer matrix.

Similarly, the theory of Tanaka and Fillmore [23] attempts to explain the deformation of the network caused by solvent diffusion. The linear formulation, presented in 1979, describes the spatial and temporal displacement $u(r, t)$ of a point in a spherical gel of radius r from a swollen state in the following way:

$$\frac{\partial u}{\partial t} = D \frac{\partial}{\partial r}\left\{\frac{1}{r^2}\left[\frac{\partial}{\partial r}(r^2 u)\right]\right\} \tag{5.12}$$

$$D=\frac{(K+\frac{4\mu}{3})}{f} \tag{5.13}$$

where D is the diffusion coefficient, K and μ are the bulk and shear modulus of the polymer network alone and f the friction coefficient between the network and the fluid medium.

The authors proved experimentally a scaling law, which defines the time of swelling τ as a function of the characteristic length L of the gel:

$$\tau = \frac{L^2}{D} \tag{5.14}$$

Tanaka theory fails to capture some physical phenomena accompanying the swelling and to confirm some significant experimental results [24]. In parallel, a linear theory was adapted from Biot's study of soil consolidation to describe the deformation of a gel as if it were a continuum. The theory proposed by Scherer et al. [25] allows the determination of the stress-strain relation by knowing the pore pressure (a volumetric chemical potential index, similar to the water potential in plant physiology), the shear modulus G, and the Poisson's ratio v of the network:

$$\sigma_{ij} = 2G\left(\varepsilon_{ij} + \frac{\nu}{1-2\nu}\varepsilon_{kk}\delta_{ij}\right) - \frac{\mu-\mu_0}{\Omega}\delta_{ij} \tag{5.15}$$

where δ_{ij}=0 when i≠j, ε_{kk} is the volumetric strain, Ω is the volume per solvent molecule and $\frac{\mu-\mu_0}{\Omega}$ is the pore pressure.

By considering small strain displacement, equation 5.15 can be rewritten as:

$$G\nabla^2 u_i + \frac{G}{1-2\nu}\varepsilon_i + p_i = 0 \tag{5.16}$$

where u_i are the gel displacements. Darcy's law can be used to relate the flux J of the gel to the pore pressure gradient:

$$J_i = \frac{D_p p_i}{\eta} \tag{5.17}$$

where D is the permeability of the network and η the viscosity of the gel liquid. Using the mass balance for the pore liquid, introduced by Biot, one can write:

$$D_c \nabla^2 \varepsilon = \frac{\partial \varepsilon}{\partial t} \tag{5.18}$$

$$D_c = \frac{D_p E_L}{\eta} \tag{5.19}$$

$$E_L = \frac{2G(1-2\nu)}{1-2\nu} \tag{5.20}$$

where E_L is the longitudinal elastic modulus, D_c the cooperative diffusion coefficient. Equations 5.16 and 5.18, with the appropriate initial conditions, define completely the quasi-static deformation of the elastic gel [26, 27].

5.2.5 Characterization methods of hydrogel properties

Hydrogel materials have been characterized in terms of:

- Chemical analysis
- Biocompatibility tests
- Morphological properties
- Swelling and diffusion properties
- Mechanical properties

The presence of specific functional groups and the quantity of crosslinking play a crucial role in the definition of all these areas. A common way to determine these data is to use different spectroscopic techniques based on infrared or UV-visible light, nuclear magnetic resonance (NMR), or mass spectrometry. FTIR detects the specific chemical groups in the material by exciting them at a particular wavelength and recording the stretching or bonding vibrations [28]. Similar techniques are based on attenuated total reflectance (ATR). X-ray diffraction (XRD) is used to determine the crystalline nature of substances [29] and to define the amorphous/crystalline ratio in the final compound. UV-VIS spectroscopy can provide information on the gelation level of the material as well as on the presence of impurities or composites, and on the phase transition of responsive materials. NMR allows obtaining the detailed information about morphology, molecular organization, specific interactions, and internal mobility of gels [30].

Biocompatibility can be considered an intrinsic property of hydrogels once the toxic un-reacted materials of the synthesis process have been rinsed away.

This is due to the massive presence of water, which provides chemical and physical compatibility with the host biological systems. *In vitro* cell culture tests are often used as initial tests to evaluate the cytotoxicity of the synthesized materials. These tests can be performed either by direct contact between the cells and the hydrogels, or by elution (incubation of the cells with a physiological solution previously in contact with the material). *In vitro* tests can also be carried out to evaluate the anti-fouling properties of the synthetic materials. Serum absorption tests can be performed as well as contact angle tests with blood (sessile drop method). Hydrophilicity of the material influences the adsorption of blood and cells, as has been demonstrated by dynamic platforms based on NIPAAM [31] [32].

In vivo tests in animals evaluate the toxicity of the synthetic materials in more complex dynamics. These tests involve the evaluation of the biodegradability of the polymers and the effects of the products of degradation on the biological environment.

Scanning electron microscopy (SEM) and Cryo- and environmental-SEM procedures [33] allow the imaging of the polymer network morphology in its hydrated state, thus revealing the shape, size, and distribution of pores in the matrix. Laser scanning confocal microscopy is used for the same purpose [34]. Surface topography is normally investigated by atomic force microscopy (AFM) or by optical profilometry, with specific attention on the change of the features between hydrogels and xerogels (dried networks).

Swelling measurements constitute the main area of investigation of hydrogel materials. Characterization is usually performed in a gravimetric way by monitoring the change of weight of samples upon immersion in water. The same principle can be used to study the stimuli-responsive behavior of

the material [35] and to evaluate the actuation kinetics of hydrogel based components [36]. Important information about the structure of the network, such as mesh size, the average molecular weight between crosslinks, and the diffusion coefficient are normally evaluated from swelling measurements [37-39].

Parallel to these studies, drug release kinetics of differently sized and shaped hydrogels is often an object of investigation. Different models have been proposed to cover all the possible mechanisms of release [40] and complex active systems involving nanocomposites have been employed to control this phenomenon [41].

Several methods are used to examine the mechanical properties of hydrogels, which constitute an essential aspect in various biomedical applications, such as tissue repair, replacement, and drug delivery. Tensile testing or strip extensiometry, involving the application of a tensile force to strips of material held between two grips, are used to obtain a stress-strain chart. These tests can be used to evaluate the elastic or viscoelastic properties of hydrogel materials, by elongating the material strip to a particular length, and examining the stress-relaxation response over time at a constant strain. The destructive nature of the test and the difficulty to block hydrogel samples constitute the main drawbacks for this method. On the other hand, compression tests allow the use of different geometries but suffer from the same limitations of the previous ones. Lately, indentation has become increasingly popular due to the possibility to characterize the micrometer sized features of the polymer network. Indentation exploits a shaped indenter connected to a force transducer to record the force required to achieve a certain depth into the tissue. Online measurements of the elastic and viscoelastic properties are possible, and data can be fit to find important

information about diffusivity [26, 42]. However, variations in the results are introduced due to different geometries of the indenter [43].

Rheology has often been employed to monitor the gelation process and the change from a viscoelastic to a mainly elastic material of polymer networks. The storage modulus (G') and the loss modulus (G'') measured upon a range of frequencies in oscillation experiments provide correlation between the kinetics of the sol-gel transition and the resulting mechanical properties [44]. Little work has been reported on the rheology of bulk crosslinked hydrogels. Nevertheless, these measurements are able to offer a full insight on the mechanical nature of the matrix and provide an alternative way to swelling to determine the mesh size [44, 45] and the stimuli response of the polymer network.

5.3 Modelling the bending of a hydrogel bilayer

The simulation of the bending behavior of a hydrogel bilayer exposed to a change of hydration has recently been the object of a multidirectional investigation. The literature offers analytical models adapted from the original theory of bending of metal bilayers and finite element modeling methods that take into account different boundary and material conditions. The problem should include a multiphysical approach, based on mass transport and large deformation, but is often simplified by considering only the mechanical aspect of swelling, which is an isotropic expansion. Here we propose a short review of the state of the art and the progresses made in analyzing complex bilayer geometries, associated with the design of actuators and microdevices.

5.3.1 The Timoshenko beam theory and other analytical models

Classical beam theory by Timoshenko [6] was first used to model bilayer bending under thermal expansion. The model is based on five ideal conditions:

- It is assumed that the coefficients of expansion remain constant during heating.

- The materials are both elastic.

- The beam thickness h is small compared to the radius of curvature: $h << R$.

- The curvature along the width can be neglected and deflection is only a function of the length.

- The strain throughout the bilayer is determined only geometrically by the curvature.

Let us consider two metals welded together and uniformly heated from T_0 to T. As seen in figure 5.2, the inner layer, or layer I is characterized by a thickness h_1, a Young's modulus E_1 and an expansion coefficient α_1. Similarly, the outer layer, or layer II is represented by the parameters h_2, E_2, α_2.

We consider $h=h_1+h_2$, as the total thickness of the strip

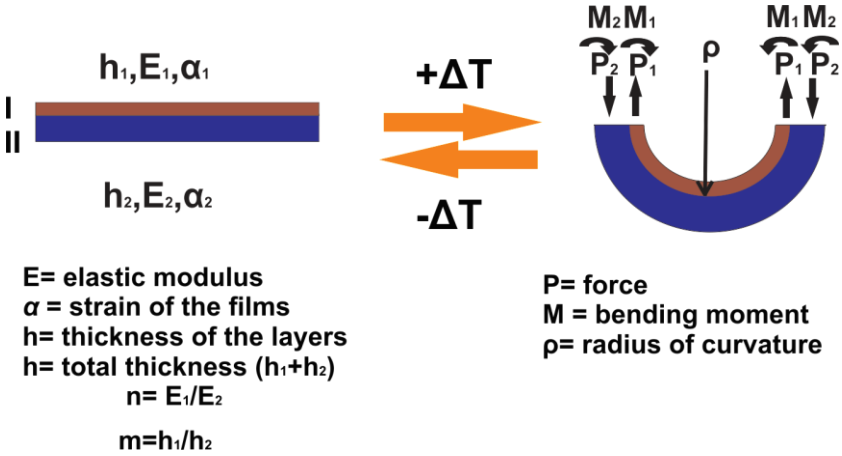

Figure 5.2. *Bending theory according to Timoshenko for bimetal thermostats. The main parameters of the analysis are listed in the figure.*

An analysis of the forces P acting on a section of the metal, bent convex down ($\alpha_2 > \alpha_1$), yields:

$$\frac{Ph}{2} = M_1 + M_2 \qquad (5.21)$$

Letting ρ being the radius of curvature of the strip, E_1I_1 and E_2I_2 the bending stiffness of layer 1 and layer 2 (with I area moment of inertia of the layer), we can then write:

$$M_1 = \frac{E_1 I_1}{\rho} \quad M_2 = \frac{E_2 I_2}{\rho} \quad \frac{Ph}{2} = \frac{E_1 I_1 + E_2 I_2}{\rho} \tag{5.22}$$

Similarly ρ and P can be calculated by considering the deformation related to the thermal expansion. For reasons of continuity, the two layers must have the same longitudinal elongation. Therefore:

$$\alpha_1(t - t_0) + \frac{P_1}{E_1 h_1} + \frac{h_1}{2\rho} = \alpha_2(t - t_0) - \frac{P_2}{E_2 h_2} - \frac{h_2}{2\rho} \tag{5.23}$$

where the first term is the temperature strain, the second the bending strain, and the third is defined as the pressure/tension strain (the signs are related to the fact that layer I is subjected to compression and layer II to tension).

By using equation 5.23, we can rewrite everything as a function of the curvature 1/ ρ:

$$\frac{1}{\rho} = \frac{(\alpha_2 - \alpha_1)(t - t_o)}{\frac{h}{2} + \frac{2(E_1 I_1 + E_2 I_2)}{h}\left(\frac{1}{E_1 I_1} + \frac{1}{E_2 I_2}\right)} \tag{5.24}$$

Or again:

$$\frac{h_1}{h_2} = m, \frac{E_1}{E_2} = n, I_1 = \frac{h_1^3}{12}, I_2 = \frac{h_2^3}{12} \tag{5.25}$$

$$\frac{1}{\rho} = \frac{6(\alpha_2 - \alpha_1)(t - t_o)(1+m)^2}{h(3(1+m)^2 + (1+mn)\left(m^2 + \frac{1}{mn}\right))} \tag{5.26}$$

Tip deflection δ can be calculated with simple trigonometric rules and starting from the radius of curvature as:

$$\delta = \frac{l^2}{8\rho} \tag{5.27}$$

The radius of curvature is inversely proportional to the film strain and is mainly dependent by variations of *m*, which represents the ratio between the thicknesses of the two layers. It is important to stress the limitations of the theory, which is applicable only for elastic deformations and does not predict the direction of folding.

Nevertheless, the analysis of Timoshenko has often been proposed to model micro actuators folding, and repeatedly used as reference for hydrogel based bilayers [1, 46]. Guan et al. [47] matched the experimental results of the folding of chitosan PEG-methacrylated bilayers with the formula of tip deflection. They calculated the Young's modulus of the swollen network by tensile tests performed on dry samples and imposed some correction factors due to the peculiarity of the materials.

Christophersen and Shapiro [48, 49] used the same mechanical approach to derive an analytical model to predict the curling of a gold/polypyrrole bilayer, upon electrochemical actuation. The formula of Timoshenko was revisited based on the fact that the properties of the polypyrrole change along the section of the bilayer, and it was expanded to include a third adhesive layer between the metal and the polymer.

Kelby et al. [50] analyzed gold/poly glycidyl-methacrylate (PGMA) bilayer objects, by experimentally measuring the swelling factor of the

polymer layer, and fitting the mechanical and geometrical data into the Timoshenko formula by nonlinear regression.

Baek et al. [51] propose self-folding PEGDA based tubes for *in vivo* sustained release of drugs. They used a formula adapted from Timoshenko theory and applied to surface coatings, to understand the mechanism of rolling, and to calculate the inner radius of the gel tubes. The authors particularly focused on the trends suggested by the formula, confirming its validity by using their experimental results on mechanical and swelling characterization.

Very recently, Palleau et al. [52] presented a series of gels, which were reversibly folding, due to electric stimuli and the controlled diffusion of cations inside the hydrated anionic gel network. The bending of the imprinted gel, due to a local increase of crosslinking, was experimentally characterized by visual imaging, by indentation and by swelling measurements. The fit between the experimental data and the theoretical trends was again only possible by introducing a correction factor, here justified to take into account the diffusion process mechanism in the gel.

This short literature review shows that the Timoshenko formula generally provides insight about the curvature of polymer-based bilayers. A perfect match between experimental data and analytical models is possible only by introducing corrective factors and revisiting the proposed assumptions.

5.3.2 FEM based models of bilayers

Aside from analytical models, numerical methods have been often used to approach the problem of instabilities and shape changes of thin hydrogel sheets during the swelling process [53]. In a similar way, recent models have taken into account the complex bending of a bilayer in three dimensions. Alben et al. [54] demonstrated that the final 3D shape of thin plates depends mainly on the development of the regions of double curvature at the edges of the 2D shape. They built an elastic model of a bilayer attached to a substrate and found the displacements minimizing the elastic energy for different actuation strains. The work also provides experimental results on the bending of polypyrrole/gold bilayers that prove the validity of the bending direction prediction. However, the model cannot cover deflections much smaller than the width of the bilayers, thus excluding phenomena like shape overlapping. Stoychev et al. monitored the rolling of thin hydrogel films [4] upon swelling, distinguishing long side, diagonal and all side rolling. A diffusion study allowed them to confirm the importance of edge detaching and adhesion forces on the preferential direction of rolling. The experimental study was supported by a FEM based simulation of the diffusion patterns, based on Fick's law, and by a thermal expansion model of two elastic materials. They used a fixed substrate as a boundary condition and they found that high levels of strain at the edges are able to drive the folding in different ways, depending on the geometry of the bilayer.

Jamal et al. [55] investigated the radius of curvature of different PEG bilayers, by changing the molecular weight of the polymer chains. The experimental results were supported by a FEM simulation of the deformation kinetics of the hydrogel structures. The model minimizes the stress defined by hyperelastic theories, and the chemical potential of the system, and uses

the shear modulus, the bulk modulus, and the Flory Huggins interaction parameters as the input values for the two materials. A good agreement was found between the simulation and the experimental results.

Very recently, work from Guo et al. [56] focused on the programmable deformation of a temperature sensitive hydrogel bilayer and modelled the mechanical behavior of the gel as a hyperelastic material. The free energy of the gel, composed of an elastic part, a mixing component (from solvent and polymer), and a chemical component, was used to derive the expression of stress to be minimized for the most probable final 3D configuration. The method showed the possibilities offered by different spatial combinations of bilayers.

5.4 Motivation: predicting the actuation of a hydrogel bilayer

Hydrogel bilayers have been recently employed as platforms for the encapsulation and release of cells and drugs [2]. Their self-folding mechanism relies on a difference in swelling and mechanical properties between the two layers, while the presence of a stimuli-sensitive layer allows external or remote control on the shape.

The design and prediction of the final shape of the polymer platform is a complex problem due to the nature of the materials. Hydrogels exhibit a union of liquid and solid properties that allow them to behave in a very different way depending on their swelling degree. Moreover, their properties can be tuned during the synthesis process, by modifying, for example, the monomer concentrations, the photoinitiator, the solvent quantity, or a combination of these parameters. Nevertheless, the prediction of the behavior of hydrogel bilayers, based on their physical and geometrical properties, represents a critical aspect that could allow significant reduction of the experimental workload.

Attempts to fit experimental data with Timoshenko's theory for bending of uniformly heated bilayer metal strips [6] (equation 5.27) were recently proposed in different polymer-metal [48] or polymer-polymer systems [47, 51]. Most of this work relied on correction factors of the materials properties or modifications of the formula, which compensated for the physical difference between metals and hydrogels.

Previous publications have proposed parametrical studies to investigate the influence of the thickness, the mechanical properties, and the expansion coefficients of the hydrogel layers on the final 3D shape [4, 5]. Some of them were supported by linear and nonlinear numerical models providing insight in the rolling mechanism of hydrogel strips [54].

Here we concentrate on a thermoresponsive double layer similar to the one recently used for the design of self-folding microrobots fabricated by photolithographic coupling of NIPAAM-AAM-PEGDA copolymer (85.15.03) and PEGDA [57]. We report a detailed characterization of the swelling and mechanical properties of the two separated layers. Hydrogels were subjected to tests of unconstrained absorption of water where the duration of the process and the final values of expansion were investigated and compared to the literature. The swelling kinetics measurements were used to extrapolate values of mesh size and molecular weight between crosslinks of the two layers, thus defining the microstructure of polymer network. Additionally, temperature dependence of the swelling expansion coefficient was also investigated for the two layers, to provide additional material for the analysis of the temperature-driven bilayer unfolding. We completed the study by showing the influence of different parameters in the equilibrium swelling ratio of the hydrogel layers. The effect of the co-monomer AAM and of the crosslinking quantity shows the flexibility of the system. Finally, we analyzed the possible drawbacks and complications derived from the used fabrication method, and we identified the interpenetration of the two layers as a possible source of uncertainty. Swelling measurements identified the possibility of having large variations from the original polymer properties.

Oscillating rheology was used to characterize the mechanical response of the two materials. Frequency sweeps were applied at defined amplitude values to monitor the viscoelastic behavior of the soft hydrogels. The results were integrated with tensile tests performed on samples cut in strips. For NIPAAM-based hydrogels, these last experiments were performed at three different temperature conditions (22°C, 33°C and 44°C) in order to provide values of material sensitivity to changes of environmental conditions.

Following the analysis of the single layers, we performed a parametrical study of the influence of the thickness ratio between the two layers on the final curvature. Different features with a rectangular shape were fabricated by photolithography [58]. Their geometry was visually evaluated at two different temperatures (22°C and 43°C). The thicknesses of the layers measured at higher temperature were assumed to be the ones in the unswollen state, as the two cases have been demonstrated to be comparable. In this way, we reduced the influence of the uncertainties related to the fabrication process. The evaluation of the width, the thicknesses, and the curvature of the bilayers in the fully swollen state, and in the collapsed state, allowed an analysis of the real expansion rates of the layers, in the final bilayer configuration, and a critical evaluation of the limitations of the proposed fabrication method. These data were also used to estimate the capability of Timoshenko's beam theory to predict the final structures' curvature.

In parallel, a FEM-based model was developed by means of commercial finite element software ABAQUS, which took into account the new expansion rates, and the other experimental values. The model offers a better approximation to the final observed bilayer curvatures.

5.5 Materials and methods

5.5.1 Materials

N-Isopropylacrylamide monomer (NIPAAM), Acrylamide (AAM), Poly(Ethyleneglycol) Diacrylate (average MW 575, PEGDA), 2,2-dimethoxy-2 phenylacetophenone (99%, DMPA), Ethyl Lactate (98%, EL), anhydrous hexane (95%) were purchased from Sigma Aldrich (USA). 1H, 1H, 2H, 2H- Perfluorodecyltrichlorosilane (PFDTCS) was purchased from ABCR (Germany. 1H,1H,2H,2H-perfluorooctanol was purchased from Alfa Aesar (USA).The main NIPAAM monomer was recrystallized after double treatment in n-hexane solution. All other chemicals were used as received. SU-8 photoresist and developer and Lift-Off Resist (LOR), used as a sacrificial layer, were purchased from Microchem (USA), while AZ 4562 photoresist and AZ 826 developer were purchased from Clariant (Germany).

5.5.2 Hydrogel fabrication

Hydrogels for the swelling and mechanical characterization were produced by UV-photopolymerization at 365 nm. NIPAAM-AAM-PEGDA hydrogels were fabricated by briefly mixing the three main components in ethyl lactate, and adding DMPA as photoinitiator. PEGDA solution was diluted in a certain quantity of ethyl lactate as well. DMPA was added as photoinitiator. The solutions were then polymerized after being poured into self-made molds or by direct photolithography. The molar ratio between different components was changed, and the resulting hydrogels were characterized by swelling experiments.

Interpenetrated polymer networks of the two layers were produced by letting the dried gels of one type swell into the other hydrogel solution. After reaching equilibrium, the swollen gels were exposed to UV and allowed to swell again in water. In this way, NIPAAM-AAM-PEGDA copolymers swollen in PEGDA solutions (NIPAAM-IPN-PEGDA) and PEGDA hydrogels swollen in NIPAAM-AAM-PEGDA copolymer solutions (PEGDA-IPN-NIPAAM) were fabricated.

The hydrogel bilayers used for the parametric study of the curvature are the result of a two-step, backside exposure, photolithographic process [58] as described previously in chapter 4. The thickness of the layers was defined using SU-8 spacers previously fabricated on the bottom silicon substrate, while the 2D features were designed on plastic foil masks (Selba S.A., Switzerland) and reproduced. The spacers varied from 1 to 40 μm in thickness. For these experiments a hydrogel solution composed of PEGDA with 3 wt% DMPA photoinitiator and 50 wt% ethyl lactate was used as the first non-swelling layer. The thermo sensitive layer was polymerized from a NIPAAM-AAM-PEGDA (molar ratio 85/15/0.3) solution, with 3 wt% DMPA photoinitiator and 70 wt% ethyl lactate After UV curing (2+4 minutes) the bilayers, attached to the mask, were released through immersion in water.

5.5.3 Chemical analysis

FTIR spectra of NIPAAM hydrogels and PEGDA samples were collected on a FTIR spectrometer (Nicolet is 10, Thermo Scientific, MA, USA). All data were recorded at room temperature in the spectral range of 4000-600 cm^{-1} by accumulating 32 scans with a resolution of 4 cm^{-1} by using dried milled particulates.

5.5.4 Swelling experiments

The swelling capacity of different hydrogels was characterized by gravimetric and optical methods. The gels (a minimum of three per type) were produced and incubated in a water bath (Julabo, Germany) at temperatures ranging from 25 to 55°C. At predefined time intervals (minimum eight hours to ensure swelling equilibrium), the samples were removed from water, carefully wiped, and their weight was recorded. The Equilibrium Swelling Ratio (*ESR*) at each temperature was defined as:

$$ESR=\frac{M_s}{M_d} \tag{5.28}$$

where M_s and M_d are the mass of the swollen hydrogel and the dried mass, respectively.

Dimensional swelling ratio was defined in a similar way as:

$$DSR= \frac{D_s}{D_d} \tag{5.29}$$

and measured by monitoring the change of the major dimensions (*D*) of the gel discs, by means of a digital camera (DNT, DigiMicroscale 2.0, Germany). From the data of swelling of the diameter and height of the gel samples, a volumetric swelling ratio was calculated in a similar way.

$$VSR=\frac{V_s}{V_d} \tag{5.30}$$

The same tools were used to perform swelling kinetics experiments on NIPAAM-AAM-PEGDA (85.15.03) and PEGDA (3wt% photoinitiator) by

monitoring the state of the gel samples until no significant change was recorded.

5.5.5 Rheological measurements

Rheological measurements were performed using a universal dynamic spectrometer (figure 5.3a, UDS 200, Anton Paar GmbH, Switzerland) with parallel plate geometry (50 mm diameter). Samples of ca. 50 mm diameter and 0.7 mm thickness were cut and constrained inside the two plates by an applied normal force of 2 N. Hydrogel skidding was avoided by the internal rough surface of the plates. An amplitude sweep (0.01-100%) was performed on every set of samples to define the linear viscoelastic range (LVR). Then, a frequency sweep from 1 to 600 Hz was performed at a defined amplitude (1% for NIPAAM hydrogels, 0.001% for PEGDA) within the LVR, taking care of maintaining the samples hydrated during and in between of experiments. The real G' and the imaginary G'' were measured, and the complex modulus G^* calculated from these data.

5.5.6 Tensile tests

The uniaxial tests were performed on a custom-made test setup (see figure 5.3b). The machine consisted of a tensile test tool with two hydraulic actuators (242 Actuator, MTS system corp, Eden Praire, MN, USA), each with 2.7 kN capacity, mounted horizontally on a steel plate, and immersed in a temperature controlled water bath. The full setup was installed on a vibration isolation table. Load cells (100 N, SMT S-type, Interface Inc., Scottsdale, AZ, USA) were applied for force measurement. Contactless measurement of the in-plane displacement field was achieved by a video extensometer system (uniDac Fast, Chemnitzer Werkstoffmechanik GmbH,

Chemnitz, Germany) consisting of a CCD camera (Pike F-100B, Allied Vision Technologies GmbH, Stadtroda, Germany) and a focusable 0.25x telecentric lens (NT55-349, Edmund Optics, GmbH, Karlsruhe, Germany).

Hydrogel samples of NIPAAM-AAM-PEGDA and PEGDA were cut in strips of defined dimensions (length, width, thickness) 50 x 10 x 2.5 mm and 25 x 5 x 0.25 mm, respectively, and were fixed to the load cells by means of custom-made clamps equipped with sandpaper. Uniaxial tensile tests were performed on a minimum of three samples per type in water at a constant speed of 2 mm/min till fracture and at 22°C. NIPAAM based hydrogels were also tested at 33°C and 43°C.

Raw data in the form of load-extension curves were converted into engineering stress-strain from the initial sample dimensions.

$$\varepsilon = \frac{L}{L_0} - 1 \tag{5.31}$$

$$\sigma = \frac{F}{A} \tag{5.32}$$

where L_0 is the initial length, F the measured force and A the cross-section of the samples. The elastic modulus was found by simple linear fitting of the resulting curve.

For the Poisson ratio calculations, the width of the sample at a given time interval was measured using the photos of the samples, taken every two seconds by the recording system. By comparing the pixel size (0.03 mm/pixel) with the change in dimensions of the layer (values analyzed every

30 seconds), an average value of lateral deformation was found and used as follows:

$$\nu = \frac{\Delta W}{\Delta L} = \frac{W - W_0}{L - L_0} \tag{5.33}$$

where W and W_0 are the cross-sectional dimensions and L and L_0 the longitudinal dimensions.

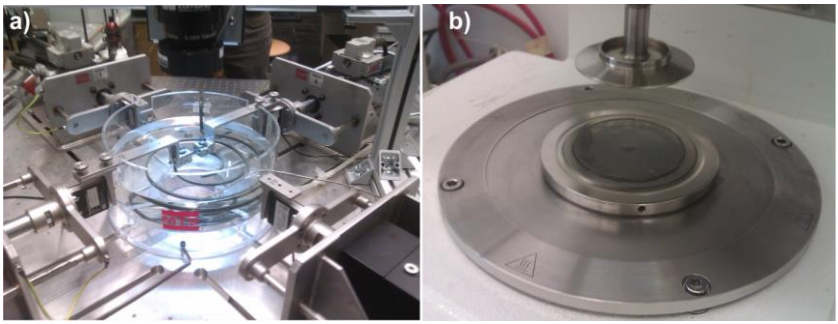

Figure 5.3*. a) Parallel plate rheometer for the dynamic mechanical analysis of hydrogel discs. b) The same materials were tested in uniaxial tensile experiments in a temperature controlled water bath by means of a biaxial test machine.*

5.5.7 In situ imaging of the bending of rectangular bilayers

A series of rectangular features (1.4 mm x 0.4 mm and 1.3 mm x 0.26 mm) were produced by photolithography, with PEGDA as the non-swelling layer, coupled with a NIPAAM-AAM-PEGDA (molar ratio 85.15.03) swelling, thermo responsive layer. The thickness of the two layers was changed by using different SU-8 spacers. The radius of curvature, side lengths and thicknesses achieved after complete swelling, at 22°C, were recorded by means of a common optical microscope (5x magnification, LEICA, USA)

and calculated from optical images by using the software ImageJ (NIH, USA). Similarly, the analysis was performed also at 43°C, which corresponded to a condition of full collapse of the NIPAAM layer. This condition was taken as reference to evaluate the initial geometrical parameters of thickness and side length of the samples. This assumption was taken to limit the uncertainty introduced by the fabrication process. The comparative visual analysis of the features at the two conditions (swollen and collapsed) was also used to estimate the real swelling ratio and expansion of the single layers in the bilayer configuration.

5.5.8 FEM simulation [1]

ABAQUS software (3DS, France) was used to model the self-folding behavior of rectangular hydrogel bilayers. The main concept behind the FEM model was the use of experimentally obtained time-dependent dimensional expansion values as input material parameters for the active and passive layer. The bilayer was modeled as the result of two isotropic linearly elastic layers attached together by a surface constraint at their interfaces. The constraint ensured equal deformation of both layers. The initial conditions of length and width were set according to the performed experiments (length 1.3 mm, width 0.26 mm and 1.4 mm, width 0.4 mm). The Poisson ratio was assumed to be 0.5 for both the materials, while the Young's moduli and the thickness of the layers were taken from experimental results. Dimensional swelling parameters taken from kinetic tests on the single layers were converted to coefficients of expansion (α_1 and α_2 for in plane and thickness direction) and first used to define the growth rates in the model. Similarly, other expansion coefficients were calculated, taking into account the constrained swelling of the layers in the bilayer configuration and the results of the experiments described in section 5.5.7. Quadratic 3D node brick

elements from the ABAQUS standard library (C3D20) were used as meshes. In order to mimic the experimental boundary conditions (the layers are attached to a substrate when they are fabricated), a user-defined subroutine was written to spatially alter α for the initial time steps. This procedure is comparable to simulate the diffusion path occurring before the layers are detached from their substrate. Bending and final curvature could be analyzed by means of the visual interface of the software.

1. The model was developed in collaboration with Gautam Munglani, Institute for Building Materials, ETH Zurich.

5.6 Results

5.6.1 FTIR analysis

Figure 5.4 presents the FTIR spectra of the two synthesized hydrogels. NIPAAM based hydrogels are characterized by a broad band appearing between 3600 and 3200 cm^{-1}, related to the N-H stretching vibrations of the secondary amide and the vibrations of the hydroxyl groups present in water. Despite the long drying process, non-freezing bound water remained attached to the polymer molecules through hydrogen bonds. The fact that the peak is quite evident is a sign of the water affinity of the copolymer. The area around 2900 cm^{-1} is typical of all organic compounds, being related to the asymmetric and symmetrical stretching of C-H groups. Peaks at 1650 cm^{-1} and 1545 cm^{-1} are assigned to the stretching vibrations of the amide I and II bonds (C-O and N-H) and overlap with the signal of unreacted vinyl bonds. However, the presence of the band of alkene groups at 1410 cm^{-1}, seems to suggest an incomplete polymerization of the compound. The area around 1380 cm^{-1} is characteristic for the vibrations of isopropyl groups, and therefore critical for a hypothetical analysis of the quantity of NIPAAM in the copolymer. A signal of the presence of PEGDA crosslinker can be seen in the peak at around 1720 cm^{-1}. This is much more visible in the PEGDA hydrogel curve, and corresponds to the C=O stretching vibrations from ester bonds. Apart from that, characteristic peaks are visible at 1098 and 1342 cm^{-1} which correspond to CO symmetric stretching and CH_2 bending, respectively. An important aspect to be noticed is the absence of a signal at

around 1620 cm^{-1}, which corresponds to the presence of C=C vinyl unreacted bonds. The result seems to indicate the complete polymerization of the monomers in the solution [59]. In the same way, the absence of a strong signal around 3500 cm^{-1} shows the limited presence of hydroxyl groups in the gel, substituted by the acrylate polymer.

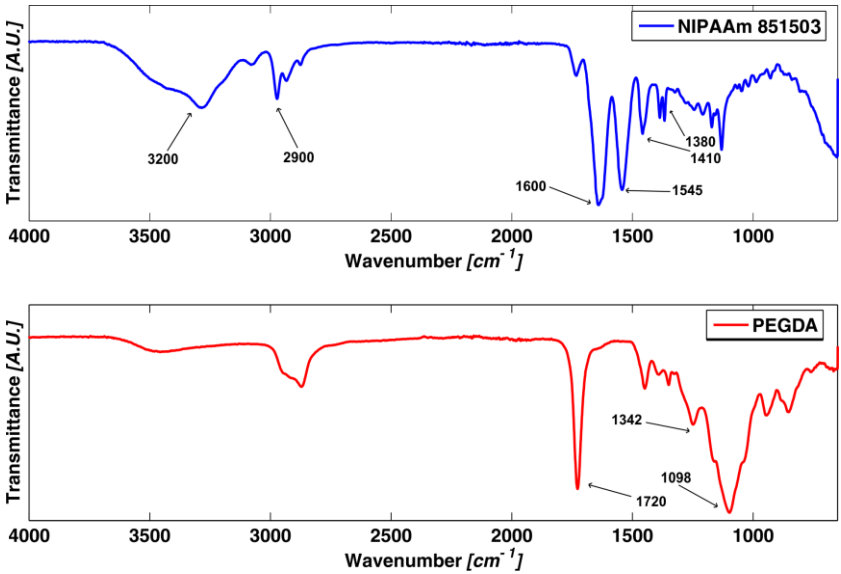

Figure 5.4. *FTIR spectra of NIPAAM and PEGDA based hydrogels, used for the bilayers.*

5.6.2 Swelling kinetics

Figure 5.5 reports the swelling induced kinetics of growth of the major dimensions of hydrogel cylindrical samples evaluated by direct visual analysis. The typical diffusion driven exponential profile was monitored until no significant increase in the dimension could be recorded by the camera. As

illustrated in figure 5.5a, (related to NIPAAM based hydrogels, 2.5 mm diameter, 2 mm height), swelling in radial and thickness directions follow a similar pattern. However, quantitative differences can be found, due to various reasons. Swelling hydrogels showed significant wrinkling and buckling zones that were hard to evaluate. These hydrogels tended to stick to the walls of the experimental cell, temporarily limiting the diffusion and growth in certain directions. Another aspect was related to the shorter diffusion path for the height than for the diameter. For this reason, the height swelling reached equilibrium faster than the other dimension, as predicted by the equation 5.14. Both the dimensions reached the same equilibrium swelling ratio of ~2.6 after approximately 24 hours. Calculation about the volume changes during swelling allowed us to estimate a water uptake on the order of 20 times the initial volume.

Figure 5.5b reports the results related to the swelling of PEGDA samples. The difference with the previous material is quite evident. These hydrogels are able to uptake an amount of water equal to ~50% of their dried weight, in an amount of time significantly smaller than one day. Their maximum dimensional swelling ratio is on the order of 40% of the NIPAAM copolymer values. The difference between the two layers is reported in table 5.2.

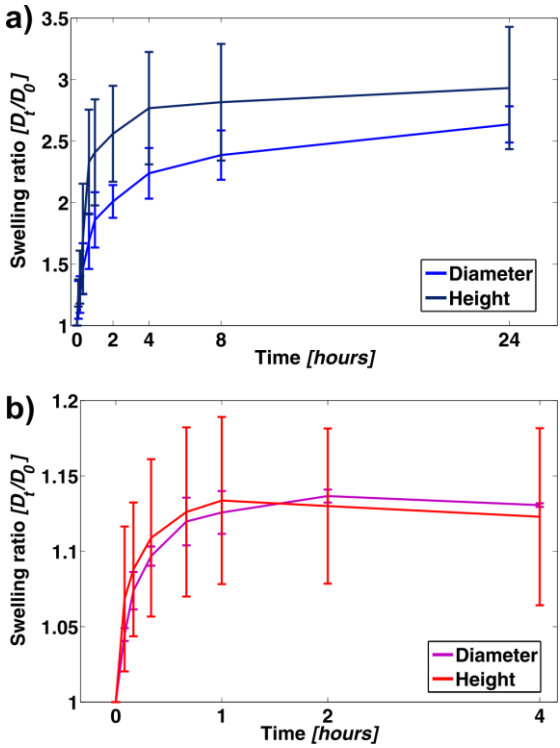

Figure 5.5*. a) Swelling kinetics of cylindrical samples of NIPAAM 85.15.03. b) Experimental results about PEGDA show a shorter swelling time, and a smaller expansion at the end of the process.*

Smaller samples were also monitored, in order to confirm the theoretical scaling law introduced by Tanaka and Fillmore [23] (equation 5.14) and commented by Peppas et al. for different gel shapes [19]. By analyzing samples with the height of 0.4 mm (1/5 of the previous value), we found a characteristic swelling time of ~ 60 minutes. This value fits perfectly with the

one predicted by the scaling law (equation 5.14, used with the experimental values gives 57.5 minutes as a result).

Polymer	NIPAAM 85.15.03	PEGDA
Dimensional equilibrium swelling ratio	2.63±0.14	1.13 ±0.00
Volume equilibrium swelling ratio	20.04 ±1.06	1.44 ±0.41
Time of swelling	~1 day	~240 minutes

Table 5.2. *Experimental data on the kinetics of swelling of cylindrical samples (diameter ~2.5 mm, height ~2 mm)*

5.6.3 Diffusion coefficients and swelling related parameters

The experimental values of the swelling volume were used to estimate the mass water uptake M_t/M_∞ at each point, by using the following equation:

$$\frac{M_t}{M_\infty} = \frac{V_t - V_o}{V_\infty - V_0} \tag{5.34}$$

Equation 5.11 was used to fit the experimental curves, and to confirm the diffusion driven mechanism of water absorption. The portion of release curve

where M_t/M_∞<0.6 was plotted in a logarithmic version against the logarithm of time, and a linear tendency was found for all the experimental set of data. *N* was found to be on the order of 0.5, by evaluating the slope of the curve. Based on this, the collective diffusion coefficients of the two polymers could be calculated following the two approximations introduced by Peppas et al. [19] and frequently reported in the literature:

$$\frac{M_t}{M_\infty} = 4\left[\frac{Dt}{\pi a^2}\right]^{1/2} \tag{5.35}$$

$$\frac{M_t}{M_\infty} = 4\left(\frac{Dt}{\pi a^2}\right)^{1/2} - \pi\left(\frac{Dt}{\pi a^2}\right) - \frac{\pi}{3}\left(\frac{Dt}{\pi a^2}\right)^{\frac{3}{2}} + 4\left(\frac{Dt}{\pi l^2}\right)^{\frac{1}{2}} - \frac{2a}{l}\left[8\left(\frac{Dt}{\pi a^2}\right) - 2\pi\left(\frac{Dt}{\pi a^2}\right)^{\frac{3}{2}} - \frac{2\pi}{3}\left(\frac{Dt}{\pi a^2}\right)^2\right] \tag{5.36}$$

Results are reported for the two polymers in the first two lines of table 5.3.

The first approximation (eq. 5.34) is able to provide a fitting to only part of the swelling curves (circa 15%), while the second equation can cover 90% of the data, and it is defined specifically for cylindrical samples [19]. For this reason it can be considered more accurate and was taken as references of the behavior of the polymer.

The data collected for the swelling kinetics were used to define the polymer volume fraction $V_{2,s}$ (equation 5.1), one of the important parameters that define an hydrogel structure. The other two parameters, namely the molar mass between two crosslinking points (equation 5.2) and the average mesh size were calculated for the NIPAAM copolymer by using the method

proposed by Fanger et al. [60]. Equation 5.37 defines the distance r between two crosslinking points in the unswollen gel as:

$$r = l\left[\frac{2Mc}{M}\right]^{\frac{1}{2}} Cn^{\frac{1}{2}} \quad (5.37)$$

where *l* is the length of a single C-C bond (0.154 nm), *Mc* is the molar mass between two crosslinking points, *M* is the molecular weight of the repeating unit (which can be calculated from the molar masses of the two monomers and their ratio in the gel), and *Cn* is the characteristic ratio, related to the disordered state of a chain of polymer (for acrylates, it is often used the value of 6.9 [38, 61]). Assuming a statistical copolymerization, M_c can be calculated for NIPAAM copolymer, according to the following equation:

$$Mc = \frac{n(NIPAAM)}{n\,(PEGDA)} M(NIPAAM) + \frac{n(AAM)}{n\,(PEGDA)} M(AAM) + M(PEGDA) \quad (5.38)$$

where *M* is the molar mass of the monomers, and *n* is the number of moles used in the formulation. Defining the values for equation 5.37 allows one to estimate the mesh size for the two polymers, by the following:

$$\xi = \frac{r}{v_{2,s}^{\frac{1}{3}}} \quad (5.39)$$

In parallel, Peppas-Merrill equation (equation 5.4) could be used to evaluate *Mc* for PEGDA hydrogels. The parameters of average molecular weight of PEG oligomers, Flory Huggin's polymer solvent interaction, and specific volume of PEGDA in its amorphous state were taken from previous publications [62] and completed with the experimental data. Results are reported in table 5.3 for the two systems. It can be seen that the highly

crosslinked short chains of the PEGDA give rise to very narrow mesh sizes one order of magnitude smaller than the NIPAAM copolymer.

Polymer	NIPAAM 85.15.03	PEGDA
Calculated water uptake	22.04	1.62
Diffusion coefficient (cm^2/sec), 15% curve approximation	$2.88x10^{-7}$	$1.23x10^{-5}$
Diffusion coefficient (cm^2/sec), 85-90% curve approximation	$5.63x10^{-8}$	$1.15x10^{-6}$
Polymer volume fraction ($v_{2,s}$)	0.05	0.7
Molar mass between two crosslinking points (g/mol)	2703,75	13
Estimated mesh size	$7.88x10^{-9}$	$3,5x10^{-10}$

Table 5.3. *Hydrogel parameters calculated from the swelling data.*

5.6.4 Temperature dependence of the swelling ratio. Influence of synthesis parameters

Figure 5.6 shows the influence of temperature on the mass swelling ratios of differently synthesized NIPAAM-co-AAM-PEGDA hydrogels. A very low percentage of crosslinking (0.3% on the number of moles in the synthesis solutions) produced polymers with high affinity for water. The incorporation of different percentages of hydrophilic AAM groups significantly affected the swelling ratio and the temperature of full collapse of the polymer (low critical solution temperature, LCST). Figure 5.6a presents a clear insight on this effect by showing a shift of the LCST from 30°C till 45°C, and a doubling of the swelling ratio at 25°C from the NIPAAM homopolymer (100.0.03), to the copolymer with the highest percentage of AAM (80.20.03). An increase of the quantity of PEGDA strongly decreased the water uptake of the resulting polymers, as can be seen in the analysis carried out on pure NIPAAM hydrogels (figure 5.6b). The dramatic change of properties is related to the short size of the PEGDA chains, which contributes to the crosslinking and to the stiffness of the resulting matrix. The values reported here, though specific for this original system, agree with the trends reported in previous publications related to NIPAAM based networks [63].

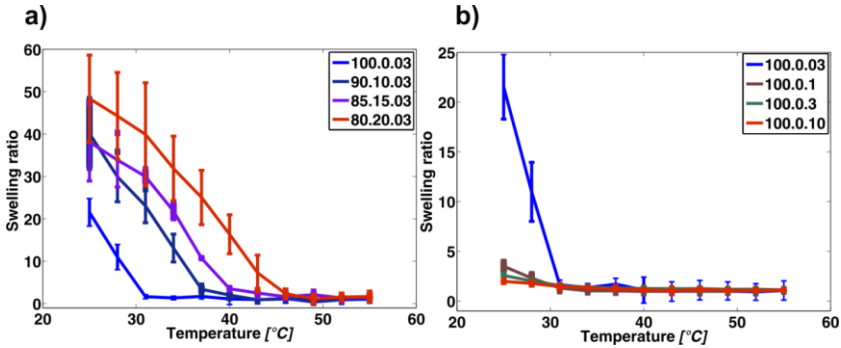

***Figure 5.6**. Temperature response of different NIPAAM based copolymers and homopolymers. The code used in the legend refers to the molar ratio between NIPAAM, AAM and PEGDA. a) The influence of AAM in the composition can be seen in the equilibrium swelling ratio and in the temperature of full collapse of the hydrogels. b) Temperature response of NIPAAM homopolymers with different crosslinking values. A slight increase of PEGDA molarity in the formulation decreases massively the swelling ratio and the water uptake of the structures.*

The difference between the polymer presented here and the one reported in chapter 4 is significant. A slight decrease of PEGDA quantity (from 0.5% to 0.3%) increased the swelling ratio by a factor of 2. The difference between these two polymers and the curve related to the PEGDA hydrogels are showed in figure 5.7. For PEGDA, a constant value of mass swelling ratio was found along the temperature range (1.98±0.07).

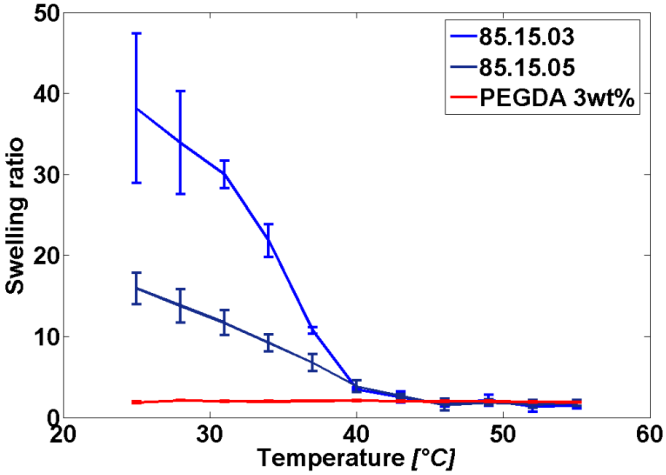

Figure 5.7. *Mass swelling ratio for the copolymers used for the hydrogel bilayers in chapter 4 (dark blue and red) and in this chapter (light blue and red).*

5.6.5 Inteprenetration: analysis of the equilibrium swelling ratio

The fabrication process of the hydrogel bilayers requires injecting the NIPAAM-AAM-PEGDA solution in the gap between the mask and the SU-8 spacer substrates after PEGDA layer has been polymerized. This procedure implies the possibility of creating interpenetrating networks, by mixing of the two solutions or by swelling of the first polymer in the second solution. The blends of these two polymers exhibit different characteristics with respect to each one of the separated polymers. Swelling tests were performed to show the possible influences of this step on the final layers. Table 5.4 shows the significant results of possible scenarios that can be encountered between NIPAAM-based and the PEGDA solutions. The list also includes the case of

directly mixing two solutions in a ratio that is related to the thickness of the two layers, as proposed in chapter 4.

Control samples (NIPAAM-AAM-PEGDA and PEGDA hydrogels) were also checked. Their response agrees with the one presented in the previous experiments (see table 5.2), showing a good repeatability of the synthesis process. A limited influence of the interpenetration can be seen for PEGDA hydrogels swollen in NIPAAM solutions and subsequently exposed to UV to create a blended matrix. The dimensional swelling ratio seems to be more sensitive than the weight related value with an increase of ca. 20% on the simple PEGDA polymer. Taking into account the fabrication steps, this scenario is most probable and slightly modifies the properties of PEGDA layers.

Conversely, NIPAAM is able to swell much more than the respective PEGDA hydrogels, even when the solvent is another polymer solution and not water. The results of the interpenetration are in this sense dramatic, with a 7-fold decrease of the weight swelling ratio and a dimensional swelling ratio reduced of the 30%. This scenario is considered very unlikely to be happening during the fabrication of the bilayers. Slightly more probable is the mixing of some remaining PEGDA solution with the NIPAAM solution during the second photolithographic step, due to not perfect drying processes. An analysis of the most pessimistic scenario (no drying or removal of PEGDA solution, and inclusion in the second solution with a ratio 4:1) shows that the resulting IPN hydrogels would have a weight swelling ratio 13 times lower than the original NIPAAM formulation and a swelling expansion of only 160% instead of 275%.

Polymer	Weight swelling ratio	Dimensional swelling ratio
PEGDA	1.60±0.12	1.07±0.10
PEGDA-IPN-NIPAAM	1.62±0.02	1.26±0.02
NIPAAM 85.15.03	48.86±7.70	2.75±0.41
NIPAAM-IPN-PEGDA	7.12±0.58	1.95±0.04
NIPAAM mixed with PEGDA (ratio 4:1)	3.64±0.09	1.60±0.03

Table 5.4*. Analysis of the equilibrium swelling ratios of interpenetrated polymer networks resulting from PEGDA and NIPAAM based polymers.*

5.6.6 Rheological studies

The viscoelastic properties of the hydrogels were characterized by oscillatory rheometry and led to the definition of the storage moduli *G'* and the loss moduli *G''*. The first one is indicative of the stored energy (elastic portion) and the second one is proportional to the dissipated energy during a cycle of deformation. The bulk hydrogels were first characterized by amplitude sweeps at a fixed frequency (10 Hz) to identify the linear viscoelastic range (LVR) of the material, the area where both the curves of the storage (*G'*) and the loss modulus (*G''*) show a constant plateau. Beyond this area corresponds to irreversible deformation and the appearance of micro

cracks in the sample. Based on these preliminary experiments, a constant amplitude value was chosen for PEGDA samples (0.001%) and NIPAAM based hydrogels (1%). A normal force (3 N) was exerted in order to maintain the contact between the fully swollen samples and the plates of the instruments, and frequency sweeps were performed. Figure 5.8 shows the near frequency independent behavior of *G'* for both the samples in the range between 1 and 600 Hz. This range corresponds to the rubber plateau, and allows us to consider these samples as "perfect gels" [45]. Moreover, *G'* exceeded *G''* over the entire range of frequency used, for NIPAAM based hydrogels (*G'/G''*>10), indicating a predominant elastic behavior, as the one of crosslinked polymers [64]. The same trend could be seen, but in a less clear way, for PEGDA samples. High standard deviations were noticed for *G'* and *G''*. However, in this case, a predominant elastic behavior could be estimated [65]. Data related to the rheological measurements and limited to the stable part of the rubber plateau (1-100 Hz) are reported in table 5.5.

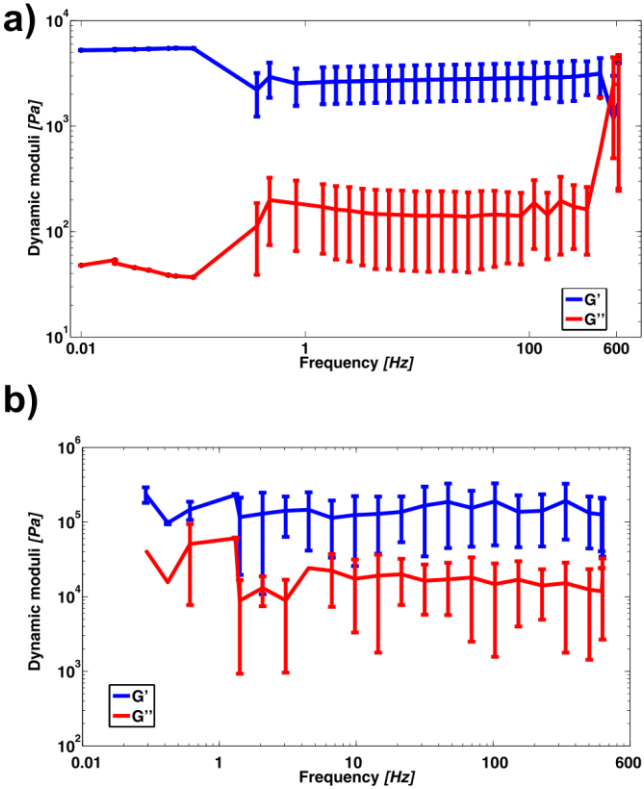

Figure 5.8. *Dynamic moduli G' and G'' of NIPAAM 85.15.03 (a) and PEGDA (b) hydrogels, as a function of frequency, between 0.01 and 600 Hz.*

Polymer	PEGDA	NIPAAM 85.15.03
G' **storage modulus (kPa)**	144.86±25.35	2.74±0.08
G'' **loss modulus (kPa)**	16.68±4.72	0.15±0.01

Table 5.5*. Experimental values of the shear modulus obtained from the rheological measurements.*

5.6.7 Tensile tests

Figure 5.9 shows some representative curves of the mechanical response of PEGDA (5.9a) and NIPAAM copolymers (5.9b) to tensile stress. For this last case, rectangular samples were tested in three different temperature conditions to analyze the effect of the induced deswelling on their behavior. A linear trend can be seen for all the samples and the conditions reported here demonstrating the completely elastic behavior at the strain rate chosen for the experiments.

PEGDA samples have a Young's modulus of ~10 MPa (table 5.6), a value in the same order of magnitude of previous works on PEG polymers [66] with short polymer chains or a high level of crosslinking. An ultimate failure stress of ~800 kPa and a maximum strain of 0.05 show the relatively high fragility of the samples.

NIPAAM copolymers exhibit a much lower stiffness and a capability to stand higher deformations before failure. The Young's modulus at room temperature (25 °C) is three orders of magnitude lower than the one of

PEGDA (5 kPa), and increases until around 20 kPa when the temperature of transition is crossed. The gels analyzed at temperature higher than 40°C did appear different in color (whiter) and in consistency than the one at room temperature. The tensile tests also showed an increase in failure stress (eight times higher at higher temperatures) but no significant difference in terms of maximum strain (0.5) confirming the extreme deformability of the material. Data were found in agreement with previous publications [67] except for the maximum strain at fracture and the change rate of Young's modulus with temperature. The samples proposed here reveal a lower strain (normal values are in the order of 1, 1.4) and only a 4-fold increase of the Young's modulus at 40°C (normally reported factors are around 10 or more). These results may be dependent on the short chains of the crosslinkers which limit the effective change of properties caused by external factors (like temperature or mechanical action). It is also worth mentioning that swelling experiments showed values of induced deformation much higher than the ones recorded during the tensile tests before fracture. These two tests correspond to different situations and physical conditions for the gels, as previously experimentally reported [68].

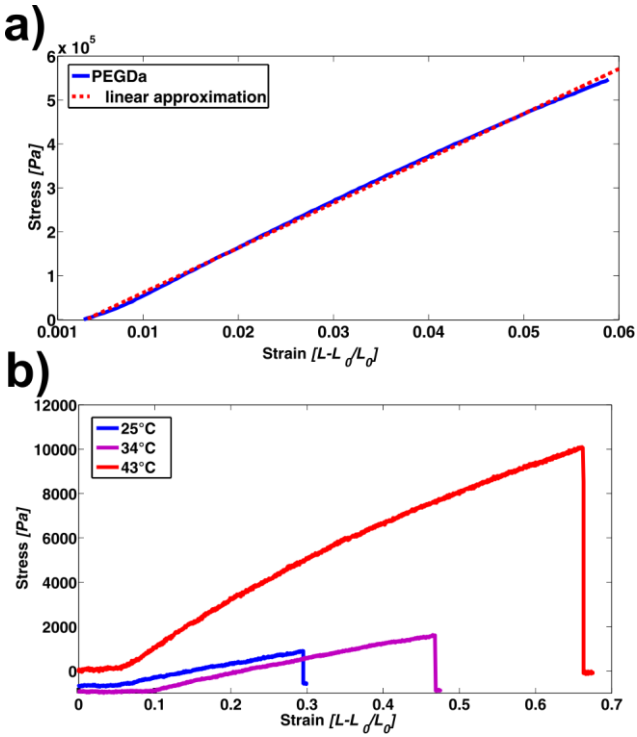

Figure 5.9. *a) Representative curve of tensile tests for PEGDA samples. The linear approximation completely fits the data, revealing a perfect elastic behavior. b) Temperature dependent stress-strain behavior of NIPAAM copolymer upon tensile loading.*

Polymer	PEGDA	NIPAAM 85.15.03 RT	NIPAAM 85.15.03 33°C	NIPAAM 85.15.03 43°C
Young's modulus (kPa)	9600.84± 3181.05	5.14 ± 0.65	6.02 ± 1.08	20.02 ± 8.12
Maximum strain (ε)	0.05 ± 0.01	0.47 ± 0.21	0.33 ± 0.12	0.49 ± 0.23
Failure stress (kPa)	811 ± 277.5	1,70 ± 0.98	0.93 ± 0.53	8 ± 2.17

Table 5.6. Experimental values related to the tensile tests measurements on PEGDA and NIPAAM copolymers.

Tensile tests were also used to provide information about the Poisson's ratio of the material. Experimental values were found on the order of v=0.20 for NIPAAM samples and 0.13 for PEGDA. The values reported are in the same range of previous publications related to hydrogel samples [26]. However, the optical measurements were often affected by a high degree of uncertainty due to the loss of tracking of the points during the deformation. For this reason, most of the following calculations and simulations were done

assuming a value of 0.5, a value often reported in the literature for hydrogel materials.

5.6.8 Visual analysis of bilayers

The double step photolithographic method described in chapter 4 was used to fabricate rectangular thermoresponsive bilayers with different final curvatures. SU-8 spacers with different thickness were used to modulate the initial geometry of the bilayers and the final curvature, as can be seen in figure 5.10.

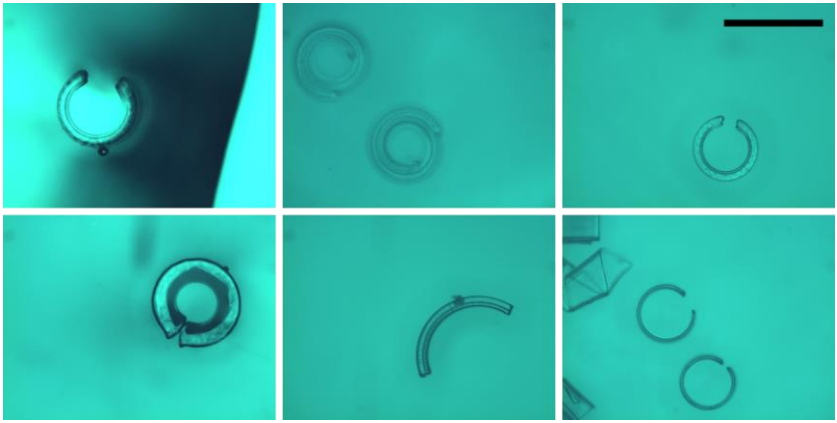

Figure 5.10. *Different examples of thickness dependent curvatures of hydrogel bilayers. The scale bar on the top right is 1 mm.*

Although not measured directly, the initial thicknesses and geometry of the two layers were assumed to approximate the ones achieved at the temperature of full collapse of the NIPAAM copolymer. For this reason, a visual analysis of the features was performed at 22°C and 43°C, assuming this second condition as the one most resembling the initial state.

Table 5.7 shows measured values of thickness of nine different samples at the two mentioned temperature conditions. Table 5.8 reports the measured values of the side lengths for the same samples. In both cases, a coefficient of expansion was found and measured. While for PEGDA these values resembled the ones found in free swelling experiments of single layers, NIPAAM copolymers appeared to swell significantly less, with similar results for in plane (side length) and out of plane (thickness) expansion. In particular, a sort of exponential trend seems to be present for both the coefficients when the data are plotted over the thickness ratio at room temperature (see figure 5.11).

Sample	NIPAAM (h2) [µm] 22°C	NIPAAM (h2) [µm] 43°C	PEGDA (h1) [µm] 22°C	PEGDA (h1) [µm] 43°C	Measured expansion coefficient NIPAAM	Measured expansion coefficient PEGDA
1	100	70	55	50	1.42	1.1
2	140	80	20	20	1.75	1
3	80	50	30	30	1.6	1
4	60	40	30	25	1.5	1.2
5	140	90	25	22	1.55	1.13
6	220	150	20	20	1.46	1
7	50	30	25	20	1.66	1.25
8	35	30	20	20	1.16	1
9	235	170	30	30	1.38	1

Table 5.7*. Evaluation of the thickness change for 9 samples of bilayers at two different temperatures, 22°C and 43°C. The coefficients of expansion are evaluated by comparing the values at room temperature and in the collapsed state.*

Sample	NIPAAM (l2) [µm] 22°C	PEGDA (l1)[µm] 22°C	Coefficient of expansion NIPAAM (Measured)	Coefficient of expansion PEGDA (Measured)
1*	1900	1500	1.35	1.07
2	2370	1400	1.82	1.07
3*	2130	1500	1.52	1.07
4	1840	1400	1.41	1.15
5	2400	1400	1.84	1.07
6	2700	1400	2.07	1.07
7	1600	1350	1.23	1.03
8	1720	1500	1.32	1.15
9	2500	1400	1.92	1.07

Table 5.8 *Evaluation of temperature dependent side length expansion for the same samples. The coefficients of expansion are measured depending on the initial mask dimension of the features. Samples with size 1400 µm x 400 µm are denoted by "*". The other samples refer to structures having dimension 1300 µm x 260 µm.*

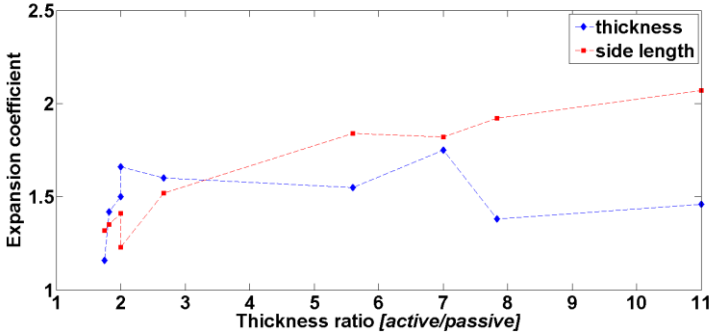

Figure 5.11*.Coefficients of expansion of the NIPAAM layer plotted over thickness ratio, as measured in the bilayer visual analysis.*

5.6.9 Analysis of curvature based on Timoshenko model

The data related to the thickness and the expansion ratios of the layers reported in table 5.7 were used to evaluate the ability of the Timoshenko formula (equation 5.26) to predict the final curvature of the bilayers. The Young's moduli resulting from the tensile tests were also used as inputs of the analysis. Table 5.9 reports the deviation of the numerical analysis from the experimental visual evaluation of the radius of curvature. In general, it can be seen that the Timoshenko analysis clearly overestimates the final configuration (with errors going from a factor of 2 to almost 50), likely due to the specific characteristics of the hydrogel layers, which do not fit into the assumptions of the mathematical model.

Sample	NIPAAM (h2) [µm]	PEGDA (h1)[µm]	Radius of curvature [µm] visual analysis	Timoshenko prediction of radius of curvature [µm]
1	70	50	360	1.57×10^4
2	80	20	230	526
3	50	30	240	3828
4	40	25	235	6804
5	90	22	230	1000
6	150	20	220	461
7	30	20	400	4400
8	30	20	270	1.13×10^4
9	170	30	250	1025

Table 5.9. *Evaluation of the radius of curvature of the bilayers structures, according to Timoshenko formula. The evaluation is based on the coefficients of expansion reported in table 5.7, and is compared to the curvature extracted from visual analysis.*

5.6.10 FEM model

An FEM based platform was established to evaluate the bending of bilayers of elastic rectangular layers exposed to large deformations, and to reproduce the various configurations found during the visual analysis (see paragraph 5.6.9). First, the model used expansion coefficients derived from the "free swelling" analysis of the single layers and combined them with their mechanical properties and the geometrical measurements (thickness and size of the rectangles) taken from the visual analysis, previously described.

The resulting simulations showed all very large deformation of the bilayers, with overlapping of the edges in all analyzed cases (see figure 5.12 for an example). The deviation from the experimental data was considered not acceptable in all cases.

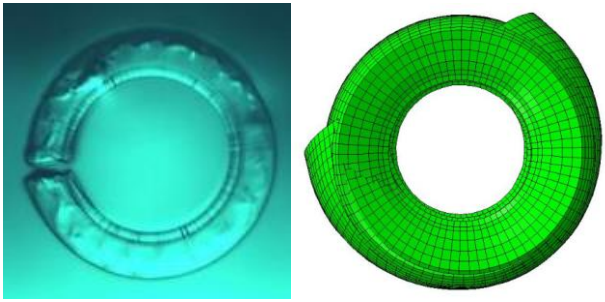

Figure 5.12. *Comparison of experimental and numerically simulated shape of one of the analyzed bilayers. The mismatch in the final curvature is evident, despite the unphysical penetration of the edges in the right figure. This was caused by absence of self-contact in the software platform.*

The time-dependence of α did not play a role in the shape of the final bending conformation of the bi-layer.

A second set of models was developed taking into consideration the "constrained" swelling measurements derived from the visual analysis reported in paragraph 5.6.8. The coefficients of expansions reported in figure 5.11 resulted in a volumetric increase that could be fit with a logarithmic trend line when plotted against the thickness ratio of the two layers. The best fit of the volume was found to be equal to equation 5.40.

$$y = 1.1616ln(x) + 1.7109 \quad (5.40)$$

The comparison of experimental and numerically calculated radii of curvature is shown in table 5.10.

Sample	Thickness ratio (NIPAAM/ PEGDA)	Experimental curvature	FEM model
1	1.27	360	370
2	4.00	230	505
3	1.67	240	210
4	1.33	235	235
5	4.09	230	630
6	7.50	220	660
7	1.50	400	530
8	1.50	270	255
9	5.67	250	720

Table 5.10. *Comparison of the curvatures found by visual analysis and by simulation for the same set of samples reported in table 5.9.*

The model was able to predict within an acceptable error degree (15%) the final curvature of all the cases with a low thickness ratio. However, as the thickness ratio increased the numerical results diverged greatly. Further analysis showed that when the thickness of bilayer was not minimal compared to the length of bending semi-axis (i.e. when the layer cannot be considered “thin” any longer), the amount of bending reduced substantially compared to the experiments, rendering the model inaccurate.

5.7 Discussion

Increasing interest in hydrogel bilayers in the last 20 years has pushed researchers to develop theoretical models to predict the final curvature and shape of different structures. A common way to approach the problem is to consider Timoshenko's theory developed for bilayer thermostats [6] and adapt it to the case of hydrogel materials [46, 47, 51]. However, this approach suffers from poor behavioral similarity between hydrogels and metals.

In particular, hydrogels exhibit a swelling induced expansion, which is temporally and spatially nonlinear, and normally it is not homogeneous between the two layers. In most cases, vinyl hydrogels are found to be elastic when completely swollen, but their behavior during swelling is not characterized, and believed to retain higher viscoelasticity. Moreover, metals are normally subjected to small deformations, while hydrogels can double their size upon water uptake.

Nevertheless, considering the fact that the existing literature predominantly uses this model as reference, we evaluated the prediction capabilities of Timoshenko's analytical model.

For this reason, the mechanical properties and swelling driven expansion rates of two hydrogel materials similar to the ones used in chapter 4, specifically PEGDA and NIPAAM-AAM-PEGDA (85.15.03), were measured. The data were also used to define some intrinsic parameters that would define the two materials, namely the mesh size, the molecular weight

between two crosslinks and the polymer volume fraction in the swollen state. These parameters are normally found by means of swelling studies [38, 39, 60], although similar information on the microstructure can be provided also by rheological studies [44].

The swelling kinetics and the ESR of the two materials were monitored by visual analysis of the expansion of cylindrical gels upon time, till completion of the process. In parallel, the measurement of the weight increase of the samples provided information on the effective water uptake. Swelling was found to be limited in the hard, crosslinked PEGDA hydrogels, with an estimated equilibrium expansion factor of 1.2 (the final dimensions were more or less 120% of the initial ones). Oppositely, NIPAAM based hydrogels were able to exhibit an expansion up to 270 % of the original size (dimensional swelling ratio).

Interestingly, it was found that the swelling kinetics of PEGDA samples was significantly faster than corresponding NIPAAM hydrogels. This result demonstrates the invalidity of the first assumption of the Timoshenko formulation (homogeneous expansion of the two layers).

The experimental results allowed us to calculate the collective diffusion coefficients for the two polymers. The most common formula for the determination of the diffusion coefficient (equation 5.35), first introduced by Ritger et al. [19] and frequently used for the characterization of drug delivery platforms [51, 69], is able to represent only the first 15-20% of the kinetic process of water uptake. Alternatively, a better approximation is given by equation 5.36, which was established for cylindrical samples and is composed by more terms of the Taylor series solving for the Fick's law. This explains the difference between the values reported in table 5.3 for the short and the

long approximation: short approximation diffusion coefficients appear higher than the second one, as they represent the first, steeper part of the diffusion kinetics curves (figure 5.5). However, the long approximation should provide a more realistic result, as the geometry and most of the swelling results are taken into account. NIPAAM copolymers' diffusion coefficient appears two orders of magnitude smaller than the value found for PEGDA, reflecting a higher affinity for water and a longer swelling time. The hydrogel parameters of polymer volume fraction, molar mass between crosslinks and mesh size are additional data that suggest the same idea of a loose, highly hydrophilic network. Similar network values are reported for macroporous gels [60]. Oppositely PEGDA data suggest a highly crosslinked network, with a low affinity for water [61] and a faster release capability.

The diffusion-based process of swelling has a scaling law related to the characteristic length of the sample (equation 5.14). This law is practically important for our purposes, to scale down the obtained values to the size of the fabricated hydrogel bilayers. We experimentally confirmed it by analyzing the swelling time of samples having different height, and we found good agreement between the experimental trends and the ones predicted by Tanaka's theory. Moreover, the formula predicts the fact that the swelling of millimeter sized bilayer structures happens in the range of a minute.

NIPAAM-AAM-PEGDA 85.15.03 is the result of a synthesis process aimed at maximizing the swelling property of the hydrogel, and at the same time having a matrix collapse at around 40°C, a value that can allow remote actuation also in the body. Figures 5.6 and 5.7 provide information about the possibility to change these two properties, swelling and LCST, by finely adjusting the amount of crosslinking and AAM molar quantity. Compared to results proposed in chapter 4, the new copolymer has a higher swelling ratio

(from 20 to more than the double), and a similar temperature of transition, resulting in a temperature dependence profile more similar to a step function. This optimization of the swelling is compensated by a higher variation during the synthesis process (see for example the values reported in table 5.4, compared to the ones that were used for figure 5.7. These results are coming from two independent measurements on different sets of same samples). Interestingly, one could modify these properties by substituting the small, stiff chains of PEGDA, with longer or more hydrophilic cross linkers [60, 70], or different comonomers [71], in order to find the desired combinations of performance. This is the main advantage of acrylic hydrogel systems for the field of micro fabrication.

Rheological and tensile tests were used to characterize the mechanical properties needed to complete Timoshenko's analysis of bending of hydrogel bilayers. Rheological studies confirmed the intrinsic elastic nature of the two layers, with values of the storage modulus steadily higher than the loss modulus for both the samples. Young's moduli were measured by means of tensile tests, and revealed a difference of three orders of magnitude between the two polymer networks. PEGDA was stiff, and with a brittle behavior, characterized by a limited rupture strain. NIPAAM copolymers exhibited a temperature dependent increase of modulus and failure stress and strain, with a strong change of behavior above 40°C. We used the measured Young's moduli as references for the definition of the parameter n in equation 5.26. The materials were then assumed to be linearly elastic, following a common simplification often used in the literature.

A visual analysis of bilayer curvatures and geometry was also performed on a limited set of samples produced with the double step photolithographic process, described in the previous chapter. Data at room temperature and at

43°C was collected to evaluate the final curvature and the initial thicknesses of the bilayers.

This was necessary, after considering the limitation of the fabrication method. Despite being able to fabricate folding structures with different materials in a simple way, the process lacks some important features. First, there is a limited precision in controlling the thickness of the layers by means of the SU-8 spacers, resulting in a mismatch between the input parameters and the effective output. Second, it allows the creation of interpenetrating layers between the two materials, thus making the prediction of the final geometry of the folding features questionable.

To limit the uncertainties introduced by the system, the geometrical values at 43°C, corresponding to a state of full collapse of the NIPAAM copolymer, were assumed to provide a close approximation of the initial state of the bilayer, and therefore of the initial thicknesses of the two layers.

The comparative analysis also allowed an estimation of the expansion coefficients of the two materials in the bilayer configuration. The values reported for thickness and side swelling are both significantly lower than the ones found for the swelling of single, unconstrained hydrogel layers, approaching instead the ones measured for IPNs of NIPAAM and PEGDA.

The geometrical and expansion values derived from this analysis, together with Young's moduli found by means of tensile tests, were used to estimate the parameters needed in the formula of Timoshenko's bending theory. The analysis revealed in all cases a large overestimation of the radius of curvatures of the folding structures. The deviation is attributed to theoretical and experimental issues. As already mentioned, the Timoshenko formula

should be rearranged to take into account the large deformation of hydrogel materials and the nonlinear swelling behavior. Aside from that, the mechanical characterization proposed reveals only one aspect of the hydrogels' behavior. Although the data for tensile and rheological studies are repeatable and valid, and agree well with similar systems, they are partial, as they evaluate the state of swollen polymer networks at specific values of strain rates or frequency ranges.

The fabrication process adds uncertainties to the full analysis. The mismatch between the planned and the effective thickness of the layers is assumed to be solved by analyzing the features at 43°C. Moreover the full characterization could be easily improved with careful use of better materials and special techniques (profilometry measurements could be performed during the fabrication). The real issue of the double-step photolithography is in any case the high probability of creation of IPN. The resulting hydrogels have been shown to behave differently from the original ones, thus limiting the predictability of the formula and the validity of the input data. The coefficients of expansions derived from the visual analysis of the bilayers agree well with the values reported in table 5.4, suggesting the impossibility of evaluating *a priori* the behavior of the bilayers, with an analysis of the single materials.

It remains a desirable alternative to have a more solid method of modeling the bending of bilayers, which could take into account more precisely the swelling and mechanical behavior of hydrogel layers. For this reason, we developed an FEM model by using the commercial platform ABAQUS. The model presents several improvements when compared to the analytical solution of Timoshenko. First, it takes into account 3D deformations, not limiting the bending in one direction. It uses the experimental data of swelling

kinetics, thus spatially and temporally following the diffusion process. In this way it defines a sort of expansion pattern, from the edges to the center of the structures, and an exponential growth of the layers. This goes into the same direction of previous publications, which stressed the importance of edges effects in the resulting configuration of bilayers [54]. These preliminary results show a better match, compared to Timoshenko's analysis of the final experimental curvatures, especially in conditions of low thickness ratio between the two layers, and therefore limited influence of the NIPAAM layer.

As reported, time-dependence of α did not significantly influenced the bending of the rectangular bi-layers. Our hypothesis is that this time-dependent property helps the bilayer to choose a bending direction when there are multiple paths which minimize energy identically. An example of this phenomenon would be a square bilayer, which has two equally probable bending directions. Allowing one set of parallel edges to bend before the other would result in the square bending along that edge. For rectangular shapes as the ones used in our experiments, there is only a single preferred bending direction along the short axis, which makes our swelling process non path-dependent. Additional work is currently being conducted to better understand the influence of the assumptions taken in the model. For example, our model does not take into account the changes of mechanical properties of the two layers during swelling, and uses instead the elastic Young's modulus found for the swollen polymer networks as a constant value during the growing.

It is, however, not entirely clear the way hydrogels behave during swelling. In this phase, while the layers are expanding, the mechanical properties change, due to the increasing percentage of water that is embedded in the system, and decreasing polymer volume ratio, as predicted by rubber

elasticity theory [16]. A certainly more viscoelastic state affects the condition of the layers, thus already limiting the validity of our assumptions. Characterization of the transition of the mechanical properties is hard to achieve and limited numbers of work can be found in the literature on the problem [72] [73]. Harmon et al found a linear trend between the increase of crosslinks in the polymer network and the elastic modulus. A possible way of analyzing the problem would be to exploit the thermal sensitivity of the polymers (when possible) and characterize the temperature dependence of their mechanical properties, with the variation of the swelling degree.

However, the framework built to analyze the problem can be easily modified and improved with new characterization techniques. The results can be easily implemented in the FEM model using built-in subroutines. This flexibility, together with the more realistic approach to the modelling of the behavior of hydrogel layers, constitutes the main qualities of the proposed work. In this sense, it provides a step further toward the understanding of the full dynamics of the self-folding behavior of hydrogel bilayers.

5.8 Conclusions and Outlook

The proposed work is intended as supporting material for the platform presented in the previous chapter. It provides information about the properties that are most relevant for self-folding hydrogel systems: the swelling kinetics, the temperature dependence of the swelling ratio, the mechanical properties. Additionally, it focuses specifically on the fabrication method used for the double layers, and points out some possible consequences of the setup: the mismatch between the predicted and the final layers due to the viscosity of the solutions, the possibility of the formation of interpenetrated networks. Finally, it analyzes the modelling abilities of the Timoshenko formula for bending bilayers, and experimentally demonstrates the limitations of this approach. This constitutes a crucial conclusion, as it contrasts the majority of the works proposed in literature. Nevertheless, the lack of experimental evidence in these efforts, the frequent use of correctional parameters [47], and a correct analysis of the assumptions of Timoshenko theory are all factors that support our conclusions.

The chapter also includes preliminary results of an FEM based simulation of hydrogel bilayers, developed as a tool for a better prediction of the bending kinetics. To the best of our knowledge, only one previous publication [55] provided a complete framework predicting the final configuration of hydrogel bilayers. Our work goes in the same direction, but with different materials, by using experimental swelling and mechanical data to predict the final curvature of our microstructures.

As already mentioned, more precise studies are needed to fully support our conclusions and the proposed model. Particularly, mechanical

characterization of the hydrogel layers require more attention, in evaluating the influence of the viscoelastic components of the material, which are here neglected. Indentation [74] and a poroelastic approach to the material might generate additional supporting evidences. Additionally, a deeper study of the consequences of the interpenetration of the two layers on the swelling and mechanical properties of the resulting materials could be beneficial.

Nevertheless, the amount of data provided and the directions taken manage to give a better insight on the complexity of the problem, and hopefully will help future research and development of hydrogel folding microrobots.

5.9 Bibliography

[1] L. Ionov, *Adv Funct Mater* **2013**, 23, 4555.

[2] L. Ionov, S. Zakharchenko, G. Stoychev, *Adv Sci Tech* **2013**, 77, 348.

[3] G. Stoychev, S. Turcaud, J. W. C. Dunlop, L. Ionov, *Adv Funct Mater* **2013**, 23, 2295.

[4] G. Stoychev, S. Zakharchenko, S. Turcaud, J. W. C. Dunlop, L. Ionov, *Acs Nano* **2012**, 6, 3925.

[5] M. Jamal, S. S. Kadam, R. Xiao, F. Jivan, T.-M. Onn, R. Fernandes, T. D. Nguyen, D. H. Gracias, *Adv Healthc Mater* **2013**, 2,1142.

[6] S. Timoshenko, *J Opt Soc Am Rev Sci* **1925**, 11, 233.

[7] M. C. Rubinstein, R. H., *Polymer Physics, Oxford University Press,* New York **2003**.

[8] A. S. Hoffman, *Adv Drug Deliver Rev* **2002**, 54, 3.

[9] K. D. Matyjaszewski, T. P, *Handbook of Radical Polymerization*, John Wiley & Sons, Inc., Hoboken, NJ, USA **2003**.

[10] C. Decker, K. Moussa, *J Coating Technol* **1993**, 65, 49.

[11] K. T. Nguyen, J. L. West, *Biomaterials* **2002**, 23, 4307.

[12] N. A. Peppas, P. Bures, W. Leobandung, H. Ichikawa, *Eur J Pharm Biopharm* **2000**, 50, 27; B. V. Slaughter, S. S. Khurshid, O. Z. Fisher, A. Khademhosseini, N. A. Peppas, *Adv Mater* **2009**, 21, 3307.

[13] P. J. Flory, J. Rehner, J Chem Phys **1943**, 11, 512; P. J. Flory, J. Rehner, *J Chem Phys* 1943, 11, 521.

[14] N. A. Peppas, E. W. Merrill, *J Appl Polym Sci* **1977**, 21, 1763.

[15] L. Brannonpeppas, N. A. Peppas, *Chem Eng Sci* **1991**, 46, 715.

[16] P. J. Flory, *Polym J* **1985**, 17, 1.

[17] A. K. Bajpai, S. K. Shukla, S. Bhanu, S. Kankane, *Prog Polym Sci* **2008**, 33, 1088.

[18] R. W. Korsmeyer, R. Gurny, E. Doelker, P. Buri, N. A. Peppas, *Int J Pharmaceut* **1983**, 15, 25.

[19] P. L. Ritger, N. A. Peppas, *Journal of Controlled Release* **1987**, 5, 23.

[20] P. L. Ritger, N. A. Peppas, *Journal of Controlled Release* **1987**, 5, 37.

[21] A. R. Berens, H. B. Hopfenberg, *Polymer* **1978**, 19, 489.

[22] N. A. Peppas, J. J. Sahlin, *Int J Pharmaceut* **1989**, 57, 169.

[23] T. Tanaka, D. J. Fillmore, *J Chem Phys* **1979**, 70, 1214.

[24] T. Komori, R. Sakamoto, *Colloid Polym Sci* **1989**, 267, 179.

[25] G. W. Scherer, *J Non-Cryst Solids* **1986**, 87, 199.

[26] N. Bouklas, R. Huang, *Soft Matter* **2012**, 8, 8194.

[27] J. W. Yoon, S. Q. Cai, Z. G. Suo, R. C. Hayward, *Soft Matter* **2010**, 6, 6004; C. Y. Hui, V. Muralidharan, *J Chem Phys* **2005**, 123.

[28] D. A. Carr, N. A. Peppas, *Macromol Biosci* **2009**, 9, 497.

[29] R. Ricciardi, F. Auriemma, C. De Rosa, F. Lauprêtre, *Macromolecules* **2004**, 37, 1921.

[30] Y. E. Shapiro, *Prog Polym Sci* **2011**, 36, 1184.

[31] M. L. Kraft, D. J. Beebe, J. S. Moore, *1st Annual International Ieee-Embs Special Topic Conference on Microtechnologies in Medicine & Biology, Proceedings* **2000**, 340.

[32] J. Kobayashi, T. Okano, *Sci Technol Adv Mat* **2010**, 11.

[33] R. P. Apkarian, E. R. Wright, *Microsc Microanal* **2005**, 11, 1088.

[34] K. E. Crompton, R. J. Prankerd, D. M. Paganin, T. F. Scott, M. K. Horne, D. I. Finkelstein, K. A. Gross, J. S. Forsythe, *Biophysical Chemistry* **2005**, 117, 47.

[35] J. Chen, Y. Pei, L. M. Yang, L. L. Shi, H. J. Luo, *Macromol Symp* **2005**, 225, 103.

[36] W. S. Cai, R. B. Gupta, J Appl Polym Sci **2002**, 83, 169; Y. Kaneko, K. Sakai, A. Kikuchi, Y. Sakurai, T. Okano, *Macromolecular Symposia* **1996**, 109, 41.

[37] A. A. Naddaf, H. J. Bart, *Polymer Networks* **2011**, 306-307.

[38] T. Canal, N. A. Peppas, *J Biomed Mater Res* **1989**, 23, 1183.

[39] T. Çaykara, R. İnam, *J Appl Polym Sci* **2004**, 91, 2168.

[40] P. Costa, J. Manuel, S. Lobo, *Eur J Pharm Sci* **2001**, 13, 123.

[41] N. S. Satarkar, J. Z. Hilt, *Acta Biomater* **2008**, 4, 11.

[42] X. M. Chen, A. C. Dunn, W. G. Sawyer, M. Sarntinoranont, *J Biomech Eng-T Asme* **2007**, 129, 156.

[43] R. A. Mirshams, R. M. Pothapragada, *Acta Mater* 2006, 54, 1123.

[44] J. Wang, V. M. Ugaz, *Electrophoresis* **2006**, 27, 3349.

[45] N. Adrus, M. Ulbricht, *React Funct Polym* **2013**, 73, 141.

[46] L. Ionov, *Macromol Chem Phys* **2013**, 214, 1178.

[47] J. J. Guan, H. Y. He, D. J. Hansford, L. J. Lee, *J Phys Chem B* **2005**, 109, 23134.

[48] M. Christophersen, B. Shapiro, E. Smela, *Sensor Actuat B-Chem* **2006**, 115, 596.

[49] B. Shapiro, E. Smela, *J Intel Mat Syst Str* **2007**, 18, 181.

[50] T. S. Kelby, M. Wang, W. T. S. Huck, *Adv Funct Mater* **2011**, 21, 652.

[51] K. Baek, J. H. Jeong, A. Shkumatov, R. Bashir, H. Kong, *Adv Mater* **2013**, 25, 5568.

[52] E. Palleau, D. Morales, M. D. Dickey, O. D. Velev, *Nat Commun* **2013**, 4.

[53] Z. Ding, Z. Liu, J. Hu, S. Swaddiwudhipong, Z. Yang, *Int J Solids Struct* **2013**, 50, 2610; X. X. Zhang, T. F. Guo, Y. W. Zhang, *J Appl Phys* **2011**, 109.

[54] S. Alben, B. Balakrisnan, E. Smela, *Nano Lett* **2011**, 11, 2280.

[55] M. Jamal, S. S. Kadam, R. Xiao, F. Jivan, T. M. Onn, R. Fernandes, T. D. Nguyen, D. H. Gracias, *Adv Healthc Mater* **2013**, 2, 1142.

[56] W. Guo, M. E. Li, J. X. Zhou, *Smart Mater Struct* **2013**, 22.

[57] S. Fusco, M. S. Sakar, S. Kennedy, C. Peters, R. Bottani, F. Starsich, A. Q. Mao, G. A. Sotiriou, S. Pané, S. E. Pratsinis, D. Mooney, B. J. Nelson, *Adv Mater* **2014**, 26, 952.

[58] C. Peters, S. Fusco, Y. Li, S. Kuhne, B. J. Nelson, C. Hierold, *Procedia Engineer* **2012**, 47, 1219.

[59] M. Bae, R. A. Gemeinhart, R. Divan, K. J. Suthar, D. C. Mancini, *J Vac Sci Technol B* **2010**, 28, C6p24.

[60] C. Fanger, H. Wack, M. Ulbricht, *Macromol Biosci* **2006**, 6, 393.

[61] N. A. Peppas, H. J. Moynihan, L. M. Lucht, *J Biomed Mater Res* **1985**, 19, 397.

[62] S. Lin, N. Sangaj, T. Razafiarison, C. Zhang, S. Varghese, Pharm Res-Dord **2011**, 28, 1422; C. S. Bahney, T. J. Lujan, C. W. Hsu, M. Bottlang, J. L. West, B. Johnstone, *Eur Cells Mater* **2011**, 22, 43.

[63] T. Çaykara, S. Kiper, G. Demirel, S. Demirci, Ç. Çakanyıldırım, *Polym Int* **2007**, 56, 275; L. Janovak, J. Varga, L. Kemeny, I. Dekany, Colloid Polym Sci **2008**, 286, 1575; D. Singh, D. Kuckling, V. Choudhary, H. J. Adler, V. Koul, *Polym Advan Technol* **2006**, 17, 186.

[64] T. G. Mezger, *The Rheology Handbook, European Coatings Tech Files*, **2011**.

[65] G. L. Puleo, F. Zulli, M. Piovanelli, M. Giordano, B. Mazzolai, L. Beccai, L. Andreozzi, *React Funct Polym* **2013**, 73, 1306.

[66] J. A. Killion, L. M. Geever, D. M. Devine, L. Grehan, J. E. Kennedy, C. L. Higginbotham, *J Mater Sci* **2012**, 47, 6577.

[67] K. Liu, T. C. Ovaert, J. J. Mason, *J Mater Sci-Mater M* **2008**, 19, 1815; T. R. Matzelle, D. A. Ivanov, D. Landwehr, L. A. Heinrich, C. Herkt-Bruns, R. Reichelt, N. Kruse, *J Phys Chem B* **2002**, 106, 2861; T. Takigawa, T. Yamawaki, K. Takahashi, T. Masuda, *Polym Gels Netw* **1997**, 5, 585.

[68] B. D. Johnson, D. J. Beebe, W. C. Crone, *Materials Science and Engineering*: C **2004**, 24, 575.

[69] B. Jeong, Y. H. Bae, S. W. Kim, *Journal of Controlled Release* **2000**, 63, 155.

[70] X. Z. Zhang, D. Q. Wu, C. C. Chu, *J Polym Sci Pol Phys* **2003**, 41, 582; N. Seddiki, D. Aliouche, *B Chem Soc Ethiopia* **2013**, 27, 447.

[71] M. E. Alf, T. A. Hatton, K. K. Gleason, *Polymer* **2011**, 52, 4429; I. Banerjee, D. Mishra, T. Das, T. K. Maiti, *J Biomat Sci-Polym E* **2012**, 23, 111.

[72] M. E. Harmon, D. Kucking, C. W. Frank, *Langmuir* **2003**, 19, 10660.

[73] C. J. Whiting, A. M. Voice, P. D. Olmsted, T. C. B. McLeish, *J Phys-Condens Mat* **2001**, 13, 1381.

[74] Y. H. Hu, J. O. You, D. T. Auguste, Z. G. Suo, J. J. Vlassak, *J Mater Res* **2012**, 27, 152.

CHAPTER 6

Ch-ch-ch-ch-changes

(turn and face the strain)

Ch-ch-changes

Just gonna have to be a different man

Time may change me

But I can't trace time

Changes-David Bowie (1971)

Morphing microrobots for medical applications: the influence of shape in drug delivery and locomotion

Work partially submitted to:

ACS applied Materials and Interfaces

Stefano Fusco, Kathrin E. Peyer, Christian Peters, Selman Mahmut Sakar, Moritz Häberli, Rocco Bottani, Anastasia Spyrogianni, Eva Pellicer, Jordi Sort, Bradley J. Nelson, Sotiris Pratsinis and Salvador Panè.

6.1 Chapter overview

A primary motivation for using smart hydrogels in the fabrication of mobile microrobots is to achieve adaptive behavior, i.e., to change the interaction of the devices with the environment depending on external stimuli and conditions. This mechanism is obviously important for living organisms and well recognizable in the animal kingdom [1, 2].

Plants also exhibit shape changes, which are involved in essential functions such as seed and pollen dispersal (squirting cucumber and exploding fruits), defense (Mimosa pudica or Kentucky bluegrass), or attack (Venus flytrap) [3]. These so called “nastic” movements are related to rapid changes in the turgor pressure of specific plant cells, and the redistribution of water in the different layers of the plants. Scaling down in size, viruses [4] and spores [5] rely on adaptive changes or mutations to survive in hostile environments, to reach target positions, and to interact with other entities.

Adaptive behavior is also an important feature for artificial systems and machines and is the focus of a huge field of research involving the development of vehicles, weapon systems, antenna structures and health monitoring devices [6]. Robots, in the same way, can be defined as autonomous intelligent systems only if they are able to react to the environment and modify their behavior [7].

Although in a different way, the self-folding microrobots presented in the previous chapters are also able to change their shape depending on environmental conditions (temperature) or on a triggered actuation (for example, by a near infrared laser shining on them). This is expected to change their behavior in terms of locomotion and actuation performance.

This chapter is intended to analyze the consequences of a conformational change for microrobots produced by the previously described photolithographic process [8]. The conformational change entails switching from a tubular shape to an open square. The focus is placed on the drag forces that oppose their propulsion by means of electromagnetic fields [9], and on their drug delivery performance.

A brief review about the role of particle shape in the biological microscale and nanoscale is presented as an introduction. This is intended to help the reader understand the advantages of the current microrobot design and the necessity for an adaptive behavior.

The aim of the chapter is then specified, focusing on two alternative designs of microdevices. Tubular microrobots were fabricated either by including graphene oxide (GO) or iron oxide superparamagnetic particles dispersed in the hydrogel matrix.

The first microdevices, being NIR light-responsive, were used for remote drug delivery applications. Their performance was studied experimentally, and the effect of light actuation and the change of shape were recorded. To give a better insight on the material properties, self-folding bilayers were compared with single responsive layers which shrunk and reduced their volume when actuated. Additionally, a simulation was used to isolate the role of the increased surface area in the diffusion-driven process.

Magnetic nanocomposite-based microrobots were fabricated to analyze their locomotion properties. A characterization of the material is proposed in terms of swelling, magnetic properties, and manipulation capabilities in the previously described Octomag setup [9]. The drag forces acting on them in a

liquid environment are influenced by the transition from a tight pipe-like shape to an open square which could be used to influence their locomotion. This aspect is analyzed by means of FEM based simulation previously used for helical swimming microrobots [10].

The end of the chapter resumes the findings and proposes a possible way to achieve a better “adaptive behavior” in intelligent hydrogel-based microrobots.

6.2. The role of shape in the microscale: natural and artificial examples

The design of a biomaterial for a specific application is a complex problem that requires an understanding of mechanics, chemistry of materials and surfaces, and physics [11]. Among the various parameters influencing the interaction with the tissues, we mainly consider stiffness, surface texture, functionalization, and the size of the artificial material. Recently, an emerging field of research focuses on studying the effect of shape and change of shape in biology and biomedical engineering with a special emphasis on the micro and nanoscale.

The discoid shape and the high deformability of red blood cells (RBC) as they pass through restrictions in the circulatory system constitute a good example of the central role of geometry in the *in vivo* micro world [12]. Their biconcave conformation seems to minimize stress and maximize laminar flow in the blood vessels [13]. Their reversible remodeling of the cytoskeleton is a crucial aspect, which allows the maintenance of a physiological viscosity of the blood tissue. The change in shape and deformability related to pathological conditions or ageing influence their ability to bypass the *in vivo* filtration mechanisms and, therefore, their biodistribution [14].

Microparticles have often been proposed for targeted drug delivery in blood vessels. Recent investigation techniques have pointed out the role of shape in their interaction with the immune system, in their biodistribution, and their ability to reach a defined target and perform an action.

Champion et al. demonstrated that macrophages and other phagocytic cells, responsible for the defensive mechanisms of vertebrate animals, are able to attach and internalize external bodies only in the presence of a certain radius of curvature at the point of first contact [15]. They designed artificial polystyrene polymer drug carriers of different shape from spheres to ellipses. Macrophages, observed by light microscopy, can internalize spheres and features with high local radius. Low curvatures and worm like structures [16] were able to almost completely inhibit the interaction with the immune cells and, therefore, circulate longer in the blood flow. Separate studies have also shown that cylindrical micelles remain in the blood flow longer than their spherical counterparts due to their more hydrodynamic morphology [17], additionally decreasing interaction with the defense immune system [18].

Non-spherical particles are more susceptible to tumble and move towards the vessel walls [19], thus making targeting of the endothelium more favorable. Once attached to the target, particle shape plays a role in the fluid dynamics interaction with the environment, thus determining the longevity of the targeted attachment.

Interaction with filtering mechanisms can also be shape-dependent. Typical examples can be found in the filtering mechanisms of the leaky vasculature of pathological tissues or in the spleen [20].

Finally, degradation of particles can differ depending on the initial condition and geometry. This was demonstrated in a drug delivery study on hemi-spherical PLGA carriers. Zero-order release, the goal of many sustained release devices, was achieved with these devices and not on comparable spherical carriers [21].

These studies were performed thanks to fabrication methods that allowed the precise definition of shape in the micro and nanoscale [22]. A relevant contribution to the field was also given by processes allowing dynamic control and switching over particle shape. The majority of these efforts rely on stimulus responsive materials arranged in order to change their shape in response to a shift of pH, temperature, or chemical concentration.

This is the case of PLGA micro/nanoparticles whose shape switch could be defined by the balance between surface tension and polymer viscosity, both controllable by the external experimental conditions [23]. Materials responsive to laser light, such as azobenzene-containing particles [24] or more *in vivo* oriented NIR light responsive nanocomposites [25], allowed additional features such as external and controlled modulation of shape switching. The same strategy has been tested for non-polymeric entities such as gold or silver nanoparticles [26]. The shape change of particles can also be attained by degradation, eroding processes [27], or guided self-assembly [28].

At a larger scale controlled self-scrolling of bilayers [29] has also recently been widely used for adapting the shape of micro devices. Most efforts have explored the potential of self-folding polymeric or non-polymeric films in drug delivery [30, 31], tissue engineering [32], biopsy encapsulation and release [33]. Only a few efforts [31, 34] have, however, concentrated on the advantages related to the control of the shape and the consequences in device performance.

6.3 Motivation: the influence of shape in drug delivery and locomotion

Multifunctional self-rolling thermoresponsive bilayers have recently been shown to be flexible platforms for robotic driven targeted drug delivery [35]. In chapter 4, GO based bilayers, responsive to NIR, have been coupled with magnetic alginate microbeads, and constituted a cell/drug delivery micro agent manipulated by external magnetic fields and actuated by short exposure to laser light. Alternatively, hydrogel magnetic nanocomposites allow magnetic manipulation and actuation by means of alternating magnetic fields, thus reversibly changing from a cylinder to an open square configuration.

Ideally, these prototypes would be able to autonomously navigate through the body fluids, recognize the target position, and, once there, deliver their payload. In the current state of research, this state of autonomy is not yet possible. However, external control on their location and their actuation can offer a good compromise. Additionally, we can exploit some smart features of the platform to allow a sort of adaptive behavior which could maximize microrobot performance. The tubular shape of the closed bilayer, for example, can be beneficial to limit spontaneous drug diffusion during travel to the target position. Moreover, the pipe-like shape minimizes the interaction with the fluids and the relative drag force during the motion. Once reaching the target position, the opening to a square conformation can be used to increase at the same time the drag force and the release due to an increase in the surface area.

This work aims at analyzing the consequences of these changes in conformation in terms of motion and actuation. We fabricated magnetic

hydrogel nanocomposites and used them in magnetic tubular bilayers that can be steered by means of an electromagnetic manipulation platform [9]. Tests on manipulation are here reported together with an analysis of their drag force in their open and closed state. An FEM-based model was developed based on previous work on helical devices [10].

In parallel, the drug delivery capability of NIR light-responsive hydrogel materials was tested, and the effect of the laser driven phase transition is reported. These materials were used to fabricate tubular bilayers, whose diffusion driven release of brilliant green (BG), a model drug, was also analyzed and compared to single layer hydrogel. Finally, a simulation on the effect of the change of conformation was proposed to clarify the influence of this phenomenon on the performance of the devices. Although proposed for millimeter sized objects, we envision that the materials and the studies here presented provide a clear step towards the fabrication of autonomous microdevices.

6.4. Materials and methods

6.4.1 Materials

N-Isopropylacrylamide monomer (NIPAAM), Acrylamide (AAM), Poly(Ethyleneglycol) Diacrylate (average MW 575, PEGDA), 2,2-dimethoxy-2 phenylacetophenone (99%, DMPA), Ethyl Lactate (98%, EL), anhydrous hexane (95%) and Brilliant Green (BG) were purchased from Sigma Aldrich (USA). 1H, 1H, 2H, 2H- Perfluorodecyltrichlorosilane (PFDTCS) and graphite powder were purchased from ABCR (Germany). The main NIPAAM monomer was recrystallized after double treatment in n-hexane solution. Graphene oxide (GO) was synthesized by controlled oxidation from graphite powder, as described in chapter 4. All other chemicals were used as received. SU-8 photoresist and developer and Lift-Off Resist (LOR), used as a sacrificial layer, were purchased from Microchem (USA), while AZ 4562 photoresist and AZ 826 developer where purchased from Clariant (Germany). Silica coated iron oxide nanoparticles (Fe203) were produced adapting the protocols described in a previous publication [36] and supplied by Anastasia Spyriogianni, PTL ETH Zurich.

6.4.2 Hydrogels fabrication

The rolled microstructures are the result of a two-step, backside exposure, photolithographic process [8] as described previously in chapter 4. The thickness of the layers was controlled using SU-8 spacers fabricated on the bottom silicon substrate, while the 2D features were designed on plastic foil masks (Selba S.A., Switzerland) and reproduced. A PEGDA solution with 3 wt% DMPA photo initiator and 50 wt. % ethyl lactate was used for the non-swelling layer and polymerized with a final nominal thickness of 10 μm. The

thermo sensitive layer was polymerized from a NIPAAM-AAM-PEGDA (molar ratio 85/15/0.4) solution with 3 wt% DMPA photoinitiator and 70 wt% ethyl lactate. Depending on the final application, 3 wt% graphene oxide (synthesis reported in chapter 4) or ~4 wt % silica coated Fe_2O_3 nanoparticles were added and dispersed into the solution by ultrasonication (4000 J, by means of a probe sonicator, SONICS, USA). The nanocomposite solution was introduced into the space between the photomask and a 40 μm thick spacer substrate after careful removal of the PEGDA unpolymerized solution. Polymerization was carried out for an additional three minutes in the case of GO and four minutes for the magnetic nanocomposite. After UV curing the cell was opened and the bilayers, attached to the mask, were released through immersion in water.

Hydrogel single layers of NIPAAM-AAM-PEGDA (molar ratio 85/15/0.4) with 3 wt% graphene oxide, used for drug delivery experiments, were fabricated by photopolymerization (3 minutes at 365 nm) between two 4-inches glass wafers separated by 180 μm thick glass spacers. The layers were allowed to swell and spontaneously detached from the glass slides. After that, cylindrical samples (3 mm diameter) were taken by using a disposable biopsy punch (Schuko, UK), deeply rinsed, and kept in ultrapure water. The same method was used to produce single layers of iron oxide nanocomposites for characterization of the magnetic performance.

6.4.3 Characterization of the magnetic nanoparticles

Particles used for the magnetic nanocomposites were partly characterized in a previous publication [36]. The dispersibility of the suspensions in ethyl lactate, the solvent used for the experiments was estimated by measuring size distributions by dynamic light scattering (DLS, Malvern Zetasizer nano series, UK). The suspensions were prepared by taking 130 mg of powder, dispersing them into 1 ml of ethyl lactate, and then sonicating them with energy density increasing from 50 to 1000 kJ/l (~30 minutes, pulse 30 seconds on, 1 second off, 95% amplitude, VCX 50, Sonics & Materials, Inc, CT, USA). The resultant solution was diluted 200 times to allow DLS analysis. The measured intensity distributions allowed the estimation of the number distribution and the Z-average particle size.

6.4.4 Characterization of the hydrogel magnetic nanocomposites

Magnetic nanocomposites were characterized in terms of swelling and magnetic properties. Swelling experiments were performed to understand the influence of the high concentration of nanoparticles on the hydration of the samples. Sections of gels of the magnetic thermoresponsive layers (a minimum of three per type) were polymerized, rinsed in ultrapure water, dried, and then allowed to swell in water. Their dried and swollen weights were recorded and the Equilibrium Swelling Ratio (ESR) defined as:

$$ESR = \frac{Ms - Md}{Md} \tag{6.1}$$

The same study was conducted on the hydrogel material, without the nanoparticles, used as control.

Magnetic hysteresis loops of the nanocomposites were measured by vibratory sample magnetometer (VSM, Oxford Instruments 1.2, and UK) by applying a magnetic field in the range between -1 and 1 T. Samples with different concentrations of nanoparticles (0.1 wt%, 1, 2, 4, 8 wt %) were considered, to find the values suitable for manipulation of the final devices. The morphology of the films was imaged by Cryo-SEM with a preparation method similar to what described in chapter 4 and 5.

6.4.5 Drug delivery experiments

Tubular-shaped hydrogel bilayers (square of 2.5 mm in open configuration) were rinsed for 24 hours after fabrication to wash away unreacted material, then dried and subsequently immersed in a 1 mM BG solution in PBS. They were allowed to swell for 24 hours, subsequently dried for 30 minutes and immersed in DI water for 1 minute to rinse the dye on the surface. Following these preparation steps, some of them were immersed in 300 µl PBS and the release of the BG embedded in the hydrogel matrices was monitored at room temperature for a period of one month. At defined times the solvent was collected and measured by UV/VIS spectroscopy (Infinite M200 Pro, Tecan AG, Mannendorf, Switzerland) at 624 nm wavelength, and finally replaced with fresh solution (in order to mimic a perfect sink condition). Release kinetics were evaluated by fitting the *in vitro* data to different empirical models using MATLAB (The mathworks, Natick, MA, USA). Similarly, a set of samples (minimum three per type) was exposed for two hours to continuous NIR laser light (wavelength 785 nm, 1.5 W power, laser spot 5 mm, SLOC lasers, China) in order to force them to stay in an open configuration. The effect on the cumulative release was monitored following the same protocol described above. Additionally, a last set of samples was exposed to short ON-OFF cycles of NIR laser light in order to

switch between open and closed configuration in a short time range (roughly two minutes).

Experiments of continuous exposure to NIR light were performed on single layers of the same light responsive material (1 mm thick, 3 mm diameter discs) and compared to control samples. Due to the bigger size, the samples released over two months. Statistical analysis of variance between the set of samples was performed with the one-way ANOVA function of MATLAB (The mathworks, Natick, MA, USA).

6.4.6 Manipulation of the magnetic hydrogel bilayers

Automated, 3D locomotion of the magnetic nanocomposite bilayers was achieved by means of the Octomag, a five degree-of-freedom (5-DOF) electromagnetic manipulation setup. The system consists of eight stationary electromagnets capable of generating multiple types of state of the art magnetic control techniques under closed.-loop control with computer vision, or visual feedback of a human operator. More information can be found in [9].

6.4.7 Simulations of the behavior of the microstructures

Finite element analysis of the drug release from folded and unfolded hydrogel tubes was performed using the commercial software Comsol Multiphysics 4.3b (Comsol, Inc, MA, USA). Fick's law of diffusion was used as governing law for the process. A hollow cylinder resembling the actual dimension of the samples (external radius 0.3 mm, internal radius of 0.14 mm, length 2.5 mm) and an open patch (square with size of 2.5 mm) were used as models, and a concentration of 1 mol/m^3 was fixed as the initial condition in the bilayers. Additionally a third model of a full cylinder with

the same volume of the first two was considered. The structures were set into a cubic cell of side length 5 mm whose initial external concentration was set to zero. The boundaries of the cubic volume of the model were set to a no-flux condition. Diffusion across the boundary between the two gels was assumed to be unobstructed. The diffusion coefficient of BG in water and hydrogels was set to the values of 1 x 10^{-9} cm^2/s (arbitrary) and 4.44x10^{-15} cm^2/s (based on the short approximation of the presented experimental results) for both the systems. A total release time of a month was simulated, and the concentration accumulated in the water volumes compared for the different models. More information about the model can be found in Appendix I.

Simulation of the drag forces acting on the hydrogel microrobots in the folded and unfolded state in the six degrees of freedom (three translations in x, y, z, three rotations in x, y, z) was compiled using the same platform (Comsol 4.3b, Inc, MA, USA). The model was built considering a cubic volume with the microstructure positioned in the middle of the space. A constant flow in the z direction of 1 μm/s constituted the simulated relative velocity of the device (the value was chosen to achieve a low Reynolds number regime). The drag forces were calculated according to the theory reported in previous work [10, 37]. Briefly, to manipulate arbitrarily shaped microrobots, their orientation-dependent dynamics is evaluated according to:

$$\vec{F}_{mag} + \vec{F}_{drag} + \vec{F}_g = m\bar{a} \tag{6.2}$$

where the first term is the magnetic force, the second is the drag force, and the third is the gravitational one acting on the microrobot and influencing its acceleration *a*. At low Reynolds number the drag force is linear:

$$\vec{F}_{drag} = -D^* \vec{v} \tag{6.3}$$

where D^* is the matrix of drag constants, and v, the relative velocity between the body and the fluid. D^* depends on the geometrical properties of the body and the coordinate frame in which the drag force is computed [38].More information on the FEM model can be found in appendix II.

6.5. Results

6.5.1 Characterization of the self-folding microtubes

A flexible and highly reproducible double step photolithographic process [8] was used to fabricate tubular hollow hydrogel bilayers (self-folded from squares of 2.5 mm size). The process allowed relative control in the final shape of the folded features by designing the 2D shape on a glass mask and setting the thickness of the two layers by means of interchangeable SU-8 spacers. No alignment was needed, due to the silane-based-driven adhesion of the hydrogels to the mask slide.

The resulting cylindrical geometry (figure 6.1) was found to have an average outer diameter of ~ 0.6 mm and 2-3 folded layers resulting in a tight configuration. A comparison between the relevant geometrical parameters of the open and closed configuration is reported in table 6.1.

	Plate	Hollow cylinder
Volume	5.62 x 10^{-1} mm^3	5.62 x 10^{-1} mm^3
Surface area	13.40 mm^2	6.72 mm^2
Surface to volume ratio	23.8 mm^{-1}	11.9 mm^{-1}
Thickness	90 µm	x
Inner radius	x	135 µm
Outer radius	x	290 µm

Table 6.1. *Comparison between the geometrical parameters of the open and closed configuration of self-folding cylinders. The values were estimated from the initial geometry of the polymerized bilayer, and from the images collected after swelling.*

An internal layer of PEGDA was first polymerized. Then, a thermo-responsive NIPAAM-AAM-PEGDA layer was used as an active layer to assure a complete folding (see figure 6.1) upon swelling. The external layer properties were tuned in order to have a high swelling ratio and a temperature of transition around 40°C. This was achieved by minimizing the quantity of crosslinking (to a value of 0.4 mol %) and copolymerizing NIPAAM with the more hydrophilic AAM (to a 15% relative molar percentage). Additional features were achieved by dispersing GO or silica coated superparamagnetic nanoparticles in the latter layer.

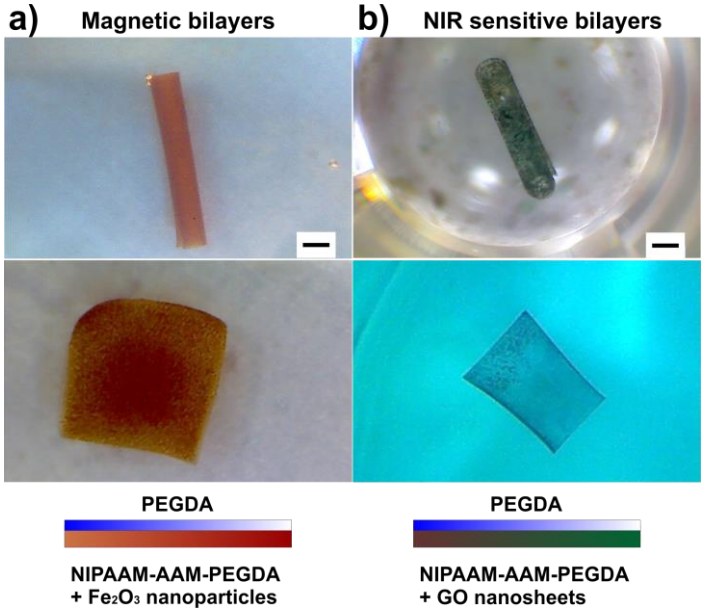

Figure 6.1. *Open and closed configuration of hydrogel nanocomposite cylindrical bilayers. a) The magnetic version is based on iron oxide nanoparticles dispersed in the polymer solution. b) An example of a NIR light responsive microtube. Scale bar is 500 µm.*

GO hydrogel nanocomposites characterization is reported in chapter 4. The nanosheets are able to disperse uniformly on the matrix networks forming NIR responsive material. The swelling ratio of the resulting nanocomposite is lower than the polymer one, indicating an influence of the GO material.

Alternatively, silica coated iron oxide nanoparticles were dispersed in the same matrix to produce magnetic nanocomposites and allow remote manipulation and actuation of the microtubes by magnetic fields. The iron oxide nanoparticles (γ-Fe_2O_3) were produced by flame spray pyrolysis and

coated with 23 wt% SiO_2 to minimize their agglomeration and increase their biocompatibility and functionality [39]. This percentage was chosen to reduce magnetic dipolar interactions without compromising their suitability for the fabrication of hydrogel nanocomposites.

The concentration, fixed at 4 wt%, was the result of a parametrical study that considered the requirements of the application (the final hydrogel based magnetic tubes were supposed to be steered by an electromagnetic manipulation system having a maximum field of 50 mT and a field gradient of 5 T/m [9, 40]) and the limitations induced by high concentration of magnetic nanoparticles into the fabrication process.

It is well-known that magnetic nanoparticles absorb UV light, which is responsible for the formation of radicals and the polymerization of the hydrogel solutions. This limits the maximum thickness of the nanocomposites, introduces localized defects, and forces a prolonged UV-exposure time. Additionally, the particle concentration influences the viscosity of the solutions creating problems of compatibility with the previously described fabrication method.

Ultrasonication was used to disperse five different concentrations of magnetic nanoparticles in the NIPAAM copolymer solution, namely 0.4, 1, 2, 4, 8 wt%. Six minutes of polymerization was found to be sufficient to create uniform layers up to 180 μm thickness for the first four cases. A concentration of 8 wt% produced thinner layers with visible agglomerations on their surfaces.

Their magnetic properties, analyzed by VSM, revealed constricted hysteresis loops at room temperature with a small coercivity on the order of

a few mT. This can be ascribed to a mixed superparamagnetic-ferromagnetic behavior arising from the coexistence of isolated nanoparticles together with small interacting agglomerates. The saturation magnetization was found to be linearly proportional to the concentration of nanoparticles in the polymer film (see table 6.2 and figure 6.2). The value at 4 wt%, corresponding to a volumetric concentration of 1%, was found equal to 0.33 emu g^{-1}. This value confirms the expected filler loading level, as the saturation magnetization of the pure particle resulted in ~30 emu g^{-1}.

Concentration (wt %)	Saturation (Emu/g)
0.4	0.002
1	0.006
2	0.142
4	0.329
8	0.658

Table 6.2. *Magnetic properties of the hydrogel nanocomposites, measured by VSM.*

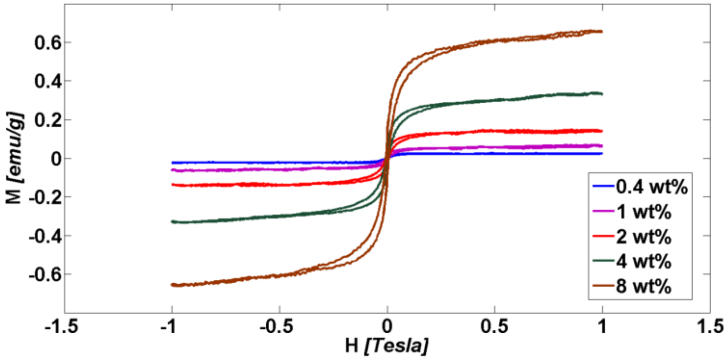

Figure 6.2. *VSM hysteresis loops for the five combinations of hydrogel nanocomposites tested. The typical soft magnetic behavior is evident in all the curves.*

The nanoparticle dispersibility in ethyl lactate, the solvent used for the preparation of the NIPAAM-based solutions, was characterized by DLS measurements. The measured Z average size, indicator of the solvated volume of the particles, was found to be 145.8±11.21 nm. The number distribution mean was calculated to be 66.13 ± 28.46 nm. These values indicate the presence of very small agglomerations (particle diameter was found to be 22.9 nm), which could not be broken with additional mixing methods. Hydrogel-nanoparticle solutions could, in any case, be prepared by ultrasonication and remained stable for more than 1 day.

Cryo-fixation was used to preserve the hydrated state of the nanocomposites and allowed imaging by SEM. As can be seen in figure 6.3, pores of the internal network of the size of ca. 20 nm are visible with a uniform distribution of the nanoparticles along the fibers of the matrix. No large agglomerates could be found during the imaging process, validating the fabrication method.

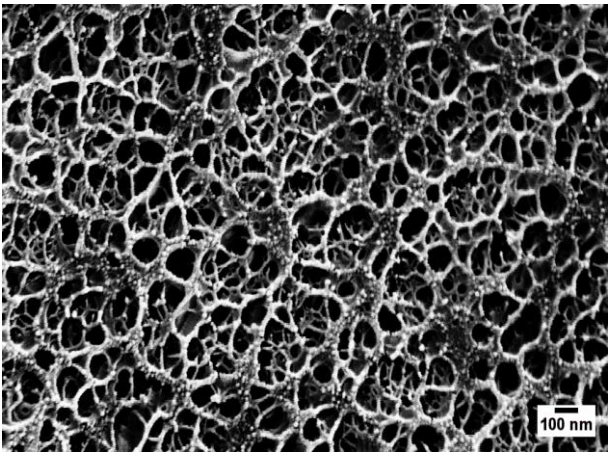

Figure 6.3. *SEM image of the network of the hydrogel nanocomposite. The white dots correspond to the magnetic nanoparticles dispersed along the fibers.*

Finally, the swelling properties of the nanocomposites were compared to nanoparticle-free hydrogel films synthesized in a similar way. The results at equilibrium (figure 6.4) showed a decrease of the ability to incorporate water of about 30%. This result contrasts with previous studies conducted on less concentrated nanocomposites [41] but could be explained by the prolonged exposition time needed for the magnetic hydrogels compared to pure polymer films. This effect, together with the presence of agglomerates, could increase the quantity of constraints inside the matrix. However, the lower swelling properties, as in the case of graphene oxide, did not influence the final design of the hydrogel-based microtubes.

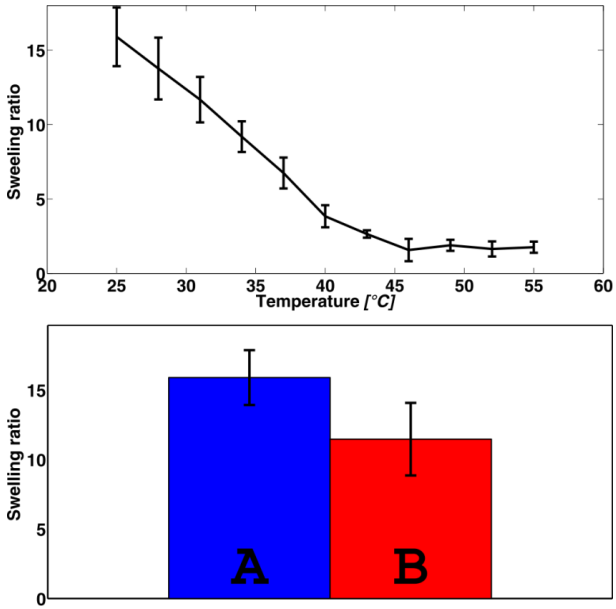

Figure 6.4. *Temperature dependence of the swelling ratio of the thermo responsive hydrogel used for the nanocomposite. In the inset, the effect of nanoparticles (red bar, B) can be seen when compared to the equilibrium swelling ratio of the polymer matrix (blue, A).*

6.5.2 Drug delivery experiments

GO single layers of NIPAAM-based nanocomposites were swollen in a solution of BG, carefully rinsed, and allowed to release the dye for a period of two months in PBS. The quantity of BG release was measured by means of spectrophotometry. A set of samples kept under constant stimulation of NIR light (785 nm) for two hours showed a significant (p=0,005, from a one-way ANOVA analysis) lower release rate (see figure 6.5a relative to the first eight hours of the experiment) when compared to non-exposed samples used

as control. The matrices appeared in a collapsed state for the duration of the experiment and released, on average, 30% less dye at the end of the first two hours. A comparable release rate between the two systems was achieved only at the end of the first eight hours of experiments. However, the curves of absolute release revealed that this initial gap was not recovered even after two months (figure 6.5b).

A completely different scenario was observed when the hydrogel self-folding micro devices were taken into consideration and exposed to different cycles of NIR light (figure 6.5c). Samples exposed to continuous stimulation changed their geometry, rapidly switching from a tubular state to an open square, thus increasing their surface area (as seen in table 6.1). Despite the collapse of the light responsive matrix, with presumably the same effects analyzed for the single layers, this transition resulted in a significant increase (more than 20%) of the fractional release for the first two hours ($p=0.025$), followed by a sort of equilibrating phase in the following two hours ($p=0.07$ at the end of the four hours), with the control samples releasing relatively more than the previously exposed samples. A more significant effect could be achieved by applying ON-OFF cycles (2 minutes on - 2 minutes off cycle) that forced the samples to alternatively open and close. This motion resulted in an increase of ca. 40% of the fractional release during the period of stimulation. The experiments were carried on for one month until the release rate for every set of samples was close to zero (figure 6.5d). Differently from the films of GO nanocomposites, the three sets of samples released a similar absolute amount of dye at the end of the analyzed timeframe proving the non-destructive nature of the actuation procedure.

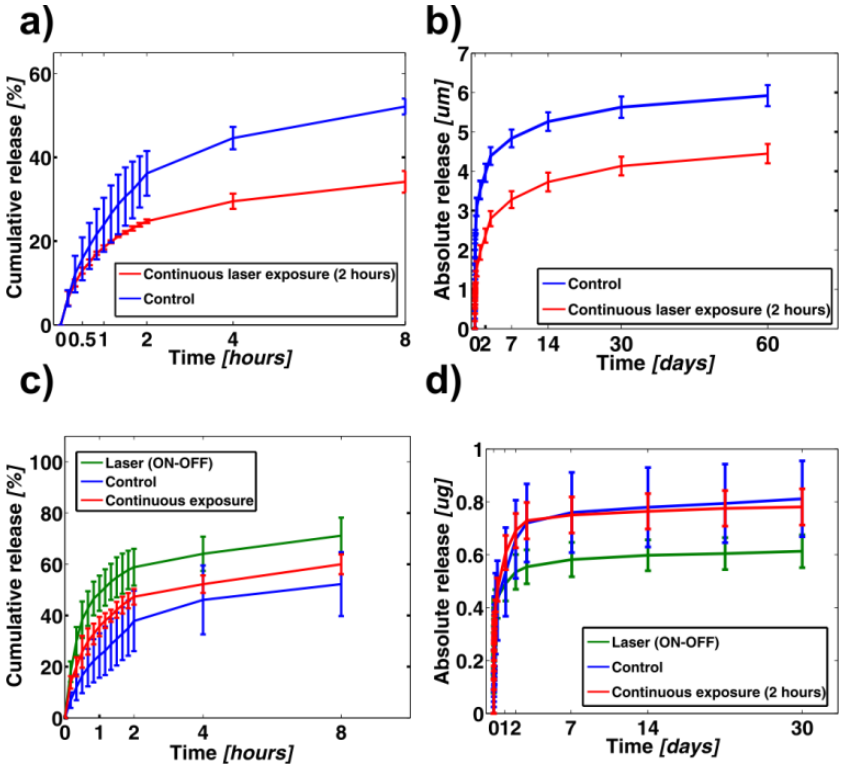

Figure 6.5. *a) and b) Drug release kinetics of GO films exposed to NIR light stimulation compared to control samples. The difference in the release can be explained by referring to the different phenomena happening during gel shrinking, including decrease of pore size, skin formation, and general decrease of surface area. c) and d) Cumulative release from morphing hydrogel microdevices. The light responsive bilayers unfold from a wrapped to an open square configuration, thereby increasing the surface area responsible for drug diffusion. Despite the contraction of the hydrogel, the general effect is a temporary increase of drug release upon unfolding. The process can be tuned by changing the exposure type and duration.*

6.5.3 Magnetic composites actuation and manipulation

Magnetic hydrogel microtubes were steered in a water environment by means of a 5-DOF electromagnetic system, the Octomag [9]. The setup could not be used with closed-loop control based on visual tracking due to the morphing geometry of the devices. However, it was possible to generate different combinations of movement either on the surface or immersed in the liquid by open loop magnetic control. Specifically it was found that magnetization of the tubes was mainly along their main axis due to their shape conformation. Translation could be achieved on the surface of water (gliding) by means of gradient fields as low as 0.1 T/m (field magnitude 5 mT). Rotation along the axis of the tubes was achieved at very low frequencies (1-2 Hz) on the water surface and immersed. In this case net motion was achieved, due to the surface effects of the walls of the experimental setup. Rotation could be also achieved along other directions which resulted in full control of the position and orientation of the devices.

6.5.4 FEM based analysis of drug release from differently shaped tubular structures

A computational analysis based on the experimental values of diffusion of the dye from the hydrogel bilayers was carried out to investigate the influence of the change of shape on the performance of tubular structures. The two geometries described before, a hollow cylinder and an open plate, were analyzed. The concentration of drugs contained in the layers at the beginning of the experiment was set equal to the maximum release of the folded bilayers, and the diffusion coefficient of the devices was fixed by analyzing the release kinetics with the methods described in chapter 5 (Ritger et al. [42]). Drug release was simulated in a water environment for a period of time

corresponding to one month. The results showed a level of release on the same order of magnitude of the experimental values, a slower kinetics, and an overestimated difference in the fractional release between the models (see figure 6.6).

Sample condition	Cumulative release after 1 month (experimental, µg)	Cumulative release after 1 month (simulation, µg)
Unfolded (Plate)	0.38 ±0.04	0.22
Folded (hollow cylinder)	0.39 ±0.07	0.21

Table 6.3. *Differences in the total release between the experimental and simulated data for the two extreme conditions of the folding microstructures.*

As a representative example, the same simulation was run for full cylinders with a tighter tube-like conformation having the same volume of the other two shapes. The fractional release in this case was again found lower than the two previous configurations.

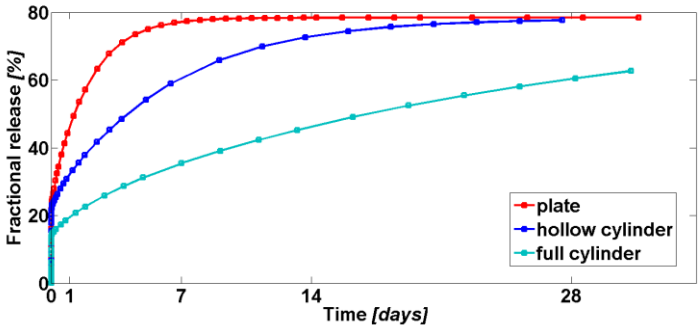

Figure 6.6. *Curves of fractional release of the cylinder and plate limited to the first 4 hours of experiments.*

6.5.5 FEM based analysis of drag forces acting on microrobots in a water flow

Figure 6.7 reports the differences in the drag forces evaluated by the Comsol model for the two configurations of the microrobots. The drag calculation was performed for a constant flow acting against a stationary microrobot, oriented along the direction of the flow (z direction) or perpendicular to it (y direction for the cylinder, xy direction for the plate). Differences could be found in general between the cylinder and the plate in both orientations. However, the most significant data involved the cylinder oriented along the flow and the plate perpendicular to it (two central columns). The simulated drag constants double when moving from the "closed "(approximately 1.0 x 10^{-5} Ns/m) to the open configuration (2.4 x 10^{-5} Ns/m, third bar in the graph) as a result of an increase of the exposed surface area.

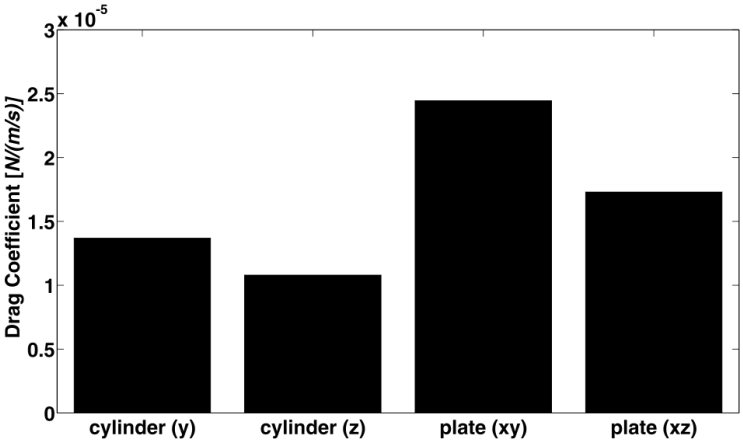

Figure 6.7. *Drag constants evaluated by simulating the forces opposing to the flow of differently oriented and shaped microstructures, and dividing them by the flow velocity.*

6.6 Discussion

Cylindrical rolled bilayers have been recently proposed for *in vivo* uniaxial sustained molecular release [31]. The work aimed at constraining the diffusional release of a PEGDA based bilayer by physically limiting the surface area exposed to the surrounding solvent. A step forward would be to develop devices able to differentiate their performance depending on requirements. This concept can be realized by exploiting responsive hydrogel bilayers whose shape could be modified from a multi-walled cylindrical configuration to an open square by increasing their internal temperature over 40 °C. The design represents a useful variation of the platform presented in chapter 4. As reported in table 6.1, these two shapes differ profoundly in terms of surface-to-volume ratio. Considering a mobile drug delivery microrobot that travels in the body fluids, reaches a target position, and releases its payload, this transition could be beneficial for two reasons: the closed, relaxed state could limit the drug loss during the transport to the location and at the same time minimize the hindrance to the liquid flow. The open configuration, achieved by activation, could be induced to maximize the release and at the same time act against further motion. The exposed principle can be compared to the action of a parachute, which exposes a high surface area against the air flow, thus limiting the landing speed.

In order to achieve this flexible behavior, this hydrogel-based platform should be fabricated according to certain requirements. Among the various criteria, already reported in chapter 4 (size of the microrobot, biocompatibility of the materials) these devices should be magnetic enough to react to the imposed fields, and they should be responsive to some kind of externally applied field which could drive the phase transition. The problem

can be modeled by decoupling these requirements. In our case we built case specific studies for drug release analysis and motion analysis. The two cases allowed us to also characterize deeper material properties of the hydrogels and nanocomposites employed during the fabrication.

Drug delivery performance was analyzed on GO nanocomposites-based bilayers fabricated according to the procedure described in chapter 4 and allowed to swell in a solution of BG dye, taken as reference of a small hydrophilic drug. In parallel, single layers of GO thermoresponsive nanocomposite (without the PEGDA layer) were also analyzed. The NIR sensitivity of these structures was ideal for testing a remotely actuated mechanism. Moreover, it is suited for *in vivo* applications because of the minimal absorption by hemoglobin and water and the consequent possibility to penetrate up to 10 cm into the tissues [43]. As recently reported [35], the layers with dispersed graphene sheets showed a high sensitivity to the light source, able to raise the temperature of the polymer networks and drive the transition to the unfolded state in less than a minute. The presence of GO partially modified the swelling properties of the hydrogel formulation by lowering its maximum swelling ability but not the transition temperature.

Depending on the physical and chemical properties of polymer networks (size of the pores, functional binding sites, size and shape), and their affinity to the model drug, the volume transition of similar hydrogel systems from a swollen to a collapsed state has been shown to induce higher [44] or reduced [45] release, when compared to a control experiment. Higher release is mainly due to a “squeezing effect” that creates a convective motion of drug molecules out of the matrix and to the aggregation of the hydrophobic polymer chains that create open channels. Additionally, the chemical transition from a hydrophilic to a dominant hydrophobic conformation

weakens the H-bonding interactions between polymer and hydrophilic drugs, thus increasing their release.

An opposite effect has been attributed to the formation of a poorly permeable skin on the collapsed matrix and to a significant decrease of the mesh size of the network, which is the representative parameter of the space available for diffusion. This was most probably the case for the single layers of GO NIPAAM nanocomposites. When stimulated continuously for two hours, they showed a significant shrinking (see figure 6.8a), and a visible reduction in the dye release. The gap in performance between the control samples and the ones exposed to light was still present at the end of the experiment (two months). This result could be the effect of a nanometric change or damage of the matrix.

Oppositely, the change in the surface area for the activated hydrogel bilayers produced a clean increase in drug release. This effect was particularly evident when analyzing the first twenty minutes of the experiment (see insert in figure 6.8b) and was enhanced by exposing the bilayers to ON-OFF cycles of the laser, thus inducing a continuous change of geometry, and, probably, a convectional flow. This increased release became less evident with time, due to the decrease in the concentration of the embedded drug, and the competing effects of reduction of the mesh size, relatively low gradient of concentration, and formation of skin effects.

To complete the analysis and elucidate the effect of change in surface area, FEM based simulations were performed on different geometries, namely a hollow cylinder, a plate and a full cylinder. The three models were built to have the same volume, initial concentration of drugs, diffusion coefficients and boundary conditions. Despite not matching the experimental results in

terms of kinetics (due to the arbitrary choice of the diffusion coefficient and the initial concentration, and the difference in the boundary conditions), the simulations show that it is theoretically possible to modulate the drug release by means of a shape change. However, in a real scenario, there are competing effects (already mentioned before), which tend to reduce the variation among different device conformations. Nevertheless, one could imagine that by playing with the shapes and the material properties a favorable release profile in the intervention site and a conformation for minimal release during the trip to the target could be achieved. Moreover, the model helped define the effect of a more compact configuration, which is experimentally achievable by over exposing the bilayers to high temperatures. Specifically, the plate configuration switched back to a tighter tube-like bilayer at temperatures higher than 50°C (as can be seen in figure 6.9). When a closed cylinder with a volume similar to the open plate was the initial geometry, it was possible to achieve much lower levels of fractional release than the two analyzed configurations in the same time range.

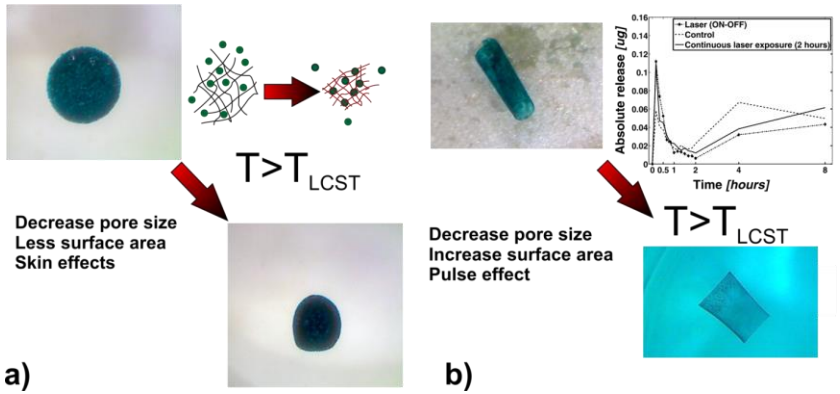

Figure 6.8. *a) Phase transition on single layers of GO nanocomposite causes a series of effects that reduce the overall drug release from the collapsed matrix. B) The change of shape for hydrogel bilayers induces an opposite mechanism due to the increased surface area. Pulse effects induced by cycles of deformation can additionally improve the performance..*

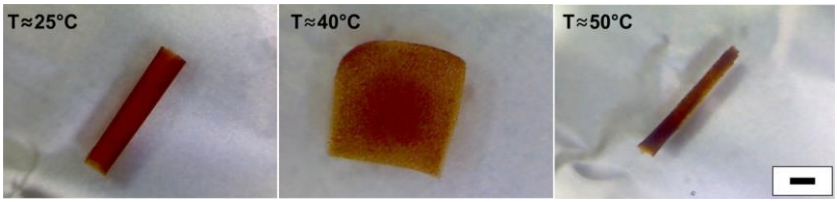

Figure 6.9. *Shape transition of a rolled microtube dependent on the external temperature. Interestingly, at temperatures higher than 45°C the tube reached a tighter conformation. Scale bar is 500µm.*

Magnetic nanoparticles were embedded in the same polymer network to produce steerable magnetic nanocomposites. This design is particularly attractive for the possibility of achieving actuation by superimposition of alternating magnetic fields, as previously described for similar materials [46].

The proposed study aimed at finding the right concentration that could provide enough magnetic material for the manipulation of the microstructures, and at the same time limit the side effects. Agglomerates, poor polymerization, and limited swelling are all cases that have been analyzed and found in some experimental cases.

Silica coated Fe_2O_3 nanoparticles (4 wt%) were found to form layers with a high degree of particle dispersion and a sufficient level of magnetization for manipulation by means of the Octomag. Interestingly, the formed bilayers were able to move on the surface and in liquid. This is probably due to the limited weight of the structures, which produce quasi buoyancy effects, as previously theorized by Palagi et al. [47].

A fluid chamber for the local control of temperature was designed for testing the change of shape and mobility of the bilayers. Despite being fabricated, it was not yet incorporated in the electromagnetic manipulation setup at the time of these experiments. Moreover, monitoring the change of speed of a travelling microrobot would require a tracking mechanism and the evaluation of all the instabilities related to the setup. As an alternative, coils for actuation by alternating magnetic fields in the current setups could be implemented in order to have motion and actuation in the same device. This will facilitate the characterization of the swimming properties of the devices.

The results of the simulation show a significant increase of the drag forces for the open plate in respect to the cylinder. This physical effect could be tuned to force the microrobot to stop in a specific position when activated or to lower its speed. Moreover, a switch from a tubular shape to a more flat configuration could improve the adhesion of drug delivery particles to the walls of a vessel [19].

All these mechanisms provide examples on how a morphing behavior could be beneficial for the performance of swimming microrobots. The relatively simple geometry of the tubes could be substituted with more elegant shapes. Magnetic helix designs have been often used for swimming devices at low Reynolds number [48] by means of rotating magnetic fields. When equipped with smart responsive hydrogels, a change of shape could be induced in order to have an optimal configuration for swimming and one not suitable for the same purpose. As an example, we propose in figure 6.10 the change of shape of a magnetic ribbon, fabricated in the same way as the rolled tubes, with decreasing temperature. Despite not being optimized, one could imagine the possibility to achieve motion by rotating magnetic fields applied to the device in the first folded state. The same stimuli could probably not provide any net motion in the last configuration.

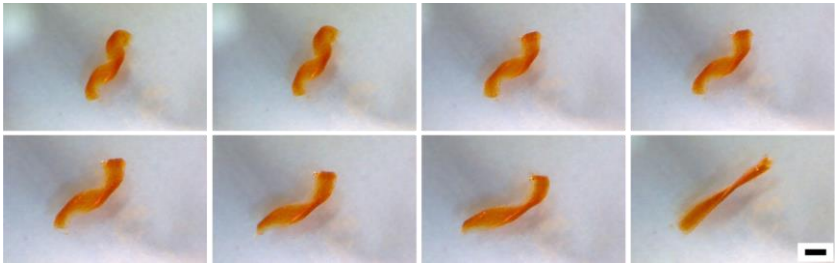

Figure 6.10. *Temperature dependent folding of a magnetic hydrogel ribbon. The gradient of temperature was set to 20°C, from 25°C (upper left image) to 45°C (lower right). Scale bar is 0.5 mm.*

6.7 Conclusions and Outlook

This chapter provides two additional examples of the significance of incorporating responsive hydrogels in microrobotic platforms. Both these examples, the drug delivery capability and the manipulation of hydrogel self-folding tubes, are the result of the possibility to control the shape of these microdevices depending on the external condition or the imposed stimulus. This feature has not yet been proposed in the field of microrobotics and is the effect of a careful choice of the material and the geometry of the devices. The proposed investigation constitutes only a suggestion for a new series of works with the final goal being the development of an autonomous microrobot.

A morphing behavior could be beneficial for this goal. For example, devices with a helical shape would be able to navigate until the external conditions are favorable (low temperature, related to a helical configuration). When in proximity to a higher temperature zone (for example an inflamed tissue) the helices would quickly unfold and no longer respond to the external rotating fields. If this effect were coupled with a significant increase in surface area, a maximum of the drug release could be achieved at the target position.

Additional studies in this direction are needed, especially towards the implementation of remote actuation mechanisms on the current manipulation platforms. These would allow the study of *in situ* effects of a change of shape in the mobility of the microrobots. Alternatively, the material design could be optimized. The bilayer structure could be used to combine a magnetic layer with a NIR light-responsive composite, so that double responsive materials could work in the current setup. Nanoparticles with higher magnetization

could allow a decrease of the side effects, or an improvement of the manipulation capabilities for the magnetic devices. In a similar way, more responsive GO (for example, obtained by a process of reduction [49]) could give the possibility to limit its percentage in the nanocomposite, with all the possible positive consequences.

This study opens new ways of designs and optimization of the current microrobotic devices, allowing us to consider a greater number of possibilities given by the intrinsic material properties. We envision that these prototypes will soon be developed and optimized for *in situ* studies of their capabilities in biological environments.

6.8 Bibliography

[1] L. Gao, S. Balakrishnan, W. K. He, Z. Yan, R. Muller, *Phys Rev Lett* **2011**, 107.

[2] H. Park, H. Choi, *J Exp Biol* **2010**, 213, 3269.

[3] Y. Forterre, J. M. Skotheim, J. Dumais, L. Mahadevan, *Nature* **2005**, 433, 421; A. G. Volkov, L. O'Neal, M. I. Volkova, V. S. Markin, *J Plant Physiol* **2013**, 170, 1317.

[4] A. Driks, *P Natl Acad Sci USA* **2003**, 100, 3007.

[5] C. M. Carr, P. S. Kim, *Cell* **1993**, 73, 823.

[6] D. P. Garg, M. A. Zikry, G. L. Anderson, *Smart Mater Struct* **2001**, 10, 610.

[7] L. Steels, *Robot Auton Syst* **1995**, 15, 3.

[8] C. Peters, S. Fusco, Y. Li, S. Kuhne, B. J. Nelson, C. Hierold, *Procedia Engineer* **2012**, 47, 1219.

[9] M. P. Kummer, J. J. Abbott, B. E. Kratochvil, R. Borer, A. Sengul, B. J. Nelson, *Ieee T Robot* **2010**, 26, 1006.

[10] K. Peyer, E. Siringil, L. Zhang, M. Suter, B. Nelson, *in Biomimetic and Biohybrid Systems*, Vol. 8064 (Eds: N. Lepora, A. Mura, H. Krapp, P. M. J. Verschure, T. Prescott), Springer Berlin Heidelberg, **2013**, 216.

[11] S. Mitragotri, J. Lahann, *Nat Mater* **2009**, 8, 15.

[12] S. Chien, *Annual Review of Physiology* **1987**, 49, 177.

[13] P. B. Canham, *J Theor Biol* **1970**, 26, 61; C. Uzoigwe, *Med Hypotheses* **2006**, 67, 1159.

[14] T. J. Merkel, S. W. Jones, K. P. Herlihy, F. R. Kersey, A. R. Shields, M. Napier, J. C. Luft, H. L. Wu, W. C. Zamboni, A. Z. Wang, J. E. Bear, J. M. DeSimone, *P Natl Acad Sci USA* **2011**, 108, 586.

[15] J. A. Champion, S. Mitragotri, *P Natl Acad Sci USA* **2006**, 103, 4930.

[16] J. A. Champion, Y. K. Katare, S. Mitragotri, *Journal of Controlled Release* **2007**, 121, 3.

[17] Y. Geng, P. Dalhaimer, S. S. Cai, R. Tsai, M. Tewari, T. Minko, D. E. Discher, *Nat Nanotechnol* **2007**, 2, 249.

[18] J. Möller, T. Luehmann, H. Hall, V. Vogel, *Nano Lett* **2012**, 12, 2901.

[19] P. Decuzzi, R. Pasqualini, W. Arap, M. Ferrari, *Pharm Res-Dord* **2009**, 26, 235.

[20] S. M. Moghimi, A. C. Hunter, J. C. Murray, *Pharmacol Rev* **2001**, 53, 283.

[21] M. Dunne, O. I. Corrigan, Z. Ramtoola, *Biomaterials* **2000**, 21, 1659.

[22] L. Tao, W. Hu, Y. L. Liu, G. Huang, B. D. Sumer, J. M. Gao, *Exp Biol Med* **2011**, 236, 20.

[23] J. W. Yoo, S. Mitragotri, *P Natl Acad Sci USA* **2010**, 107, 11205; K. J. Lee, J. Yoon, S. Rahmani, S. Hwang, S. Bhaskar, S. Mitragotri, J. Lahann, *P Natl Acad Sci USA* **2012**, 109, 16057.

[24] Y. Li, Y. He, X. Tong, X. Wang, J Am Chem Soc **2005**, 127, 2402; N. Anwar, T. Willms, B. Grimme, A. J. C. Kuehne, *Acs Macro Lett* **2013**, 2, 766.

[25] X. Huang, Q. Qian, X. Zhang, W. Du, H. Xu, Y. Wang, *Part Part Syst Char* **2013**, 30, 235.

[26] G. P. Lee, A. I. Minett, P. C. Innis, G. G. Wallace, *J Mater Chem* **2009**, 19, 8294; S. Link, C. Burda, B. Nikoobakht, M. A. El-Sayed, *J Phys Chem B* **2000**, 104, 6152.

[27] D. Klinger, K. Landfester, *Soft Matter* **2011**, 7, 1426; D. K. Hwang, J. Oakey, M. Toner, J. A. Arthur, K. S. Anseth, S. Lee, A. Zeiger, K. J. Van Vliet, P. S. Doyle, *J Am Chem Soc* **2009**, 131, 4499.

[28] T. D. Nguyen, E. Jankowski, S. C. Glotzer, Acs Nano **2011**, 5, 8892; K. L. Kohlstedt, S. C. Glotzer, *Phys Rev E* 2013, 87, 032305.

[29] L. Ionov, *Soft Matter* **2011**, 7, 6786; L. Ionov, *Adv Funct Mater* **2013**, 23, 4555; C. L. Randall, E. Gultepe, D. H. Gracias, *Trends Biotechnol* **2012**, 30, 138.

[30] R. Fernandes, D. H. Gracias, *Adv Drug Deliver Rev* **2012**, 64, 1579.

[31] K. Baek, J. H. Jeong, A. Shkumatov, R. Bashir, H. Kong, *Adv Mater* **2013**, 25, 5568.

[32] S. Pedron, S. van Lierop, P. Horstman, R. Penterman, D. J. Broer, E. Peeters, *Adv Funct Mater* **2011**, 21, 1624; S. Zakharchenko, N. Puretskiy, G. Stoychev, M. Stamm, L. Ionov, *Soft Matter* **2010**, 6, 2633.

[33] E. Gultepe, J. S. Randhawa, S. Kadam, S. Yamanaka, F. M. Selaru, E. J. Shin, A. N. Kalloo, D. H. Gracias, *Adv Mater* **2013**, 25, 514; T. G. Leong, C. L. Randall, B. R. Benson, N. Bassik, G. M. Stern, D. H. Gracias, *P Natl Acad Sci USA* **2009**, 106, 703.

[34] H. Y. He, J. J. Guan, J. L. Lee, *Journal of Controlled Release* **2006**, 110, 339.

[35] S. Fusco, M. S. Sakar, S. Kennedy, C. Peters, R. Bottani, F. Starsich, A. Mao, G. A. Sotiriou, S. Pané, S. E. Pratsinis, D. Mooney, B. J. Nelson, *Adv Mater* **2014**, 26, 952.

[36] A. Teleki, M. Suter, P. R. Kidambi, O. Ergeneman, F. Krumeich, B. J. Nelson, S. E. Pratsinis, *Nanotech Conference & Expo 2009, Vol 1, Technical Proceedings* **2009**, 71.

[37] H. Marino, C. Bergeles, B. J. Nelson, 2012 *Ieee International Conference on Robotics and Automation (Icra)* **2012**, 2498.

[38] Happel, J. B., H., *Low Reynolds number hydrodynamics*. *Springer Netherlands: The Hague*, **1983**; Vol. 1.

[39] A. H. Lu, E. L. Salabas, F. Schuth, *Angew Chem Int Edit* **2007**, 46, 1222.

[40] S. Schuerle, S. Erni, M. Flink, B. E. Kratochvil, B. J. Nelson, *Ieee T Magn* **2013**, 49, 321.

[41] R. A. Frimpong, S. Fraser, J. Z. Hilt, *J Biomed Mater Res A* **2007**, 80A, 1.

[42] P. L. Ritger, N. A. Peppas, *Journal of Controlled Release* **1987**, 5, 23.

[43] R. Weissleder, *Nat Biotechnol* **2001**, 19, 316.

[44] X. Ma, L. Dong, X. Ji, Q. Li, Y. Gou, X. Fan, M. Wang, Y. Di, K. Deng, *J Sol-Gel Sci Technol* **2013**, 68, 356; K. Deng, H. Zhong, X. Zheng, X. Song, H. Tian, P. Zhang, X. Ren, H. Wang, Polym *Advan Technol* **2010**, 21, 584; Y. Bae, T. Okano, S. Kirn, *Pharm Res-Dord* **1991**, 8, 624.

[45] N. S. Satarkar, J. Z. Hilt, *Acta Biomater* **2008**, 4, 11; C. S. Brazel, N. A. Peppas, *Journal of Controlled Release* **1996**, 39, 57; R. Dinarvand, A. D'Emanuele, *Journal of Controlled Release* **1995**, 36, 221.

[46] N. S. Satarkar, J. Z. Hilt, *Journal of Controlled Release* **2008**, 130, 246.

[47] S. Palagi, B. Mazzolai, C. Innocenti, C. Sangregorio, L. Beccai, *Appl Phys Lett* **2013**, 102, 124102.

[48] K. E. Peyer, L. Zhang, B. J. Nelson, *Nanoscale* **2013**, 5, 1259; S. Tottori, L. Zhang, F. M. Qiu, K. K. Krawczyk, A. Franco-Obregon, B. J. Nelson, *Adv Mater* **2012**, 24, 811; L. Zhang, J. J. Abbott, L. X. Dong, B. E. Kratochvil, D. Bell, B. J. Nelson, *Appl Phys Lett* **2009**, 94; K. E. Peyer, S. Tottori, F. M. Qiu, L. Zhang, B. J. Nelson, *Chem-Eur J* **2013**, 19, 28.

[49] B. Adhikari, A. Biswas, A. Banerjee, *Acs Appl Mater Inter* **2012**, 4, 5472.

CHAPTER 7

It's the end of the world as we know it

It's the end of the world as we know it

It's the end of the world as we know it

And I feel fine.

It’s the end of the world as we know it (and I feel fine)-REM (1987)

7.1 Conclusions

Medical microrobotics is a multidisciplinary field that covers aspects of mechanics, physics, microfabrication, biology, medicine, computer vision, and automation. The overall goal consists of providing treatments of pathological conditions in a minimally invasive way, or to enhance the possibilities or the precision of current medical procedures. Micro- and nanorobots would be able to precisely reach confined locations of the human body and perform their medical tasks at target areas. These tasks may include releasing drugs or cells, realizing small surgical interventions, or providing sensory feedback [1]. "Intelligence" is needed to sense the exact location and operate according to requirements. The current state of the art in the field strongly relies on the deterministic control of the position and motion of relatively simple effectors by means of electromagnetic fields. Complex platforms have been developed to provide motion in 3D environments [2] [3] as well as visual or magnetic feedback of their position and orientation. Some examples are related to the *in vitro* and *ex vivo* studies conducted in areas like the posterior segment of the eye [4] or the small vessels of the vascular network [5] with the use of tiny elliptical magnets or microparticles. Most efforts have focused on propulsion and control challenges. Requirements such as biocompatibility, interaction with human tissues, as well as embedded intelligent mechanisms of sensing and actuation remain to be considered.

Soft, smart materials appear to be ideal for these proposed tasks. Softness and deformability is a property currently being investigated in areas such as electronics [6], energy harvesting [7], MEMS fabrication [8], and robotics [9].

Hydrogels are polymer networks undergoing large volumetric changes upon solvent adsorption and resemble biological tissues in their consistence and mechanics [10]. Because of their intrinsic properties, they have been used in tissue engineering, drug delivery, and regenerative medicine. Their properties are easily tunable during their synthesis and can be enhanced by the inclusion of nanomaterials [11]. Some of them can be used as sensors, or remotely controlled platforms, thanks to their smart behavior [12].

The work presented in this thesis focused on the development of smart hydrogel based microrobots. The rationale behind this choice was the possibility to intrinsically satisfy the requirements previously mentioned for medical applications, such as biocompatibility, soft interaction with biological tissues, and smartness, by choosing the right materials. The challenges included the relatively limited techniques for the fabrication of appropriate 3D hydrogel platforms, the incorporation of hydrogel parts on hard bodies, and the nature of the materials in terms of poor adhesion and limited mechanical properties. The final goal was to provide features that could range from a deterministic magnetotactic external control of the microrobots to environmental and semi-autonomous behavior requiring limited intervention by external users.

A first experimental part of the thesis (chapter 3) deals with the definition of a method for the incorporation of smart hydrogel layers on hard microrobotic bodies. Considering the complexity of the shape of these devices, the fabrication issues, and the need for a flexible platform, electrodeposition was found to be a suitable method for the creation of smart coatings. Chitosan, a pH responsive polymer able to form hydrogels at pH > 6.3 [13], could be firmly deposited on hard substrates from water based solutions due to the electro induced electrolysis of water and the creation of

a pH gradient on the cathode [14]. The material and the method were used to fabricate smart drug delivery coatings for targeted therapies in the eye [15]. The process was tested on flat gold surfaces and successfully implemented on tubular millimeter sized implants. Chitosan layers could be deposited in a linear and repeatable fashion. The layers ensured sustained and significant release of a model drug, incorporated during deposition, for a period up to four weeks at physiological pH (7.4). The kinetics could be varied thanks to simple dip coating processes not involving toxic chemicals. Crosslinking was achieved by electrostatic interaction with sodium trypolyphosphate (TPP). An increase in swelling properties was possible by short immersion in sodium hydroxide (NaOH) solution. A smart environmental behavior was demonstrated by analyzing the release of the drug in simulated pathological conditions (pH 6.0 similar to the ones that can be found in tumor tissues or inflamed areas [16]). In this case, the fast dissolution of the chitosan matrix allowed a release ten times faster than in the "physiological" conditions. The platform, developed for chitosan, could be easily adapted to other similar biological polymers such as alginate, or combined with synthetic materials added in the deposition bath, or chemically attached to the saccharide polymer backbone [17].

Next (chapter 4), we investigated the fabrication of 3D hydrogel microrobots that could be successfully steered in fluids by means of electromagnetic manipulation systems [2, 18]. The devices were required to be magnetic, to be able to carry drugs or cells, and to release them by means of an external remote actuation. The final design relied on the presence of magnetic alginate coated microbeads as propellers and cell carriers wrapped into a self-folding, near infrared light responsive hydrogel bilayer. This layer had the double function to protect the cell carriers from direct attack from the

immune response and to act as a remotely controlled delivery device with drugs absorbed into its matrix [19].

Magnetic beads with size varying from 10 to less than 100 μm were produced by controlled drop-wise reaction of a solution of alginate and iron oxide with calcium ions. Cells could be successfully introduced during the fabrication and were shown to proliferate with no adverse effects introduced by the materials or the methods.

The external double layer was created by exploiting a two-step photolithographic process [20] specifically designed for these applications. The process allows for high throughput production of a variety of features, from jellyfish like containers, to tubes, to spheres or Venus flytrap-like shells. An internal layer of poly(ethylenglycol) diacrylate (PEGDA) constituted the biocompatible barrier between the internal payload and the external environment. A thermo responsive N-isopropylacrylamide (NIPAAM) based hydrogel solution, specifically tuned to have a phase transition over 40°C, was used together with a graphene oxide (GO) nanosheets dispersion to achieve a near infrared (NIR) light responsive layer. This kind of stimulation was chosen as a biocompatible and non-invasive source of actuation [21], and successfully tested on hydrogel nanocomposites. Single layers were able to collapse within tens of seconds of exposure to a 1.5 W commercial laser. Nanocomposites coupled to PEGDA in self-folding layers changed conformation from a closed folded state to an open shape in a similar way.

The layers were characterized in terms of temperature response, cytocompatibility (completely inert behavior), incorporation of microbeads, and manipulation. Complex magnetic steering was possible due to gradient propulsion and rotational frequencies controlled by the Octomag system [2].

Remote actuation and release of the microbeads was achieved inside the experimental field of the manipulation setup.

Considering the potential of the design and the relative novelty of the field of self-folding hydrogel bilayers [22], the fabrication method and the materials were further exploited. The goal of the third experimental part of the thesis (chapter 5) was to characterize the swelling and mechanical properties of the two layers in order to model their behavior and predict the degree of folding of bilayers with different thickness and shapes.

A number of previous publications [23] considered the classical model of Timoshenko for predicting the rate of bending of hydrogel bilayers [24]. However, a brief theoretical analysis of the assumptions reveals that large deformations, the nonlinear expansion ratio, and the mechanics of hydrogel layers cannot be well represented by this model. An experimental study was conducted to demonstrate our conclusions. Swelling was measured by *in situ* visualization of the time dependent growth of hydrogel samples of the two layers by means of a digital camera. Mechanical characterization was performed by rheometry and uniaxial tensile testing. The first set of results revealed the elastic nature of the swollen hydrogels, while the second test provided information about the Young's moduli (E~ 5 kPa for NIPAAM, and E~5-10 MPa for PEGDA) and the temperature dependent increase of stiffness (4x) of the NIPAAM layer. *In situ* characterization of the folding of bilayers with different thicknesses and thickness ratio was also performed, and the experimental results were compared with the ones predicted by the Timoshenko formula. It was found that the analytical model largely overestimated the radius of curvature of the folding materials in all cases. Moreover, a clear mismatch between the behavior of the "free swelling"

hydrogels and the ones “constrained” in the bilayer configuration was found suggesting the presence of interpenetration between the polymer networks.

The experimental data were used to build a finite element method (FEM) based platform taking into consideration the realistic swelling behavior of the gels. The model constituted a much better approach to the analysis of the folding behavior and is a good starting point for the correct prediction of performance.

In chapter 6, the influence of a change in shape of self-folding hydrogel microrobots on their performance was investigated. As the devices were intended to move towards a destination and deliver the embedded drug loads in the target location, we envisioned the possibility to “force” them to optimize their motion in one configuration and their delivery efficiency in another one.

A set of experiments was carried out regarding the influence of NIR light exposure on drug delivery from rolled microtubes (height 2.5 mm, diameter ~0.6 mm). It was found that the folded configuration retained relatively more drugs than the open square one. The difference between these two states was attributed to the increase of surface area, and this conclusion was supported by FEM analysis on similar geometries. Despite being statistically significant, the real gap between the two configurations was limited by the competing effects of decrease pore size and collapse of the matrix, as demonstrated on tests on single NIR responsive layers. In this case, release was significantly hindered by exposure to the power source.

In parallel magnetic nanocomposites based bilayer tubes were fabricated and characterized. Their magnetic content was tuned in order to achieve

maneuverability in the experimental manipulation setups without limiting the actuation performance or create agglomerates. The effect of their change of shape in their manipulation was investigated by means of an FEM based model. The simulation calculated the drag forces exerted on the devices in the different configurations. The results showed the possibility of almost doubling the drag forces, and therefore, reducing the velocity of these devices when changing from a tight tube to an open square feature.

The chapter and the thesis concluded suggesting the possibility of using these changing mechanisms on more complex shapes, such as helices, to achieve higher degrees of autonomous control. These geometries have often been proposed as optimal for navigation at low Reynolds numbers [25], with the possibility to tune their swimming performance by changing the pitch angle or the length of the microdevices [26]. The fabrication of these features out of smart responsive materials, as the ones presented here, could create "intelligent" microrobots able to move until environmental conditions are favorable, i.e, until the shape remains optimal for swimming. As the shape changes to a suboptimal swimming configuration, the microrobot will then remain close to its target location, eventually accomplishing its mission.

7.2 Bibliography

[1] B. J. Nelson, I. K. Kaliakatsos, J. J. Abbott, *Annual Review of Biomedical Engineering,* Vol 12 **2010**, 12, 55.

[2] M. P. Kummer, J. J. Abbott, B. E. Kratochvil, R. Borer, A. Sengul, B. J. Nelson, *Ieee T Robot* **2010**, 26, 1006.

[3] S. Martel, *Int J Adv Robot Syst* **2013**, 10.

[4] O. Ergeneman, G. Chatzipirpiridis, J. Pokki, M. Marin-Suarez, G. A. Sotiriou, S. Medina-Rodriguez, J. F. F. Sanchez, A. Fernandez-Gutierrez, S. Pane, B. J. Nelson, *Ieee T Bio-Med Eng* **2012**, 59, 3104.

[5] S. Martel, *Control Systems, IEEE* **2013**, 33, 119.

[6] J. A. Rogers, T. Someya, Y. G. Huang, *Science* **2010**, 327, 1603; A. Nathan, A. Ahnood, M. T. Cole, S. Lee, Y. Suzuki, P. Hiralal, F. Bonaccorso, T. Hasan, L. Garcia-Gancedo, A. Dyadyusha, S. Haque, P. Andrew, S. Hofmann, J. Moultrie, D. P. Chu, A. J. Flewitt, A. C. Ferrari, M. J. Kelly, J. Robertson, G. A. J. Amaratunga, W. I. Milne, *P Ieee* **2012**, 100, 1486.

[7] R. D. Kornbluh, R. Pelrine, H. Prahlad, A. Wong-Foy, B. McCoy, S. Kim, J. Eckerle, T. Low, *Mrs Bull* **2012**, 37, 246.

[8] K. C. Cheung, P. Renaud, Proc Eur S-State Dev **2005**, 345; C. Liu, *Adv Mater* **2007**, 19, 3783; J. S. Randhawa, K. E. Laflin, N. Seelam, D. H. Gracias, *Adv Funct Mater* **2011**, 21, 2395.

[9] E. Guizzo, R. Pfeifer, Ieee Robot Autom Mag **2012**, 19; S. Kim, C. Laschi, B. Trimmer, *Trends Biotechnol* **2013**, 31, 23.

[10] N. A. Peppas, J. Z. Hilt, A. Khademhosseini, R. Langer, *Adv Mater* **2006**, 18, 1345.

[11] N. S. Satarkar, D. Biswal, J. Z. Hilt, *Soft Matter* **2010**, 6, 2364.

[12] N. Annabi, A. Tamayol, J. A. Uquillas, M. Akbari, L. E. Bertassoni, C. Cha, G. Camci-Unal, M. R. Dokmeci, N. A. Peppas, A. Khademhosseini, *Adv Mater* **2014**, 26, 85; J. F. Mano, *Adv Eng Mater* **2008**, 10, 515; S. Chaterji, I. K. Kwon, K. Park, *Prog Polym Sci* **2007**, 32, 1083.

[13] Y. Liu, X. W. Shi, E. Kim, L. M. Robinson, C. K. Nye, R. Ghodssi, G. W. Rubloff, W. E. Bentley, G. F. Payne, *Carbohyd Polym* **2011**, 84, 704.

[14] Y. Cheng, X. L. Luo, J. Betz, S. Buckhout-White, O. Bekdash, G. F. Payne, W. E. Bentley, G. W. Rubloff, *Soft Matter* **2010**, 6, 3177.

[15] S. Fusco, G. Chatzipirpiridis, K. M. Sivaraman, O. Ergeneman, B. J. Nelson, S. Pané, *Adv Healthc Mater* **2013**, 2,1037.

[16] I. F. Tannock, D. Rotin, Cancer Res **1989**, 49, 4373; R. Haas, F. Marelli-Berg, C. Mauro, *American journal of clinical and experimental immunology* **2013**, 2, 146.

[17] M. C. Lin, H. Y. Tai, T. C. Ou, T. M. Don, *Cellulose* **2012**, 19, 1689.

[18] S. Schuerle, S. Erni, M. Flink, B. E. Kratochvil, B. J. Nelson, *Ieee T Magn* **2013**, 49, 321.

[19] S. Fusco, M. S. Sakar, S. Kennedy, C. Peters, R. Bottani, F. Starsich, A. Mao, G. A. Sotiriou, S. Pané, S. E. Pratsinis, D. Mooney, B. J. Nelson, *Adv Mater* **2014**, 26, 952.

[20] C. Peters, S. Fusco, Y. Li, S. Kuhne, B. J. Nelson, C. Hierold, *Procedia Engineer* **2012**, 47, 1219.

[21] A. J. Welch, *Ieee J Quantum Elect* **1984**, 20, 1471.

[22] L. Ionov, S. Zakharchenko, G. Stoychev, Adv Sci Tech 2013, 77, 348; L. Ionov, *Adv Funct Mater* **2013**, 23, 4555.

[23] J. J. Guan, H. Y. He, D. J. Hansford, L. J. Lee, *J Phys Chem B* **2005**, 109, 23134; K. Baek, J. H. Jeong, A. Shkumatov, R. Bashir, H. Kong, *Adv Mater* **2013**, 25, 5568.

[24] S. Timoshenko, *J Opt Soc Am Rev Sci* **1925**, 11, 233.

[25] J. J. Abbott, K. E. Peyer, M. C. Lagomarsino, L. Zhang, L. X. Dong, I. K. Kaliakatsos, B. J. Nelson, *Int J Robot Res* **2009**, 28, 1434; K. E. Peyer, L. Zhang, B. J. Nelson, *Nanoscale* **2013**, 5, 1259.

[26] K. E. Peyer, S. Tottori, F. M. Qiu, L. Zhang, B. J. Nelson, *Chem-Eur J* **2013**, 19, 28; L. Zhang, J. J. Abbott, L. X. Dong, K. E. Peyer, B. E. Kratochvil, H. X. Zhang, C. Bergeles, B. J. Nelson, *Nano Lett* **2009**, 9, 3663.

APPENDIX I

Drug delivery from differently shaped microstructures: FEM model

Comsol Multiphysics 4.3b was used to compare the drug release from differently shaped microstructures, namely a hollow cylinder, a plate and a full cylinder. The size of the three geometries were taken from pictures of the real devices and fixed in order to have the same volume in all the cases. The analysis was performed in 3D in a cubic volume having a side length of 5 mm. The simulations were based on the Fick's law of diffusion (eq.S1):

$$\frac{\partial c_i}{\partial t} = D\nabla^2 c_i \qquad \text{(S1)}$$

Where *c* is the concentration of the drug and *D* is the diffusion coefficient in the solvent. For our purpose we fixed the initial concentration in the structures to the arbitrary value of 1 mol/m^3, which is similar to the experimental total release measured for all the samples analyzed. It was also assumed a diffusion coefficient for brilliant green in water of 1 x 10^{-9} m^2/s, which is reported to be a good value for small molecules. The diffusion coefficient of the drug in the polymer structure was fixed to 4.44 x 10^{-15} m^2/s, which was found by analyzing the experimental data of release from the cylinder. However, these two values can be considered arbitrary and do not influence the final observations of the model. Boundaries of the cubes were fixed to a condition of no flux in all the cases (eq.S2):

$$-n\,N_i = 0 \qquad \text{(S2)}$$

Domain probes with integration setting (integration order equal to 4) were used as tools to calculate the cumulative release of the time dependent study (1 month of release). Table 1 resumes all the geometrical and physical parameters for the three models.

Parameter	Hollow cylinder	Full cylinder	Plate
Side length	2.5 mm	2.5 mm	2.5 mm
Thickness	x	x	90 µm
Internal radius	134 µm	x	x
External radius	300 µm	267 µm	x
Full volume	0.56 nm^3	0.56 nm^3	0.56 nm^3
Diffusion coefficient water	1 x 10^{-9} m^2/s	1 x 10^{-9} m^2/s	1 x 10^{-9} m^2/s
Diffusion coefficient polymer structure	4.44 x 10^{-15} m^2/s	4.44 x 10^{-15} m^2/s	4.44 x 10^{-15} m^2/s
Initial concentration	1 mol/m^3	1 mol/m^3	1 mol/m^3
Total volume of the simulation	125 mm^3	125 mm^3	125 mm^3
Time of release	1 month	1 month	1 month

Table 1. *Geometrical and physical parameters considered for the three models*.

The volumes of the simulations were meshed with tetrahedral elements having different size depending on the regions and the domains. The internal quality evaluation of the meshing was taken into consideration to establish an appropriate number of elements for each model. As a term of comparison, mesh quality was maintained in any case above the value of 0.10 (considered acceptable for 3D models). This resulted in an average number of elements of ~400000 and a time of simulation of ~four hours per model.

Mesh refinement studies were taken into account to evaluate the effect of the maximum mesh size on the initial conditions of release (supposed equal to 0). It was found that approximating the initial concentration in the volume of release to 0 would have taken a minimum number of elements of 3×10^6, with consequent crash of the software.

In order to reduce the number of elements and provide a reasonable result and simulation, the drug release was evaluated only in the external partition of the cubic volume. An internal cube of side length 3 mm was built around the structures and the space between the two cubes was only considered in the cumulative release analysis. In this way, the computational errors related to the most sensitive meshes (around the narrow areas of the structures) were minimized and the initial concentration could be set to zero. Figure 1 represents the meshed volume of analysis for a full cylinder case.

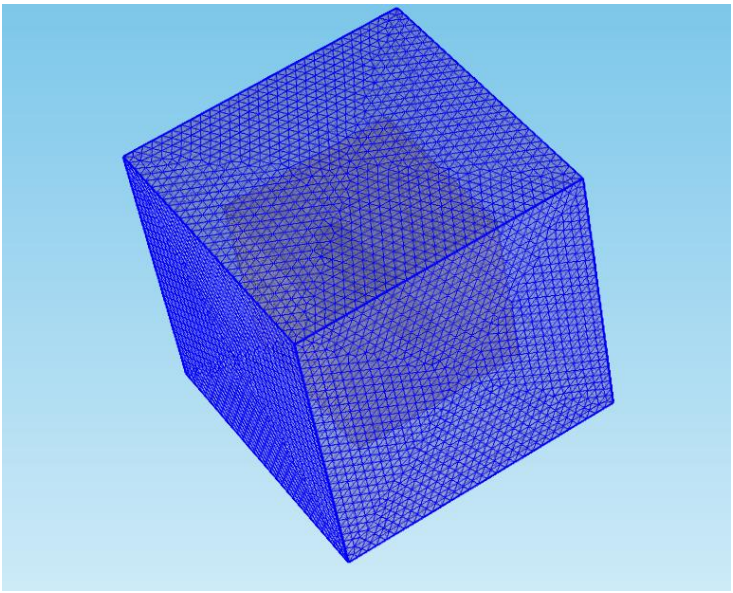

Figure 1. *Volume of analysis for the FEM simulation. The cylinder is at the center of two cubes. The calculation of the cumulative drug release is done only in the space between the cubes.*

All the simulations showed an initial concentration in the structures of ~4.30 x 10^{-10} mol, which corresponds to 82% of the theoretical ones (calculated from the volume and the initial concentration). Better results could be found for the full cylinder (4.62 x 10^{-10} mol, equal to 88% of the theoretical value) due to the less complex geometry. An initial value of ~2 x 10^{-13} mol was found in the volume of analysis for all the three cases, which was considered acceptable for our scope of interest and allowed us to make comparative analyses of the results.

APPENDIX II

Drag forces simulation

Simulations of the drag forces acting on the hydrogel microrobots were run by using the same platform (Comsol 4.3b, Inc, MA, USA). The model was built considering a cylinder with the microstructure positioned in the middle of the space. A creeping flow condition was established, which corresponds to modelling freely moving fluids using the Stokes Equations (equation S3, as conservation of the momentum and S4 as continuity equation), in very low Reynolds numbers regimes.

$$\rho\left(\frac{\partial v}{\partial t} + \vec{v} + \nabla\vec{v}\right) = -\nabla p + \mu\nabla^2\vec{v} + \vec{f} \quad \text{(S3)}$$

$$\rho\nabla\vec{\boldsymbol{v}} = 0 \quad \text{(S4)}$$

Where v is the flow velocity, ρ is the fluid density, μ is the dynamic viscosity, p the pressure, and f represents the body forces acting on the fluid. No-slip conditions were set for the boundaries of the microstructures. The cylindrical volume consisted of an inlet and an outlet, defining the flow (simulating the movement of the microrobot) and moving walls on the lateral sides (where the velocity of the walls is set to be equal to the one of the fluid, resulting in no walls effects).

The drag forces of the objects were calculated by means of integration of the total stresses acting on the microstructures and summation of the reaction forces on the same boundaries. The drag constants reported are calculated by

dividing the calculated drag forces by the velocity of the fluid. Model optimization was performed by mesh refinement and minimization of the errors between the simulated and the analytical results of the cylinder case.

Publications

International journals

S. Fusco, F. Ullrich, J. Pokki, G. Chatzipirpiridis, B. Ozkale, K. Sivaraman, O. Ergeneman, S. Pané, B. J. Nelson. “Microrobots: a new era in ocular drug delivery”. ***Informa Healthcare, Expert Opinion on Drug delivery***, 2014, accepted.

Chatzipirpiridis, G., Ergeneman, O., Pokki, J., Ullrich, F., Fusco, S., Ortega, J. A., Sivaraman, K. M., Nelson, B. J. and Pané, S. “Electroforming of Implantable Tubular Magnetic Microrobots for Wireless Ophthalmologic Applications”. ***Advanced Healthcare Materials,*** 2014, accepted.

S. Fusco, M. S. Sakar, S. Kennedy, C. Peters, R. Bottani, F. Starsich, A. Q. Mao, G. A. Sotiriou, S. Pané, S. Pratsinis, D. Mooney, B. J. Nelson, "An integrated microrobotic platform for on-demand, targeted therapeutic interventions", ***Advanced Materials***, 2014, 26 (6), 952-957.

S. Fusco, G. Chatzipirpiridis, K. Sivaraman, O. Ergeneman, B. J. Nelson, S. Pané, "Chitosan Electrodeposition for Microrobotics Drug Delivery", ***Advanced Healthcare Materials***, 2013, 2 (7), 1037-1044.

A. M. Zeeshan, S. Pané, S. K. Youn, E. Pellicer, S. Schuerle, J. Sort, S. Fusco, A. M. Lindo, H. G. Park, B. J. Nelson, "Graphite Coating of Iron Nanowires for Nanorobotic Applications: Synthesis, Characterization and Magnetic

Wireless Manipulation", ***Advanced Functional Materials***, 2013, 23, 823-831**.**

E. Pellicer, S. Pané, V. Panagiotopoulou, S. Fusco, K. Sivaraman, S. Suriñach, M. D. Baró, B. J. Nelson, J. Sort, "Localized Electrochemical Deposition of Porous Cu-Ni Microcolumns: Insights into the Growth Mechanisms and the Mechanical Performance", ***International Journal of Electrochemical Science***, 2012, 7, 4014-4029.

S. Pané, V. Panagiotopoulou, S. Fusco, E. Pellicer, J. Sort, D. Mochnacki, K. Sivaraman, B. E. Kratochvil, M. D. Baró, B. J. Nelson, "The effect of saccharine on the localized electrochemical deposition of Cu-rich Cu–Ni microcolumns", ***Electrochemistry Communications***, 2011, 13, 973-976.

International conferences

S. Fusco, M. S. Sakar, S. Kennedy, C. Peters, S. Pané, D. Mooney, B. J. Nelson, "Self-Folding Mobile Microrobots for Biomedical Applications", ***Proc. in IEEE International Conference on Robotics and Automation (ICRA2014), Hong Kong, China,*** June 2014 (Finalist for the Best Medical Paper Award).

S. Fusco, B. J. Nelson, S. Pané, "Magnetic biomedical microrobots functionalized with chitosan for targeted drug delivery", ***Proc. in 2013 MRS fall meeting & Exhibit, Boston, USA,*** December 2013.

B. J. Nelson, M. S. Sakar, S. Fusco, "Self Folding microrobots for biomedical applications", ***2013 International Workshop on Soft Robotics and Morphological Computation,*** July 2013.

S. Fusco, B. J. Nelson, S. Pané, "Electrodeposited chitosan hydrogel layers for micro robotic drug delivery", ***Proc. in XVIII World Interfinish Congress & Exhibition, Milano, Italy,*** November 2012.

C. Peters, S. Fusco, Y. Li, S. Kühne, B. J. Nelson, and C. Hierold, "Backside liquid Phase Photolitography for Fabricating self-organizing hydrogel bilayers," ***26th European Conference on Solid-State Transducers, EUROSENSOR 2012, (Procedia Engineering), Kraków, Poland,*** September 2012.

A. M. Zeeshan, K. Shou, S. Schuerle, E. Pellicer, S. Pané, J. Sort, K. Sivaraman, S. Fusco, S. Muntwyler, M. D. Baró, B. J. Nelson,

"Ferromagnetic Nanowires as Potential Drug-Delivery Wireless Nanorobots", ***Proc. of IEEE International Conference on Nano/Molecular Medicine and Engineering, HongKong/Macau*,** December 5-8, 2010.